2013-8

Grid Voltage Unbalance and The Integration of DFIG's

Joseph Kearney
Technological University Dublin, joseph.kearney@tudublin.ie

Grid Voltage Unbalance and The Integration of DFIG's

Joseph Kearney, **M.Eng.**

A thesis submitted for the degree of Doctor of Philosophy
to the Dublin Institute of Technology

Supervised by

Prof. Eugene Coyle and Dr. Michael Conlon

School of Electrical and Electronic Engineering

Dublin Institute of Technology

Kevin Street

Dublin 8

August 2013

DEDICATED TO

MY MOTHER

MY WIFE

AND

MY DAUGHTER

Abstract

Double-fed induction generators (DFIG's) became the predominant generator installed for wind generation applications in the mid 1990's. Issues pertaining to the operation and control of DFIG's subsequently became apparent, particularly in weak areas of the grid network. Ironically weak areas of the grid tend to be where the average wind speed is high and the usual location of wind farms. One of the issues that emerged was the quality of the voltage in the network at the point of common coupling (PCC) with the DFIG's. An important issue is the question of voltage unbalance at the PCC.

As part of this work, research was undertaken into the issue of voltage unbalance in a distribution network. Investigative studies were undertaken on a small wind farm connected to the Irish distribution network. The results obtained were then analysed and conclusions drawn, with recording of daily, weekly and seasonal variation of voltage unbalance. The behaviour of DFIG's to varying levels of network voltage unbalance at the wind farm was analysed, and it was observed that the DFIG's had difficulty remaining connected to the distribution network when voltage unbalance exceeded certain threshold levels.

The behaviour of DFIG's to the effects of grid network voltage unbalance is further investigated in this work. A literature review was undertaken of the effects that utility network voltage unbalance has on DFIG's. Emerging from this research, the suitability of appropriate control schemes to alleviate the problems caused by grid voltage unbalance were investigated. Control techniques to improve performance of a DFIG during conditions of asymmetrical grid voltage including measures to control the rotor-side and grid-side converters in a DFIG, were designed and then implemented in

Matlab/Simulink and results showed improved behaviour. A synchronous generator system was similarly investigated and improvements shown.

This research also includes development of a laboratory based DFIG test system. A DSP based digital microcontroller and interfacing hardware has been developed for a 5kVA DFIG laboratory based system. The system comprises of a machine set; a dc machine with common shaft coupling to a three-phase wound rotor induction machine. The dc machine emulates a wind turbine, and drives the induction machine in response to required speed. A converter has been constructed to control the rotor power of the induction machine. Interfacing schemes for the required feedback signals including voltage and current transducers and speed measurement were designed to enable control of both the rotor-side and grid-side converters of the DFIG. Grid/stator voltage oriented control is implemented to control both the rotor side and grid side converters respectively. An additional feature is the implementation of a single DSP controller, configured to control both the rotor side and grid side converters simultaneously.

Initially the DFIG test rig was tested as a standalone system, with a load bank connected to the stator terminals of the induction machine. Testing of the DFIG was also conducted with the test rig connected directly to the grid, and the system operated in sub-synchronous and super-synchronous modes of operation.

Hardware and software solutions were implemented to reasonable success. The laboratory based test rig has been designed for operation as a rotor converter for a DFIG; however the converter can also be configured to operate as a system for a synchronous generator, or for operation as a machine drive. Further research may allow the rig to be used as a DFIG/UPQC (unified power quality controller) test bed.

Declaration

I certify that this thesis which I now submit for examination for the award of Doctor of Philosophy, is entirely my own work and has not been taken from the work of others save and to the extent that such work has been cited and acknowledged within the text of my work.

This thesis was prepared according to the regulations for post graduate study by research of the Dublin Institute of Technology and has not been submitted in whole or part for an award in any other Institute or University.

The work reported on in this thesis conforms to the principles and requirements of the Institute's guidelines for ethics in research.

The Institute has permission to keep, to lend or to copy this thesis in whole or in part, on condition that any such use of the material of the thesis be duly acknowledged.

Signature _____*Joseph Kearney*_____ Date ___*8/8/2013*_____

Candidate

Acknowledgements

I would like to thank my project supervisors Dr. Michael Conlon for his help and support and Prof. Eugene Coyle for his loyalty, patience and understanding. Sincere thanks to Terry Kelly for his assistance with the test rig and all matters concerning the Electrical Energy Laboratory. I would also like to thank my office colleagues Dr. Richard Hayes and Kevin Sullivan for their support. And many thanks to friends John and Aideen for all their good wishes and moral support.

Most especially I most sincerely thank my wife and daughter for their support, patience, forbearance and love throughout the work involved in the preparation of this thesis. And also a very special thanks to my mother who always encouraged and supported me.

List of Abbreviations

ABS	Absolute Value
AC	Alternating Current
ADC	Analogue to Digital Converter
CSI	Current Source Inverter
CSS	Code Composer Studio
DAC	Digital to Analogue Converter
DC	Direct Current
DSO	Distribution System Operator
DFIG	Doubly-fed Induction Generator
DG	Distributed Generation
DSP	Digital Signal Processor
DTC	Direct Torque Control
EOC	End of Conversion
EU	European Union
EVA,B	Event Manager A, B
FOC	Field Oriented Control
FRT	Fault Ride Through
FSIG	Fixed Speed Induction Generator
IGBT	Insulated Gate Bipolar Transistor
IG	Induction Generator
IM	Induction Machine
ISR	Interrupt Service Routine
MIPS	Million Instructions Per second
PCC	Point of Common Coupling
PCB	Printed Circuit Board
p.u.	Per Unit (i.e. referred to normalised value)
PQ	Power Quality
PWM	Pulse Width Modulation
PI	Proportional Integral controller
PLL	Phase Locked Loop
SCIG	Squirrel Cage Induction Generator
SOC	Start of Conversion
SFO	Stator Flux Oriented Control

SVC	Static VAR Compensator
SVM	Space Vector Modulation
SVO	Stator Voltage Oriented Control
THD	Total Harmonic Distortion
THDv	Total Harmonic Voltage Distortion
THDi	Total Harmonic Current Distortion
TI	Texas Instruments
TSO	Transmission System Operator
UPS	Uninterruptible Power Supply
VSI	Voltage Source Inverter
WECS	Wind Energy Conversion Systems
WFPS	Wind Farm Power Stations
CWFS	Contiguous Wind Farm Site
TR	Transformer

Contents

APPENDICES 302

List of Figures

List of Tables

General conventions

The following subscripts are frequently used:

max	Maximum value for the considered variable
min	Minimum value for the considered variable
ref	Reference value for the considered variable
err	Error value for the considered variable
rated	Rated value for the considered variable
base	Base value for the considered variable
ave	Average value of the considered variable
r	Rotor; rotor reference frame
s	Stator; stationary reference frame
e	Synchronous reference frame
+	Positive component
-	Negative component
$^{+}$	Positive sequence reference frame
$^{-}$	Negative sequence reference frame

The following operators are frequently used:

*	complex conjugate;
| |	absolute value of complex (phasor) variable.

List of symbols

B	[Tesla]	-	Magnetic flux density
C_p	[-]	-	Power coefficient
C_{dc}	[-]	-	DC link capacitance
F_s	[Hz]	-	Rated stator frequency
F_r	[Hz]	-	Rotor frequency
f_{sw}	[Hz]	-	Switching frequency
H	[A/m]	-	Magnetic field strength
I_{crow}	[A]	-	Current flowing via crowbar resistor
i_{dcg}	[A]	-	DC current flowing between DC link and grid side converter
i_{dcr}	[A]	-	DC current flowing between DC link and rotor-side converter
i_s	[A]	-	Space vector of the stator current
i_r	[A]	-	Space vector of the rotor current
i_m	[A]	-	Space vector magnetizing current
$i_{\alpha s}$, $i_{\beta s}$	[A]	-	Sator α, β axis currents
$i_{\alpha r}$, $i_{\beta r}$	[A]	-	Stator α, β axis currents
i_{dr}, i_{qr}	[A]	-	Rotor-side converter current components in the two-axis (d,q) Rotational reference frame
i_{ds}, i_{qs}	[A]	-	Stator-side converter current components in the two-axis (d,q) Rotational reference frame
I_{ag}, I_{bg}, I_{cg}	[A]	-	Grid-side converter ac currents
$i_{\alpha s}$, $i_{\beta s}$	[A]	-	stator α, β axis currents
I_s	[A]	-	Stator current phasor;
I_r	[A]	-	Rotor current phasor;
J_{gen}	[kg m^2]	-	Induction generator moment of inertia
J_{dc}	[A]	-	DC machine moment of inertia
K_{gear}	[-]	-	Gearbox ratio
K_P	[-]	-	Proportional gain
K_I	[-]	-	Integral gain
L_s, L_r, L_m	[H]	-	Stator and rotor self-inductances and magnetizing inductance
L_r'	[H]	-	Rotor inductance (referred to stator quantities)
$L_{s\sigma}$, $L_{r\sigma}$	[H]	-	Stator and rotor leakage inductance
N	[-]	-	Number of turns of the induction machine

N_g	[-]	-	Generator nominal speed
N_s	[-]	-	Number of stator windings;
N_r	[-]	-	Number of rotor windings;
p	[-]	-	Number of pole pairs
P_{grid}	[W]	-	Grid-side converter active power
P_{rotor}	[W]	-	Rotor-side converter active power
P_s	[W]	-	Stator active power
$pf\__{\text{ref}}$	[W]	-	Reference power factor
P_{mech}	[W]	-	Mechanical power
P_N	[W]	-	Rated power of induction generator
R	[Ω]	-	Blade radius
R_{crow}	[Ω]	-	Crowbar resistor
R_{s}, R_{r}	[Ω]	-	Stator and rotor resistances of the phase windings
R_r'	[Ω]	-	Rotor resistance (referred to stator quantities);
R_{g}	[Ω]	-	Grid-side converter line filter resistance
L_{g}	[H]	-	Grid-side converter line filter reactance
Q_{grid}	[VAr]	-	Grid-side converter reactive power
Q_{ref}	[VAr]	-	Desired reactive power
Q_s	[VAr]	-	Stator reactive power
s	[pu]	-	Generator slip
S	[pu]	-	Apparent power
S_a, S_b, S_c	[-]	-	Switching state of the converter
T_e	[Nm]	-	Induction generator electromagnetic torque
$T_{\text{e\_ref}}$	[Nm]	-	Reference electromagnetic torque
T_{L}	[Nm]	-	Load torque

T_{shaft}	[Nm]	-	Mechanical torque of the shaft system
T_I	[S]		Integral time of PI controller
V_{crow}	[V]	-	Voltage over the crowbar resistor
V_s	[V]	-	Generator stator voltage
V_r	[V]	-	Generator rotor voltage
$V_{max,r}$	[V]	-	Generator maximum rotor voltage
V_{ph}	[V]	-	Phase voltage
V_{dc}	[V]	-	DC link voltage
V_{ag}, V_{bg}, V_{cg}	[V]	-	Grid-side converter ac voltages
$v_{\alpha s}$, $v_{\beta s}$	[V]	-	Stator α, β axis voltages
v_s, v_r	[V]	-	Pace vectors of stator and rotor voltage
v_{ds}	[V]	-	Stator voltage, *d*-component in *(d,q)*-reference frame [per unit];
v_{qs}	[V]	-	Stator voltage, *q*-component in *(d,q)*-reference frame [per unit];
v_{dr}	[V]	-	Rotor voltage, *d*-component in *(d,q)*-reference frame [per unit];
v_{qr}	[V]	-	Rotor voltage, *q*-component in *(d,q)*-reference frame [per unit];
v_∞	[m/s]	-	Wind speed
X_r'	[Ω]	-	Rotor reactance (referred to stator quantities)
X_s	[Ω]	-	Stator reactance
x_{dm}	[Ω]	-	Generator magnetising reactance, *d*-component in *(d,q)*-reference frame
x_{qm}	[Ω]	-	Generator mutual reactance, *q*-component in *(d,q)*-reference frame
x_{dr}	[Ω]	-	Generator rotor reactance, *d*-component in *(d,q)*-reference frame
x_{qr}	[Ω]	-	Generator rotor reactance, *q*-component in *(d,q)*-reference frame
x_{ds}	[Ω]	-	Generator stator reactance, *d*-component in *(d,q)*-reference frame
x_{qs}	[Ω]	-	Generator stator reactance, *q*-component in *(d,q)*-reference frame

ψ	[pu]	-	Flux linkage
ψ_s, ψ_r	[pu]	-	Space vectors of the stator and rotor flux linkages
ψ_{ds}, ψ_{qs}	[pu]	-	Generator stator direct and quadrature flux linkages *(d,q)*-reference frame
ψ_{dr}, ψ_{qr}	[pu]	-	Generator rotor direct and quadrature flux linkages *(d,q)*-reference frame
$\psi_{\alpha s}$, $\psi_{\beta s}$	[pu]	-	Stationary α, β axis stator flux
$v_{\alpha s}$, $v_{\beta s}$,	[V]	-	Stationary dq-axis voltages
λ	[-]	-	Tip speed ratio (propeller tip speed divided by wind speed)
θ	[deg]	-	Pitch angle of Blades
θ_r	[deg]	-	Generator rotor shaft position
θ_e	[deg]	-	Park's angle (angle of rotational transformation between reference frames in DFIG control - synchronous reference frame)
ρ	[kg/m³]	-	Air density
ω_e	[rad/sec]	-	Synchronous angular velocity of voltage
ω_r	[rad/sec]	-	Mechanical angular speed of the rotor shaft
ω_{sl}	[rad/sec]	-	Induction machine slip speed
σ	[-]	-	Stator and rotor reactance leakage factor
τ_s	[s]	-	Simulink discrete time step
V_w	[m/s]	-	Wind speed
R_{turb}	[m]	-	Turbine radius
C_p	[-]	-	Coefficient of performance (propeller aerodynamic efficiency)

Chapter 1 Introduction

1.1 Introduction

Developments in wind power generation techniques increased significantly in Europe in the 1980's. With respect to wind generation schemes Ireland lagged behind a number of proactive countries including Denmark and Germany, however in the early 1990's, the installation of wind power energy conversion systems (WECS) in Ireland gained momentum. Initially the majority of wind turbine installations incorporated fixed speedgenerators; however double-fed induction generators (DFIG's) became the predominant generator installed for wind generation applications in the mid 1990's.

This thesis had its genesis in initial investigations into power quality issues associated with the transmission and distribution systems in Eire. During this period it also became clear that perhaps one of the biggest issues in the general area of power quality was the connection of renewable energy generation systems, specifically wind energy conversion systems to the transmission and distribution networks. Attention was shifted to the power quality issues associated with the connection of wind energy generation to transmission and distribution networks.

According to the TSO Eirgrid [51], the current installed wind generation capacity[1] in the distribution system is 988 MW and in the transmission system 772 MW, a total capacity of 1760 MW. This is in the order of 16% of total capacity of the grid. This installed capacity is expected to rise substantially over the coming years as global trends towards a decrease in reliance on carbon fuels and an increase in sustainability become increasingly popular and necessary. This growth trend is shown in Figure 1.1, based on data obtained from Eirgrid.

[1] As of Spring 2013

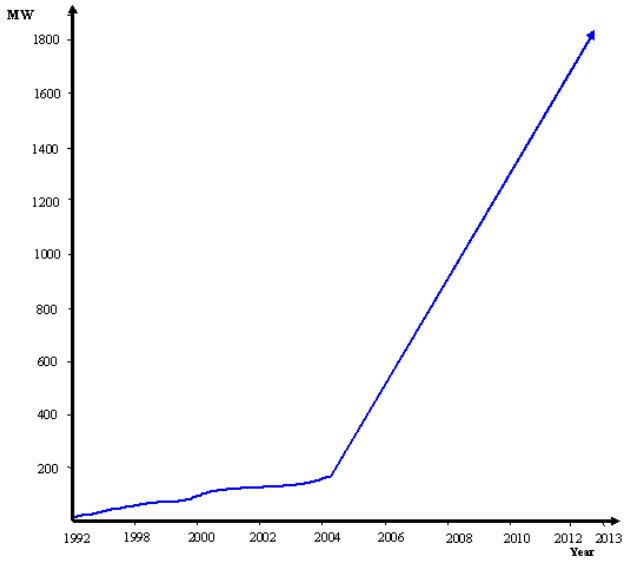

Figure 1.1 Increase in installed wind energy capacity in Eire

European targets are for 20% for all energy to come from renewable energy sources by 2020 with renewable energy contribution to gross electricity consumption of 40% by 2020 [5]. Ireland is committed to this target with the vast majority of renewable contribution coming from wind energy.

Research into the issues associated with power quality and wind-turbines involves the study of the effects of grid networks on wind turbines and the affects of wind turbines on grid networks. Power quality problems can originate in utility supply systems, due to faults or natural hazards, which can affect the operation of wind turbines. Wind turbines can also introduce poor power quality into a network. Power quality problems associated with the network can lead to tripping of individual turbines and perhaps a whole wind farm. Among the power quality issues associated with a network that can impinge on the performance and operation of wind turbines are voltage sags/swells, harmonics, flicker, transient interruptions and voltage unbalance. Each of these power quality issues was investigated to establish and understand the issues and develop a strategy for research. Collaboration with an Irish wind farm operator, Airtricity, proved beneficial. Airtricity indicated that they would welcome cooperation in investigating problems and

developments in wind energy integration into the national grid. They requested help in investigating problems they were experiencing with a small two-turbine wind-farm in County Cavan.

D.I.T in association with Premium Power plc, a company specialising in power quality issues, monitored the power quality of the wind-farm. A single ION 7600[2] Meter was connected to one turbine to monitor the power quality of the 690 V supplied to it. The generator technology connected to the turbines is the Double-Fed Induction Generator (DFIG). A report and presentation was made to Airtricity. Airtricity were happy with the investigations and further collaboration ensued. It appeared that voltage unbalance was an issue, however a comprehensive analysis of each turbine and of the 10 kV utility voltage supply was required. On our recommendations three ION 7600 [29] power quality meters were installed at the wind-farm, one meter connected to the 690 V supply of each turbine and one connected to the utility 10 kV network side of the turbine transformers. The wind-farm was monitored through a dial-up connection in a laboratory at DIT Kevin Street.

Following on from the initial investigations of the wind farm, further monitoring continued, with intent of obtaining data during the winter and spring periods when electrical demand was high. The wind-farm was monitored and data collected for real and reactive power, voltage and current from each power-quality meter. A second report was produced. Utility voltage unbalance appeared to be an issue with a number of faults and trips of the turbines. On the recommendation outlined in the report adjustments were made to the DFIG protection settings on each turbine. As a result of these adjustments downtime decreased and average power output increased.

[2] A power quality meter from Power Measurement, now under the ownership of Schneider Electric.

During this research on power quality, including the power quality assessment of a rural wind-farm in County Cavan, it was discovered that voltage unbalance in weak rural networks can result in poor performance of wind-turbines connected to it. While faults and transients will always occur in a distribution network, usually in a random fashion, voltage unbalance can be periodic or seasonal in nature. Also voltage unbalance in weak rural networks is difficult to eliminate. For these reasons a greater understanding of voltage unbalance is required and solutions required for induction-generators connected to unbalanced networks.

1.2 Research objectives

The work in this thesis focuses on the following objectives:

- Initial work:
    - Investigations of issues associated with voltage unbalance in transmission and distribution networks.
    - Improve understanding of voltage unbalance and the integration of WECS.
- DFIG and Synchronous Generator System:
    - Investigation and design of control strategies to improve performance of DFIG's and synchronous generator converter systems to grid voltage unbalance.
    - Modelling of DFIG and synchronous generator converter systems.
    - Investigation of the performance of designed systems in a network through dynamic simulations.
- Develop a laboratory based test rig system, suitable for operation as a DFIG converter, (also adaptable for other applications, including converter for

synchronous wind generator, and Variable Speed Drive (VSD) converter for induction motors), including:

- Design and development of measurement circuits and interfacing circuits for Digital Signal Processor (DSP) and power circuits of the test-rig.
- Implementation of single DSP to operate both the rotor side and grid side converters in a DFIG simultaneously.
- Design and development of software to enable operation as a DFIG. Software designed on a modular basis for ease of transferability to other applications as described.
- Testing of the converter test-rig as a DFIG under various load and supply configurations, including stand-alone mode and synchronised to the grid.

1.3 Thesis Organisation

To further this research it was necessary to conduct a literature review (Chapter 2), into the issues of voltage unbalance in distribution networks and the effect this unbalance has on wind turbines. The review focuses on voltage unbalance and its effects on induction generators, converters and double fed induction generators. Chapter 3 deals with current wind turbine technologies connected to the Irish Transmission and Distribution Network. Chapter 4 investigates the effects that voltage unbalance has on induction machines, converters and DFIG's. In Chapter 5 the induction machine steady state and dynamic equations are outlined and Chapter 6 investigates the control of DFIG's. The topology and structure of the rotor side and grid side converters are illustrated, and equations for the control of the rotor side and grid side converter are developed. Chapter 7 investigates the current status of control techniques to improve the performance of DFIG's during network voltage unbalance conditions.

Chapter 8 is devoted to the construction of a rotor converter for a laboratory based DFIG. Hardware and software details are illustrated and discussed. Testing of the test rig is documented in Chapter 9. The chapter includes details of the performance of the DFIG when connected in stand-alone mode and when synchronised to the grid. A summary of the contributions of the research in this thesis is presented in Chapter 10, including an outline of possible future research possibilities.

Chapter 2 Voltage Unbalance Literature Review

To establish where the issue of network voltage unbalance "fits" within the broader aspects of electrical power quality, the following sections provide some elucidation.

2.1 Introduction to Power Quality

The importance of power quality internationally is increasing. The term *power quality* can be used to describe any abnormal behaviour in a power system arising from voltage, frequency or current variations which adversely affects the usual operation of electrical equipment [4]. "Power quality is a set of electrical boundaries that allow a piece of equipment to function in its intended manner without significant loss of performance or life expectancy" [77]. However the work presented in this thesis is mainly associated with one area of power quality referred to as voltage unbalance or asymmetric voltage. The causes and effects of voltage unbalance will be reviewed in section 2.4**,** but before that a discussion about general aspects of network power quality is presented, particularly with respect to issues associated with the connection of wind-turbines.

2.1.2 Power Quality of Wind Turbines.

Power quality can be described in terms of issues associated with voltage, frequency and interruptions. The quality of the voltage must fulfil requirements stipulated in national and international standards. In Ireland, the Transmission Grid Code, administered by the TSO (Eirgrid) and the Distribution Code, administered by ESB Networks are the relevant codes. In these standards, voltage disturbances are subdivided into voltage variations, flicker, transients and harmonic distortion [2].

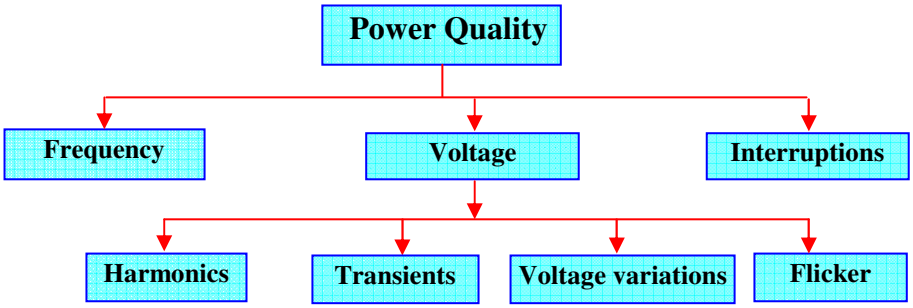

Figure 2.1 General characteristics of power quality.

Figure 2.1 provides the classification of various power quality phenomena. This thesis primarily addresses voltage issues; hence the focus will not be afforded to interruption and grid frequency variation. In general, grid-connected wind turbines can affect the quality of power in the grid, and they in turn can also be affected by poor network power quality, which will depend on the interaction between the grid and the wind turbine.

2.1.3 Voltage Sags/Dips

Voltage dips normally occur as a result of a network disturbance, with the degree of disturbance mainly determined by amplitude reduction/increase and time duration. Voltage dips are normally due to some event within the network, e.g. the occurrence and termination of a short-circuit fault or other extreme increase in current due to motor starting, transformer switching etc. In networks with wind turbines a single-phase or two-phase voltage sag or dip in the network can result in voltage unbalance at the point of common coupling with the generators.

2.2 Potential problems associated with connection to g rid.

An important feature of wind farms is their ability to deal with problems that may arise on the distribution or transmission network to which they are connected. Figure 2.2

shows how power quality issues which may originate in the transmission and distribution networks, can impact on the voltage to which turbines are connected [2].

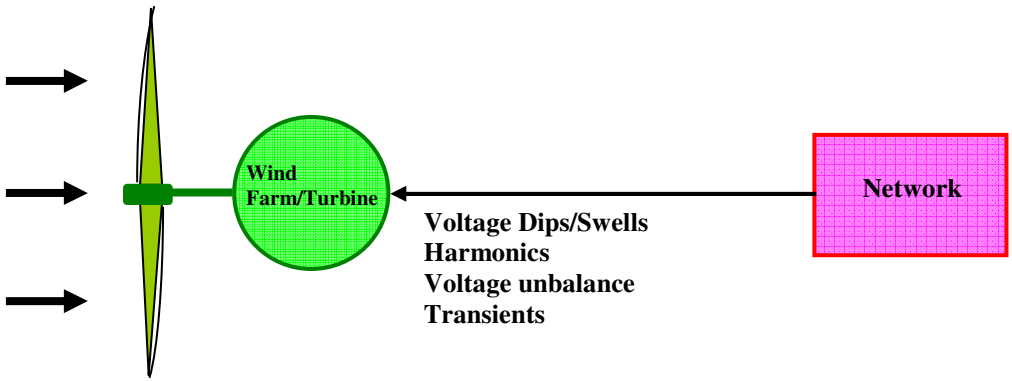

Figure 2.2 Influence of network power quality on wind farms

Such network problems can lead to tripping of individual turbines and/or an entire wind farm. One of the most important features of wind farms is their ability to ride through network faults. Figure 2.3 describes power quality effects a wind farm may impose on a distribution-transmission network, including flicker, transients, harmonics and increase in reactive power [2].

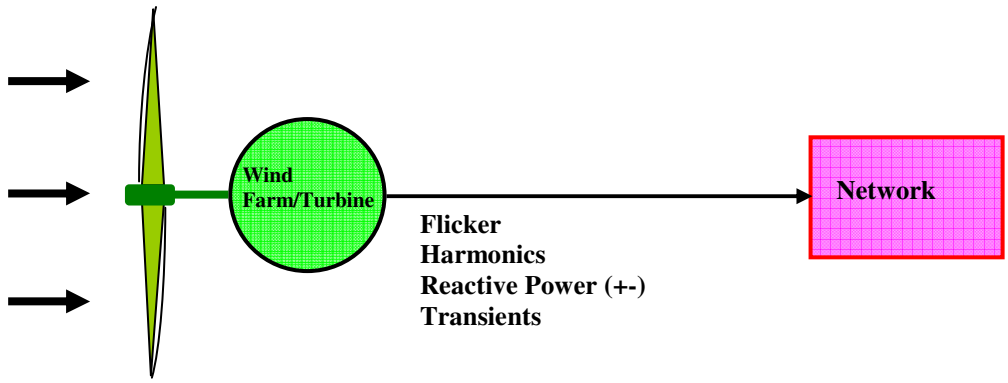

Figure 2.3 Influence of wind farm power quality on network

The principle focus of this research is the effect of network voltage unbalance on wind turbines; the impact by wind turbines on the network is not addressed per say.

2.3 Integration of Wind Energy in National Grids

Network integration of distributed generation is a complex issue, raising significantly different issues to traditional network integration of power generation into transmission networks. Innovative solutions are required in addressing the interface between DG and the distribution systems to which it connects [55].

Wind power generation in Ireland has significantly increased in recent years. From a low base position of connectivity to either the transmission or distribution grids in the 1990's in comparison to other countries, the growth has been significant in recent years. The amount of wind power connected to the National Grid in 1997 was 20 MW, but has now increased to approximately 1763 MW[3] of installed wind power in 50 separate wind farms around the country [6], [51]. A further 575 MW in wind farm projects are at various stages of planning. Wind from 159 wind farms accounted for 15.5% of total generated electricity in 2012 [6]. Accommodating the expansion of wind power generation, whilst ensuring the orderly and reliable development of the power system, has not been faced before by system operators, and is not straightforward [50].

2.3.1 Connection Requirements of Wind Turbines

Gardner et al assumed in [50] that wind turbines would become available that would ride-through-faults and meet the Grid Code requirements. Increasingly wind turbine manufacturers are providing improved technology with such capability, however in terms of sustained voltage unbalance in distribution networks, technological challenges remain.

It is only in recent years that Grid Codes have been developed to accommodate wind power generation. Transmission System Operators (TSOs) in Ireland and countries

[3] March 2013

throughout Europe have produced documents that outline the requirements for the performance of wind farms connected at transmission voltages. Many of the grid codes have specific requirements for the behaviour of wind turbines connected to utility networks [57]. The grid code requirements vary with the capacity (MW) of wind-farms connected. These requirements include tolerance levels for frequency, voltage, reactive power, harmonics and fault-ride-through. Many countries, including Ireland, now have Grid Codes that allow for the expansion of wind energy conversion systems (WECS). In early 2005 the Distribution Code and the Transmission Grid Code [51], were approved by the Commission for Energy Regulation (CER) [52], and for the first time, included comprehensive requirements for the connection of distributed generation.

In grid code requirements the emphases is on the affects that wind-farms may have on the network, and the ability of wind turbines to remain connected to the network under certain conditions. To enable wind turbines remain connected under voltage unbalance conditions, continuing research in improving generator performance is important.

2.3.2 Voltage Drop Ride-through Requirements

TSOs in most countries have issued grid connection requirements and fault ride-through requirements for distributed generators and among the first to issue such requirements were Eltra[4] and E.ON[5], of Denmark and Germany respectively were the first countries to install large amounts of distributed generation capacity, mainly wind power generators. Their connection requirements were used as a reference for other TSOs facing the same challenges. Fault ride-through requirements specify the extent and duration of a voltage or frequency drop or rise that may not lead to a disconnection of the generator. Research institutes, TSOs and generator manufacturers recognise that the

[4] Eltra, Transmission System Operator, TSO - Denmark
[5] EON, Transmission System Operator, TSO - Germany

most critical grid disturbance is a voltage drop, as this is a disturbance that regularly occurs, and can also result in unstable generator behaviour. If a voltage drop is restricted to just one or two of the three phases then severe transient voltage unbalance results.

2.3.3 Distribution System in Ireland

Grid codes in a good number of countries world-wide have been and are undergoing major reform to facilitate the connection of ever increasing amounts of distributed generation, specifically wind turbines. The grid code connection requirements to the distribution system (DS) in Ireland for distributed generation as well as specific requirements for wind farms are provided in [52]. The development of the distribution grid code in Ireland is a direct result of the increasing amounts of distributed generation requiring connection to the distribution grid. These additional requirements are applied to Wind Farm Power Stations (WFPS) with Registered Capacity of 5 MW or more, or with Registered Capacity less than 5MW due to be developed on a Contiguous Wind Farm Site (CWFS) where the development of the WFPS results in the total Registered Capacity of WFPS on the CWFS exceeding or remaining above 5 MW.

There are various voltage levels and configurations in the transmission and distribution networks to which wind-farms can be connected. Based on the connection type and voltage level five categories of Wind Farm Power Stations (WFPS) are identified as shown in Figure 2.4 [86].

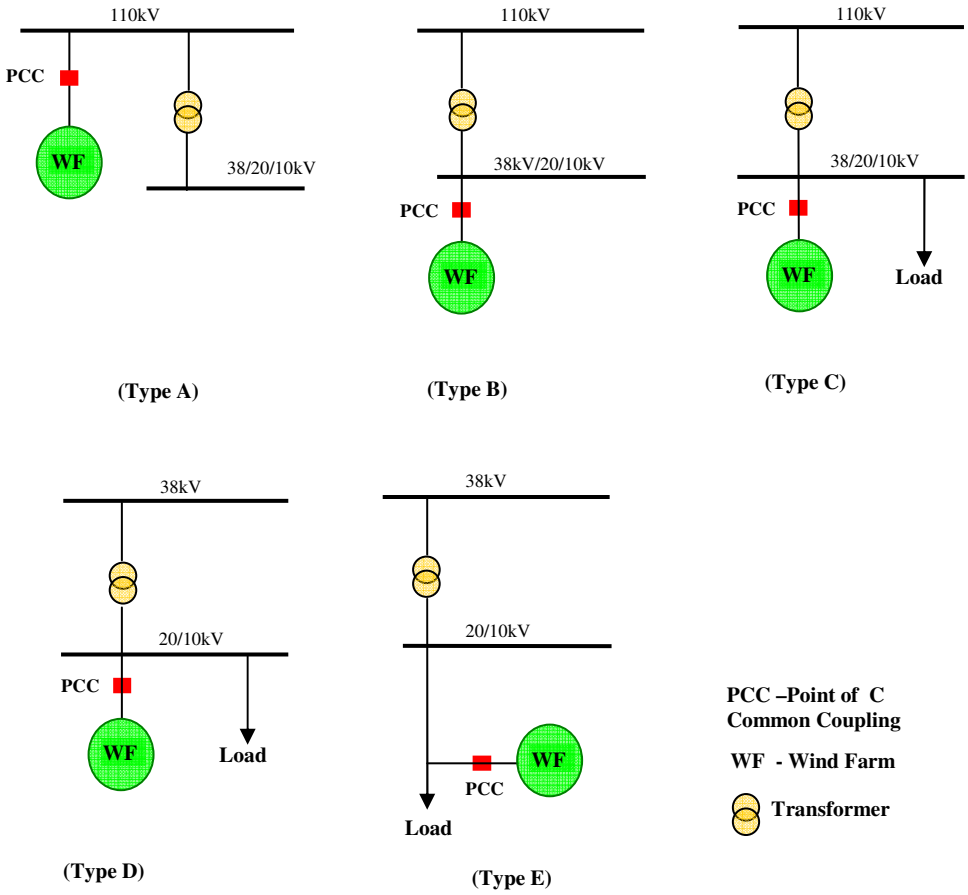

Figure 2.4 Classification of wind farm power stations connected to Ireland's distribution system.

In the connection configurations illustrated in Figure 2.4, network voltage unbalance is more likely to affect wind turbines connected as Types C, D and E due to the lower voltage levels and the possibility of adjacent local loads being substantially single-phase and also the aspect of loads not being distributed equally among all three-phases.

2.4 Voltage Unbalance

In many electrical power system designs, it is normally convenient to assume that the electrical system is symmetrical (balanced). However in reality, perfect symmetry rarely occurs. Mutual coupling effects between transmission lines, transformer windings and unevenly distributed single-phase loads are typical causes for system unbalance. In some

parts of Ireland for example, it would appear that voltage unbalance may be attributed to uneven distribution of domestic load. In small rural substations loads are frequently distributed on single phase lines and thus fluctuating power from each single phase load can cause voltage unbalance. The primary source of voltage unbalance less than 2% is that of unbalanced single phase loads on a three-phase circuit [64]. Voltage unbalance can also be the result of capacitor bank anomalies, such as a blown fuse on one phase of a three-phase bank. Severe voltage unbalance (greater than 5%) can result from single-phasing conditions [64].

Voltage unbalance can be of concern at the electricity distribution level. Although generated voltages are well balanced at the generator and transmission levels the voltages at the utilisation level can become unbalanced due to unequal system impedances and unequal distribution of single-phase loads. An excessive level of voltage unbalance can have serious impacts on some mains connected plant, e.g. induction machines. The negative or zero sequence voltages in a power system generally result from unbalanced loads causing negative or zero sequence currents to flow.

Utility supply voltage unbalance is typically maintained at less than 1%, although 2% is not uncommon. Voltage unbalance greater than 2% should be reduced where possible [20], by balancing single-phase loads, as phase current unbalance is usually the cause. Phase monitors are often required to protect three-phase motors from the adverse affects of single phasing.

In induction machines the elevel of current unbalance can be several times the level of the voltage unbalance at the stator [1]. Such unbalance in the line currents can lead to excessive losses in the stator and rotor windings that may cause protection systems to operate thus causing loss of production. Although induction machines are designed to

tolerate a small level of voltage unbalance they have to be derated if the voltage unbalance is excessive. If operated at the nameplate rated capacity i.e. without derating, the useful life of such induction machines can become quite short. It should be noted that if an induction machine is oversized to a given application the machine may not operate at best efficiency and power factor.

Voltage unbalance also has an impact on ac variable speed drive systems, with front end three-phase rectifier systems. The triplen harmonic line currents that are uncharacteristic to these rectifier systems can exist in such conditions leading to problematic harmonic issues. Although it is practically impossible to eliminate voltage unbalance it can be kept under control at both utility and plant level by several practical steps.

2.5 Voltage Measurement and Voltage Unbalance Standards

A three-phase power system is considered balanced or symmetrical if the three-phase voltages and currents have the same amplitude and are phase shifted by 120^{o} with respect to each other. If either or both of these conditions are not met, the system is considered unbalanced or asymmetrical [3], [4].

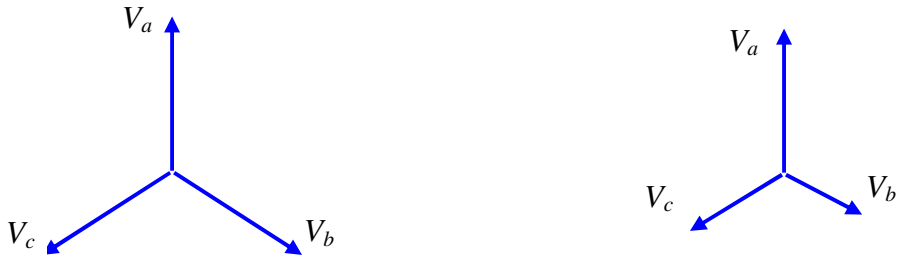

(a) Balanced System **(b) Unbalanced System**

Figure 2.5 Representation of a balanced and unbalanced three-phase voltage

Figure 2.5 illustrate a balanced and a magnitude unbalanced three-phase voltage. Voltage unbalance (or imbalance) can also be defined as the ratio of the negative sequence component to the positive sequence component [4]. It can also be expressed as

the maximum deviation among the three phases from the average three-phase voltage divided by the average three-phase voltage [3].

There are a number of accepted definitions for determining voltage unbalance. Unbalanced three-phase systems can be described in terms of Voltage Unbalance Factor (VUF). The percentage negative sequence voltage unbalance factor (% VUF), or true definition is given by the ratio of the phase voltage negative sequence component to positive sequence component [4]. The voltage positive and negative sequence components are obtained by resolving three-phase unbalanced line voltages V_{ab}, V_{bc}, and V_{ca} (or phase voltages) into two symmetrical components, positive sequence voltage V_p and negative sequence voltage V_n [33]. The VUF of a system can be determined by three phase voltage magnitudes and phase angles that depend on load conditions and system configuration [33]. The VUF transformation (Fortescue) can be described as:

$$\begin{bmatrix} V_0 \\ V_1 \\ V_2 \end{bmatrix} = \frac{1}{3}\begin{bmatrix} 1 & 1 & 1 \\ 1 & a & a^2 \\ 1 & a^2 & a \end{bmatrix}\begin{bmatrix} V_a \\ V_b \\ V_c \end{bmatrix} \qquad \begin{bmatrix} V_a \\ V_b \\ V_c \end{bmatrix} = \begin{bmatrix} 1 & 1 & 1 \\ 1 & a^2 & a \\ 1 & a & a^2 \end{bmatrix}\begin{bmatrix} V_0 \\ V_1 \\ V_2 \end{bmatrix}$$

where V_a, V_b *and* V_c are three line voltages and V_1 is the positive sequence voltage, V_2 is the negative sequence voltage and V_0 is the zero sequence voltage and a is the operator $1\angle 120°$.

Positive, negative and zero sequence voltages can be obtained using the Fortescue transformation using only the rms line-to-line voltages and without having to measure the phase angles between these voltages [18].

Alternative definitions of voltage unbalance are also available. The NEMA definition [15] of voltage unbalance, also known as the line voltage unbalance rate (LVUR), is given by the ratio of maximum deviation from the average line voltage, to the average line voltage. The NEMA definition considers magnitude only, phase angles are not

included [16]. Voltage unbalance can be estimated as the maximum deviation from the average of the three-phase voltages or currents, divided by the average of the three-phase voltages or currents, expressed in percent [64]. The NEMA[6] definition for voltage unbalance is:

$$\frac{\text{maximum deviation from average voltage}}{\text{average voltage}}.100\%$$

For example, with phase-to-phase voltage readings of 230V, 232V, and 225V, the NEMA definition of voltage unbalance is calculated as:

$$\frac{4}{229}.100 = 1.7\%$$

The IEEE definition of voltage unbalance [17], also known as the phase voltage unbalance rate (PVUR), is given by the ratio of maximum deviation from the average phase voltage to the average phase voltage. The IEEE definition is similar to NEMA in that the definition only addresses magnitude, phase angles are not included. The IEEE definition uses phase voltages rather than line-to-line voltages as used by NEMA.

Positive and negative sequence voltages may be used when analysing induction machines performance under unbalanced conditions. The 'true' definition involves both magnitude and phase angles when calculating the positive and negative sequence voltage components; Pillay and Manyage [16] however apply an expression that avoids the use of complex algebra and gives a good approximation to the true definition.

Standards for voltage unbalance are required to determine international performance levels. There are several such standards [[19], [20], [21]]. Gosbell et al [22] investigated some of these standards and examined possible errors, which can arise with incorrect averaging procedures and the use of phase voltages in voltage unbalance calculations. Among the findings in [22] were that the VUF, calculated from 10 minute average

[6] National Electrical Manufacturers Association of USA

voltages (Unbalance of the Average), gives a lower value than the correctly calculated 10-minute rms average VUF, determined from voltages over a small time scale (Average of the Unbalance) for the sites investigated. Also determined in [22], sline-line voltage calculations provide best accuracy in determining VUF calculations.

2.6 Voltage Unbalance and Weak Networks

Voltage unbalance tends to arise in certain rural (sometimes termed weak) networks. Voltage unbalance in rural distribution networks is normally more pronounced than in urban distribution networks [8]. Voltage unbalance can arise due to the predominately single-phase nature of the loads, owing to the difficulty of balancing these loads on each phase of the utility supply [[7], [8], [10], [31], [47]]. To reduce the degree of voltage unbalance, efforts are normally made to distribute single-phase loads among three-phases as uniformly as possible; however this is not always successful. The reoccurring nature of the unbalance can correspond to characteristics of the load in the local supply area [60].

The geometrical configuration of overhead lines can lead to asymmetric impedance resulting in a difference in the electrical parameters of the line (the impedance of electrical network components may not be exactly equal among each phase) [[3], [7], [8], [31], [48], [59]]. As stated earlier, the primary source of voltage unbalance less than two percent is the dominance of single-phase loads on a three-phase distribution network [4]. ESB Networks estimate that roughly two thirds of voltage unbalance in the distribution network is as a result of single-phase loads. In the USA many utilities do not normally record unbalance because adverse affects are not immediately apparent or recognised, and voltage unbalance is only addressed when a complaint is received [7].

Utilities require that wind-farm operators do not cause the network power quality to deteriorate below agreed standards, including EN 50160 [48].

Wind turbines can have a positive effect on network voltage unbalance at the point of common coupling, PCC. Wind-farms were investigated for unbalance in reports produced for Airtricity, and in [[12], [13]], and results showed a decrease in voltage unbalance at the PCC as generated power from the wind-farms increased. A paper by Davidson [12], on a study of a wind farm containing fixed-speed induction generators, observed that voltage unbalance at the PCC decreased from 1% at zero power generated to 0.2% when generating power at 6 MW.

2.7 Voltage Unbalance Sags/Dips – Types

There are many unbalanced voltage profiles possible with the same voltage unbalance factor (VUF). Among the possibilities are: single-phase under-voltage unbalance, two phases under-voltage unbalance, three phases under-voltage unbalance, two phases over-voltage unbalance, three phases over-voltage unbalance [27]. Voltage unbalance sags can be classified according to type. Bollen [26] considers single-phase, two-phase and three–phase voltage sags on star and delta-connected equipment, and transformer configurations. There are three main types of three-phase voltage unbalance sags, B, C, D. Types B, C and D are due to single-phase and phase-to-phase faults. A type B voltage sag is a magnitude sag and is confined to one phase only. Type E is a voltage sag on two phases. For types C, D, F and G sags, the phase voltages change by different amounts and their phase angles also change [34].

Siddique et al [27] have analysed the effects of above described unbalance phase faults on various rated three-phase induction motors. The six faults described in Figure 2.5, with identical VUF, were applied to an induction motor. Results obtained from each test indicated a difference in operating performance.

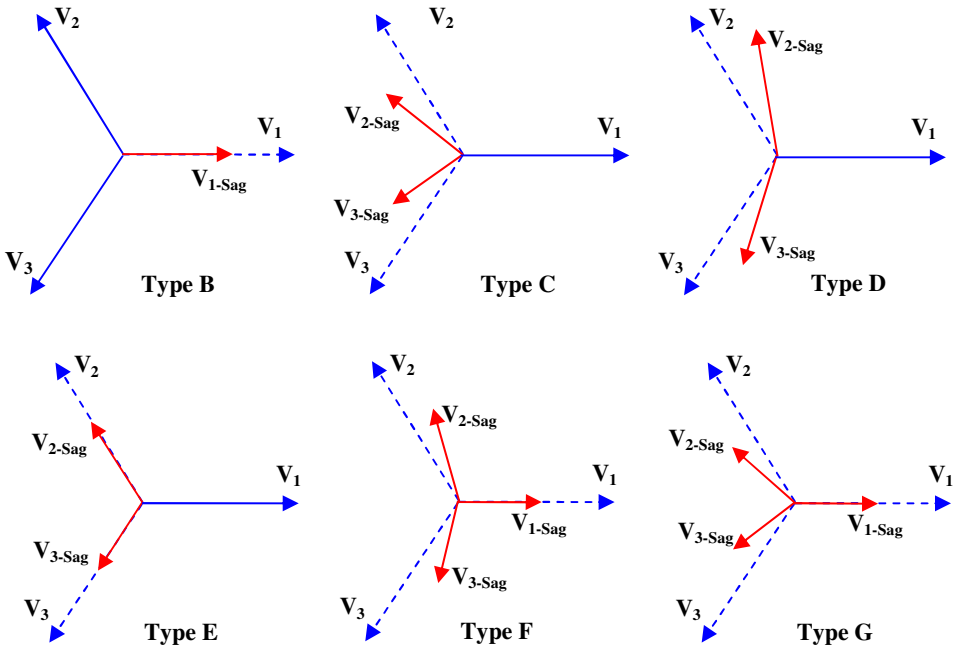

Figure 2.5 Phasor diagrams of voltage unbalance sags

Losses in the induction machine varied depending on the type of fault initiated and to assess the real condition of the machine, the positive sequence voltage should be considered. For example with lower positive sequence voltage and with the same VUF, losses in the machine are higher. Also with the same VUF, a higher positive sequence voltage leads to a higher motor efficiency [28].

2.8 Voltage Unbalance Behaviour of Induction Machines

An understanding of the effects that voltage unbalance has on wind turbines is important in determining solutions to the problem. Ghorashi et al [33] uses symmetrical components to investigate the effect of voltage unbalance on weak grids. A voltage can be analysed using positive, negative and zero sequence components. The combination of a positive sequence component and negative sequence component will result in a second harmonic ripple [56], [59]. Under the unbalanced operational condition, an induction generator has very low equivalent impedance due to the presence of negative phase

sequence voltage. This condition can be explained using the per-phase equivalent circuit of the induction machine (Chapter 5) and observing the rotor resistance $R_r`$. The rotor resistance is divided by the slip [10], [33], and under normal operating conditions, slip is small (< 0.1) i.e. the rotor resistance is large. However during unbalanced voltage conditions a negative phase sequence occurs. In practice, induction generators are normally star-connected with no neutral connection. With no neutral connection zero sequence current cannot flow [8]. If negative sequence voltages result from an unbalanced supply and are applied to an induction generator, a revolving magnetic field is established in the air gap between the stator and rotor. This negative phase sequence rotates in the opposite direction to the grid voltage, and the negative sequence slip is (2-s). The effective negative sequence rotor resistance is then $R_r`/(2-s)$. Due to much lower impedance to a negative sequence voltage, high current magnitudes are induced in the rotor. The negative phase voltage sequence will therefore drive a large negative phase sequence current, (six to eight times that of the positive phase sequence current [8]) which might trip the protection equipment and hence prevent the turbine from riding through the fault [32].

The negative sequence current in an induction machine tends to increase the losses, raise the temperature of the machine (stator and rotor), beyond their published rating, which can lead to winding failures (reduce the insulation life of a generator) and bearing failures [8], [10], [11] and [47]. Insulation life is approximately halved for every 10^oC increase in winding temperature [11], [44]. The percent increase in temperature of the highest current carrying winding is approximately two times the square of the voltage unbalance. For example a 3 percent voltage unbalance will cause a temperature rise of about 18 percent [11], [44]; (3^2 x 2 = 18 %).

NEMA standards recommend a maximum voltage unbalance of 2 percent before derating of the machine is required. Machines can be derated down to 75% for a maximum of a 5 percent voltage unbalance. If the voltage unbalance exceeds 5 percent it is not recommended that induction machines be operated. The flow of the unbalance current in a motor may act to magnify the voltage unbalance already existing on the network [14].

When the stator phase voltages are unbalanced, the negative sequence currents produced as a result, may also create torque pulsations on the shaft resulting in audible noise and extra stress. These torque pulsations can also damage the rotor shaft, gearbox or blade assembly [10], [11]. The locked-rotor and breakdown torque are decreased when the voltage is unbalanced. If the voltage unbalance is extremely severe, the torque might not be adequate for the application [44]. The negative-sequence torque has a detrimental effect on induction motor speeds, which tend to decrease and may be unable to recover [45]. Bearings may also suffer mechanical damage because of induced torque pulsations at double the system frequency [3].

Losses due to voltage unbalance are illustrated in [44] where for example a 6% voltage unbalance results in a 50% increase in losses, and a 10% increase results in a 100% increase in losses. However there is little consensus on the voltage unbalance limits at which a generator can still operate reliably. Since the main effect of voltage unbalance is the heating of machine windings, higher short-term levels of unbalance may be acceptable for a few seconds or even minutes [44].

The type of unbalance protection installed can exacerbate this situation. Many unbalance relays operate by measuring the percentage of current unbalance being drawn by the machine. The problem is that this increases, as the turbine is unloaded, resulting in turbine trips with low valus of current. The negative phase sequence voltage sees

relatively constant impedance (related to the locked rotor impedance) while the positive phase sequence current varies with output. The result can be nuisance tripping with disputes arising between the wind-farm and network operator regarding responsibility.

Table 1 displays the effects of unbalanced phase voltages applied to class A and class B three-phase motors running at rated load. In addition to motor damage, voltage unbalance in three phase systems can cause connected electronic equipment to malfunction [102].

Table 1 Voltage unbalance effects in motors

Voltage Unbalance (%)	0	2	3.5	5
Negative Sequence Current (%)	0	15	27	38
Increase in Losses (%)	0	9	25	50
Class A Temperature Rise (^{o}C)	60	65	75	90
Class B Temperature Rise (^{o}C)	80	85	100	120

Table 1 [46], shows that even a small unbalance in voltage can cause significant heating of motors running at full load. For this reason, NEMA MG1 [15] sets a voltage unbalance guideline of no more than 1% unbalance in order to prevent damage to sensitive loads.

2.9 Voltage Unbalance and Converters

Voltage unbalance, magnitude fluctuation and phase deviation, affects both induction generators and the converters associated with these machines during variable speed operation. In converters, voltage unbalance can produce undesirable low frequency power ripple, which can result in current harmonics and poor DC link voltage regulation [34], [47].

Voltage unbalance in a rectifier-inverter system is investigated in [112], indicating double frequency voltage oscillations on the dc link bus. The investigations reveal that with appropriate values for DC link capacitance and line filter inductor, significant improvements can be achieved in the Total Harmonic Current Distortion (*THDi*) of the input current and DC link ripple factor during unbalance input voltage conditions. Rectifier and converter systems draw non-sinusoidal current waveforms from the grid. If the grid voltage supply is balanced the line current waveform may take the "double pulse per half cycle" shape as shown in Figure 2.6, that contain characteristic harmonic orders given by [68]:

$$h = 6k \pm 1$$

where h = harmonic order and k = 1, 2, etc. giving only 5th, 7th, 11th, 13th etc. order harmonics.

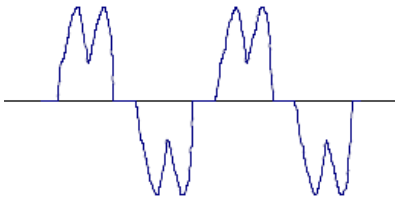

Figure 2.6 Typical line current waveform of a three-phase diode rectifier system when the supply system is balanced

With unbalanced grid voltage supply the line current waveform can deviate away from the double pulse formation of Figure 2.6 to single pulse formation as shown by Figures 2.7(a) and 2.7(b) leading to uncharacteristic triplen harmonics. Supply voltage unbalance can lead to tripping of drive systems caused by excessive ac line currents on some phases and under voltage on the DC link. This can also lead to excessive thermal stress on diodes and DC link capacitor. Increase in the unwanted triplen harmonic currents can also lead to undesirable harmonic problems in the supply system.

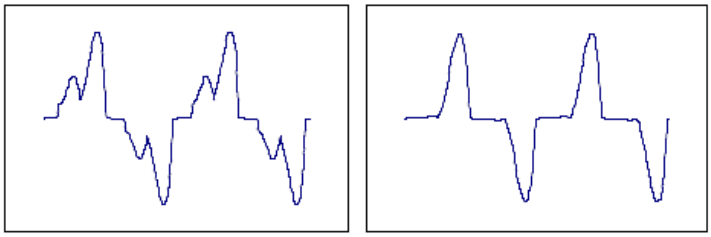

(a) Voltage unbalance – 5% (b) Voltage unbalance – 15%

Figure 2.7 Line current waveforms of a three-phase diode rectifier system when the supply system is unbalanced

Converters are used with variable speed wind turbines. Various electrical systems are used to obtain broad and narrow speed ranges. Variable speed operation allows a wind turbine to capture more energy and can smooth the power fluctuations by essentially using the rotor as a flywheel. Power electronics offer the most effective method for providing variable speed operation. In addition power electronics converters can supply reactive power to the utility on demand and provide the capability to limit torque loads in the drive-train [42].

The following variable speed wind energy conversion systems (WECS) use converters:

- Variable speed based synchronous generator, including direct drive.
- Variable speed with squirrel cage induction generator.
- Variable speed with doubly fed induction generator.

The operation of a converter in variable speed operation of wind turbines, during voltage unbalance conditions, whether allowing full power as in the case of synchronous generators and squirrel cage induction generators, or partial power in the case of doubly-fed induction generators, will have similar effects to drives used with induction motors. Quantifying the effect of voltage unbalances on adjustable speed drives (ASDs) under input voltage unbalance and sag conditions represents an important step in developing appropriate mitigation measures [34], [47].

Investigations into voltage unbalance problems and solutions' pertaining to variable speed drives using induction motors have been documented [23], [34], [37], [38], [39], [40], [47]. Lee et al [37] investigates the relationships between the unbalanced input voltages and input currents on an induction motor adjustable speed drive (ASD). The investigations are for a Type C source voltage unbalance (section 2.4) and were evaluated through theoretical analysis simulation and experimentation. Some of the conclusions reached are that ASD input current can reach twice its rated value at full load conditions with up to 5% input voltage unbalance. Input current unbalance is up to 100% for input voltage unbalance of only 5%. Simulation models used Space Vector Pulse Width Modulation (SVPWM) for inverter operation

The analysis and design of a direct nine switch three phase pulse-width modulated controller, capable of correcting input voltage unbalance in an ASD, is presented in [38]. The correction method is validated trough experimentation and simulations. Low order harmonics were eliminated with this method.

Positive and negative sequence components can be used to analyse the effects of voltage unbalance on converters. The product of positive and negative sequence components of voltage and current generate a double supply frequency power ripple causing DC link voltage ripple [36], [39]. In [39] the authors present an unbalanced voltage compensation strategy for a PWM converter. Counter-unbalancing currents are obtained which contain the negative sequence components, which cancel the power ripples, and they reduce the second harmonics of the DC link ripple. Tsai and Sun [40] investigated the effects of voltage unbalance and harmonics on a three-phase PWM AC-to-DC converter. Among their conclusions are that harmonics will appear in the current reference if the power source of the converter is unbalanced. The effects of voltage unbalance and harmonics

can be compensated for by installing a low pass filter, which completely attenuates 2ω components or higher ones [41].

2.10 Voltage Unbalance, Fault Ride-Through and Protection

To maintain high reliability and security in both grid and wind turbines, the wind turbines must be disconnected from the grid in the event of a malfunction of the grid and vice versa. According to the IEC 61400 standard, wind turbine protection should provide for under-voltage, over-voltage and over-current, phase unbalance, and also under and over frequency. Wind turbine generators, are usually fitted with protection to detect unbalance. If the supply unbalance is sufficient, the single-phasing protection may respond to the unbalanced currents and trip the machine. Polyphase converters, in which the individual input phase voltages, contribute in turn to the dc output, are also affected by an unbalanced supply, which causes an undesirable ripple component on the dc side, and non-characteristic harmonics on the ac side [30].

The type of unbalance protection installed in WECS can exacerbate the situation. Many unbalance relays operate by measuring the percentage of current unbalance being drawn by the machine. The problem is that this increases, as the turbine is unloaded. The negative phase sequence voltage sees relatively constant impedance (related to the locked rotor impedance) while the positive phase sequence current varies with output. The result can be nuisance tripping with disputes arising between the wind-farm and network operator regarding responsibility. Among the various grid code requirements, perhaps the main challenge for wind turbine manufacturers is the ability to ride through faults [33], [58].

2.11 Voltage Unbalance and DFIG's

An analysis of the top ten manufacturers in 2001 [62] established that most were supplying doubly fed induction generators with a rotor connected IGBT-based frequency converter. Recently, synchronous generator systems have increased in popularity however DFIG's still account for a large share of the market [9]. The most significant reason for the popularity of the doubly fed induction generator concept is the relatively small size of power converter- approximately 10-30% of rated turbine power. For example a typical variable speed DFIG might have an operating region $0.7\ \omega_S < \omega_r < 1.3\omega_S$. The rotor converter must be bi-directional with a smooth transition through $s = 0$ [65].

Wind generators equipped with a DFIG have a frequency converter connected to the rotor that operates in four quadrants. With under-voltage grid faults, with rapid voltage drops, there will be high rotor currents in the generator, which result in a high dc voltage in the frequency converter. Akhmatov [35] observed during simulation studies that the converter in a DFIG was the most sensitive part of the wind-turbine.

Voltage unbalance can cause voltage harmonics on the dc bus of a DFIG, and lead to current harmonics. Increased current harmonics on the DC link can shorten the life of the capacitor, or lead to capacitor failure. The bus ripple voltage can also lead to the generation of pulsating torques at twice the network frequency [35], [36]. Brekken and Mohan [36] investigated a control scheme to compensate for these torque pulsations. Compensations terms are calculated by equating the terms of the balanced torque equation with the unbalanced torque equation. Mohamad et al [54] compares the steady state performance of a DFIG with an induction generator and particularly the effect of the rotor converter on harmonic current generation, and the harmonic torques and losses

as a result. Santiago et al [59] investigates a speed controller to compensate for voltage unbalance on the stator.

In double-fed induction generators grid voltage unbalance can affect both the induction generator and the rotor converter. In DFIG's, it is possible to control the rotor currents to correct for the problems caused by unbalanced stator voltages [[24], [71], [95], [96], [104], [105], [115], [116], [117], [118], [120], [121], [122], [123], [124], [125], [127], [129], [130], [131], [132], [133], [135]]. A method for alleviating voltage unbalance in a DFIG using a Statcom was investigated by Naess et al [24] based on a DFIG with PWM control and transformer in the rotor circuit was implemented in PSCAD/EMTDC, where a negative-sequence current was injected from the STATCOM to compensate for the unbalanced load voltage. To completely neutralise all issues associated with the detrimental effects that supply voltage unbalance has on DFIG's, requires compensating control techniques to both the rotor-side and grid-side converters. Current trends to control the DFIG rotor-side and grid-side converters during voltage unbalance conditions is based on previous work carried out to improve the performance of converters for dc and ac machines as outlined above in section 2.9.

These methods include isolating the positive and negative sequence direct and quadrature components, I_d and I_q respectively and applying a parallel control scheme to compensate for the oscillating components due to supply voltage unbalance. This method has been used by [[71], [76], [96], [97], [105], [108], [110], [113], [114], [115], [117], [118], [120], [121], [122] and [124]].

The behaviour of DFIG's in wind farms and improvements in the control structures is investigated in [[120], [122]] and improvements are outlined using positive and negative sequence controllers. A similar study by [121] also incorporated FSIG's and DFIG's in a wind farm. The investigation demonstrated that not only can the DFIG's control system

improve its own performance but it can also improve the stability of the FSIG with the same grid connection in the wind farm. The method uses the fact the DFIG can control the total power at the terminals and thus the overall voltage unbalance.

Jiabing and He et al [[117], [118]] also use a dq^+ reference frame and developed a rotor side control scheme with a resonant compensator in parallel with a PI controller (PIR control) and tuned at twice the grid frequency. The PIR method was also investigated by [[125], [126], [127], [129], [133]]. Jiabing et al [118] incorporates a similar scheme in both the rotor side and grid side converters to improve the performance of a DFIG during network voltage unbalance conditions. The idea is that the controller consists of a PI regulator and a harmonic resonant (R) compensator tuned at twice the grid frequency and the positive and negative sequence components of the rotor and grid side converters are controlled without the requirement of extrapolating the positive and negative components, and resulting in improved dynamic performance. The PIR control method was implemented in stand-alone mode (i.e. not grid connected) by Phan et al [[130], [131], [132]].

2.11.1 Coordinated Control

Normally when controlling the rotor-side converter for the reduction of stator power and torque pulsations due to supply voltage unbalance it was not possible to reduce both the stator power and torque pulsations simultaneously, due to the limitations of the control variables. However by analysing both converters with respect to the total power supplied by the DFIG, it is possible to reduce both the stator power and torque oscillations. The control variables of both the rotor-side and grid-side converters can be used in a coordinated fashion and thus it is possible to reduce both the stator power and torque pulsations [[113], [115], [124]].

2.11.2 Resonant Controllers

The use of a resonant controller in parallel with the PI current controller can also be used to control generated unbalance currents and current harmonics in converters and DFIG's. The controller is often referred to as a PIR controller and requires less positive and negative sequence decomposition and thus less time delay and errors [[96], [116], [117], [118], [125], [129], [130], [131], [132], [134], [135]]. If a number of frequencies are controlled it can be referred to as multi-frequency proportional resonant (MFPR) controller [125].

During conditions of network voltage unbalance the voltage, current and flux all contain both dc values of the positive sequence components and double frequency ($2\omega_e$) ac values of the negative sequence components in the dq^+ reference frame. The dc components are regulated normally by the PI controller however this controller cannot regulate the double frequency components. The negative sequence control currents I_{dqr}^- have a frequency of $2\omega_e$ (100 Hz) and to control these currents adequately it is thus necessary to use a controller that is tuned to 100 Hz. A multi-frequency proportional resonant (MFPR) controller can be implemented for directly controlling both the positive and negative sequence components. This controller has a very high gain around the resonance frequency and it eliminates the steady state error between the reference and the measured signal. The width of the frequency band around the resonance point depends on the integral gain value. A small value produces a very narrow band, whereas a large value produces a wider band. The cut-off frequency ω_c also increases the band-width. Multilevel MFPR controllers can be implemented to control and reduce converter generated harmonic currents injected into power systems.

DFIG's can also be operated in stand-alone mode, i.e. not connected to a grid system. Stand-alone operation of DFIG's with improved control using PIR techniques was

investigated in [[124], [130], [131] and [132]] with similar improved operational performance results achieved. The behaviour of a synchronous generating system to grid voltage unbalance was investigated in [134] with control strategies modified to improve performance during network voltage unbalance conditions.

2.12 Conclusion

This literature survey is by no means exhaustive; however it providees an insight into the current issues associated with utility voltage unbalance and the integration of WECS.

Chapter 3 Wind Power Technologies

3.1 Wind Power Technologies

This work concentrates on DFIG's (Double Fed Induction Generators) and the issues associated with improved operation during network voltage unbalance conditions. Before a discussion of these topics a general overview of wind power technologies is presented to see where the DFIG "fits" within the wind power generation community. Presently several main types of technologies are used for the conversion of wind aerodynamic power into electrical power. The main types of technology can be classified as follows:

- Fixed Speed Synchronous Generator.
- Fixed Speed Induction Generator.
- Variable Speed Induction Generator.
- Double Fed Induction Generator.
- Variable Speed Synchronous Generator System.
- Direct Drive or Gearbox.
- Pitch Control versus Stall Control of Rotor Blades.

Figure 3.1 shows a schematic of technologies used in wind energy conversion systems [62].

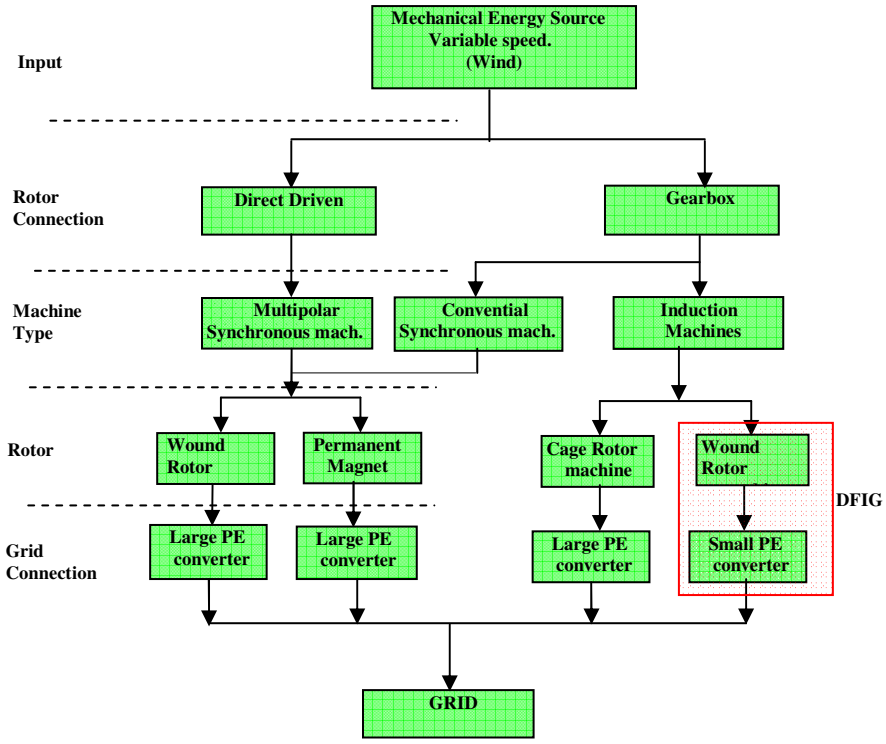

Figure 3.1 Technologies of wind turbines

In terms of the turbine speed there are two main classifications of wind turbine generator systems, constant speed and variable speed. Throughout the world constant speed operation was the most common type of technology used until the early 1990's. In constant speed operation the generator stator windings are connected directly to the electrical grid with a simple electrical connection. Variable speed wind turbine generators gained momentum as the preferred choice of wind farm developers during the early 1990's. Variable speed operation requires power electronic converters to operate with generators, allowing wind turbines to capture more energy, and can smooth the power fluctuations by essentially using the rotor as a flywheel. Power electronics offer the most effective method for providing variable speed operation. In addition power electronics converters can supply reactive power to the utility on demand and provide the capability to limit torque loads in the drive train.

A constant speed wind turbine is designed to obtain a maximum efficiency at one wind speed that will give the optimum tip speed to wind speed ratio for the rotor blade. The variable speed machine can obtain the optimum tip speed to wind speed ratio at any wind speed by changing the rotor speed as the wind speed changes. During the previous twenty years three main technologies have been developed and used by the different wind turbine manufacturers (Figure 3.4) [65]:

- Gearbox and induction generator (IG) with single and double stator winding.
- Gearbox with double-fed induction generator (DFIG) with power converter.
- Direct-Drive generator with power converter.

Constant-speed wind turbines produce stochastic as well as periodic power fluctuations. The resulting voltage fluctuations can cause serious light flicker. This problem has lead to a recommendation in many European countries that the amount of wind power installed should not be more than 5% of the short-circuit capacity [79]. Figure 3.2 shows a typical installation of a DFIG including tower and associated switchgear.

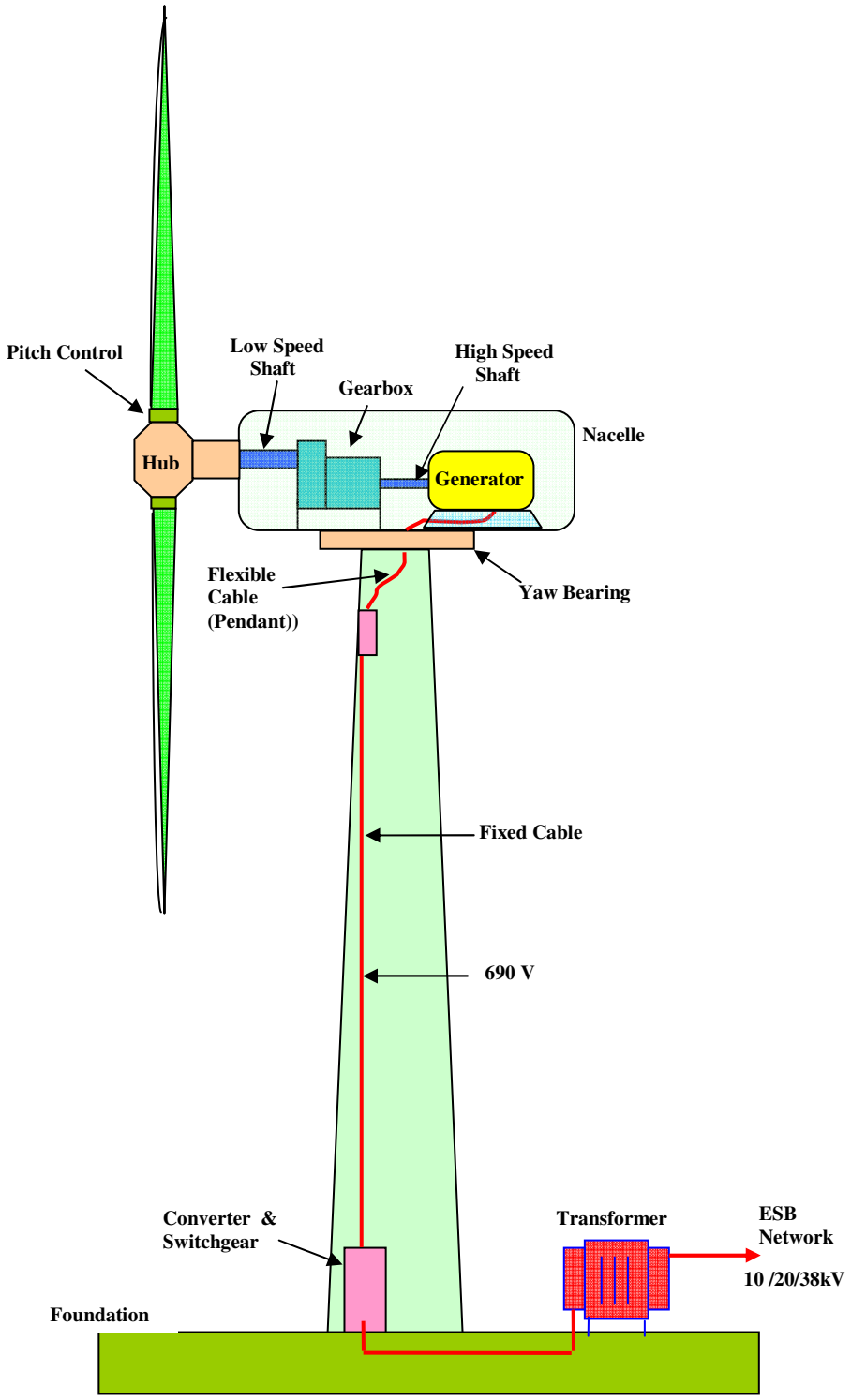

Figure 3.2 Typical wind turbine components including induction generator, DFIG converter and three-phase transformer (not to scale).

3.2 Current Wind Turbine topologies.

3.2.1 Grid-connected Squirrel Cage Induction Generator

In the past the squirrel cage induction generator (SCIG) has been the most widely used generator type for wind turbines [78]. For fixed-speed wind turbines the induction generator is directly connected to the electrical grid according to Figure 3.3. The rotor speed of the fixed-speed wind turbine is in principle determined by a gearbox and the pole-pair number of the generator.

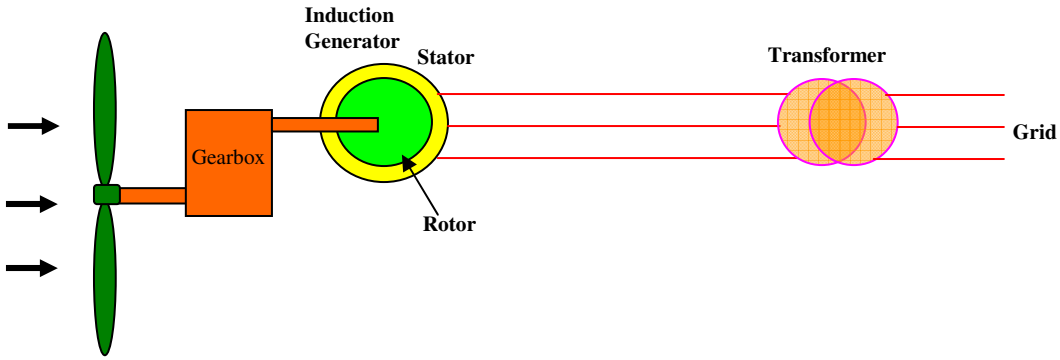

Figure 3.3 Induction generator fixed-speed wind turbine

The torque-speed characteristic for a typical induction machine is shown in Figure 5.2 (Chapter 5). The generator operation is only stable in the narrow range around the synchronous speed n_s (s = 0). In this zone the machine speed n varies very little with varying torque and cannot be controlled. Turbines equipped with this generator type are often called fixed-speed systems, although the speed varies over a narrow range. The range becomes broader with increasing rotor resistance.

The slip is mostly not higher than 5% for SCIG's and generator operation only occurs for speeds higher than n_s (synchronous speed). As the number of pole pairs p is usually 2 or 3 in commercial wind turbine generators with SCIG's, the synchronous speed in a

50Hz grid is normally 1500 rev/min. (2 pole pairs) or 1000 rev/min. (3 pole pairs). This system (one or two-speed) was the "conventional" concept used by many Danish manufacturers in the 1980s and 1990s [57].

The main variable speed configurations for wind turbines are shown in Figure 3.4. From the mid 1990's until the present day the most popular installed wind turbine design has been the DFIG.

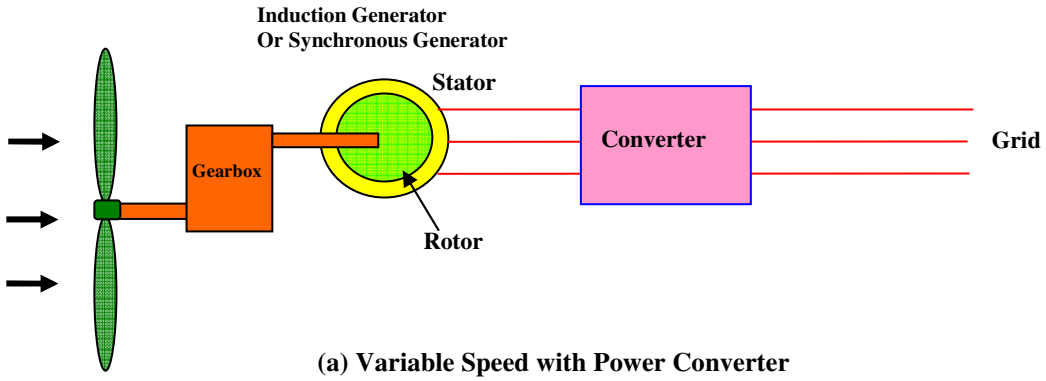

(a) Variable Speed with Power Converter

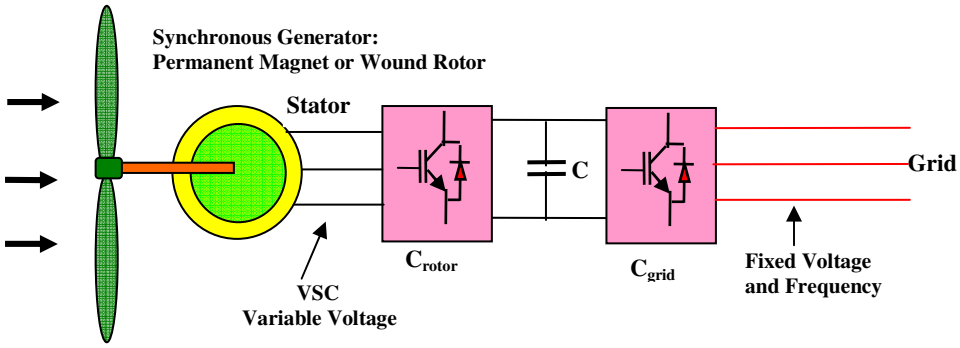

(b) Direct-drive generator with power converter

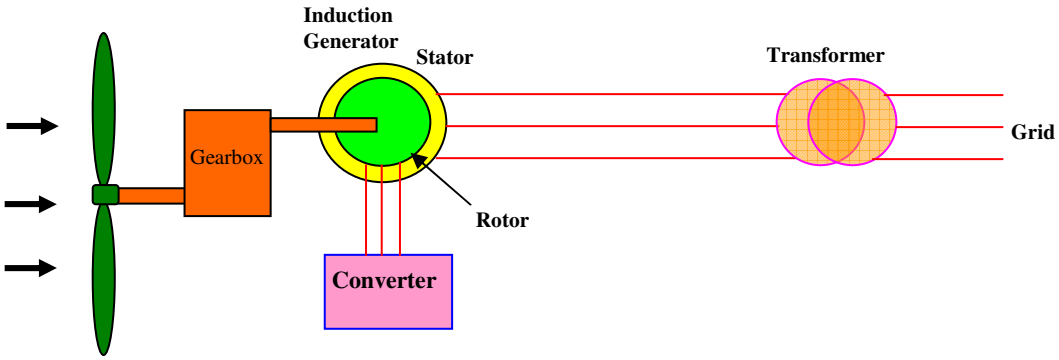

(c) Variable Speed: Variation of Rotor Resistance with with Power Converter

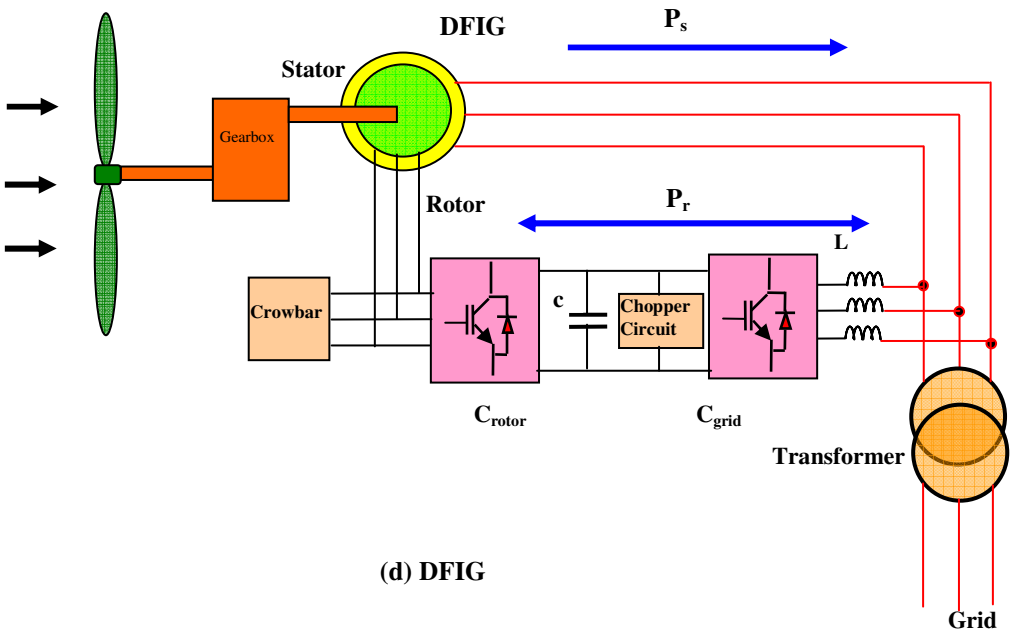

(d) DFIG

Figure 3.4 Wind Turbine Systems: Induction Generator and Synchronous Generator, (a) Variable Speed Operation, (b) Direct Drive Variable Speed, (c) Variable Speed: Variation of Rotor Resistance with Power Converter (d) DFIG Variable Speed.

The main types of generator and their connection with the network, as outlined in Figure 3.4 above will vary in performance, with some performing as good if not better than conventional synchronous generators [62]. In the case of the method shown in Figure 3.4(b) for example, the power converter can in principle bring to a weak network all the benefits of a Static VAR Compensator of the same rating. However there is some way to go in suitably defining the network operators' technical requirements before the benefits of this technology are fully exploited. The DFIG concept has less capability, but is still able to meet network operators' requirements. Table 2, tabulates the real power flow in a DFIG during subsynchronous and super-synchronous modes of operation.

Table 2 Power flow direction in DFIG

Subsynchronous	**P_s**	**Stator → Grid**
$n < n_s$; $s > 0$	**P_r**	**Grid → Rotor**
Supersynchronous	**P_s**	**Stator → Grid**
$n > n_s$; $s < 0$	**P_r**	**Rotor → Grid**

Operation of DFIG's (Figure 3.4 (d)) stator reactive power Q_s can be controlled by controlling rotor currents within the converter. Furthermore, the grid-side of the rotor converter can control reactive power $Q_{r,grid}$, independently of the generator operation. This allows the performance of voltage support towards the grid. Some of the drawbacks are [65]:

- A gearbox is still necessary in the drive train to achieve the necessary generator rotor speed for 50 Hz operation.
- The control of the rotor power by means of a grid-connected converter requires an electrical connection between a rotating and fixed system. Such a connection is given by carbon brushes on the slip rings and these brushes require regular maintenance, are a potential cause of machine failure and increase the electrical losses.
- Also the power electronic converter is a fragile component: it is very sensitive to over-currents. In case of a grid voltage dip, the stator and rotor currents may dramatically increase for a short time (~100 ms). To protect the converter from over-currents, it is bypassed by a 'crowbar' (Figure 3.4), which is normally open. In case of rotor over-currents the rotor winding is short-circuited by closing the crowbar switch, resulting in the same behaviour as a SCIG for a short time. Normally, the crowbar switching is followed by the shut-down of the entire turbine.

- The dynamic behaviour of the installation in case of grid disturbances (especially in case of crowbar switching) is very complex. Detailed dynamic models and good knowledge of the machine parameters are required to make a correct estimate of occurring torques and speeds, and also of the impact of the machine behaviour on the grid [81]. Dynamic modelling aspects will be discussed in Chapter 6.

3.3 Wind Turbine Aerodynamic model

Production of energy in a wind turbine requires a transfer of energy between the wind and the turbine rotor. The blades of a wind turbine rotor extract some of the power from the wind energy, convert it into rotational energy and it is then transferred via a gearbox or mechanical drive to a generator [100].

3.3.1 Extraction of power from the air-stream

A simple model generally attributed to Betz (1926), can be used to determine the power from an ideal turbine rotor. The analysis assumes a control volume, essentially a tube, with the flow across the ends of the tube; details can be obtained in [100].

The relationship between the wind speed and aerodynamic power and torque can be described by the following equations [100]. The power developed by the wind can be described as:

$$P_w = \tfrac{1}{2} \rho \pi R^2 U^3 C_p(\theta, \lambda) \quad (3.1)$$

The aerodynamic torque can be expressed as:

$$T_w = \tfrac{1}{2} \rho \pi R^2 U^2 C_p(\theta, \lambda) \quad (3.2)$$

*w*here: P_w is the aerodynamic power extracted from the wind [W]

T_w is the aerodynamic torque extracted from the wind [Nm]

ρ is the air density [kg/m3], R is the wind turbine rotor radius [m]

U is the wind speed [m/s], θ is the pitch angle of rotor [deg]

$\lambda = \frac{\omega_{rot}.R}{v_w}$ is the tip speed ratio, where w_{rot} is the wind turbine rotor speed [rad/s].

Figure 3.5 illustrates the power coefficient *Cp* curves as a function of tip speed ratio and pitch angle [65].

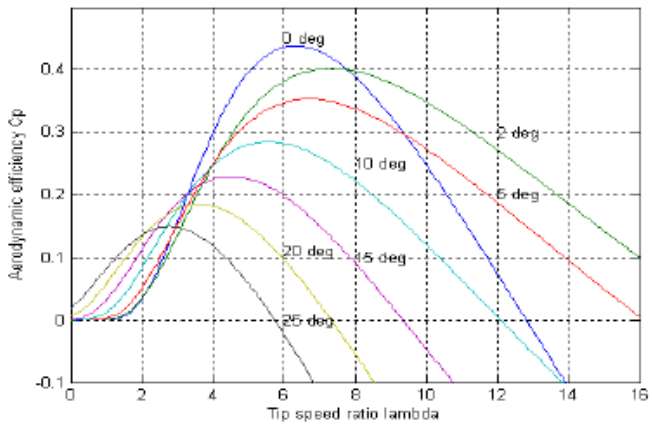

Figure 3.5 Power coefficient Cp curves as a function of tip speed ratio & pitch angle

3.4 Stall and Pitch Control

Methods are available to limit wind power transferred to the shaft of the wind turbine if the power available in the wind becomes higher than the power for which the wind turbine is designed. Two common methods of controlling the maximum power that the airfoil blades can safely withstand are stall and pitch control. Stall control can also be sub-divided into passive stall control and active stall control.

Passive stall control requires the rotor blades to be fixed to the hub, whereas for active stall control and pitch control the rotor blades can be pivoted around their axis [100]. Wind turbines use the fact that the angle of attack grows with increasing wind speed in such a manner that the angle of attack where stall occurs is reached when the wind speed reaches rated wind speed. For passive stall the rotor blades are mounted fixed on the hub and are installed at the required angle during the construction of the turbine. This means that the wind turbine rests completely passive and only when the wind speed reaches a particular velocity will passive stall causes the power taken by the blades to reduce, similar to the stall effect on aircraft wing blades when the aircraft is not travelling at sufficient speed.

Active stall and pitch control require motorised control of the blade angle and so they require the ability to rotate around their axis. Active stall can cause the blades to stall when required. As this concept requires the wind turbine to actively do something, it is known as active stall controlled concept. Also, rotor blades can also be turned in the opposite direction in order to reduce the angle of attack and thereby the aerodynamic forces and the power output. This is normally called a pitch controlled concept. As these two main characteristics are completely independent, they can be combined in various ways. This can be shown in a combination matrix, which is given in Table 3.

Table 3 Possible combinations of Stall/Pitch and speed of WECS

	(Passive) Stall	**Active Stall**	**Pitch**
Single Speed	Stall Controlled Single Speed Concept	Active Stall Controlled Single Speed Concept	Pitch Controlled Single Speed Concept
Two Speed	Stall Controlled Two Speed Concept	Active Stall Controlled Two Speed Concept	Pitch Controlled Two Speed Concept
Variable Speed	Stall Controlled Variable Speed Concept	Active Stall Controlled Variable Speed Concept	Pitch Controlled Variable Speed Concept

Chapter 4 Investigations into Voltage Unbalance

4.1 Introduction

Chapter four outlines investigations with respect to grid voltage unbalance, and the effects and performance of induction generators and DFIG's, when subjected to conditions of voltage unbalance. An important part of this research is the collection of data on a weak or rural network and to this end a small wind farm in County Cavan has been monitored using remote power quality measuring instruments. The details of this research are included in section 4.2. The effects of voltage unbalance on induction generators are outlined in section 4.4. Equations are derived for torque showing the effects of positive and negative sequence components. Simulations are performed in Matlab/Simulink confirming the negative effects of the negative sequence components. In section 4.5 the effects of voltage unbalance on the behaviour of a three-phase PWM inverter and a three-phase PWM controlled rectifier are investigated. The observations include power and torque pulsations at twice the applied frequency. In section 4.6 and section 4.7 DFIG's and synchronous generator systems are investigated for performance during applied voltage unbalance conditions. Section 4.8 is a brief introduction to the concept of using sequence (symmetrical) components to analyse the behaviour of systems when subjected to voltage unbalance conditions.

4.2 Distribution Networks - Corneen Wind-Farm

To establish the level of problems that voltage unbalance has on wind-turbines, measurements of voltage, current and power at the point of common coupling (PCC) of a wind-farm and a distribution grid are beneficial. Collaboration with a wind farm operator Airtricity allowed DIT to obtain measurements of a small wind-farm in Ulster. Corneen Wind Farm consists of two 1.5 MW GE Wind Turbine-Generators, which are connected to the ESB distribution network at 10 kV. Both generators are Double Fed Induction Generators (DFIG), operating at 690 V. Each generator has its own 10 kV/690 V, 1.6 MVA transformer. Due to frequent tripping of the turbines DIT were asked to investigate the power quality of the utility voltage at the PCC.

Over a period of two years the wind-farm was monitored for power quality issues. Electrical faults that tripped one or both turbines on the wind farm were analysed. It was observed that transient faults and voltage sags occurred on a random and intermittent basis. Analysis showed that voltage unbalance in the network occurred on a more regular or seasonal basis. This scenario is likely in many rural or weak networks where balancing of the three phase loads or distribution lines may prove difficult. An analysis of the Richfield wind farm in County Wexford observed similar results. This wind farm is connected to the 38 kV distribution network. Voltage measurements were recorded and analysed and it was observed that voltage unbalance trending on a daily and weekly basis was remarkably similar to that obtained at Corneen wind farm.

The results of an assessment of the power quality at the Corneen Wind Farm were presented in three reports. In particular, power quality problems of voltage unbalance, voltage sags and transient events were considered. The data on which the assessment is based was collected on ION 7600 Power Quality Meters [29]. The reports of generator

trips from the turbine's SCADA system were correlated with the data from the power quality equipment. The following sections present a selection of the analysis associated with voltage unbalance presented in the three reports.

4.2.1 Power Quality Measurement of Wind Farm

A first report was completed in summer 2003. A single ION 7600 Power Quality Meter was installed and commenced recording on 8 April 2003. The ION 7600 was configured to monitor the voltage and current at the terminals of turbine T2 (Figure 4.1). The configuration allowed for the monitoring of voltage (and later current) unbalance on a 10-minute basis and also the capture of several cycles of the voltage and current wave shapes. The unbalance monitoring was continuous whereas the wave shape capture (for voltage sags and transient disturbances) was triggered when internal threshold levels were exceeded.

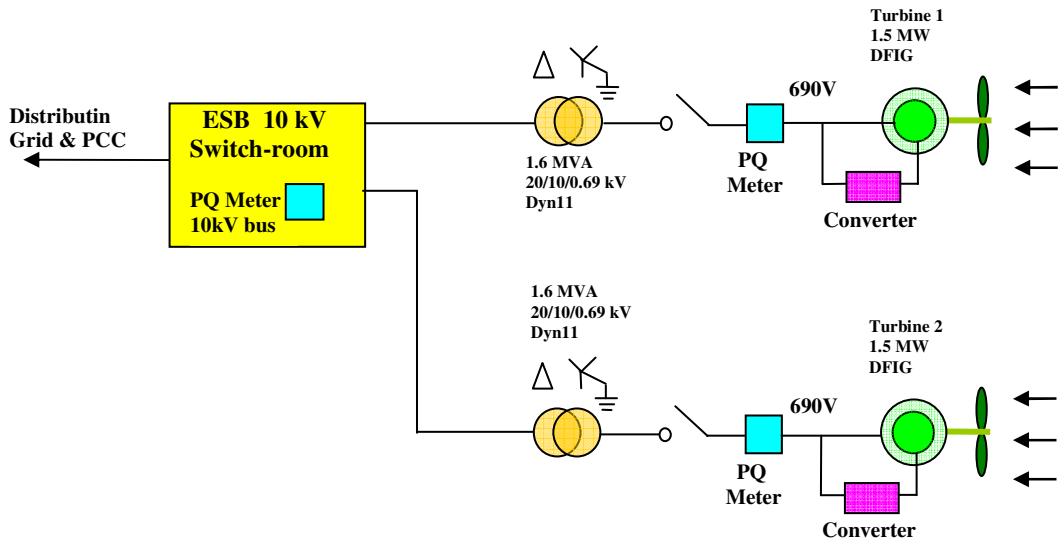

Figure 4.1 Corneen wind-farm single line diagram

An example of data recorded from the ION 7600 Meter during the monitoring period, is shown in Figure 4.2. The figure shows a voltage sag, which was recorded while turbine

T2 was out of service. This trace shows a three-phase voltage waveform at the terminals of the generator during a voltage sag without any involvement of the generator. It can be noticed that the sag also introduces voltage unbalance at the terminals of the generator.

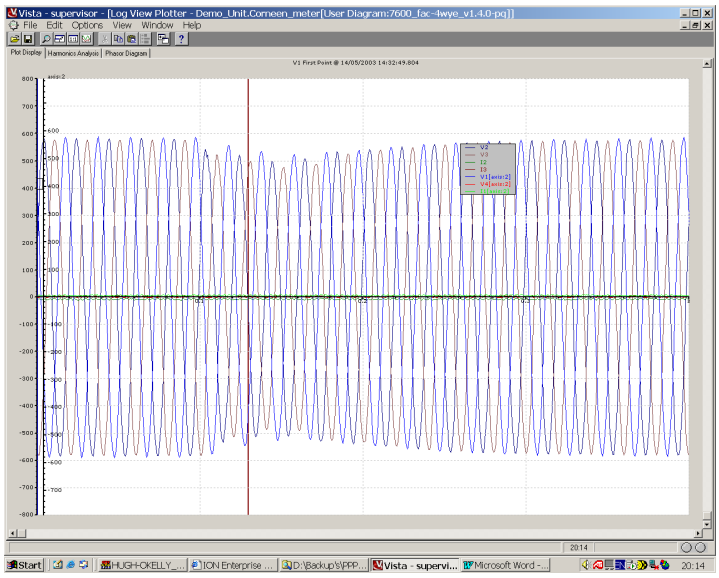

Figure 4.2 Voltage sag at the terminals of a turbine

4.2.2 Analysis of Voltage Unbalance at Turbine Terminals

The first report presented an analysis of the result of power quality monitoring over a seven-week period at the Corneen wind farm. A number of reported trips have been associated with observed power quality events during this period. Figure 4.3 shows the recorded voltage unbalance over a seven week period. These results show the mean unbalance during each 10 min. interval. The daily variation in voltage unbalance is obvious from Figure 4.3, with the daily peaks occurring in the late afternoon/early evening period. Also, the highest voltage unbalance peaks recorded during each 10 min. interval tended to occur at weekends.

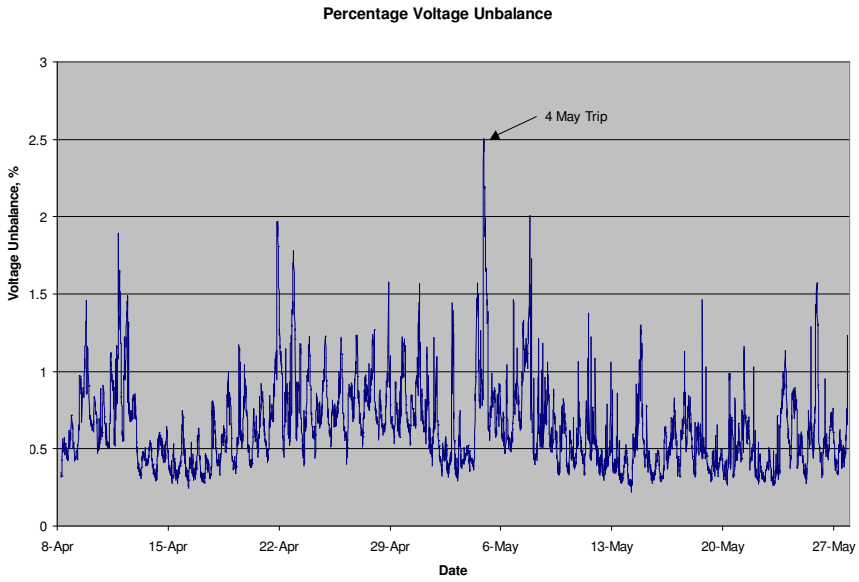

Figure 4.3 Voltage unbalance (%) recorded on Turbine 2 over seven weeks

The variable nature of the voltage unbalance is clear from Figure 4.3. In order to investigate the degree of severity of the voltage unbalance and to quantify the duration when the unbalance exceeds defined threshold levels over a certain period, a cumulative graph of voltage unbalance against duration of exceedance was produced. Figure 4.4 shows the graph for all periods over the duration of the study. For example, it can be noted from the graph that a voltage unbalance of 1% was exceeded for approximately 10% of the time.

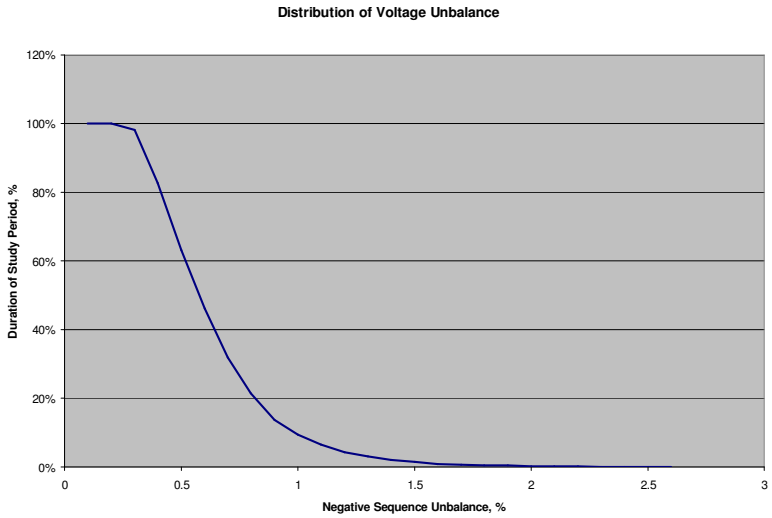

Figure 4.4 Distribution of voltage unbalance

Although the period of study was limited, and only one turbine was monitored, it served as a useful initial study and allowed for a number of recommendations to be made with regard to future work in this area. DIT was asked to monitor Corneen due to a high level of trips during the winter months of 2003/2004 and produce a report. This report focused on the period winter 2003 to spring 2004 as recommended in the previous study. On the basis of the recommendations in the first report, three ION 7600 Power Quality Monitors were installed at the Corneen Wind Farm to enable further assessment of the causes of trips on the wind farm turbines over an extended period and, in particular, an assessment over the winter period when the perception was that the voltage unbalance was at its highest.

The second report demonstrated similar findings to the first report in terms levels of voltage unbalance. To enable continuous monitoring of the wind-farm power quality monitors were installed on both wind turbines, and also on the 10kV bus where connection is made to the ESB distribution network. The data collected on the 10 kV bus was used to determine the voltage unbalance at the distribution network side of the wind farm.

The voltage unbalance factor at Turbine 1 determined during the month of January 2004 is shown in Figure 4.5. An analysis of the voltage unbalance at Turbine 2 provided similar results. The daily variation in voltage unbalance at Turbine 1 shows daily peaks occurring in the late afternoon/early evening period. It would appear that the predominant load is domestic, with an evening peak, and that peak domestic load is inherently unbalanced.

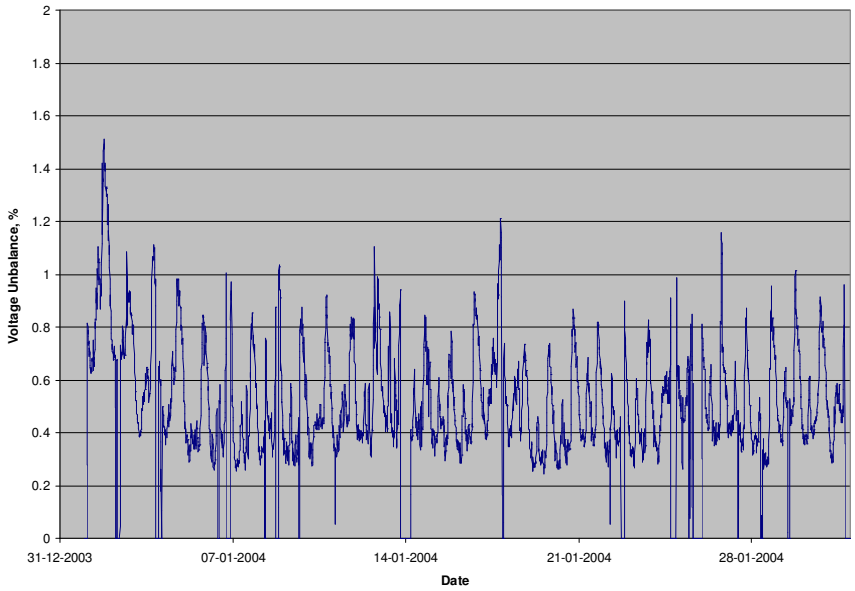

Figure 4.5 Voltage unbalance (%) at Turbine 1

To quantify the degree of voltage unbalance and compare with the requirements of the relevant codes and standards, the distribution of voltage unbalance was calculated on a weekly basis over the period described. Figure 4.6 shows the distribution of the voltage unbalance for each of the weeks in the period under consideration for Turbine 1. The duration of unbalance was greatest over the Christmas and New Year period (weeks 22 December and 29 December) for Turbine 1; conditions of high domestic loading.

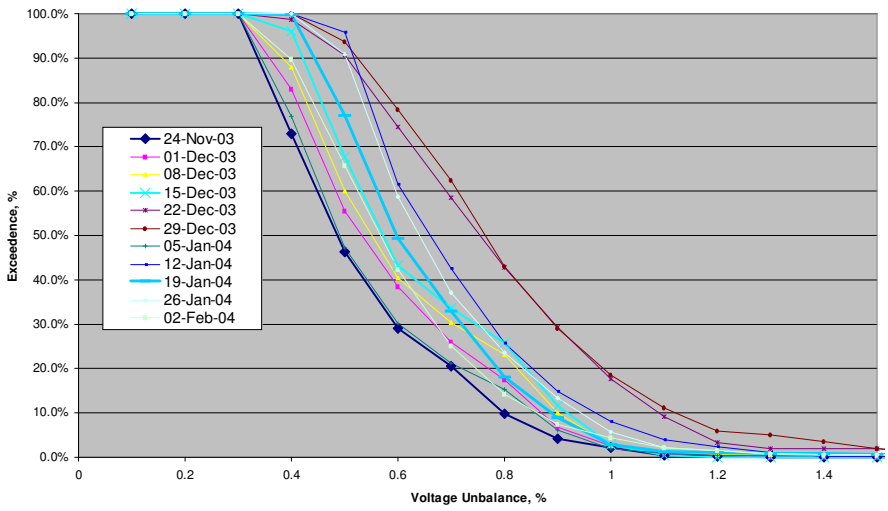

Figure 4.6 Distribution of voltage unbalance for Turbine 1

Figure 4.7 shows an example of recorded percentage voltage unbalance factor for the 26th December 2003 for both turbines. It is evident that protective relay settings on the turbines are dissimilar; Turbines 2 trips at a lower level of voltage unbalance when compared to Turbine 1. The steady increase in network voltage unbalance throughout the day particularly after 4 pm is clearly evident. The calculated voltage unbalance drops to zero when the protective relays open the circuit breakers and isolate the power quality meters.

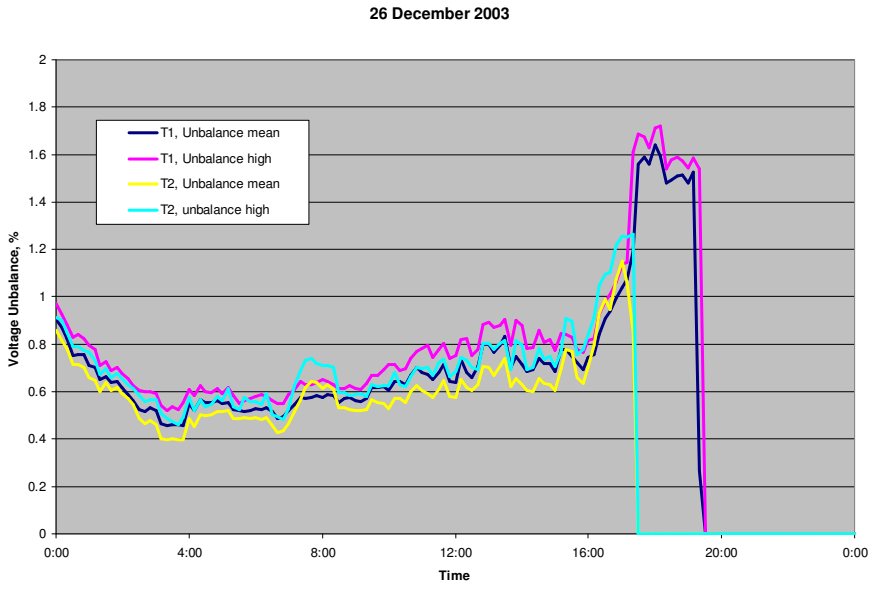

Figure 4.7 Negative sequence voltage on Turbines 1 and 2

The relevant Irish Standard relating to the power quality of distribution networks is I.S. EN 50160:200 [43]. Section 3.10 of the Standard states that "under normal operating conditions, during each period of one week, 95% of the 10 minute mean rms values of the negative phase sequence component of the supply voltage shall be within the range 0 to 2% of the positive sequence component"[7]. The analysis indicated that for the weeks

[7] The Standard also states that "In some areas with partly single phase or two phase connected customers' installations, unbalances up to about 3% at three-phase supply terminals occur."

considered the level of voltage unbalance did not exceed the limits defined in the Standard.

The results presented in the reports indicated that the degree of voltage unbalance was quite variable over the course of the study. It appears that the degree of voltage unbalance was highest over the Christmas and Easter holiday periods, when possibly the industrial/commercial load was low and the domestic load was higher. Fault times for Turbine 2 over a six week period over Christmas and New Year, are illustrated in Figure 4.8. All faults presented occurred for asymmetrical voltage. Discounting the earliest and latest event times, the mean time for faults during the six week period is in the region of 5.45 pm.

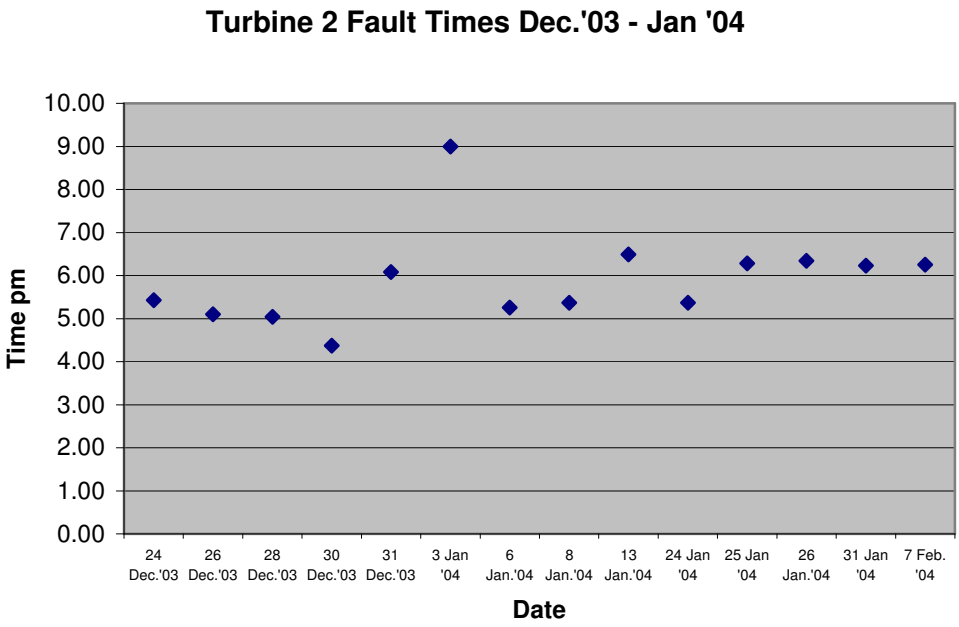

Figure 4.8 Turbine 2 fault times, Christmas holidays

A very similar fault trend occurred on Turbine 1. It can clearly be observed that all faults occurred in the evening and except for two faults, one on Turbine 1 and one on Turbine 2 all faults occurred after 5.00 pm. The faults that occurred on both turbines on the 31st Dec. (New Years Eve) at approximately 9 pm occurred within minutes of each other.

4.2.3 Analysis of Voltage Unbalance at 10 kV Distribution Voltage

The percentage voltage unbalance profile at the switch room 10 kV bus during the 30th Dec. is shown in Figure 4.9. Both turbines tripped at about 4.30 pm (Turbine 1 trip times are illustrated in Figure 4.8).

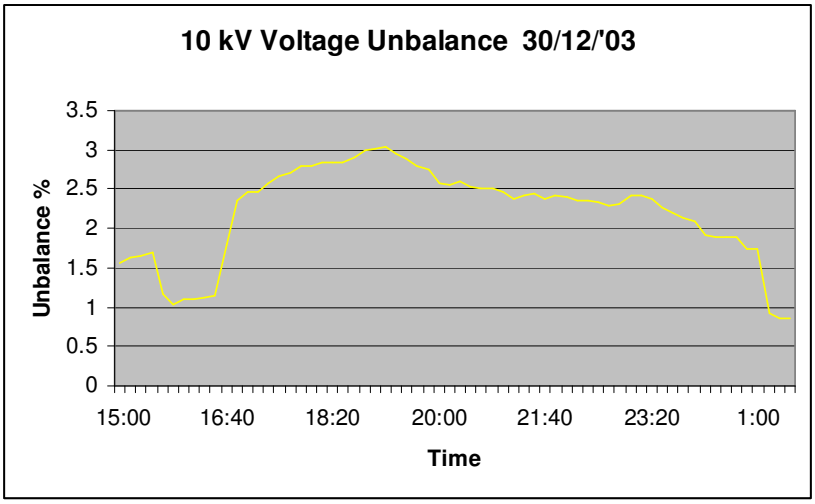

Figure 4.9 Switch Room 10 kV voltage unbalance

When both turbines are not operating, the 10 kV voltage unbalance rises sharply, eventually reaching a value in excess of 3 %. The voltage unbalance at the 10 kV bus over a four week winter period is illustrated in Figure 4.10. The voltage unbalance profile can be compared with the results for Turbine 1 in Figure 4.3.

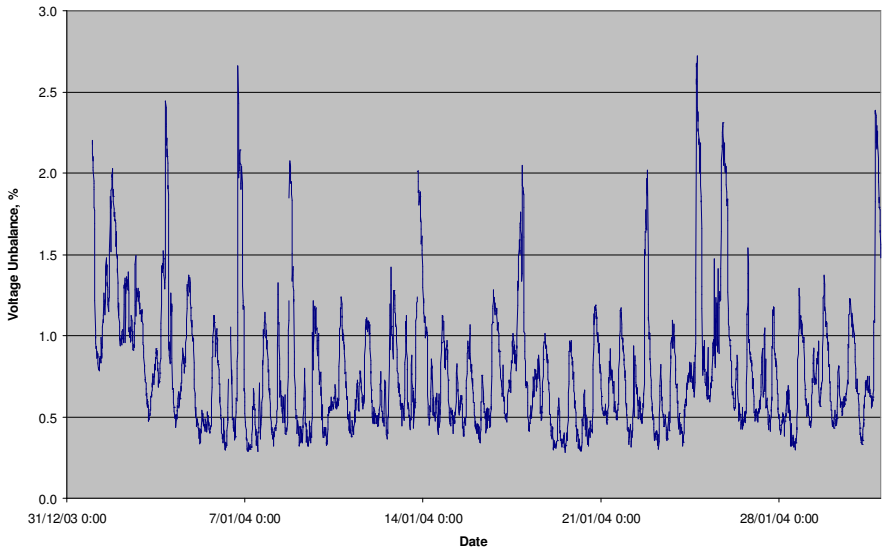

Figure 4.10 Voltage unbalance (%) at the 10kV bus for January 2004

In general, the level of voltage unbalance at the 10 kV bus is higher than that recorded at the terminals of turbines 1 and 2. It is clear that the degree of voltage unbalance inherent in the network varies in response to the network load. Whereas the voltage recorded for both turbines is obviously zero after a trip occurs (circuit breakers isolate PQ meters), the voltage at the 10kV bus can be continuously monitored if only the individual turbine circuit breakers operate. The data collected at the 10kV bus was used to analyse the impact of the operation of turbines on the degree of voltage unbalance in the network. When the turbines were not operating, the inherent voltage unbalance present in the network was observed. By comparing the unbalance recorded with and without the turbines operating, an indication was obtained as to the effect the turbines have on the network voltage unbalance. Separate assessments were made of the statistical distribution of the voltage unbalance during the operating and non-operating periods of both turbines. Figure 4.11 shows the distribution for the operating period is centred on a value of 0.7% voltage unbalance. The distribution for the non-operating period is clearly shifted to the right, centred on a voltage unbalance of 1.6%. It can be seen from these results that the effect of the operation of the turbines at Corneen is to reduce the degree of unbalance as observed at the 10 kV bus (discussed in Section 2.5 (Chapter 2)).

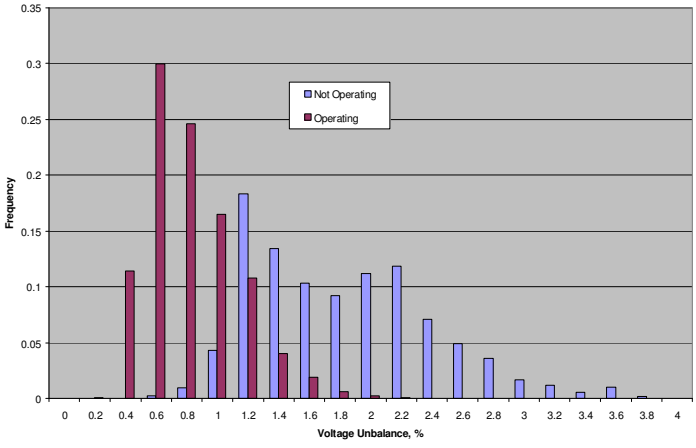

Figure 4.11 Distribution of voltage unbalance at 10 kV bus during operating and non-operating periods of the turbines.

The results presented in Figure 4.12 also serve to illustrate this point. The graph shows the probability of exceedance of the indicated degree of voltage unbalance for both the operating and non-operating periods. (This result is essentially a cumulative distribution of the probability density function presented in Figure 4.11). In particular, the results show that the voltage unbalance is well inside the Irish Standard EN 50160:2000 as the 2% unbalance is exceeded for less than 0.1% of the time when one or both turbines are operating. On the other hand, for the non-operating case, the 2% unbalance level is exceeded for 32% of the non operating period.

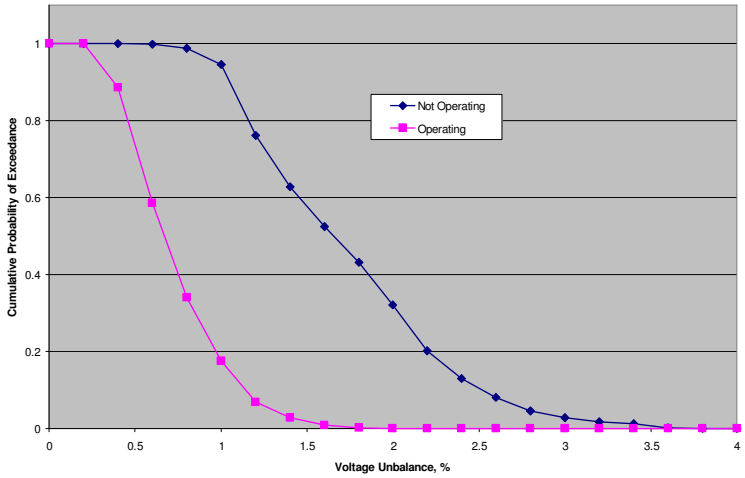

Figure 4.12 Cumulative probability distribution of voltage unbalance

The results presented in Figure 4.13 further illustrate the relationship between turbine generated power and grid voltage unbalance. Figure 4.13 is a plot of percentage voltage unbalance and output power in kW of one wind turbine measured over two days. The figure shows that the inherent voltage unbalance of the utility network without the operation of the wind farm is higher when the generator is not connected and delivering power. It is clear from the results that when the generator is on load it has a positive effect on the supply voltage unbalance. This feature was also observed in a study of a wind-farm in Wales [12].

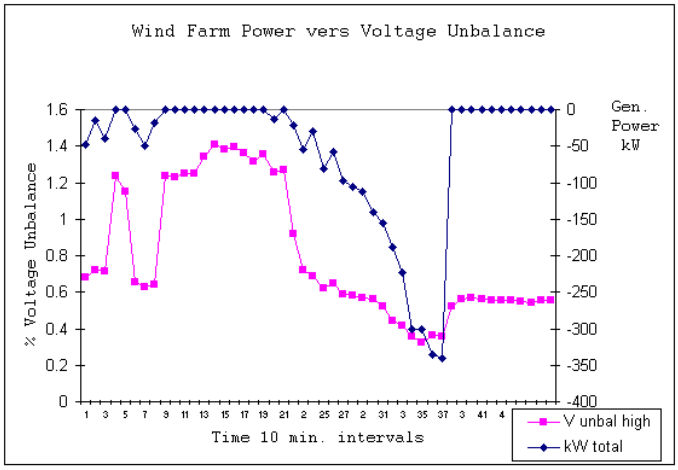

Figure 4.13 Voltage unbalance and generated power of one turbine at a Wind Farm in County Cavan. The ION 7600 PQ meter was set for a sampling rate of 10 mins.

4.3 Effect of Distribution Power Transformers on the Dip Type

When considering wind-turbines which are mainly rated at low voltage (generally 690V) a three-phase power transformer is normally connected between generator terminals and the ESB distribution network. The connection scheme of the power transformers can affect phase voltages. Depending on the winding connections of the transformer the retained voltages seen at the secondary side due to an unsymmetrical voltage dip or fault at the primary side may be altered. This means that a voltage dip type on one side of a three-phase transformer may change to an alternative type of voltage dip when observed on the opposite side of the transformer. The transfer from one voltage dip type to another is listed in Table 4 [119]. The voltage dip classification is described in Chapter 2 Section 2.7.

Table 4 Voltage dip classification

Voltage Dip Type on Primary Side	**A**	**B**	**C**	**D**	**E**	**F**	**G**
Delta/Star Transformer (Secondary)	**A**	**C**	**D**	**C**	**F**	**G**	**F**

An overview regarding the influence of transformer winding connections on the propagation of voltage dips is given in [86], [87]. In delta-star transformers a phase shift

is introduced by the phase winding connections of the transformer and it is necessary to consider this transformation when investigating voltage faults or unbalanced voltages. Such a phase shift is seen in practice as a transformation between fault types. In other words a phase-to-phase fault at one side of a three-phase delta-star transformer is seen as a phase-to-ground fault at the other side.

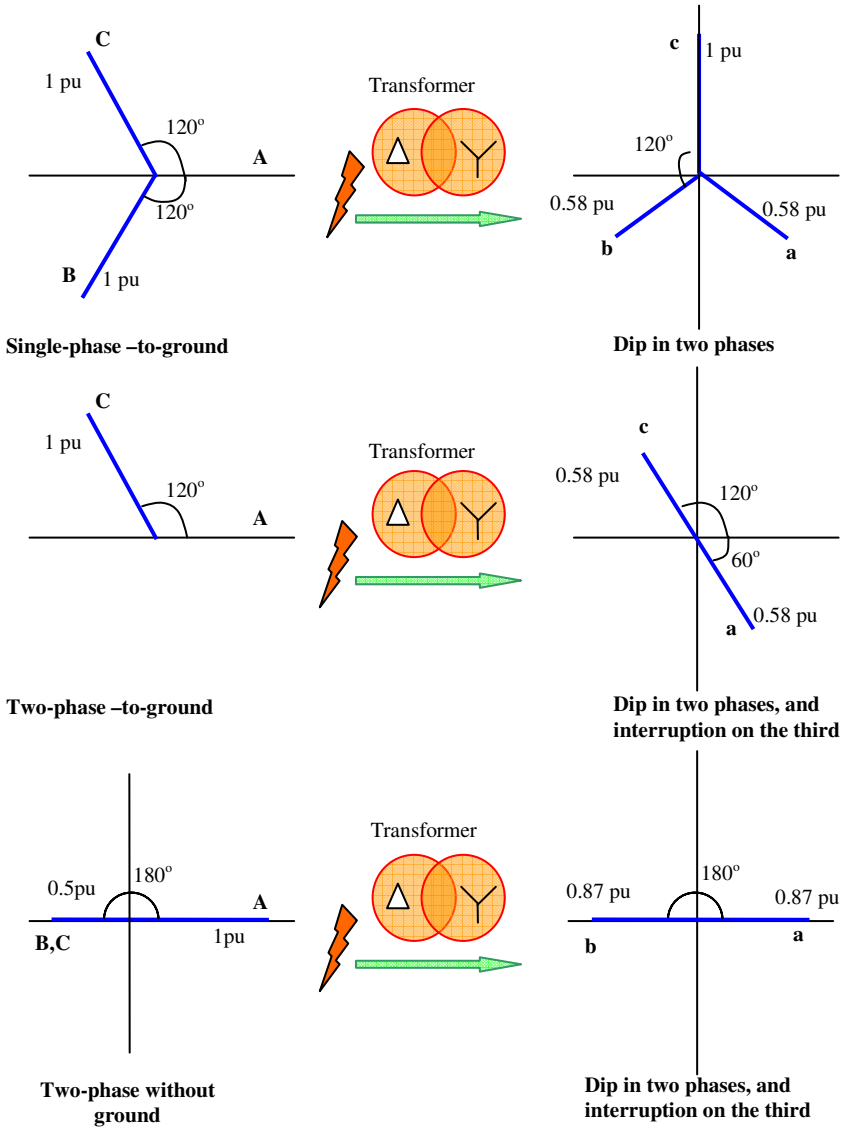

Figure 4.14 Propagation of voltage dips caused by asymmetrical faults on a Dy1 transformer

For example various short-circuit fault types on high-voltage windings of a Dy1 or Dy11 transformer (common transformer configuration installed in wind turbine systems), can

lead to a different voltage dip classification on the low voltage side as shown in Figure 4.14 [86].

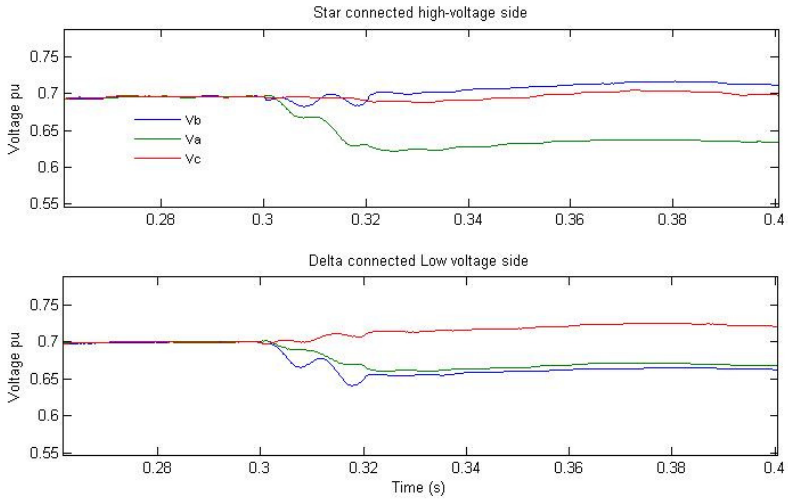

Figure 4.15 Voltage unbalance propagation through a delta-star transformer

A model of a three-phase star-delta transformer was developed using the power system toolbox "SimPowerSystems" in Matlab/Simulink. Figure 4.15 is the result of a simulation performed on the transformer model. The figure shows that at the input to the transformer high voltage side there is a reduction in 'a' phase, (v_a, green trace) results in a drop in phases v_a and v_b (v_a green and v_b blue) on the low voltage side of the transformer. This result is similar to the single-phase to ground fault in Figure 4.14.

Delta-star transformer connections are normally the preferred choice in wind turbine installations. For transformers manufactured according to the ANSI/IEEE standard [87], the low voltage side whether in star or delta, has a phase shift of 30^o lagging with respect to the high voltage side phase-to-neutral voltage vector. These phase displacements are applicable to positive-sequence voltages. Hence in passing through the transformer from the fault side to the observation side, the positive-sequence phase voltages of the corresponding phase are shifted 30° in one direction, and the negative-sequence

quantities are shifted 30° in the opposite direction. A delta or ungrounded star winding removes the zero-sequence voltage component, however positive and negative-sequence voltages and currents pass through the transformer. In sequence networks, the impedance is the same value independently of the winding connections.

Hence the positive-sequence voltage does not need to be shifted, but the negative-sequence voltage needs to be shifted ± 60° to take into account the effect of the transformer. To clarify this, consider Figure 4.16.

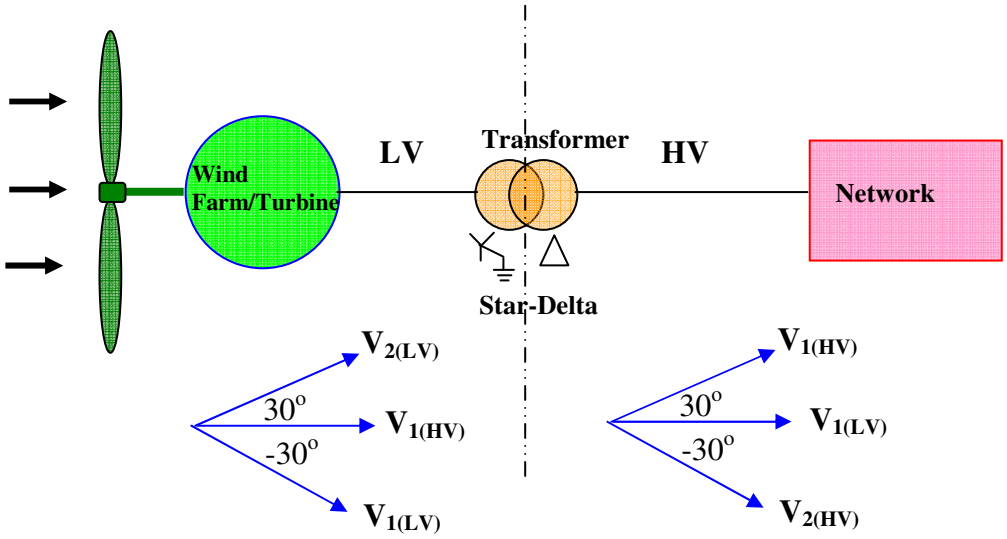

(a) Phase shift w.r.t. to HV side **(b) Phase shift w.r.t. to LV side**

Figure 4.16 Star-delta power transformer located between a wind-turbine and a network; V_1 is positive sequence voltage and V_2 is negative sequence voltage

According to (ANSI/IEEE, 1988) the positive-sequence phase to neutral voltage at the network has a phase shift of -30° with respect to the positive-sequence phase to neutral voltage of the wind-turbine. In terms of voltage unbalance, this phase shift is seen as a ±60° phase shift in the negative sequence voltage with respect to the positive sequence voltage of the same side [87]. If phase voltage unbalance originates at the HV side and is observed at the LV wind-turbine side, the rotation in the negative sequence is +60°,

Figure 4.16(a). For voltage unbalance originating at the LV side and observed at the HV sector a -60º shift needs to be considered in the negative sequence, Figure 4.16(b).

4.4 Induction Machines and Voltage Unbalance

Phase voltage unbalance in utility distribution networks can affect WECS and the level of interference will depend on how they are configured. For example in the case of directly connected induction generators, voltage unbalance at the stator terminals will create a negative sequence voltage. Negative sequence voltage can produce negative sequence currents in induction generators. The amplitude of these currents will depend on the level of negative sequence impedance of the machine.

Induction machines can be represented in steady-state analysis by a per-phase equivalent circuit. Equivalent circuits can be obtained separately for positive and negative sequence components illustrated in Figure 4.17 and Figure 4.18.

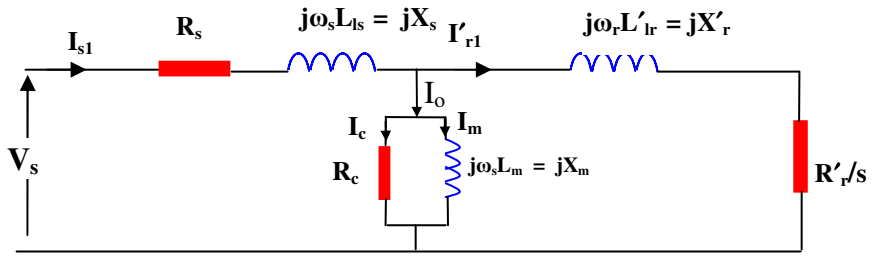

Figure 4.17 Positive sequence equivalent circuit of an induction machine

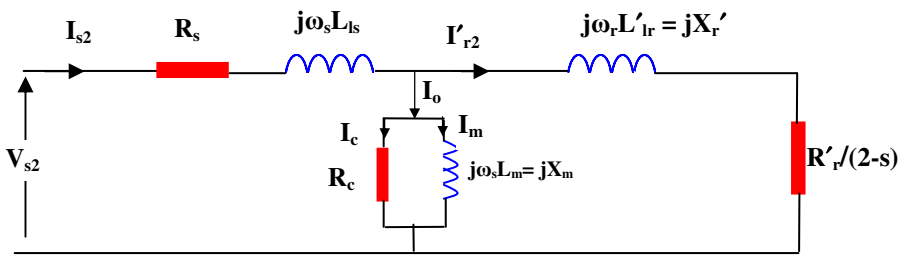

Figure 4.18 Negative sequence equivalent circuit of an induction machine

where ;

v_s	=	Terminal voltage.
R_s	=	Stator winding resistance.
$j\,\omega_s L_s$	=	Stator leakage reactance.
$j\,\omega_s L_m$	=	Magnetising reactance.
R_c	=	Core loss resistance.
E_s	=	Induced voltage in the stator winding.
E_r	=	Induced voltage in the rotor winding.
$j\,\omega_r L`_r$	=	Rotor leakage reactance referred to stator
$R`_r$	=	Rotor winding resistance referred to stator.
N	=	Ns/Nr = Turns Transformation ratio.
s	=	Slip

Stator referred negative sequence rotor resistance is $\frac{R'_r}{(2-s)}$ as indicated in Figure 4.18.

For low values of slip this is approximately equal to $\frac{R'_r}{2}$, considerably lower than the positive sequence resistance. With a low value of negative sequence voltage large negative sequence currents may flow.

The developed power (P_e) of an induction machine consists of the positive sequence real power (P_1) and the negative sequence real power (P_2) components [14], [46]:

$$P_e = P_1 + P_2 \tag{4.1}$$

where

$$P_1 = 3\,I_{1r}{}^2\,\frac{(1-s)}{s}R_r` \tag{4.2}$$

$$P_2 = -3\,I_{2r}{}^2\,\frac{(1-s)}{(2-s)}R_r{}' \tag{4.3}$$

The developed power is:

$$P_e = P_1 + P_2 = 3R_r' I_{1r}{}^2 \frac{(1-s)}{s} - 3R_r' I_{2r}{}^2 \frac{(1-s)}{(2-s)} \quad (4.4)$$

For values of slip less than 1, P_1 is positive and P_2 is negative.

The torque due to positive sequence current (T_1) and torque due to negative sequence current (T_2) are:

$$T_1 = \frac{P_1}{\omega_m} = \frac{P_1}{\omega_s(1-s)} = \frac{3I_{1r}{}^2 R_r}{s\omega_s} \quad (4.5)$$

$$T_2 = \frac{P_2}{\omega_m} = \frac{P_2}{\omega_s(1-s)} = -\frac{3I_{2r}{}^2 R_r}{(2-s)\omega_s} \quad (4.6)$$

The developed torque in the machine is:

$$T_e = T_1 + T_2 = \frac{3R_r}{\omega_s}\left(\frac{I_{1r}{}^2}{s} - \frac{I_{2r}{}^2}{(2-s)\omega_s}\right) \quad (4.7)$$

Negative sequence torque T_2 will cause a torque reduction that can introduce unwanted effects in induction machines as described in the literature survey. There is a reduction in both the developed power and torque due to the negative sequence current as indicated in equations (4.4) and (4.7). The positive and negative sequence currents are functions of their sequence voltages, machine parameters and the slip s.

The power in an induction machine can also be described in terms of positive and negative sequence components as:

$$P = \text{Real } [3*(V_1 I_1{}^* + V_2 I_2{}^*)] \quad (4.8)$$

4.4.1 Simulation

To demonstrate negative sequence power and torque in an induction machine, a Simulink model was developed based on a simple circuit shown in Figure 4.19.

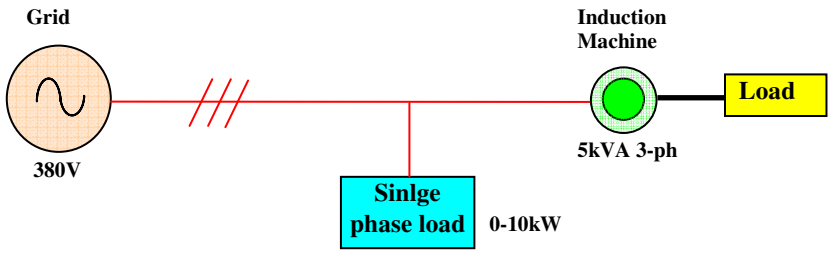

Figure 4.19 Circuit implemented in Matlab/Simulink

Induction machine parameters in the model are based on a four-pole 5 kVA machine, and are tabulated in Table 14A (Appendix A). Induction machine parameters were obtained from standard machine tests. In Table 14, R_s and X_s are the stator resistance and leakage reactance respectively and $R_r`$ and $X_r`$ are the stator referred rotor resistance and leakage reactance respectively. R_c is the core loss resistance and X_m the magnetising reactance.

A Matlab/Simulink model of the simple network shown in Figure 4.19 is shown below in Figure 4.20.

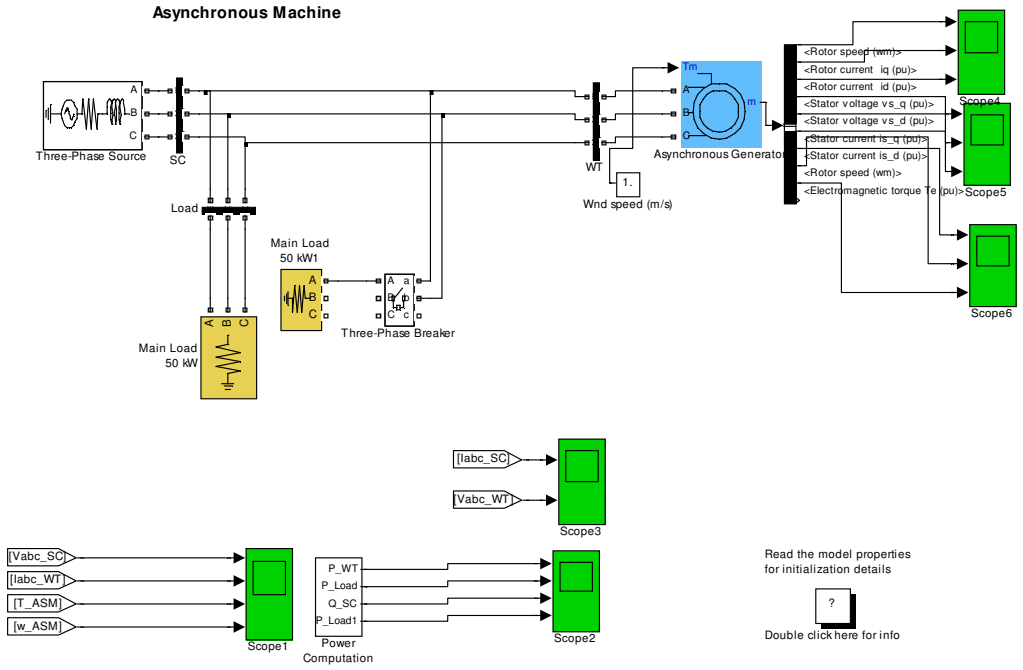

Figure 4.20 Simulink model of 5 kW induction machine

In the Simulink model a single phase load is connected across one phase and ground of the grid supply. This single-phase load draws a current in one phase only, reducing the voltage amplitude in that line. The other two phases remain unaffected. Three-phase voltage unbalance is thus applied to the stator terminals of the induction machine. The requirement of the model was to simulate a voltage unbalance relating to a change in the applied voltage magnitudes, therefore the line voltage phase angles were not altered. The single-phase voltage dip (other two phases remained unchanged) produced a phase voltage unbalance of 5.2 percent applied to the 5 kVA induction machine terminals. The single-phase load was timed to be connected to phase A at 0.3 seconds. Operation of the induction machine as a generator required negative per unit torque be applied.

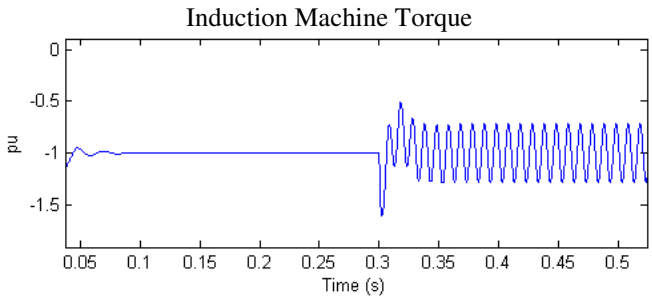

(a)

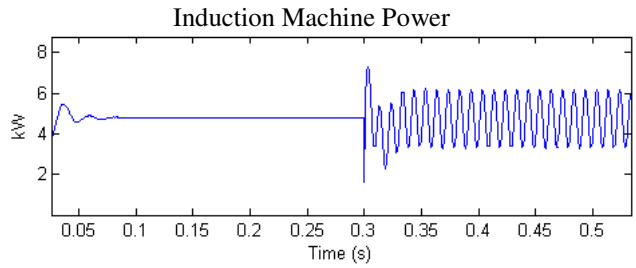

(b)

Figure 4.21 Induction machine: (a) Torque and (b) Stator Power

Torque and power pulsations at a frequency of 100 Hz, double the applied frequency of 50Hz, are observed in Figure 4.21, demonstrating the effects of the negative sequence torque T_2, equation (4.7) and the negative sequence power P_2, equation (4.4). The periodic torque pulsations reach a peak value of -1.25pu and peak oscillating power is 6.3 kW.

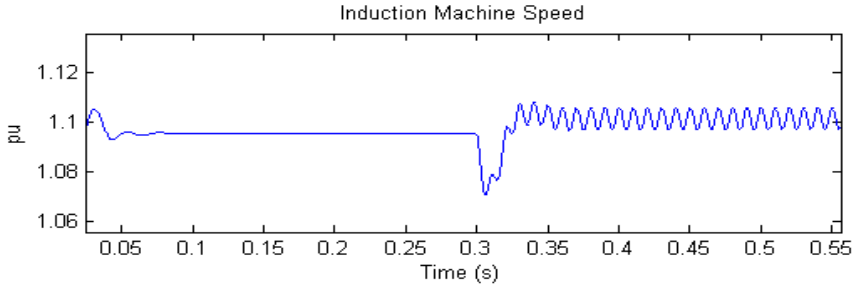

Figure 4.22 Induction machine speed

A plot of speed versus time of the induction machine is illustrated in Figure 4.22. Speed oscillations at a frequency of 100Hz are observed.

4.4.2 Assessment of Negative Sequence Impedance

To establish the effects of unbalanced voltage on the impedance of a laboratory based 5 kVA machine, tests were carried out to determine the negative sequence impedance of the machine [1]. The stator voltage supply was made unbalanced by incorporating a single phase variac in series with one of the three phase voltages supplied by a three-phase variac as shown in Figure 4.23. When the single phase variac was set to maximum output voltage, three balanced line voltages were applied to the machine. Reducing the output of the single-phase variac reduced the magnitude of one phase voltage. This introduced a voltage unbalance magnitude applied to the stator of the induction machine. The level of voltage unbalance was adjusted by altering the voltage magnitude output of the single-phase variac.

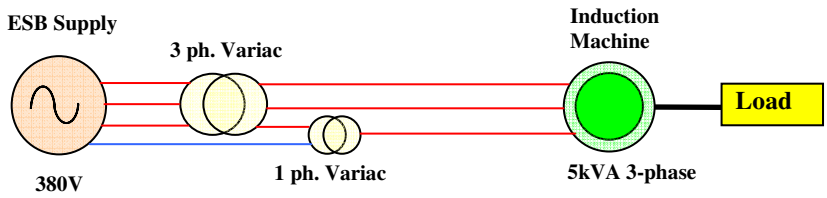

Figure 4.23 Induction machine circuit for voltage unbalance testing

Tests were then performed and the negative sequence impedance was determined. These results were compared with those predicted by the equivalent circuit in Figure 4.19 using the impedance parameters in Table 14A in Appendix A.

The single phase variac connected as shown in Figure 4.23 was adjusted to deliver voltage unbalance levels of 2%, 3% and 4% to the stator of the induction machine. The three stator line voltages and currents were then measured. In addition to these tests, a series of measurements were made to directly determine the negative sequence

impedance. These tests involved rotating the induction machine in the reverse direction by means of a dc machine directly coupled to the induction machine. The stator was connected to a low-voltage positive sequence supply and the stator voltage and current were measured. The technique proposed by Oliveira et al [49] was used for the voltage unbalance calculation:

$$VUF = \sqrt{\frac{1-\sqrt{3-6\beta}}{1+\sqrt{3-6\beta}}} \tag{4.9}$$

$$\text{where } \beta = \frac{|V_{ab}|^4 + |V_{bc}|^4 + |V_{ca}|^4}{\left(|V_{ab}|^2 + |V_{bc}|^2 + |V_{ca}|^2\right)^2}$$

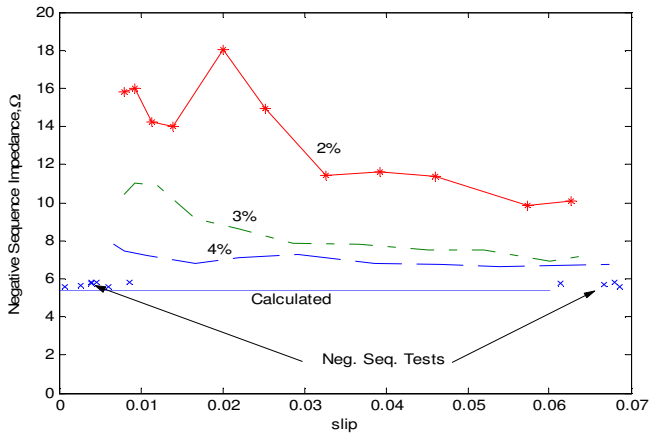

Figure 4.24 Evaluation of negative sequence model

Figure 4.24 shows a summary of these results. The solid line shows the calculated negative sequence impedance (calculated from the equivalent circuit, Figure 4.18 using the parameters in Table 14A). The figure shows that impedance is largely independent of the slip. From Figure 4.18 neglecting the magnetising branch, the impedance is:

$$Z_2 = R_1 + R_2'/(2-s) + j(X_1 + X_2') \tag{4.10}$$

When operating with full load, the slip s of the induction generator is 0.095, so the operating region for slip between no load and full load is 0 to 0.095. Therefore neglecting slip s in the above equation does not introduce appreciable error. The impedance then becomes:

$$Z_2 \quad \approx \quad R_1+R_2'/2 \; + j\,(X_1+X_2') \tag{4.11}$$

Inserting the machine parameters into equation (4.11) the negative sequence impedance is approximately 5.5Ω. The results of the measurements at the nominal levels of unbalance of 2%, 3% and 4% are also shown. As can be seen, the agreement is quite poor for an unbalance level of 2% but improves as the level of unbalance increases. The measured values also tend towards the calculated value for increasing slip. Direct measurements of negative sequence impedance were made at 1500 rev/min. (s = 0) and 1400 rev/min. (s = 0.07). As can be seen from Figure 4.24, there is good agreement with the calculated impedance for the two speeds.

4.4.3 Losses in Induction Machine

As utility voltage unbalance increases, losses in induction machines can increase due to an increase in negative sequence currents. The 5 kVA induction machine model described previously was simulated in the program Matlab/Simulink to analyse the losses in the machine due to voltage unbalance.

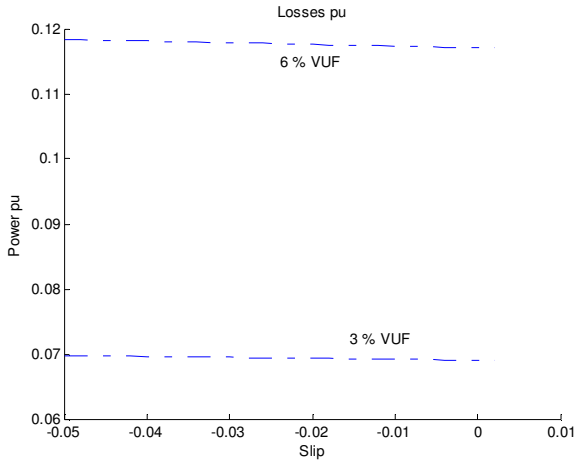

Figure 4.25 Losses as a result of applied voltage unbalance to an 800 kW induction machine

The results obtained are illustrated in Figure 4.25. The electric power losses of the induction machine under voltage unbalance conditions are plotted against slip. (Table 1 in Chapter 2, Section 2.8, also showed increased losses in motors due to voltage unbalance). In Figure 4.25 two plots are shown, the top plot is for a voltage unbalance of 6% and the bottom plot is for a voltage unbalance of 3%. It can be observed that as the level of voltage unbalance increases the electric power losses increase. This power loss will result in heating of the machine windings and is the reason for degrading the induction machine when subjected to voltage unbalance as outlined in Chapter 2, Section 2.8.

4.5 Unbalance Voltage Applied to Converters

4.5.1 Converter - Controlled Rectifier.

An unbalanced three-phase voltage source can be decomposed into two balanced positive and negative sequence components [38]:

$$\left.\begin{aligned} V_a &= V_p \cos(\omega t + \alpha) + V_n \cos(\omega t + \beta) \\ V_b &= V_p \cos(\omega t - 2\pi/3 + \alpha) + V_n \cos(\omega t + 2\pi/3 + \beta) \\ V_c &= V_p \cos(\omega t + 2\pi/3 + \alpha) + V_n \cos(\omega t - 2\pi/3 + \beta) \end{aligned}\right\} \quad (4.12)$$

Where V_p is the positive sequence voltage and V_n is the negative sequence voltage.

Equation 4.12 can be rewritten in space vector form:

$$V_s = V_{pm} e^{j(\omega t+\alpha)} + V_{nm} e^{-j(\omega t+\beta)} \quad (4.13)$$

where V_{pm} is the positive sequence space vector voltage and V_{nm} is the negative sequence space vector voltage.

Unbalanced currents flowing into a PWM converter can also be obtained as:

$$I_s = I_{pm} e^{j(\omega t+\lambda)} + I_{nm} e^{-j(\omega t+\theta)} \quad (4.14)$$

The power in the converter can be obtained as:

$$P + jQ = V_s . I_s^*$$

$$V_s I_s^* = V_{pm} I_{pm} e^{j(\alpha-\lambda)} + V_{nm} I_{nm} e^{-j(\beta-\theta)} + V_{pm} I_{nm} e^{j(2\omega t+\alpha+\theta)} + V_{nm} I_{pm} e^{j(2\omega t+\beta-\lambda)} \quad (4.15)$$

The product terms in equation (4.15) between the positive and negative sequence components of voltage and current generate 2-ω frequency power ripple causing DC link voltage ripple.

To illustrate the effects of supply voltage unbalance on converters, simulations were performed in Simulink of a model of a PWM controlled rectifier (Figure 4.26). The control technique incorporated Space Vector Pulse Width Modulation (SVPWM).

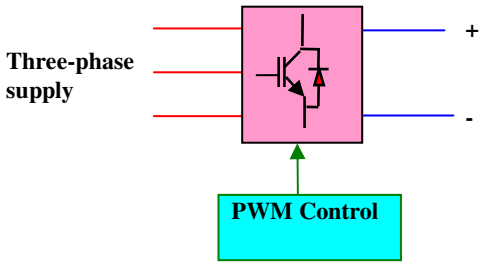

Figure 4.26 PWM Controlled Rectifier

A library model obtained in Simulink (and subsequently modified), of a PWM three-phase controlled rectifier is shown in Figure 4.27. The model consists of a three-phase IGBT voltage source bridge converter (VSC). The converter is controlled using PWM to produce a 500 V dc voltage. In this example, the converter switching frequency is 1350 Hz and the power system frequency is 50 Hz. A 100 kW load was connected to one phase of the supply voltage through a circuit breaker. When the load was switched to ground, a voltage dip was introduced on this phase resulting in supply voltage unbalance of 2.2% at the terminals of the converter.

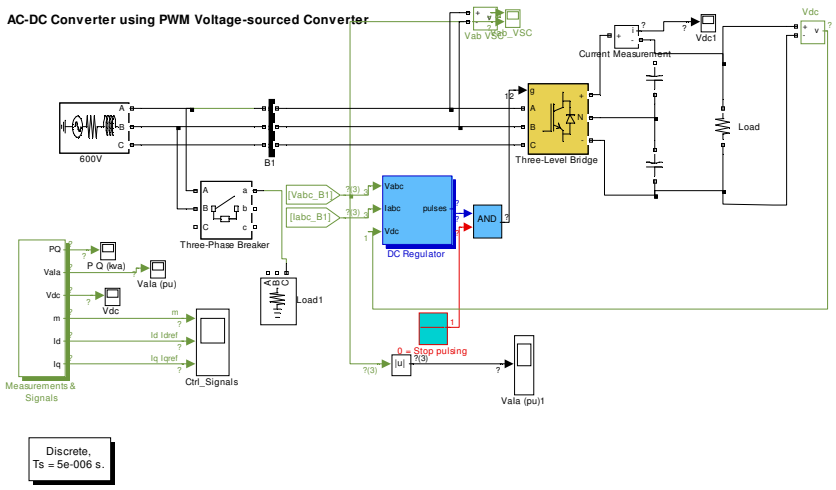

Figure 4.27 Simulink model of a PWM controlled rectifier

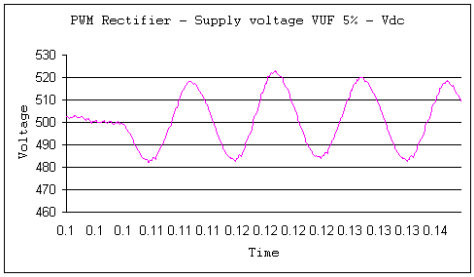

Figure 4.28 Rectifier DC link voltage V_{dc}

The switch was timed to close the circuit breaker at 0.1 seconds after commencement of the simulation. The model in Figure 4.27 was simulated and a plot of the DC link voltage is shown in Figure 4.28. It can be seen in Figure 4.28 at 0.1 seconds oscillations occur on the DC link bus due to the voltage unbalance at the converter supply terminals. The dc output voltage V_{dc} oscillates at a frequency of 100 Hz, at twice the voltage supply frequency of 50 Hz.

4.5.2 Inverters

To establish the effects of voltage unbalance on DFIG's an investigation of induction motor drives under voltage unbalance conditions is advantageous. To this end a Simulink model of a Space Vector Pulse Width Modulated (SVPWM) induction motor drive was implemented (Figure 4.29).

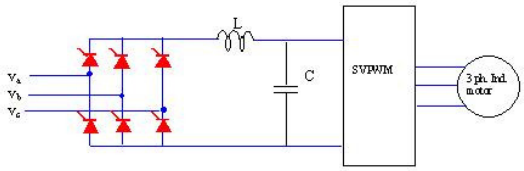

Figure 4.29 SVPWM Induction Machine Drive

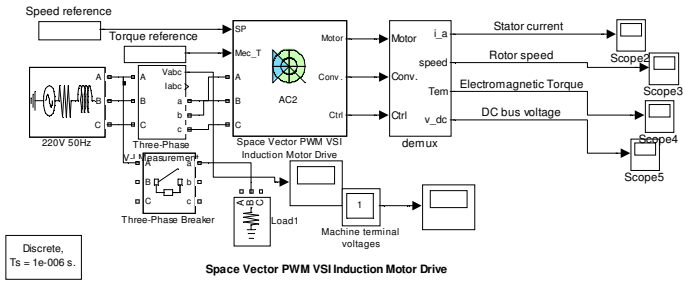

Figure 4.30 Matlab/Simulink model of space vector PWM VSI induction motor drive

Figure 4.30 is a Simulink model of a PWM VSI coupled to a 2.2 kW ac induction motor. The motor drives a mechanical load characterized by inertia *J*, friction coefficient *B*, and load torque T_L. The three-phase breaker in Figure 4.30 was set to close at 0.5 seconds and connect a load between phase A and ground, introducing a voltage dip on phase A. The model in Figure 4.30 was compiled and simulated in Matlab/Simulink. The resulting voltage unbalance factor measured at the terminals of the drive was 6%. Results of the simulations are shown in Figures 4.31 and 4.32.

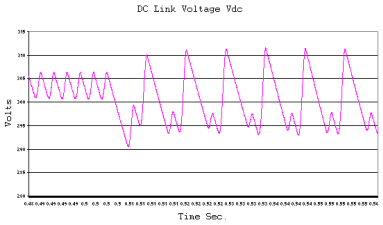

Figure 4.31 DC Link Voltage of SVPWM Induction Machine Drive

Voltage oscillations on the DC link voltage bus due to a supply voltage unbalance in the induction machine drive, as referred to in Chapter 2 Section 2.9**,** are observed in Figure 4.31. Similarly the torque pulsations at twice the applied frequency can be observed in Figure 4.32.

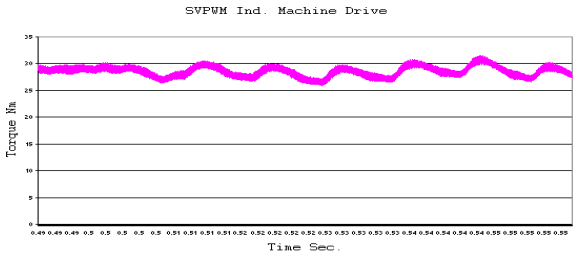

Figure 4.32 Induction machine torque

4.6 Double-Fed Induction Generators

The stator windings on a typical DFIG are normally connected directly to the grid, and a wound rotor configuration accessible through slip rings and brushes. The induction generator rotor winding connections are normally connected to a power electronic voltage-source four-quadrant converter which can vary the voltage applied to the rotor windings. The rotor currents are normally controlled to manipulate active and reactive power output from the turbine as required. The main benefit of this scheme when connected to a fixed frequency grid is the ability to vary rotor speed within a certain range (depending on the rating of the rotor side converter), and to control the active and reactive power flows into and out of the generator. The power flow in a DFIG is indicated with direction arrows in Figure 4.33.

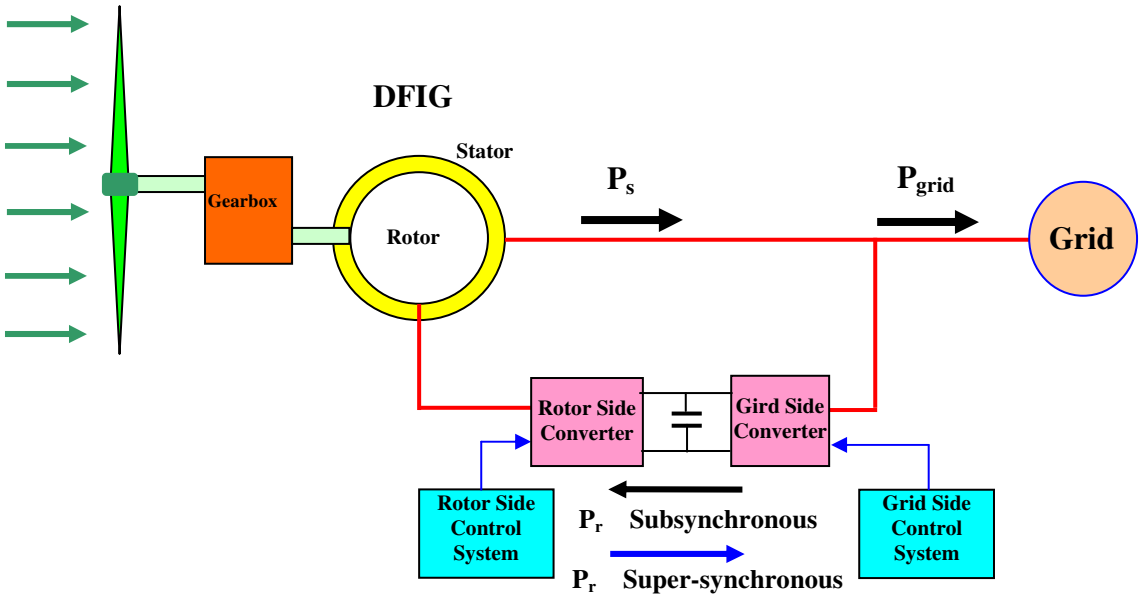

Figure 4.33 Subsynchronous and super-synchronous power flow in a DFIG

Unbalanced grid voltage affects the induction generator as described previously and it can also affect the normal operation of the DFIG converter in a detrimental manner. Under such abnormal conditions, wind turbines may be disconnected from the grid for their own protection, significantly impacting their energy production.

Volltage unbalance will directly affect the stator windings and also the normal operation of the grid-side converter. The grid-side converter is designed to accept a balanced three-phase supply voltage and the control of the DC link voltage in the converter is based on this assumption. Voltage unbalance affects the operation of the grid side converter resulting in DC link voltage oscillations.

The most critical problems which can be experienced by DFIG's during grid voltage unbalance are [82]:

- Rotor over-current, risking rotor converter power electronic component damage.
- DC link over-voltage and capacitor failure.

- DC link voltage oscillations resulting in loss of control of rotor current.
- Temporary loss of control of turbine active and reactive power output.
- Power and shaft torque oscillations resulting in possible generator damage.
- Stator and rotor unbalanced currents resulting in generator uneven heating and possible reduction of generator life-span.
- Complete loss of DFIG control in extreme cases.

The frequency of the rotor currents during an unbalanced fault will be dominated by two main components [82]:

- Positive sequence component at the slip frequency. This is the fundamental component.
- Negative sequence component at a frequency of (slip plus twice system frequency). This is a reaction to the negative sequence component of the source voltage.

4.7 Synchronous Generator Systems

The development of WECS in the period from the early 1990's to the late 2000's was predominantly Double Fed Induction Generators (DFIG's'), however in recent years the frequency of installations of synchronous generators has increased. These systems are also susceptible to problems associated with grid voltage unbalance and grid faults [134]. Synchronous generators systems can be configured as permanent magnet (PM) or electrically excited, and can be connected through a gearbox or direct driven. Figure 4.34 illustrates a typical synchronous generator system, consisting of a wind turbine connected through a gearbox to an electrically excited synchronous generator and a full converter connected to the stator. The stator of the synchronous generator is connected

to an uncontrolled three-phase rectifier, a DC/DC boost converter, DC link and a three-phase IGBT voltage source inverter.

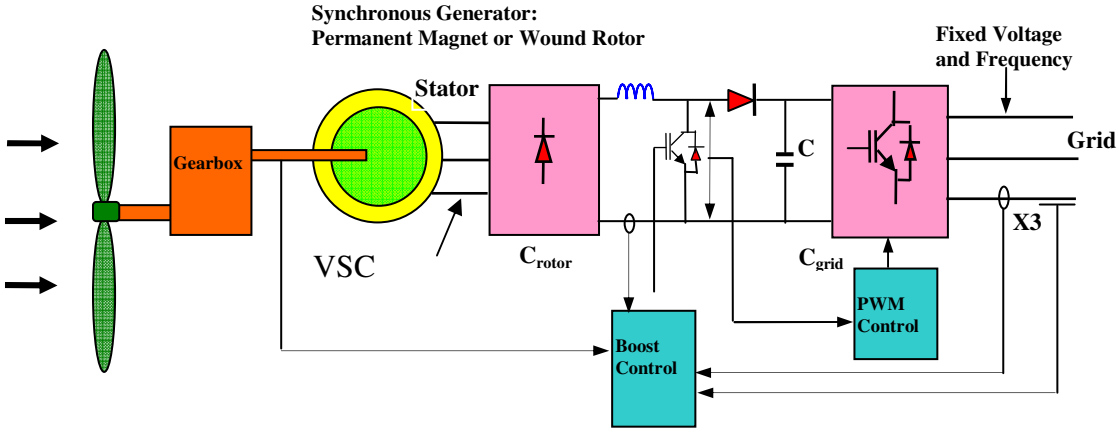

Figure 4.34 Synchronous Generator System

Grid disturbances including grid voltage unbalance and single-phase faults can affect synchronous generator systems and result in distorted converter currents and problematic operation. The performance of a synchronous generator system to the effects of voltage unbalance and grid faults is investigated in [134]. Improvements in performance of the synchronous generator WECS to grid disturbances are analysed.

A comparison of the performance of a DFIG and a synchronous generator WECS to the affects of single-phase faults and network voltage unbalance conditions has been investigated [136]. Among the conclusions reached are that synchronous generators connected to the grid through a converter and DFIG's are affected by single-phase faults and grid voltage unbalance. However the performance and ride-through capability during grid voltage problems of synchronous generator systems is superior when compared to the performance of a DFIG. The differing responses of both systems to grid voltage unbalance can be explained by their connection configurations. The synchronous generator is not directly connected to the grid. It is connected to a converter, and this in turn is directly connected to the grid. Thus any voltage

abnormalities originating in the grid, are not transferred directly to the synchronous generator stator terminals. The DFIG has a direct connection to the stator and a grid side connection to the rotor. It is the direct connection to the stator terminals, and associated low value of negative sequence impedance of the induction generator, that result in large negative sequence current and power oscillations. And therefore the synchronous generator responds better to voltage unbalance when the compensation scheme is introduced.

4.8 Sequence Components

Causes of voltage unbalance include unequal impedances of three-phase transmission and distribution system lines, large and/or unequal distribution of single-phase loads, phase to phase loads and unbalanced three-phase loads. When a balanced three-phase load is connected to an unbalanced supply system the currents drawn by the load also become unbalanced. While it is difficult or virtually impossible to provide a perfectly balanced supply system to a customer every attempt has to be taken to minimise the voltage unbalance to reduce its effects on customer loads.

Using symmetrical component theory enables the analyses of an unbalanced set of voltages and currents by means of two symmetrical three-phase systems having opposite phase sequences (positive and negative) plus a third set of three identical vectors having zero phase displacement (zero sequence) [83], [84]. The technique requires describing the system by means of its sequence networks: positive, negative and zero. Each sequence network represents the behaviour of the system to that sequence source, voltage or current. By deduction power systems can also be described by their positive-sequence impedance, negative-sequence impedance, and zero-sequence impedance. For

symmetrical faults only the positive-sequence impedance matrix is required. For non-symmetrical faults the three sequence networks may be required.

4.8.2 Negative Sequence Calculation

Three-phase systems are not always balanced, particularly in weak and remote parts of the network. During unbalanced conditions a system may have positive, negative and even zero sequence components. An example of three phase voltages under an unbalanced condition follows.

Consider the following set of phasors: V_a = 0.5 ∠0°, V_b = 1.0 ∠-120°, V_c = 1.0 ∠-240°. Figure 4.27 shows the time domain representation of this three-phase unbalanced system.

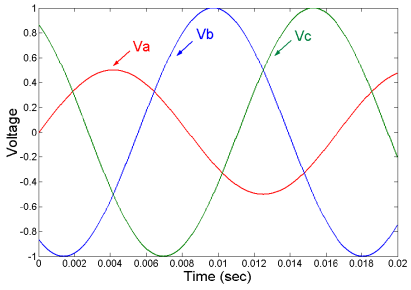

Figure 4.35 Unbalanced voltage system

The symmetrical components of this unbalanced system are obtained as:

$$V_1 = 0.833\angle 0°,\ V_2 = \text{-}0.167\angle 0°,\ V_0 = \text{-}0.167\angle 0° \qquad (4.16)$$

The symmetrical components transformation is a good tool to determine the type of distortion or asymmetry the system has. Figure 4.36 shows the trajectory followed by the rotating space vector of the unbalanced system in the d-q-o plane using Clarke's

transformation (Chapter 5 section 5.3.2.1). This trajectory is clearly distorted from the ideal one, and the space vector no longer follows a circular path.

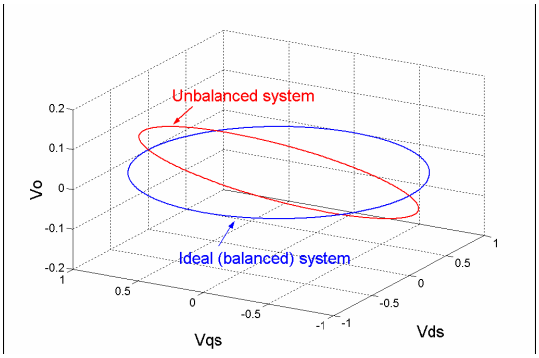

Figure 4.36 Space vector trajectory of an unbalanced system in the d-q-o plane

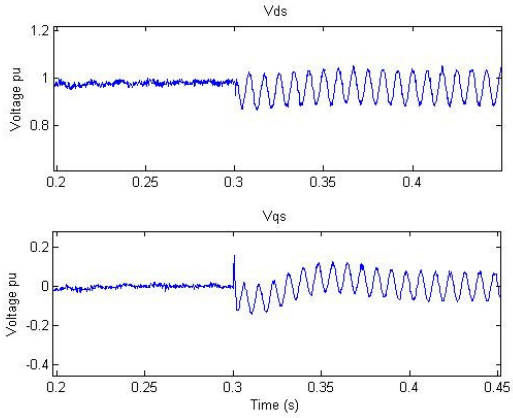

Figure 4.37 Results of a Matlab/Simulink simulation of a DFIG showing the direct and quadrature components V_{ds} and V_{qs} respectively.

A model of a DFIG was implemented and simulated in Matlab/Simulink. Results of simulations are shown in Figure 4.37 of plots of stator quadrature components V_{ds} and V_{qs} at the terminals of a DFIG. It can be observed that when voltage unbalance is introduced at the terminals of the DFIG at 0.3 seconds, double frequency voltage oscillations are introduced in both V_{ds} and V_{qs}. Similar results occur with the rotor side converter direct and quadrature currents I_{dr} and I_{qr} illustrated in Figure 4.38. Grid voltage

unbalance is introduced in the model at 0.5 seconds and double frequency oscillations occur in the rotor currents I_{dr} and I_{qr}.

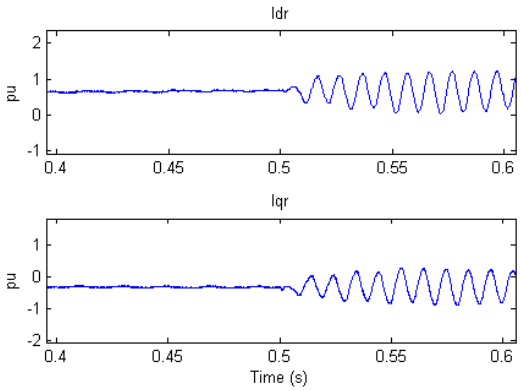

Figure 4.38 Results of a Matlab/Simulink simulation of a DFIG showing the direct and quadrature components I_{dr} and I_{qr} respectively.

In the synchronous reference frame the fundamental component (50Hz) appears as DC, and negative sequence component appears as twice the fundamental (100Hz) as illustrated in Figure 4.39. With respect to Figure 4.39 in the frequency domain, the positive sequence component (ω) in the synchronous reference frame (blue) appears as dc, a dc component appears as a fundamental component (ω) and a negative sequence component (-ω) appears as a double frequency (2ω) component.

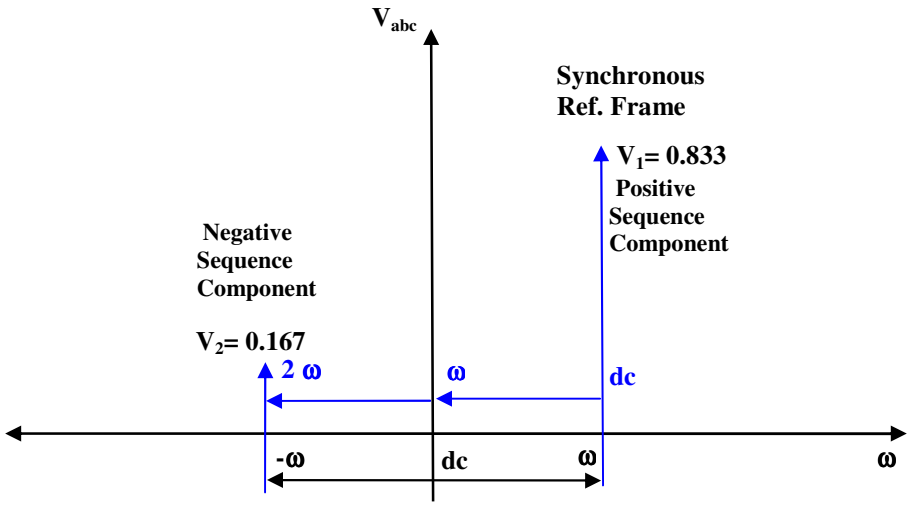

Figure 4.39 Sequence Components in the Frequency Domain

4.9 Impact of Voltage Dips

In WECS voltage dips generate most problems for converters as they occur much more frequently than interruptions. In many electrical converters, voltage dips are not acceptable and will cause under-voltage circuit breakers to trip and disconnect the drive [68]. In wind-turbines with directly connected converters or converters connected in the rotor circuits of induction generators as in the case of DFIG's, the effects that voltage dips has on the converter is similar to that of induction motor drives.

Voltage dips can be either balanced (all three phase reduce in magnitude) or unbalanced (one or two phases reduce in magnitude). Unbalanced dips can produce a negative sequence voltage. Figure 4.40 shows the effects of a voltage dip with all three phases decreased and the effects of a two-phase voltage dip resulting in negative sequence voltage generated.

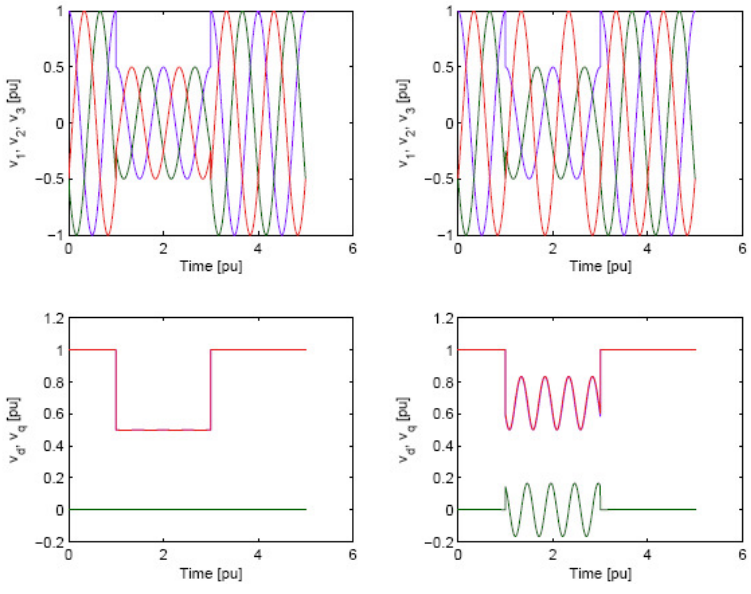

(a) (b)

Figure 4.40 Balanced (a) and unbalanced (b) voltage dips.

The upper left plot in Figure 4.40 shows a three-phase voltage dip down to 50% remaining voltage, and the lower left plot shows the corresponding *d* and *q* voltage components. The upper right plot of Figure 4.40 shows a two-phase voltage dip down to 50% remaining voltage and the lower right plot shows the corresponding *d* and *q* components. There are double frequency oscillations in the v_d and v_q components.

4.10 Conclusion

Issues associated with voltage unbalance in grid networks have been reported on. Investigative studies were undertaken on two wind farms in Ireland to ascertain the level and severity of voltage unbalance at 10kV and 38kV. Among the findings are that voltage unbalance of the utility network at the PCC is higher when wind farm generators are not connected and delivering power. The effects of grid voltage unbalance on three-phase star-delta power transformers were also investigated. Simulations were performed to verify the influence that star/delta and delta/star connected transformers have on unbalanced voltage sags and voltage unbalance.

Three-phase induction machines were analysed through simulations and testing, to illustrate the effects of asymmetric voltage applied to the stator windings of a machine. Negative effects included torque pulsations, power oscillations, heating of windings and increased losses. Three-phase rectifiers and converters were also studied to observe the effects of asymmetric voltage including double frequency voltage oscillations on the dc link bus. The effects of asymmetric voltage on DFIG's and synchronous generator converter systems were also reported on. The process of negative sequence components was outlined and negative sequence calculations illustrated.

All of the engineering plant and equipment investigated, behaved in a detrimental manner when subjected to grid voltage unbalance conditions.

Chapter 5 Induction Generator and DFIG Modelling

5.1 Induction Generator

A Double-Fed Induction Generator (DFIG) is an induction generator that can be "fed" voltage supply to both the stator and rotor, hence the term "double-fed". However it is usually the case that a description of the DFIG includes the induction generator and the back-to-back converter connected to the rotor windings. Before an analysis of the DFIG is described, it is important to first analyse the induction generator.

5.2 Steady State Analysis of Induction Generator

In this section suitable models of a standard induction machine (IM) and the double-fed induction generator (DFIG) for steady-state calculations are presented. Also the operational characteristics (speed-torque) of the induction machine and methods to alter these characteristics are outlined. Two main types of rotors are commonly featured in induction machines: the short-circuited squirrel-cage rotor and the wound rotor containing slip rings that can either be short-circuited or connected to an external electric circuit. External rotor circuits can either be connected to a passive load (resistors) or an active source (converter). In early wind turbine development the most commonly used rotor was the short-circuited squirrel-cage rotor. In applications where it is desired to influence the rotor circuit, a wound rotor machine with slip rings can be used, to enable variation of the speed-torque characteristics without changing the stator supply. For example, external rotor resistance can be added to a wound rotor machine to increase the starting torque or to control the speed of a wind turbine. The rotor current can also be controlled with a series converter.

5.2.1 Equivalent Circuit of Induction Machine

The slip of an induction machine is:

$$s = \frac{\omega_s - \omega_r}{\omega_s} \tag{5.4}$$

where ω_s is the synchronous angular velocity and ω_r is the angular velocity of the rotor.

Figure 4.17 (Chapter 4 Section 4) shows the per phase equivalent circuit with respect to the stator. The stator referred rotor current, neglecting stator resistance is:

$$\grave{i_r} = \frac{V_s}{\left(\frac{\grave{R_r}}{s}\right) + j\omega_r L_r'}. \tag{5.5}$$

Power in an induction machine can be described using the following equations.

Power across the air-gap: $P_g = \frac{3|\grave{i}_r|^2 R'_r}{s}$ (5.6)

Shaft power: $P_m = P_g(1 - s) = \frac{3|\grave{i}_r|^2 R'_r(1-s)}{s}.$ (5.7)

Developed mechanical power: $P_m = T.\omega_m$ (5.8)

where ω_m is the angular velocity.

The synchronous speed: $\omega_s = \frac{\omega_m}{(1-s)} = \frac{2\pi f}{p}$ (5.9)

where p is the number of pole pairs and f is the frequency.

The developed torque is:

$$T = \frac{P_{\mathrm{m}}}{\omega_{\mathrm{m}}} = \frac{3|\mathrm{i_r`}|^2 R_r`}{s} \cdot \frac{p}{2\pi f} \tag{5.10}$$

Equation (5.10) can also be described as:

$$T = \frac{P_{\mathrm{m}}}{\omega_{\mathrm{m}}} = \frac{P_g(1-s)}{\omega_s(1-s)} \tag{5.11}$$

Figure 5.1 is a plot of the shaft torque-speed characteristics of an induction machine. The torque and speed scales are in per unit. The rotor is short-circuited i.e. V_r is zero. It is observed in Figure 5.1 that the torque-speed characteristic is quite linear around synchronous speed (slip s = 0). Below synchronous speed (positive slip) the induction machine operates as a motor and above synchronous speed (negative slip) the induction machine operates as a generator.

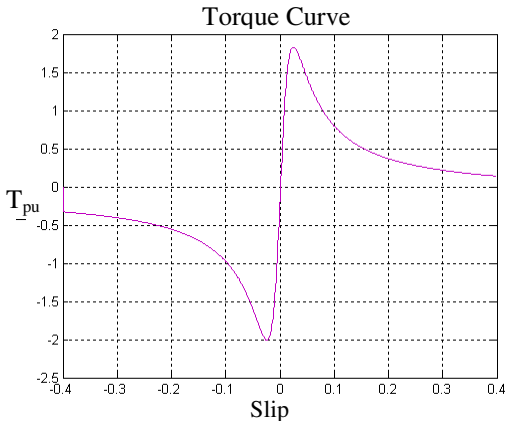

Figure 5.1 Shaft Torque of the induction machine with a short-circuited rotor, as a function rotor speed.

The speed/torque characteristic of the induction machine developed in equation 5.10 is proportional to the rotor resistance. It is possible to have external rotor resistors connected in series with the rotor windings of a wound-rotor induction machine. Adding external resistance to the rotor windings changes the slope of the speed-torque

characteristic. Figure 5.2 shows the speed-torque characteristics for five values of external rotor resistances. A disadvantage implementing this method is that it is only possible to increase the slip by inserting external rotor resistors. By increasing the value of external rotor resistance applied to an induction machine, in generation mode the rotor speed will increase for a given value of shaft torque, illustrated in Figure 5.2.

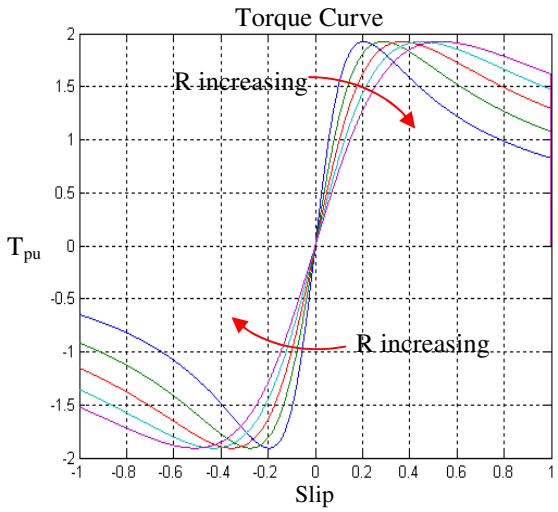

Figure 5.2 Shaft Torque of the induction machine.

In Figure 5.2 the blue plot-line is the induction machine torquer versus slip characteristic without external rotor resistance inserted; the other coloured lines are with progressively increasing levels of rotor resistance connected to the rotor windings.

To influence the rotor circuit, the induction machine must be equipped with a wound rotor equipped with slip rings. To analyse a wound rotor induction machine with slip rings, it is necessary to consider the per-phase equivalent circuit with an applied rotor phase voltage v_r. A per-phase steady-state equivalent circuit for a DFIG is shown in Figure 5.3, with quantities on the rotor side are referred to the stator side.

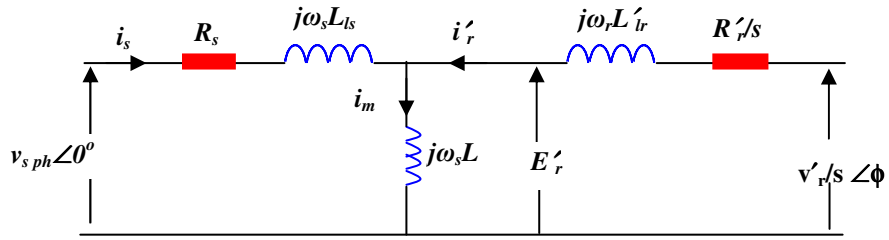

Figure 5.3 DFIG steady state equivalent circuit

In the equivalent circuit, v_s and v'_r are the applied stator phase voltage and rotor phase voltage to the induction machine respectively. Applying Kirchoff's voltage law to the equivalent circuit in Figure 5.3, equations (5.12) to (5.15) can be determined:

$$v_s = i_s R_s + i_s j\omega_s L_{ls} - E'_r \tag{5.12}$$

$$v'_r/s = i_r' R'_r/s + i'_r j\omega_r L_{lr} - E'_r \tag{5.13}$$

$$E'_r = i_m j\omega_s L_m \tag{5.14}$$

$$i_m = i_s + i_r' \tag{5.15}$$

The per-phase equivalent circuit in Figure 5.3 is based on calculations with rms values of voltages and currents and can only be applied for steady state analysis of an induction generator. For dynamic analysis a model in the form of differential functions has to be employed, which will be introduced in following sections.

The phasor diagram in Figure 5.4 of the simplified equivalent circuit Figure 5.3, shows stator current 180^o out of phase with stator voltage; the induction generator is generating current, and rotor referred current i'_r supplies i_m and i_s.

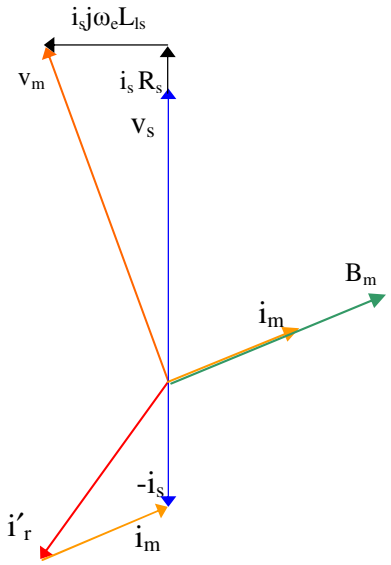

Figure 5.4 Phasor diagram of simplified equivalent circuit

The rotor referred current i_r' is composed of a real part i_{ra}' and an imaginary or reactive part i_{rr}'. The rotor referred current can be calculated with the following equation ($V_r = 0$, short circuit rotor) [65]:

$$i_r' = i_{ra}' + i_{rr}' = \frac{sE_r'}{(R_r' + sj\omega_r L_{lr}')} = \frac{sE_r'(R_r' + sj\omega_r L_{lr}')}{(R_r' + sj\omega_r L_{lr}')(R_r' + sj\omega_r L_{lr}')}$$

$$= \frac{sE_r' R_r'}{(R_r')^2 + (s\omega_r L_{lr}')^2} + \frac{sE_r' sj\omega_r L_{lr}'}{(R_r')^2 + (s\omega_r L_{lr}')^2} \qquad (5.16)$$

Thus the real part of rotor current $i`_{ra}$ is:

$$i_{ra}' = \frac{sE_r' R_r'}{(R_r')^2 + (s\omega_r L_{lr}')^2} \qquad (5.17)$$

Neglecting rotor reactance in (5.17) yields:

$$i_{ra}' \approx \frac{sE_r'}{R_r'} \qquad (5.18)$$

If an external voltage is applied to the rotor windings in a DFIG, the real current in the rotor circuit can be described as:

$$i'_{ra} = \frac{s'E'_r + V'_r}{R'_r} = \frac{sE'_r}{R'_r} \tag{5.19}$$

where $s`$ is the generator slip after the voltage v_r is applied to the rotor circuit.

The equations above indicate that it is possible to control the speed of the generator and also the stator-side power factor by modulating the magnitude and phase of the applied voltage, while keeping the electromagnetic torque constant. This is illustrated in the phasor diagram of Figure 5.5 with the stator resistance neglected [65].

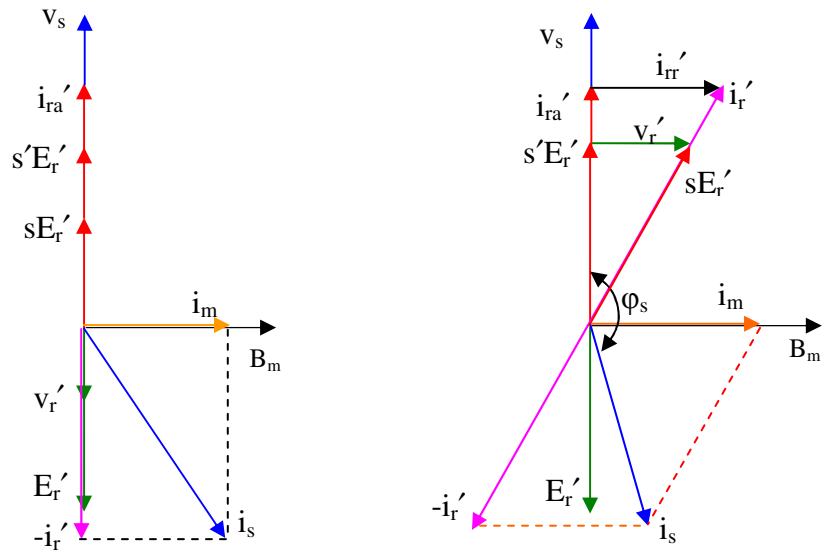

(a) v_r – Opposite to $s`E_r$** **(b) $v_r$ – Perpendicular to $s`E_r$

Figure 5.5 Phasor diagram of DFIG

In Figure 5.5 B_m is the air-gap magnetic flux intensity in Tesla, i_{rr}' is the reactive current in the rotor circuit, φ_s is the angle between v_s and i_s in degrees. If the rotor voltage ($v_r`$), is applied in the opposite direction to sE_r', (supersynchronous) the real current in the rotor circuit will decrease, leading to a reduction in electromagnetic torque. Maintaining

a constant applied load torque, a reduction in the electromagnetic torque causes the rotor to accelerate. When the generator slip reaches a new value of s' where $v_r' + s'E_r'$ is equal to sE_r', the rotor real current recovers and the torques will rebalance. If v_r' and sE_r' have the same phasor direction, the generator slip will increase (speed decreases) until the torques are balanced. The generator can also be operated at sub-synchronous speed provided that the magnitude of v_r' is sufficiently large.

The stator-side power factor can be modified by modulating the phase of v_r' with respect to the phase direction of v_s. If the applied rotor voltage v_r' is applied perpendicular to the direction of sE_r' (Figure 5.5(b)) the stator-side power factor will alter accordingly.

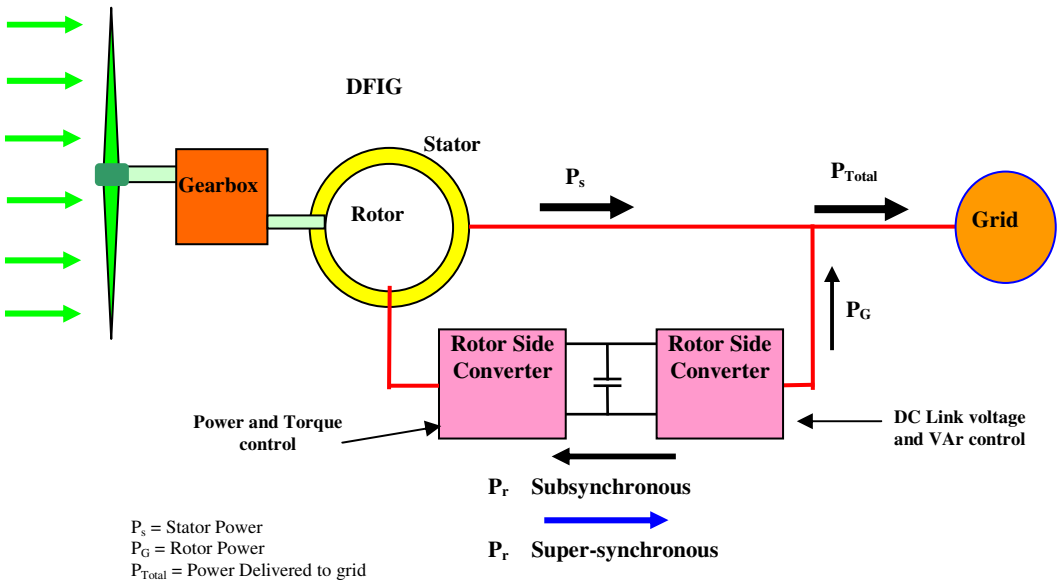

Figure 5.6 Subsynchronous and super-synchronous power flow in a DFIG.

Power flow through the rotor converter in a DFIG will flow according to operating speed. For example during subsynchronous operation power is supplied from the grid to the rotor windings through the converter, whereas during super-synchronous operation power is delivered to the grid through the converter. This feature is illustrated in Figure 5.6. Phasor diagrams corresponding to DFIG operating in sub-synchronous and super-

synchronous modes are shown in Figure 5.7, where φ_r is the angle between the rotor voltage v_r' and rotor current i_r' and φ_s is the angle between stator voltage v_s and stator current i_s. Figure 5.7 also includes the effects of the stator impedance.

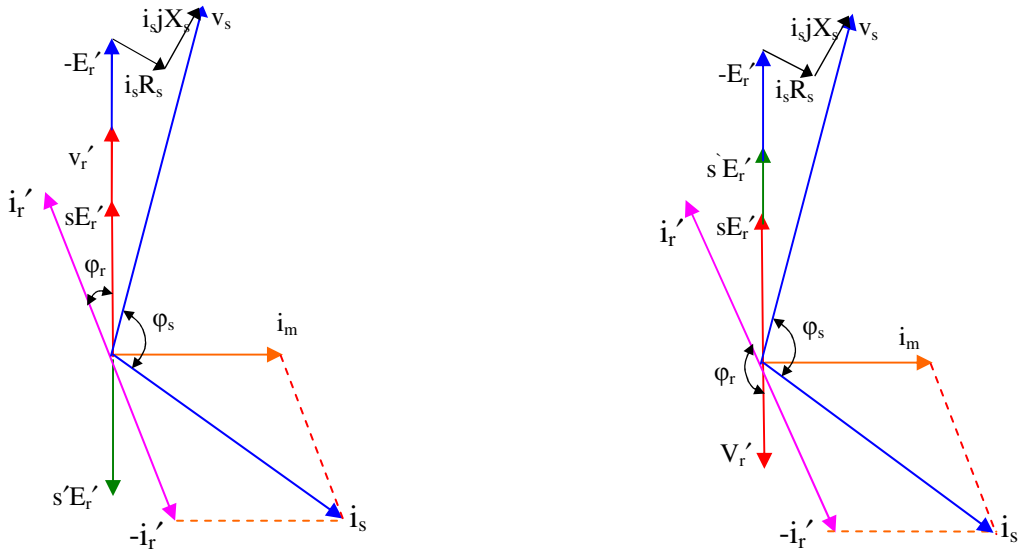

(a) Sub-synchronous mode **(b) Super-synchronous mode**

Figure 5.7 Phasor diagram of DFIG

With fixed values of stator voltage, frequency and speed (slip), the rotor current $i`_r$ (equation (5.20)) will change depending on the magnitude and phase angle of the rotor voltage ($v`_r/s$). The rotor current, based on the equivalent circuit Figure 5.3 [65] is:

$$i_r' = \frac{v_s \angle 0° - \frac{v_r'}{s}\angle\phi}{\sqrt{\left(R_s + \frac{R'_r}{s}\right)^2 + \omega_e^2 \left(L_{ls} + L_{lr}\right)^2} \angle \tan^{-1}\left(\frac{\omega_e \left(L_{ls} + L_{lr}\right)}{R_s + \frac{R'_r}{s}}\right)} \qquad (5.20)$$

Substituting equation (5.20) into the equation for torque (5.10) yields:

$$T_e = 3.(p)\frac{R_r^{`}}{s\omega_e}\frac{\left(v_s\angle 0^\circ - \frac{v_r'}{s}\angle\phi\right)^2}{\left(R_s + \frac{R'_r}{s}\right)^2 + \omega_e^2\left(L_{ls} + L_{lr}\right)^2} \quad (5.21)$$

The electromagnetic torque developed (5.21) is dependent on the rotor voltage ($v_r^{`}/s$). The rotor voltage ($v_r^{`}/s$) can be controlled to allow the generator operate at various speeds. Also by changing the phase angle of the rotor voltage the stator-side power factor can be controlled. Modulating the voltage in the rotor circuit, the DFIG can be operated in both sub-synchronous and super-synchronous modes. Power can also be obtained from equation (5.21). DFIG power is plotted against slip for varying values of the magnitude of rotor voltage $v_r^{`}$ and the resulting characteristics are plotted in Figure 5.8.

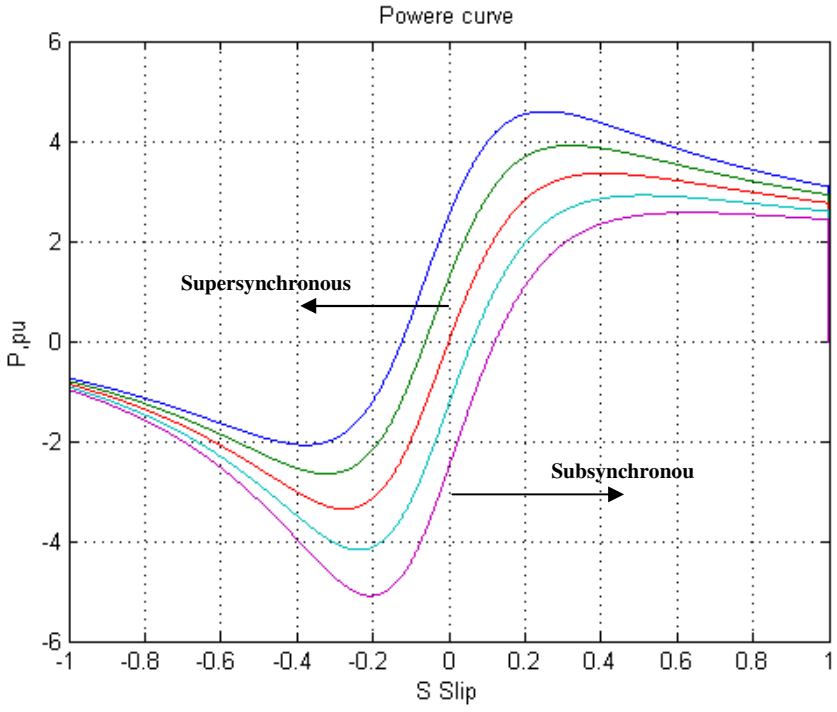

Figure 5.8 Plots of DFIG power versus slip s.

Values of magnitude rotor voltage $v_r^{`}$, Blue: $v_r^{`}$= -0.12pu; Green: $v_r^{`}$= -0.06pu, Red: $v_r^{`}$= 0 (short circuited rotor), Cyan: $v_r^{`}$= +0.06pu and Purple: $v_r^{`}$= +0.12pu

Figure 5.9 illustrates the typical bidirectional nature of the relationships of power transferred between grid-side and rotor side converters in DFIG's. Included are stator power P_s, total developed power P_T, power in the rotor side converter P_r and the power in the grid side converter P_g. In Figure 5.9 values of the DFIG real powers are in per unit and are typical for a variable speed range of ± 30% of rated speed. It is observed that power delivered by the stator is constant at 0.75 pu throughout the speed range. However power through the rotor converter alters. For example when the DFIG shaft speed is 0.7 pu (slip s = +0.3, sub-synchronous mode), power is supplied by the grid-side converter (P_g = -0.25 pu) to the DC link bus, through to the rotor converter (P_r = + 0.25 pu) and injected into the rotor windings of the generator. The grid-side converter receives power from the grid (-0.25 pu), therefore total power supplied to the grid is 0.5 pu (0.75 pu(stator) – 0.25 pu (converter)). Similarly if the DFIG is operating in super-synchronous mode the grid-side converter delivers power to the grid and total power supplied to the grid is 1.0 pu (0.75 pu (stator) + 0.25 pu (converter)).

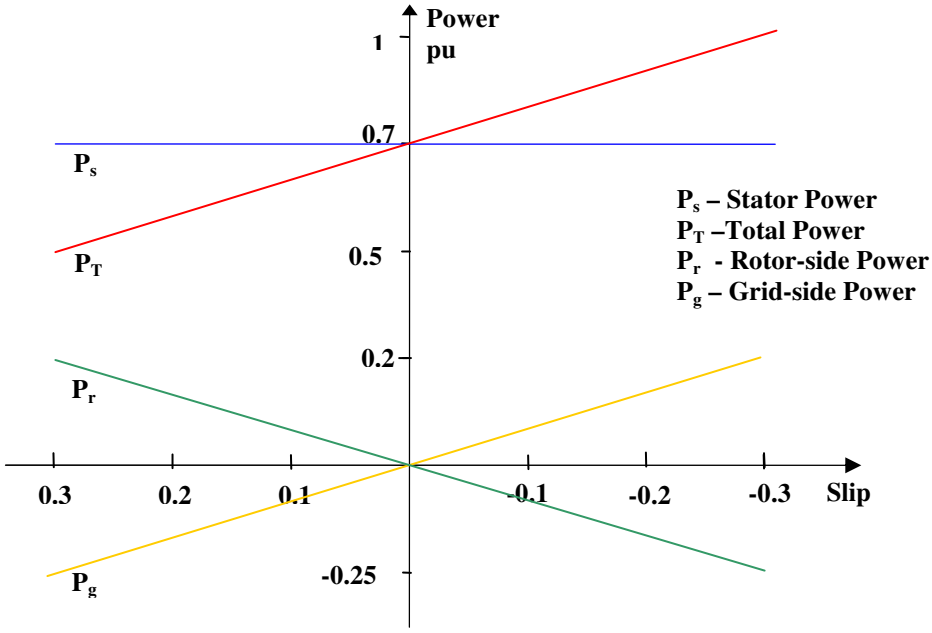

Figure 5.9 Power flow versus slip in a DFIG

A DFIG connected to a grid with a constant level of voltage unbalance, and delivering constant stator power, stator power and current oscillations will be constant throughout the speed range of the DFIG. However the power in the grid side converter varies from negative power (power supplied by the grid) to positive power delivered to the grid. Grid voltage unbalance may influence the operation of the grid-side converter depending on the speed of the DFIG.

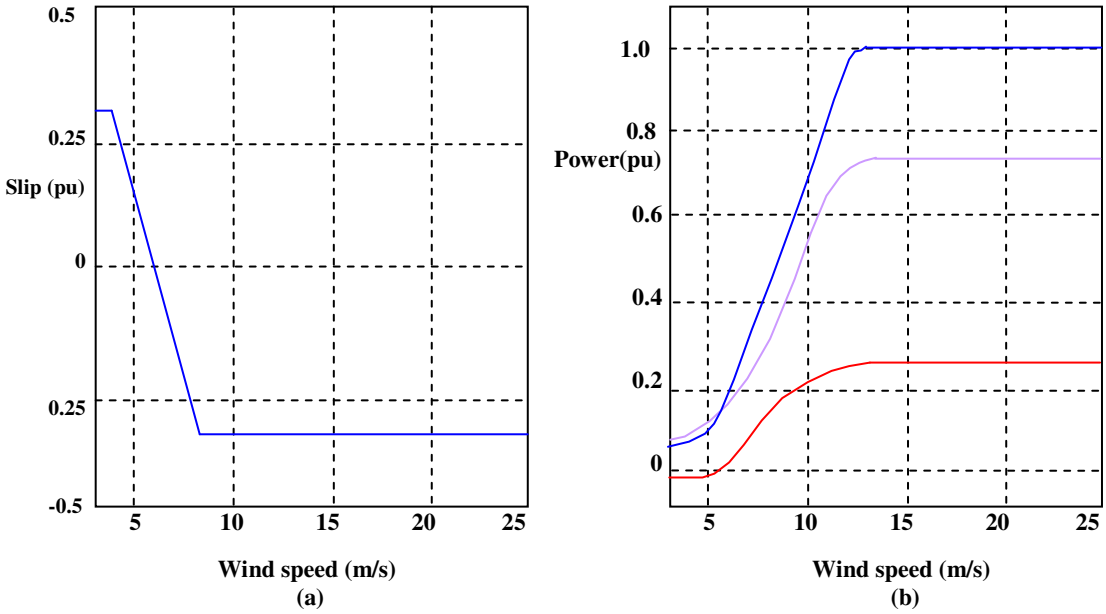

Figure 5.10 Typical characteristic for a DFIG. (a) Slip as a function of wind speed. (b) Mechanical power (Blue), rotor power (Red) and stator power (purple) as a function of wind speed.

Figure 5.10 (a) shows typical wind speed versus slip and Figure 5.10 (b) the mechanical and electrical powers versus wind speed. Observing the DFIG characteristics shown in Figure 5.10, stator power delivers only 0.75 times the rated power of a DFIG the remainder being obtained from the rotor windings through the grid side converter. Maximum rated power of a DFIG is composed of 0.75 pu from the stator and 0.25 pu from the rotor converter.

5.3 Dynamic Modelling of the Induction Machine

Dynamic models of induction machines can be described in space vector notation and are based on the fifth-order two-axis representation commonly known as the “Park model" [65], [67]. Voltage equations for a three-phase induction machine can be developed by considering an idealised induction machine [69]. Figure 5.11 shows the displaced stator and rotor windings of a three-phase induction machine. The rotor angle θ_r is the displacement between the stator and rotor windings. The windings for each phase should ideally produce a sinusoidally distributed radial field (F, B and H)[8] in the air-gap [67].

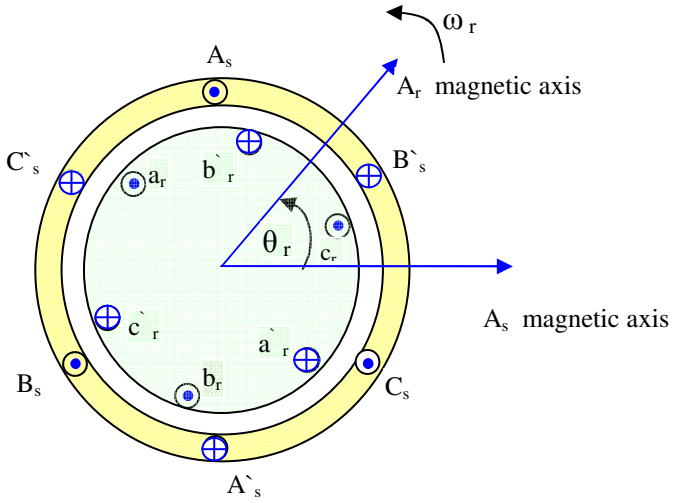

Figure 5.11 Three-phase induction machine windings

Stator voltage equations can be expressed as [69]:

$$v_s^{abc} = i_s^{abc} R_r + \frac{d\psi_s^{abc}}{dt} \qquad (5.22)$$

[8] F - magnetising force, B - flux density and H- field intensity-

And the rotor voltage equation is:

$$v_r^{abc} = i_r^{abc} R_r + \frac{d\psi_r^{abc}}{dt} \tag{5.23}$$

For control purposes it is desirable to transform the model of the induction machine to synchronous coordinates (Section 5.3.2.2). Transformation to synchronous reference coordinates implies that the variables will be dc quantities in the steady state. Transformation to synchronous coordinates implies substituting $d \rightarrow dt + j\omega_e$ where ω_e is the stator frequency (synchronous speed). The stator and rotor voltage equations become:

$$v_s^{abc} = i_s^{abc} R_r + \frac{d\psi_s^{abc}}{dt} + j\omega_e \psi_s^{abc} \tag{5.24}$$

$$v_r^{abc} = i_r^{abc} R_r + \frac{d\psi_r^{abc}}{dt} + j\omega_e \psi_r^{abc} \tag{5.25}$$

The flux linkages are:

$$\begin{bmatrix} \psi_s^{abc} \\ \psi_r^{abc} \end{bmatrix} = \begin{bmatrix} L_{ss}^{abc} & L_{sr}^{abc} \\ L_{rs}^{abc} & L_{rr}^{abc} \end{bmatrix} \begin{bmatrix} i_s^{abc} \\ i_r^{abc} \end{bmatrix} \tag{5.26}$$

Where:

$$\psi_s^{abc} = \begin{bmatrix} \psi_{as} \\ \psi_{bs} \\ \psi_{cs} \end{bmatrix}, \quad \psi_r^{abc} = \begin{bmatrix} \psi_{ar} \\ \psi_{br} \\ \psi_{cr} \end{bmatrix} \tag{5.27}$$

$$i_s^{abc} = \begin{bmatrix} i_{as} \\ i_{bs} \\ i_{cs} \end{bmatrix}, \qquad i_r^{abc} = \begin{bmatrix} i_{ar} \\ i_{br} \\ i_{cr} \end{bmatrix} \tag{5.28}$$

The stator-to-stator winding inductances are:

$$L_{ss}^{abc} = \begin{bmatrix} L_{ls} + L_{ss} & L_{sm} & L_{sm} \\ L_{sm} & L_{ls} + L_{ss} & L_{sm} \\ L_{sm} & L_{sm} & L_{ls} + L_{ss} \end{bmatrix} \tag{5.29}$$

And the rotor-to-rotor winding inductances are:

$$L_{rr}^{abc} = \begin{bmatrix} L_{lr} + L_{rr} & L_{rm} & L_{rm} \\ L_{rm} & L_{lr} + L_{rr} & L_{rm} \\ L_{rm} & L_{rm} & L_{lr} + L_{rr} \end{bmatrix} \tag{5.30}$$

The stator-to-rotor mutual inductances are dependent on the rotor angle:

$$L_{sr}^{abc} = \left[L_{rs}^{abc}\right]^T = L_{sr} \begin{bmatrix} \cos\theta_r & \cos\left(\theta_r + 2\pi/3\right) & \cos\left(\theta_r - 2\pi/3\right) \\ \cos\left(\theta_r - 2\pi/3\right) & \cos\theta_r & \cos\left(\theta_r + 2\pi/3\right) \\ \cos\left(\theta_r + 2\pi/3\right) & \cos\left(\theta_r - 2\pi/3\right) & \cos\theta_r \end{bmatrix} \tag{5.31}$$

where:

L_{ls}	=	Stator winding per phase leakage inductance
L_{ss}	=	Self inductance of stator winding
L_{lr}	=	Rotor winding per phase leakage inductance
L_{rr}	=	Self inductance of rotor winding
L_{sr}	=	Stator to rotor mutual inductance
L_{rs}	=	Rotor to stator mutual inductance
L_{sm}	=	Stator mutual inductance

The ideal machine can be described by six first-order differential equations, one for each winding. These differential equations are coupled to each other by the mutual inductances between the windings. The stator-to-rotor coupling terms are a function of

the rotor position, therefore when the rotor rotates the coupling terms change with time. This problem is solved when the induction machine equations are transferred to quadrature *dq* rotating reference frame and values appear as dc.

5.3.1 Space-Vector Notation

Vector control or field-oriented control can be used in converters associated with induction machines. The main idea behind vector control is to transform the model of the induction machine so that it is mathematically equivalent to a separately excited shunt dc machine.

Induction machine windings displaced by ±120° can be described as complex vectors [67]. For convenience, the real part of the complex space vector is aligned to phase *a* of the three-phase stator system or three-phase rotor system. The complex vector "*a*" can be expressed as:

$$a = 1\angle 120^o = -\frac{1}{2} + j.\frac{\sqrt{3}}{2} = e^{j\frac{2}{3}\pi} \tag{5.32}$$

Three current vectors can be described as:

$$\boldsymbol{i}_a = i_a, \quad \boldsymbol{i}_b = i_b.a, \quad \boldsymbol{i}_c = i_c.a^2 \tag{5.33}$$

where i_a, i_b and i_c are the absolute values of the current time vector. A resulting current vector can be achieved through an addition of the three phase current vectors as:

$$\underline{\boldsymbol{i}}_s = 2/3(i_a + i_b.a + i_c.a^2) \tag{5.34}$$

Similarly space vectors can also be used for voltages and fluxes. For example stator voltage, current and flux vectors can be described as:

$$\left.\begin{aligned} \underline{v}_s &= 2/3\,(v_{as} + v_{bs}\,a + v_{cs}\,a^2) \\ \underline{i}_s &= 2/3\,(i_{as} + i_{bs}\,a + i_{cs}\,a^2) \\ \underline{\psi}_s &= 2/3\,(\psi_{as} + \psi_{bs}\,a + \psi_{cs}\,a^2) \end{aligned}\right\} \qquad (5.35)$$

Using the above introduced complex space vector, the general machine equations can be expressed more conveniently compared to the vector presentation per phase [67].

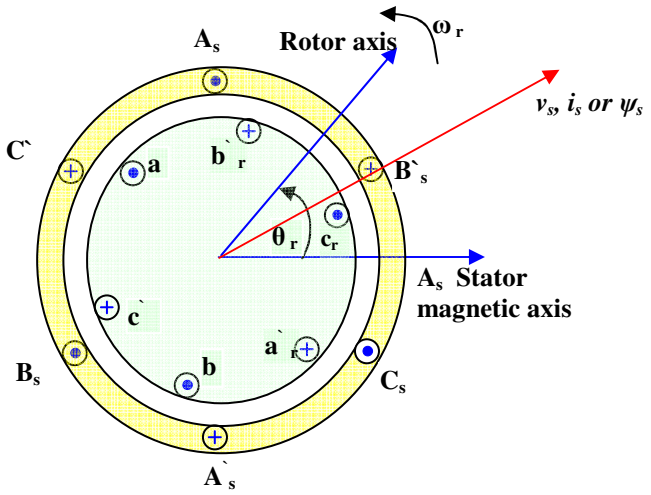

Figure 5.12 Three-phase induction machine windings showing space vectors v_s, i_s and ψ_s.

The dynamic equivalent circuit of a DFIG can be described as shown in Figure 5.13.

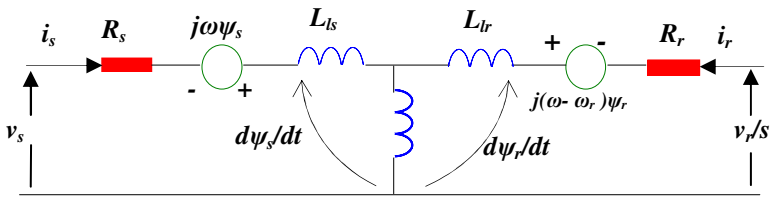

Figure 5.13 Equivalent circuit of a DFIG in an arbitrary reference frame

The stator space vector equations of the three-phase induction machine can be obtained by combining the individual phase equations [67]:

$$\left.\begin{aligned} (v_{as} &= i_{as} R_s + d\psi_{as}/dt) \,.\, e^{j0} \\ (v_{bs} &= i_{bs} R_s + d\psi_{bs}/dt) \,.\, e^{j2\pi/3} \\ (v_{cs} &= i_{cs} R_s + d\psi_{cs}/dt) \,.\, e^{j4\pi/3} \end{aligned}\right\} \qquad (5.36)$$

If the three voltages in equation (5.36) are summed and the definition of space vectors is applied, the stator and rotor equations in the stator reference frame (5.24) and (5.25) can be written as:

$$v_s^s = i_s^s R_s + \frac{d\psi_s^s}{dt} + j\omega_e \psi_s^s \qquad (5.37)$$

$$v_r^s = i_r^s R_r + \frac{d\psi_r^s}{dt} + j\omega_e \psi_r^s \qquad (5.38)$$

where v_s^s is the stator voltage space vector, v_r^r is the rotor voltage space vector, ψ_s^s is the stator flux space vector and ψ_r^r is the rotor flux space vector.

The complex space vector representation for the stator and rotor voltage equations (5.37) and (5.38) respectively can be expressed through stator flux ψ_s and rotor flux ψ_r [89].

The flux in the stator of the machine can be expressed with flux created by the stator phases itself and the flux part influencing the stator originating from the rotor phases. Similarly the rotor flux can be separated into the flux belonging to the rotor and a part penetrating the rotor windings originating from the stator phases. The fluxes can be defined with the following equations:

$$\psi_s^s = \psi_{s(s)} + \psi_{s(r)} \tag{5.39}$$

$$\psi_r^r = \psi_{r(r)} + \psi_{r(s)} \tag{5.40}$$

where the subscript (*s*) refers to the flux due the stator windings and subscript (*r*) the flux due to the rotor windings.

The flux components can also be described as [78]:

$$\psi_s^s = i_s^s L_s + i_r^r L_m e^{j\theta_r} = i_s^s (L_{ls} + L_m) + i_r^r L_m e^{j\theta_r} \tag{5.41}$$

$$\psi_r^r = i_r^r L_r + i_s^s L_m e^{-j\theta_r} = i_r^r (L_{lr} + L_m) + i_s^s L_m e^{-j\theta_r} \tag{5.42}$$

$$\psi_m^s = i_s^s L_m + i_r^r L_m e^{j\theta_r} \tag{5.43}$$

where L_s is the stator inductance, L_r is the rotor inductance, L_{ls} is the stator leakage inductance, L_{lr} is the rotor leakage inductance and L_m is the magnetising inductance.

The fluxes in stator coordinates are:

$$\psi_s^s = i_s^s L_s + i_r^s L_m \tag{5.44}$$

$$\psi_r^s = i_r^s L_r + i_s^s L_m \tag{5.45}$$

$$\psi_m^s = i_s^s L_m + i_r^s L_m \tag{5.46}$$

5.3.2 Three-Phase to Two Phase Representation

5.3.2.1 Clarke Transformation

Space vectors can describe the induction machine with two phases instead of three. The main advantage of this transformation is in the ease in which control schemes can be implemented. In an induction machine the three-phase stator currents generate a rotating flux in the air gap. The same rotating flux could also be formed with only two phases, as shown in Figure 5.14. This is the principle of space vectors. The figure shows a voltage transformation from three-phase time varying voltages, v_a, v_b and v_c all 120° or 2π/3 radians apart, to two-phase voltages v_α and v_β along the α and β axis. If the α axis is aligned with the a axis, this is normally referred to as the stationary frame. The β axis is rotated by -90° as shown by v_β in Figure 5.14.

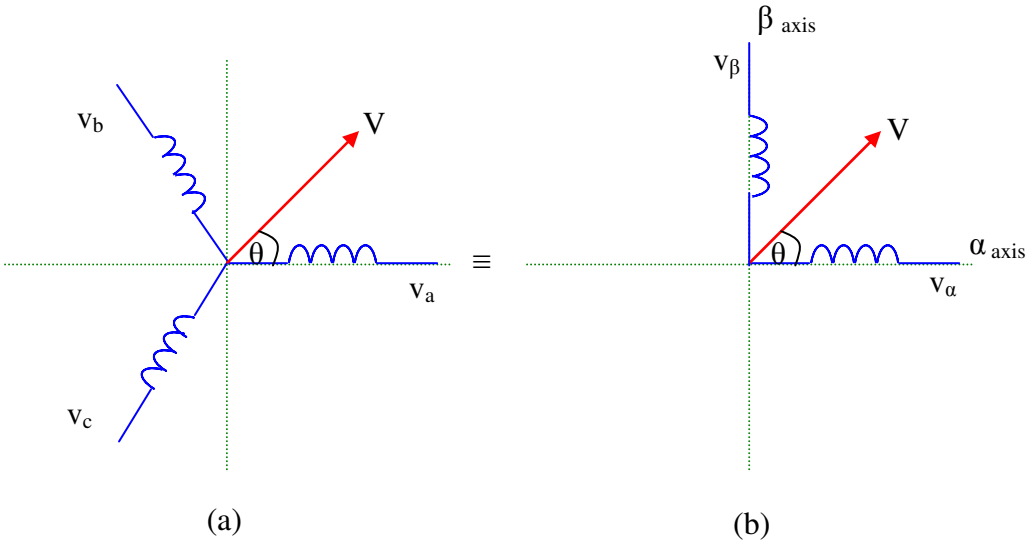

Figure 5.14 Equivalent two phase machine from three-phase machine using Clark Transformation

To determine the space vector v_s, of a three-phase voltage quantity v_a, v_b and v_c, with a balanced system ($v_a + v_b + v_c = 0$) the following transformation can be applied [65]:

$$\begin{bmatrix} v_a \\ v_b \\ v_c \end{bmatrix} = \begin{bmatrix} 1 & 0 & 1 \\ -\frac{1}{2} & \frac{\sqrt{3}}{2} & 1 \\ -\frac{1}{2} & -\frac{\sqrt{3}}{2} & 1 \end{bmatrix} \begin{bmatrix} v_\alpha^s \\ v_\beta^s \\ v_0^s \end{bmatrix} \tag{5.47}$$

where superscript (^{s}) indicates the stationary frame.

The inverse transformation is:

$$\begin{bmatrix} v_\alpha^s \\ v_\beta^s \\ v_0^s \end{bmatrix} = \frac{2}{3} \begin{bmatrix} 1 & -\frac{1}{2} & -\frac{1}{2} \\ 0 & -\frac{\sqrt{3}}{2} & \frac{\sqrt{3}}{2} \\ \frac{1}{2} & \frac{1}{2} & \frac{1}{2} \end{bmatrix} \begin{bmatrix} v_a \\ v_b \\ v_c \end{bmatrix} \tag{5.48}$$

In star connected three-phase induction machines the star point is normally not connected and therefore the zero sequence v_0 is equal to zero. For induction machines the three-phase to two-phase transformation can be used for voltage, currents and associated fluxes in both the stator and rotor. The two-phase transformation analysis described by α and β (and also *d, q*) in induction machines makes it less onerous to use vector control methods. The method of transformation from three-phases to two phases is usually referred to as the Clark Transformation [67].

5.3.2.2 The Park Transformation

Similar to the α, β components described in the section 5.3.2.1, the *d-q* components are a separation of the complex space vector in real and imaginary part.

$$i_{dq} = i_d + j.i_q = \tfrac{2}{3} (i_a + a.i_b + a^2.i_c)\, e^{-j\theta} \tag{5.49}$$

The Clarke transformation referred space vector to a stationary frame, however in the Park transformation the complex space vector can be expressed in any rotating reference

frame. For example it could be expressed in a rotating orthogonal system linked with the rotor of the machine i.e. the rotor reference frame. The advantage by doing so is that rotating space vectors appear stationary in a rotating reference frame, which means alternating traces of the space vector are steady state and the changes in absolute value of the vector is depicted clearly. This is advantageous in the control schemes of electrical machines.

Reference frame theory is an importance part of electric drives associated with induction machines. By using reference frame theory it is possible to transform machine variables (voltages, currents and fluxes) to another reference frame to reduce and improve the implementation of control structures [67], [69]. There are normally three reference frames that are associated with induction machine control; stationary reference frame (usually referred to applied voltage of the machine) and denoted by superscript (^{s}), synchronous reference frame (usually aligned with an internal flux, stator, air-gap or rotor flux) and denoted by superscript (^{e}), and a rotor reference frame (aligned with the rotating shaft) and denoted by superscript (^{r}). The three reference frames are illustrated in Figure 5.15.

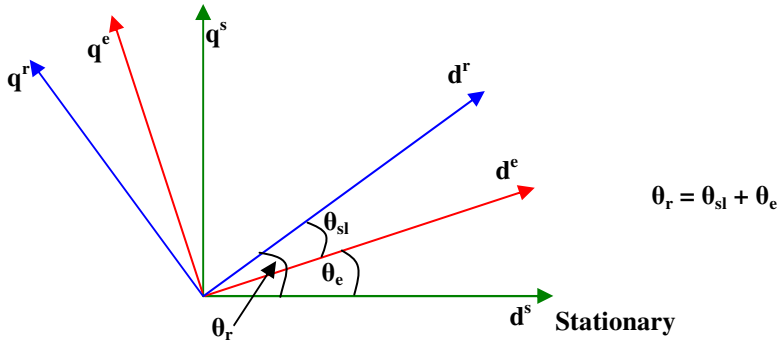

Figure 5.15 Reference frames where the superscript (^{s}) indicates the stationary frame, superscript (^{e}) indicates the synchronous frame and superscript (^{r}) is the rotor frame. The position of the rotor reference indicates it is in the supersynchronous region.

For example the current i_{dq} can be represented in the stationary frame or the synchronous frame. This is illustrated in Figure 5.16.

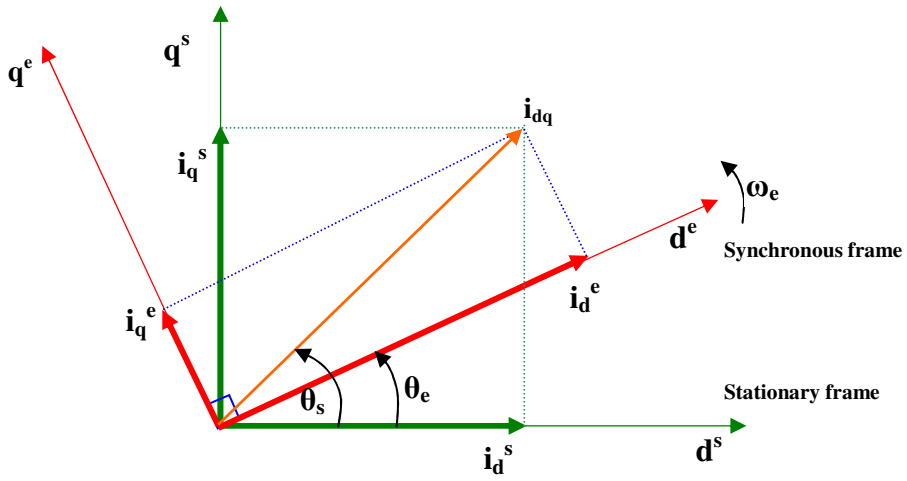

Figure 5.16 Stationary and synchronous frames.

Observing Figure 5.16 if the dq coordinates in both the stationary frame and synchronous frame produce the same current i_{dq} at any instant then it follows that:

$$\begin{bmatrix} i_q^e \\ i_d^e \end{bmatrix} = \begin{bmatrix} \cos\theta_e & -\sin\theta_e \\ \sin\theta_e & \cos\theta_e \end{bmatrix} \begin{bmatrix} i_q^s \\ i_d^s \end{bmatrix} \tag{5.50}$$

$$\begin{bmatrix} i_q^s \\ i_d^s \end{bmatrix} = \begin{bmatrix} \cos\theta_e & \sin\theta_e \\ -\sin\theta_e & \cos\theta_e \end{bmatrix} \begin{bmatrix} i_q^e \\ i_d^e \end{bmatrix} \tag{5.51}$$

In induction machines the current i_{dq} can be transferred from the stationary frame (^{s}) to the synchronous frame (^{e}) by the transformation or vector rotation (5.50) [65]. This transformation ensures that sinusoidal time variations along the stationary frame d^s, q^s will appear as constant values onto the synchronous rotating reference frame d^e, q^e. The inverse Park transformation (5.51) transforms the synchronous frame back to stationary frame. This Park transformation will be used in vector control techniques, discussed in Chapter 6.

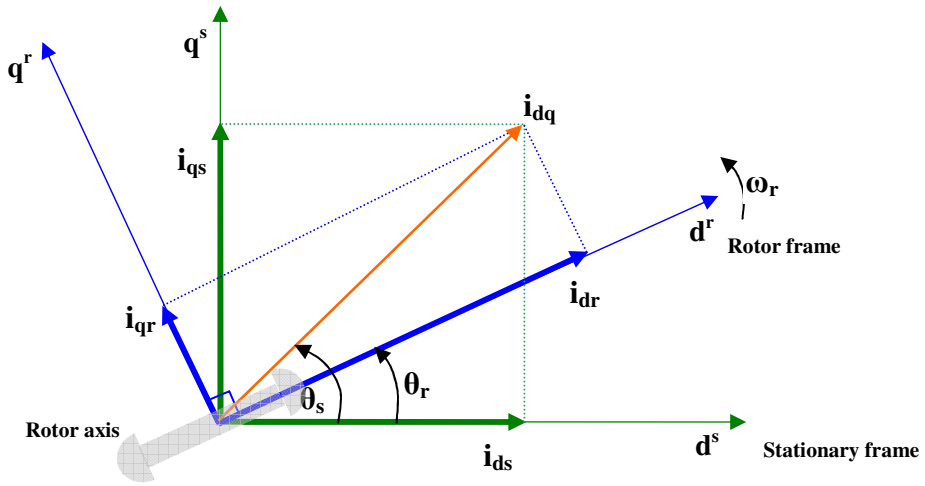

Figure 5.17 Stationary and rotor reference frames.

The current i_{dq} can be transformed from the stationary frame to the rotor frame (Figure 5.17) and from the rotor frame to the stationary frame with the following transformations:

$$\begin{bmatrix} i_{qs}^{r} \\ i_{ds}^{r} \end{bmatrix} = \begin{bmatrix} \cos\theta_r & -\sin\theta_r \\ \sin\theta_r & \cos\theta_r \end{bmatrix} \begin{bmatrix} i_{qs}^{s} \\ i_{ds}^{s} \end{bmatrix} \tag{5.52}$$

$$\begin{bmatrix} i_{qs}^{s} \\ i_{ds}^{s} \end{bmatrix} = \begin{bmatrix} \cos\theta_r & \sin\theta_r \\ -\sin\theta_r & \cos\theta_r \end{bmatrix} \begin{bmatrix} i_{qs}^{r} \\ i_{ds}^{r} \end{bmatrix} \tag{5.53}$$

For a three-phase induction machine with an isolated neutral where all three phase currents add to zero at any time instant, the variables in the *a-b-c* windings can be calculated in terms of the *dq* winding variables [67]. Figure 5.18 illustrates graphically the transformation of equation (5.52).

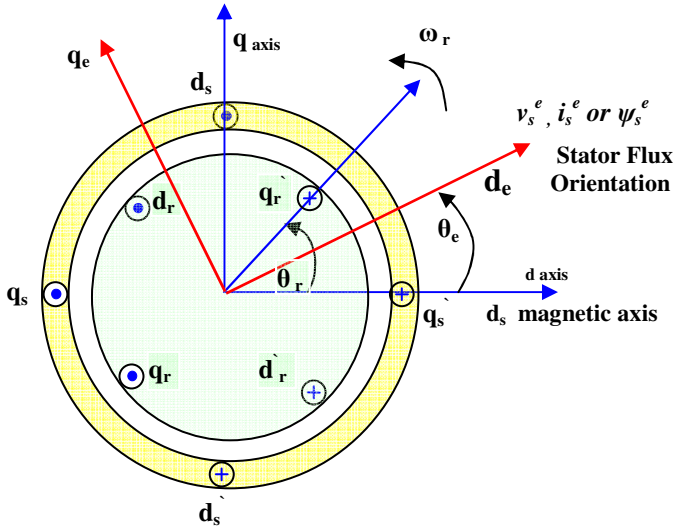

Figure 5.18 Three-phase induction machine windings, showing space vectors v_s^e, i_s^e and ψ_s^e aligned with the synchronous frame.

5.3.3 Induction Machine Dynamic Equations

The stator winding flux linkages are:

$$\psi_{ds} = L_s i_{ds} + i_{ds} L_m \tag{5.54}$$

$$\psi_{qs} = L_s i_{qs} + i_{qs} L_m \tag{5.55}$$

where $L_s = L_{ls} + L_m$

$$\psi_{dr} = L_r i_{dr} + i_{dr} L_m \tag{5.56}$$

$$\psi_{qr} = L_r i_{qr} + i_{qr} L_m \tag{5.57}$$

where $L_r = L_{lr} + L_m$

Stator voltage in the *dq* stationary reference frame can be described as:

$$v^s_{dqs} = i^s_{dqs} R_s + \frac{d\psi^s_{dqs}}{dt} \quad (5.58)$$

To transform to the synchronous frame, it is necessary to incorporate the angle between the stationary frame and the synchronous reference frame, θ_e. Implementing equation (5.50), $v^e_{dqs} = v^s_{dqs}.e^{j\theta_e}$:

$$v^s_{dqs} = v^e_{dqs}.e^{j\theta_e} = i^s_{dqs} R_s.e^{j\theta_e} + \frac{d(\psi^s_{dqs}.e^{j\theta_e})}{dt}$$

$$v^e_{dqs}.e^{j\theta_e} = i^s_{dqs} R_s.e^{j\theta_e} + \frac{d\psi^s_{dqs}}{dt}.e^{j\theta_e} + j\frac{d\theta_e}{dt}\psi^s_{dqs}.e^{j\theta_e}$$

$$v^e_{dqs} = i^s_{dqs} R_s + \frac{d\psi^s_{dqs}}{dt} + j\omega_e \psi^s_{dqs} \quad (5.59)$$

In *dq* windings, equation (5.59) where $v_{dqs} = v_{ds} + jv_{qs}$ can be written for v_d and v_q as real and imaginary

components as [65], [67], [72], [78], [89]:

$$v^e_{ds} = i^e_{ds} R_s - \omega_e \psi^e_{qs} + \frac{d\psi^e_{ds}}{dt} \quad (5.60)$$

$$v^e_{qs} = i^e_{qs} R_s + \omega_e \psi^e_{ds} + \frac{d\psi^e_{qs}}{dt} \quad (5.61)$$

or in matrix form:

$$\begin{bmatrix} v^e_{ds} \\ v^e_{qs} \end{bmatrix} = R_s \begin{bmatrix} i^e_{ds} \\ i^e_{qs} \end{bmatrix} + \frac{d}{dt}\begin{bmatrix} \psi^e_{ds} \\ \psi^e_{qs} \end{bmatrix} + \omega_e \begin{bmatrix} 0 & -1 \\ 1 & 0 \end{bmatrix}\begin{bmatrix} \psi^e_{ds} \\ \psi^e_{qs} \end{bmatrix} \quad (5.62)$$

Similarly the rotor winding voltages are:

$$\text{ed}\, v_{dr} \quad = \quad i_{dr} R_r + \frac{d\psi_{dr}}{dt} - \omega_{sl}\, \psi_{qr} \tag{5.63}$$

$$v_{qr} \quad = \quad i_{qr} R_r + \frac{d\psi_{qr}}{dt} + \omega_{sl}\, \psi_{dr} \tag{5.64}$$

or in matrix form:

$$\begin{bmatrix} v_{dr} \\ v_{qr} \end{bmatrix} = R_r \begin{bmatrix} i_{dr} \\ i_{qr} \end{bmatrix} + \frac{d}{dt} \begin{bmatrix} \psi_{dr} \\ \psi_{qr} \end{bmatrix} + \omega_{sl} \begin{bmatrix} 0 & -1 \\ 1 & 0 \end{bmatrix} \begin{bmatrix} \psi_{dr} \\ \psi_{qr} \end{bmatrix} \tag{5.65}$$

5.3.3.1 dq axis equivalent circuits

From equations (5.60) - (5.64) the *dq* equivalent circuit in the synchronous reference frame can be described as shown in Figure 5.19.

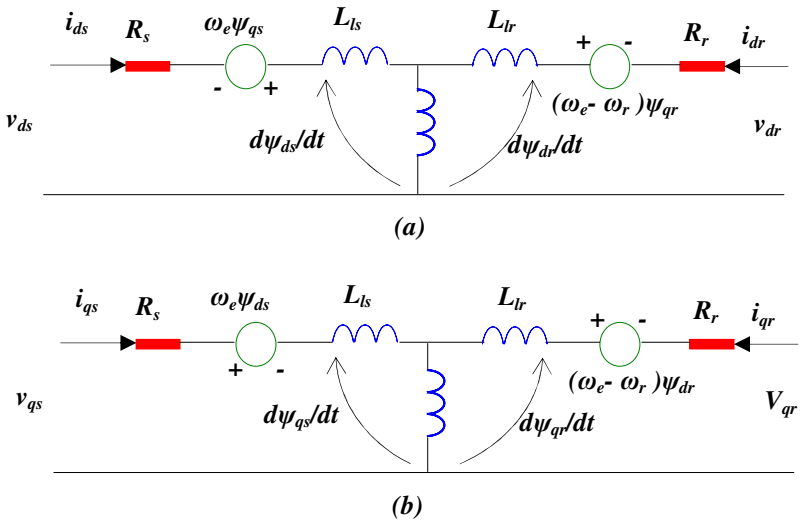

Figure 5.19 dq equivalent circuit in the synchronous reference frame.

Figure 5.20 illustrates reference frames with stator flux orientation and stator voltage orientation. If the *d*-axis is fixed to the stator flux ($\psi_s = \psi_{ds}$) illustrated in Figure 5.20 (a) referred to as Stator Flux Oriented (SFO) control, whereas if the *d*-axis is fixed to the edrtstator voltage ($V_s = V_{ds}$) shown in Figure 5.20 (b), this is referred to as Stator Voltage Oriented (SVO) control.

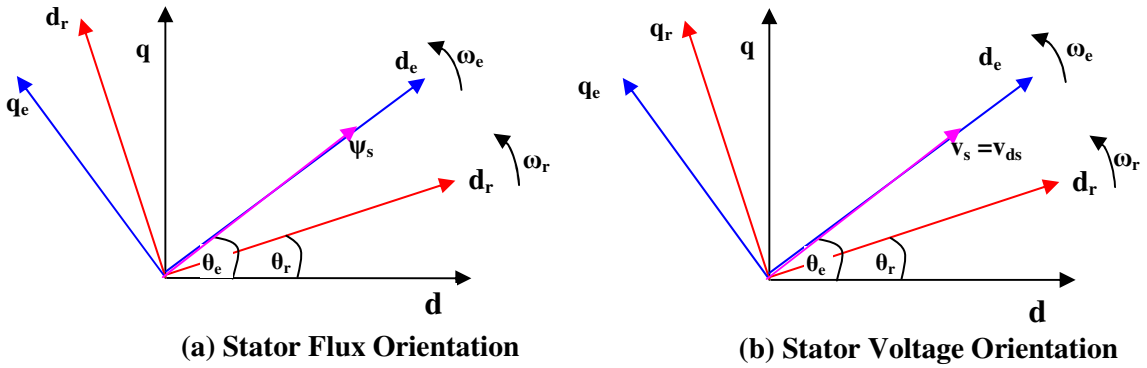

Figure 5.20 Stator vector orientation

Control techniques implemented on DFIG's can include vector control based schemes based on (SFO) [71], [74], [75], [89], [95], or (SVO) [74], [91], [97], [98], [99]. Transformation of the machine stator voltage equations, neglecting the zero component, from the stationary stator reference frame into the rotating stator flux coordinate system requires the equation to be rotated with the stator flux angle θ_e, whereas the transformation of the rotor voltage equations, from the rotating rotor reference frame on to the rotating stator flux coordinate system requires the equations to be rotated with the slip angle θ_{sl} (see Figure 5.15).

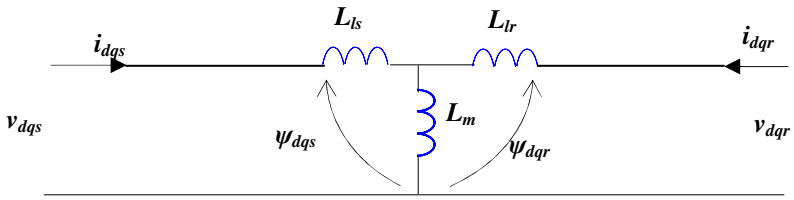

Figure 5.21 Equivalent Circuit in the Stationary Reference Frame.

The control of active and reactive powers in a DFIG can be described by the phasor *d-q* diagram of Figure 5.22 based on the equivalent circuit in Figure 5.21 in the stationary reference frame (ω_e=0), with stator and rotor resistances neglected [106]. The stator flux is aligned with the d_{axis} (SFO) and the stator current component i_{qs} controls the active power P_s and i_{ds} controls the stator reactive power Q_s [106]. This is achieved by controlling the rotor currents i_{qr} and i_{dr} in field oriented control described in Chapter 6.

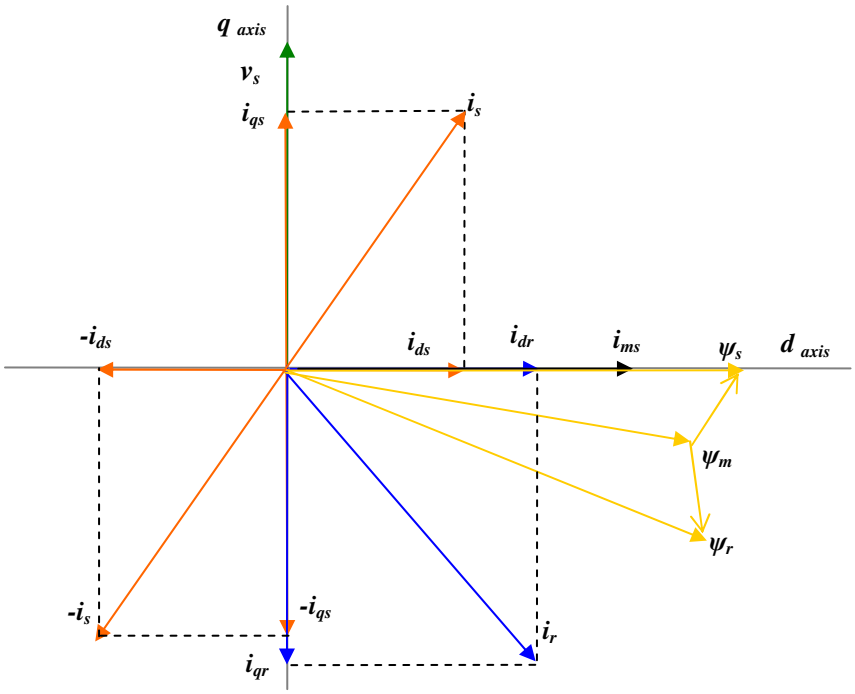

Figure 5.22 D-Q Phasor diagram of induction machine with Stator Flux Orientation (SFO)

The effects of injecting the rotor currents i_{qr} and i_{dr} on the air-gap flux ψ_s and rotor flux ψ_r can be obtained by subtracting and adding the respective leakage fluxes.

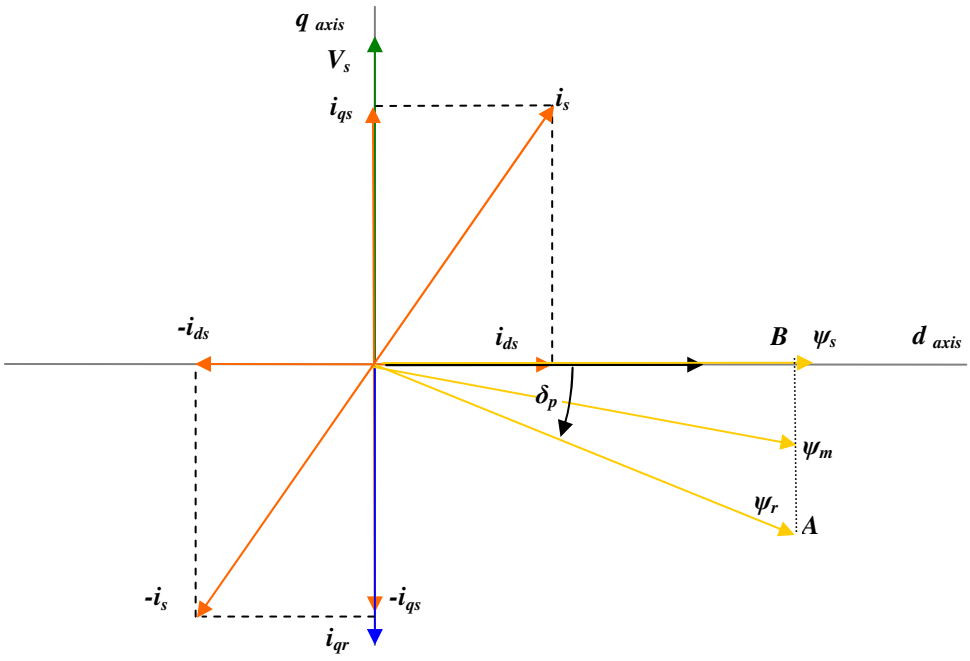

Figure 5.23 Phasor Diagram Active Power Control.

. The variation in the rotor flux with variations in the active and reactive power demand is shown in Figures (5.22) and (5.23).

In Figure 5.23, i_{dr} is equal to zero, i.e. the reactive power is fed from the stator side. (The phasor diagrams illustrated in Figures (5.22) to (5.24) will remain similar with any reference frame used). In this condition if i_{qr} is varied from zero to full load, the locus of ψ_r varies along A-B in Figure 5.23 with a change in the angle δ_p between ψ_s and ψ_r. It can be noticed that the magnitude of ψ_r changes little. Therefore a change in the angle δ_p results in a change in the active power through the stator.

In Figure 5.24 the stator active power output is maintained constant so quadrature rotor current i_{qr} is constant and i_{dr} is varied from zero to full rated load current. The locus of the rotor flux ψ_r varies along C-D, resulting in a change in the magnitude of ψ_r, with the variation of δ_p remaining small. Reactive power delivered by the grid to the stator can be decreased by increasing the magnitude of the rotor flux, whereas decreasing the magnitude of the rotor flux increases reactive power delivered to the stator [106].

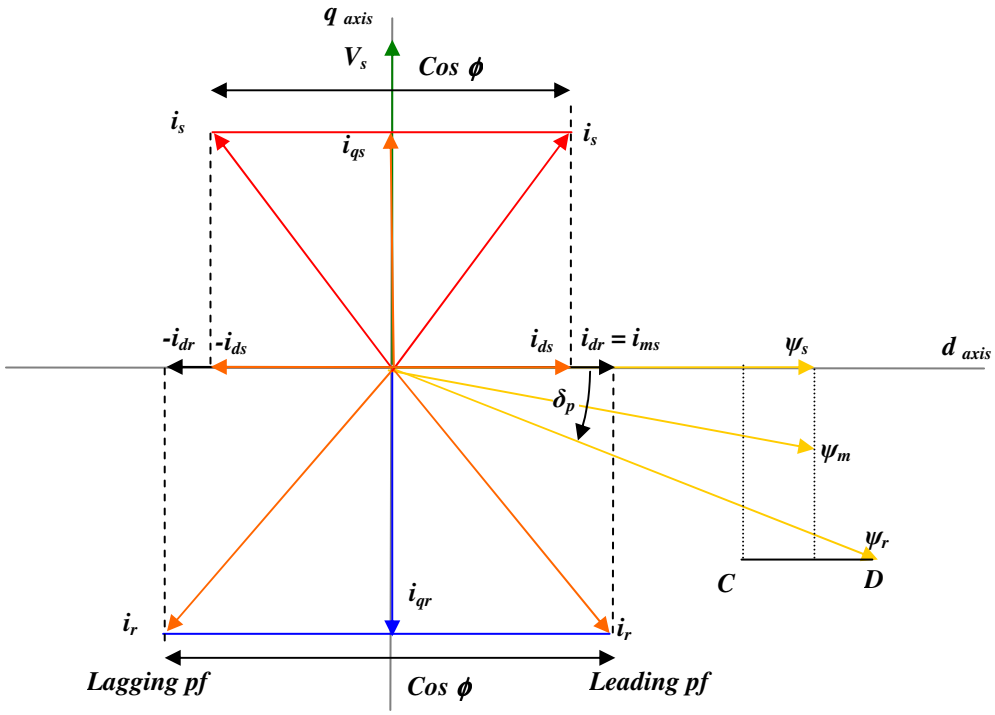

Figure 5.24 Phasor diagram, constant active power

From the above discussion the following is observed:

- The stator active power can be controlled by controlling the angular position of the rotor flux vector.
- The stator reactive power can be controlled by controlling the magnitude of the rotor flux vector.

The switching states of the rotor-side converter in a DFIG can be altered to control the active and reactive power, as observed in Figure 5.25. When the *d*-axis is aligned with stator flux space vector (ψ_s), the stator current i_s can be operated in any of the four quadrants and the machine can produce or absorb real or reactive power. Normal operation of a DFIG is with the stator current i_s in the bottom half of Figure 5.25 [36].

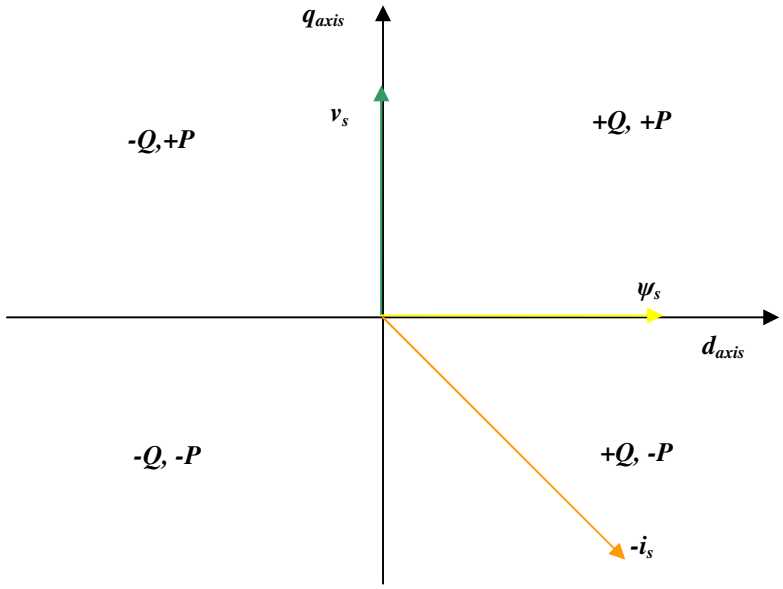

Figure 5.25 Relationship between DFIG power and stator current space vector

Chapter 6 Control of DFIG

6.1 Doubly-Fed Induction Machines

Chapter six concentrates on describing methods to control the power generated by a DFIG. The DFIG induction generator is double-fed; the stator windings are supplied directly by the grid voltage and the rotor windings have a voltage impressed on them by the rotor converter. Since the stator windings are connected to the grid, the flux is mainly determined by the voltage and frequency of the grid. The applied rotor voltage (v_r) in a DFIG can be adjusted to get the desired slip or torque responses. The frequency of the converter will depend on the slip speed. It is also possible to control power factor or reactive power in the stator circuit similar to a synchronous generator [70].

The DFIG back-to-back AC/DC/AC rotor converter is comprised of a rotor-side converter (C_{rotor}) and a grid-side converter (C_{grid}) as shown in Figure 6.1. C_{rotor} and C_{grid} can be Voltage-Source Converters or Current Source Converters that use forced-commutated power electronic devices (normally IGBT's) to synthesize an ac voltage from a dc voltage source. A capacitor is normally connected on the DC link acts as a dc voltage source. The three-phase rotor windings are connected to C_{rotor} by slip rings and brushes and the three-phase stator windings are directly connected to the grid.

Power captured by the wind turbine is converted into electrical power by the induction generator and is transmitted to the grid by the stator and the rotor windings. The DFIG control system generates the pitch angle command and the current command signals for the rotor-side and grid-side converters respectively (Figure 6.1). These command signals control the power delivered by the wind turbine, the dc bus voltage and the reactive power at the grid terminals.

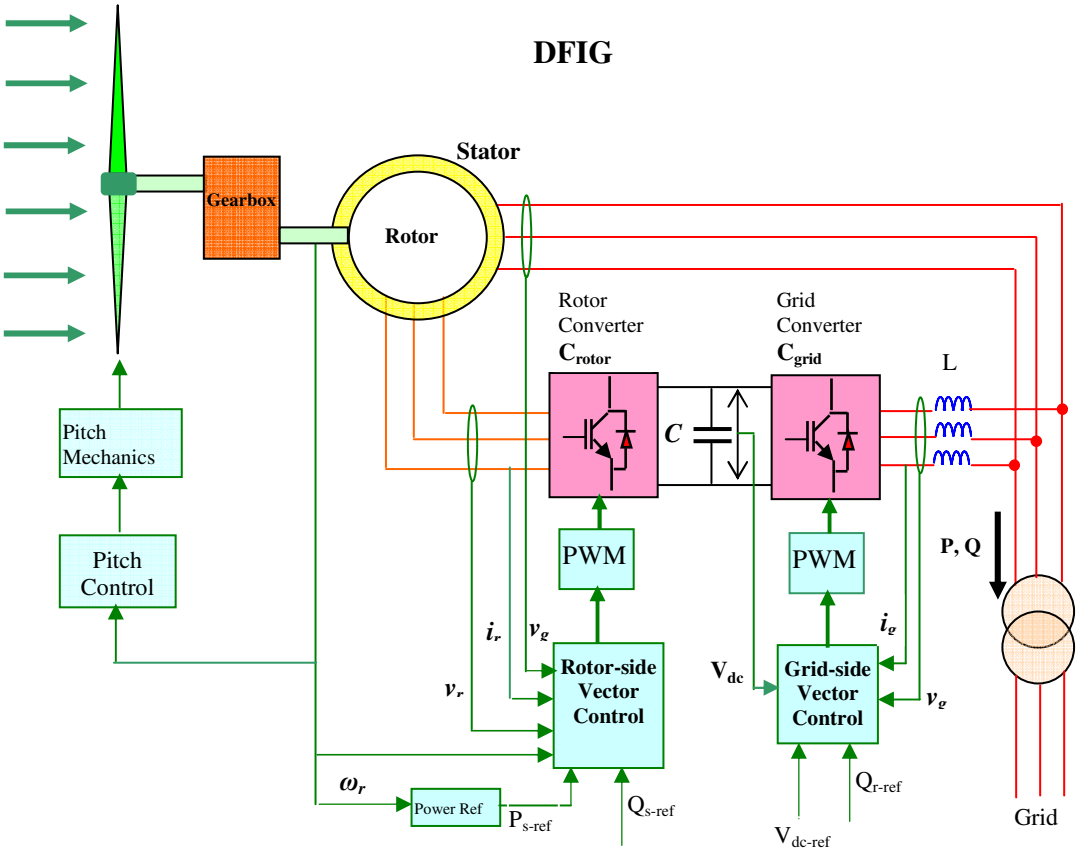

Figure 6.1 Block diagram of DFIG and control elements

The rotor side and grid side converters in a DFIG can be controlled by vector control techniques. Vector-control techniques have been well developed for DFIG's using back-to-back PWM converters [72] and are applied to control power/torque and DC link voltage. The objective of the vector-control scheme for the grid-side PWM voltage source converter is to maintain the DC-link voltage constant regardless of the magnitude and direction of the rotor power whilst also maintaining sinusoidal grid currents. The grid-side converter can control reactive power flow into the grid according to the reference Q_{r_ref}. The vector-control scheme for the rotor-side PWM voltage source converter controls the power delivered by the DFIG to the grid and ensures decoupling control of stator-side active and reactive power drawn from the grid.

In vector control schemes it is necessary to align the stator voltage with either a *d*-axis voltage vector or *d*-axis flux vector. If the stator voltage is aligned with the flux vector the method is referred to as Stator Flux Oriented (SFO) control whereas if the stator voltage is aligned with the voltage vector then the method is referred to as Stator Voltage Oriented (SVO) control (Chapter 5 section 5.3.2).

6.2 Rotor Side Converter

6.2.1 Voltage Equations

The dynamic model for a DFIG is based on the general equations obtained for an induction machine. The stator and rotor voltage and flux equations in the synchronous *dq* reference frame (Chapter 5 section 5.3.3) are rewritten here as:

$$v_{ds}^{e} = i_{ds}^{e} R_s - \omega_e \psi_{qs}^{e} + \frac{d\psi_{ds}^{e}}{dt} \tag{6.1}$$

$$v_{qs}^{e} = i_{qs}^{e} R_s + \omega_e \psi_{ds}^{e} + \frac{d\psi_{qs}^{e}}{dt} \tag{6.2}$$

$$\psi_{ds} = L_s i_{ds} + i_{dr} L_m \tag{6.3}$$

$$\psi_{qs} = L_s i_{qs} + i_{qr} L_m \tag{6.4}$$

$$v_{dr}^{e} = i_{dr}^{e} R_r - (\omega_e - \omega_r) \psi_{qr}^{e} + \frac{d\psi_{dr}^{e}}{dt} \tag{6.6}$$

$$v_{qr}^{e} = i_{qr}^{e} R_r + (\omega_e - \omega_r) \psi_{dr}^{e} + \frac{d\psi_{qr}^{e}}{dt} \tag{6.7}$$

$$\psi_{dr} = L_r i_{dr} + i_{ds} L_m \tag{6.8}$$

$$\psi_{qr} = L_r i_{qr} + i_{qs} L_m \tag{6.9}$$

6.2.2 Power and Electromagnetic Torque Equations

Power in a DFIG can be described as:

$$S = P + jQ = -\frac{3}{2} v_s . i_s^* = -\frac{3}{2} v_{dqs} . i_{dqs}^* \tag{6.10}$$

Active and reactive powers can be obtained from (6.10) as [65]:

$$P_s = \frac{3}{2} \mathrm{Re}\left(v_{dqs} . i_{dqs}^* \right) \tag{6.11}$$

$$Q_s = \frac{3}{2} \mathrm{Im}\left(v_{dqs} . i_{dqs}^* \right) \tag{6.12}$$

Aligning the *d*-axis of the synchronous reference frame to be along the stator flux linkage, SFO will yield $\psi^e_{qs} = 0$, or using SVO, $v^e_{qs} = 0$ [65], [89], [93], [94] and [101]. The stator-side active power P_s and reactive power Q_s power can now be described in stator voltage orientation as:

$$P_s = 3/2 \left(v^e_{ds} i^e_{ds} + v^e_{qs} i^e_{qs} \right) = \frac{3}{2} v^e_{ds} i^e_{ds} = -\frac{3}{2} \frac{L_m}{L_s} v^e_{ds} i^e_{dr} \tag{6.13}$$

$$Q_s = 3/2 \left(-v^e_{qs} i^e_{ds} + v^e_{ds} i^e_{qs} \right) = \frac{3}{2 L_s} v^e_{ds} \left(\psi_{ds} - L_m i^e_{qr} \right) \tag{6.14}$$

It is observed in (6.13) and (6.14) that adjustment of the *d*-axis component of the rotor current controls the stator real power of the DFIG and adjustment of the rotor *q*-axis current component controls the stator reactive power [73], [75].

The electromagnetic torque equation of a DFIG is [65], [89]:

$$T_e = \frac{3}{2} \left(\frac{p}{2} \right) \mathrm{Re}\left(\psi^e_{dqs} . i^{e*}_{dqs} \right) = \frac{3}{2} \left(\frac{p}{2} \right) \mathrm{Re}\left(\psi^e_{dqr} . i^{e*}_{dqr} \right) \tag{6.15}$$

where i_{dqs}^{e*} and i_{dqr}^{e*} are the complex conjugate stator and rotor dq currents respectively. Equation (6.15) can be expanded as:

$$T_e = \frac{3}{2}\left(\frac{p}{2}\right)\left(\psi_{ds}^e . i_{qs}^e - \psi_{qs}^e . i_{ds}^e\right) = \frac{3}{2}\left(\frac{p}{2}\right)\left(\psi_{dr}^e . i_{qr}^e - \psi_{qr}^e . i_{dr}^e\right) \qquad (6.16)$$

Using (6.3) in SVO:

$$i_{ds} = -i_{dr} L_m / L_s = -i_{dr} L_m / (L_{ls} + L_m) \qquad (6.17)$$

If i_{ds}^e is now substituted into the equation for electromagnetic torque (6.16), the torque can be described in SVO as:

$$T_e = \frac{3}{2}\left(\frac{p}{2}\right)\psi_{qs}^e . i_{dr}^e \, L_m / (L_{ls} + L_m) \qquad (6.18)$$

It is observed in (6.18) that adjustment of the d-axis component of the rotor current controls the electromechanical torque of the DFIG. The rotor side converter controller can control the active and reactive power of the DFIG [73] and is normally comprised of ra parallel two stage controller where the active and reactive powers are controlled independently [75].

6.2.3 Calculating the Rotor Voltages to be applied.

The switching frequency of the power electronic rotor converter is normally maintained constant, therefore it is necessary to calculate the voltage modulation signal to ensure the rotor currents are equal to their reference values [67]. Also with a decoupled control scheme any change in voltage component in d or q-axis results in a change in both d and q components. To alleviate this problem it is necessary to develop equations to compensate for cross coupling between d and q axis components [89].

A leakage factor is defined as [67], [71], [89];

$$\sigma = 1-\frac{L_m^2}{L_s L_r} = 1-\frac{L_m^2}{(L_{ls}+L_m)(L_{lr}+L_m)} \tag{6.19}$$

Substituting (6.17) for i_{ds} into (6.8) yields:

$$\psi_{dr}^e = L_r i_{dr}^e + \frac{L_m}{L_s}(-i_{dr}^e L_m) = \sigma L_r i^e{}_{dr} \tag{6.20}$$

Also substituting (6.4) into (6.9):

$$\psi_{qr}^e = i_{qr}^e (L_r - \frac{L_m^2}{L_s}) + \frac{L_m}{L_s}\psi_{qs} = \sigma L_r i_{qr}^e + \frac{L_m}{L_s}\psi_{qs} \tag{6.21}$$

Substituting equations (6.20) and (6.21) into (6.6) and (6.7) respectively yields:

$$v_{dr}^e = i_{dr}R_r - (\omega_e - \omega_r)\sigma L_r i_{qr}^e + \sigma L_r \frac{di_{dr}^e}{dt} \tag{6.22}$$

$$v_{qr}^e = i_{qr}R_r + (\omega_e - \omega_r)\sigma L_r i_{dr}^e + (\omega_e - \omega_r)\frac{L_m}{L_r}\psi_{ds}^e + \sigma L_r \frac{di_{qr}^e}{dt} \tag{6.23}$$

The first and third terms on the right side of equation (6.22) are as a result of *d*-axis current i_{dr} and $\frac{di_{dr}^e}{dt}$. The term due to i_{qr} can be considered as disturbances [67]. Similarly in (6.23) the terms i_{dr} and ψ_{ds} can be considered as disturbances. Equations (6.22) and (6.23) can therefore be expressed as [76], [89]:

$$v_{dr}^e = v_{dr}^{e\prime} + v_{dr,comp}^e \tag{6.24}$$

$$\text{where } v_{dr}^{e\prime} = i_{dr}R_r + \sigma L_r \frac{di_{dr}^e}{dt} \tag{6.25}$$

$$\text{and} \quad v^{e}_{dr,comp} = -(\omega_e - \omega_r)\sigma L_r i^{e}_{qr} \tag{6.26}$$

Similarly equation (6.23) for v_{qr}, can be expressed as:

$$v^{e}_{qr} = v^{e\prime}_{qr} + v^{e}_{qr,comp} \tag{6.27}$$

$$\text{where} \quad v^{e\prime}_{qr} = i_{qr}R_r + \sigma L_r \frac{di^{e}_{qr}}{dt} \tag{6.28}$$

$$\text{and} \quad v^{e}_{qr,comp} = (\omega_e - \omega_r)\sigma L_r i^{e}_{dr} + (\omega_e - \omega_r)\frac{L_m}{L_r}\psi^{e}_{ds} \tag{6.29}$$

Adding (6.26) and (6.29) to the uncompensated voltage terms (6.25) and (6.28) allows decoupled performance of the rotor-side converter. This is sometimes referred to as "Feed Forward Control". Voltage equations (6.24) and (6.28) can be incorporated into the vector control scheme shown in Figure 6.2 where *PI* controllers are applied to control rotor current and shaft speed. The control scheme can utilise cascade control (Figure 6.2) i.e. the inner current control loops are employed for controlling the *d* and *q* axis rotor currents and the outer power control loops are used to control active and reactive power of the stator. The power control loops generate the *d*-axis and *q*-axis reference rotor currents for the current control loops.

The two parallel controllers in the rotor-side converter determine the converter reference voltage signals v^{*}_{dr} and v^{*}_{qr} by comparing the i_{dr}^{*} and i_{qr}^{*} current set points to the actual i_{dr} and i_{qr} currents of the DFIG rotor. The slip angle, θ_{slip}, is obtained by subtracting the rotor angle, θ_r, from the obtained grid angle θ_e (Figure 6.2). Correct calculation of the slip angle θ_{slip} ensures the reference values v_a^{*}, v_b^{*} and v_c^{*} for the PWM block are obtained (Figure 6.2).

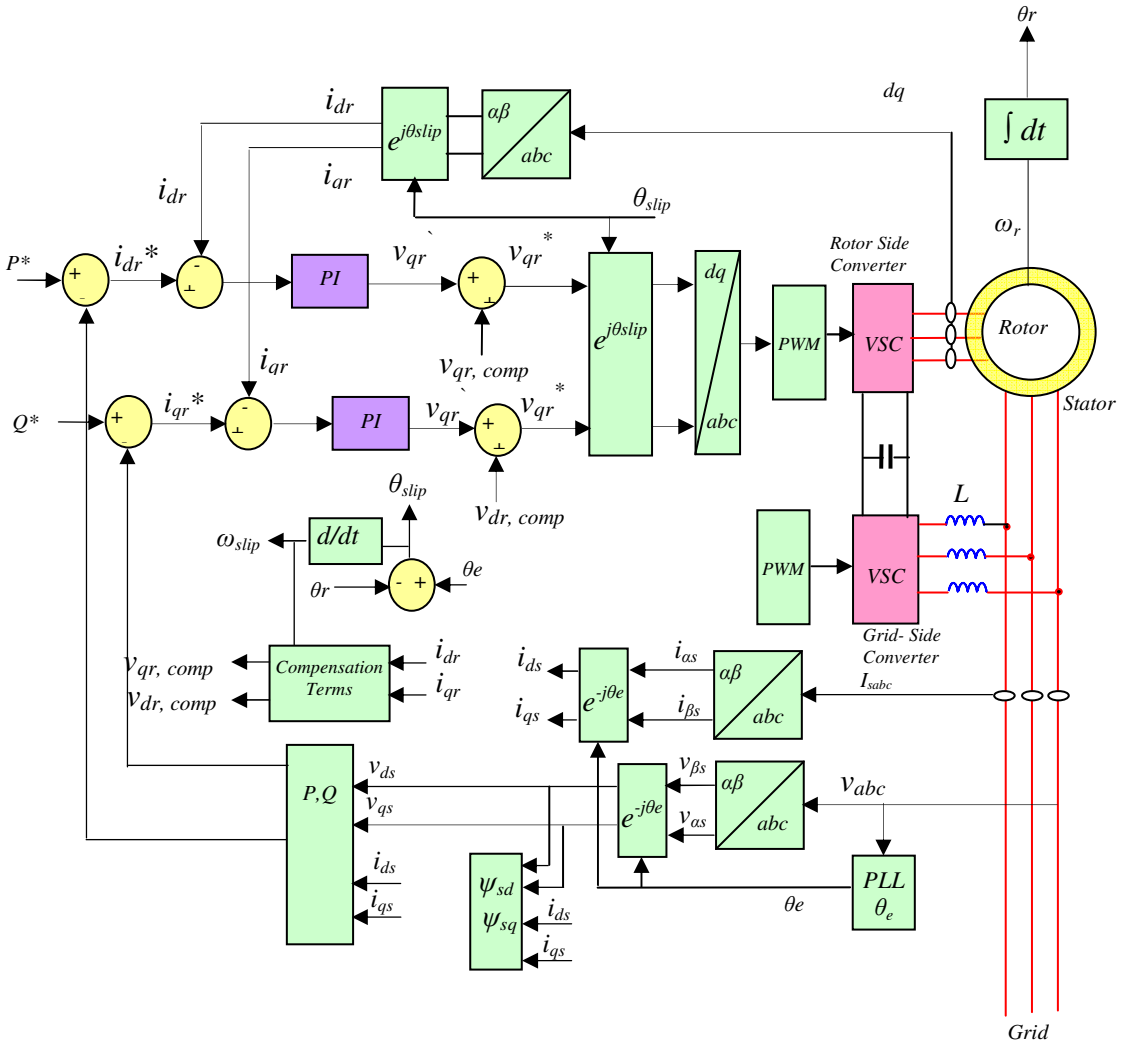

Figure 6.2 Vector control of rotor-side converter of DFIG

6.3 Design of PI Controllers.

Designing PI control schemes is often done in continuous-time rather than discrete-time, and in this work the continuous-time PI-controller design methods are applied. There are a number of standard methods for designing PI-controllers, such as Ziegler-Nichols tuning, root-locus, Bode, pole-placement and internal model control, etc. In the following sections, the pole-placement and internal model method are utilised, for their straightforwardness and simplicity to design PI-controllers in control loops. Internal model control, which is considered as a robust control method, has been used for ac machine control. The benefit of the internal model control is that the controller

parameters are expressed directly in the machine parameters and the desired closed-loop rise time. Thus internal model control is applied to design the DC-link voltage controller.

6.3.1 Rotor Side Converter

In the vector-control scheme of the rotor-side PWM voltage source converter, the *d*-axis and *q*-axis rotor currents are decoupled for individual stator-side active and reactive power control. Voltage-compensation terms are used for decoupling the current control loops. Equations (6.22) and (6.23) can be expressed as:

$$v_{dr}^{e} = i_{dr}R_r - (\omega_e - \omega_r)\sigma L_r i_{qr}^{e} + \sigma L_r U_{dr}^{e} \tag{6.30}$$

$$v_{qr}^{e} = i_{qr}R_r + (\omega_e - \omega_r)\sigma L_r i_{dr}^{e} + (\omega_e - \omega_r)\frac{L_m}{L_r}\psi_{ds}^{e} + \sigma L_r U_{qr}^{e} \tag{6.31}$$

where:

$$U_{dr}^{e} = k_p\left(i_{dr}^{e*} - i_{dr}^{e}\right) + k_i\int\left(i_{dr}^{e*} - i_{dr}^{e}\right)dt \tag{6.32}$$

$$U_{qr}^{e} = k_p\left(i_{qr}^{e*} - i_{qr}^{e}\right) + k_i\int\left(i_{qr}^{e*} - i_{qr}^{e}\right)dt \tag{6.33}$$

where k_p and k_i are the proportional and integral gains of the current controllers.

Assuming ideal decoupling between *d*-axis and *q*-axis currents, the current control loop is shown in Figure 6.3. The i_{dr} and i_{qr} errors are processed by the PI controllers to obtain reference voltages v_{dr}` and $v_{qr}$`.

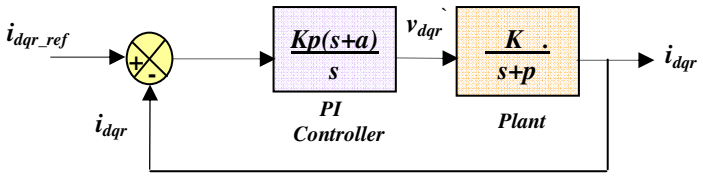

Figure 6.3 Rotor converter current-control loop

The gains of the proportional and integral parameters of the PI controllers are computed assuming that compensation is perfect [67]. The transfer function of the plant based on equations (6.25) and (6.28) is [67], [89]:

$$G(s) = \frac{i^e_{dqr}(s)}{v'^e_{dqr}(s)} = \frac{1}{r_r + s\sigma(L_{lr} + L_m)} \tag{6.34}$$

Transfer functions of the current control loops are stable with only one single dominant nonzero pole. In this condition, a straightforward approach for designing a PI controller is to place the zero of the PI controller to cancel (or approximately cancel) the dominant pole of the plant. This method is called pole-placement. The open loop transfer function of Figure 6.3 including the PI regulator is [65]:

$$G(s) = \frac{i^e_{dqr}(s)}{i^e_{dqr-ref}(s)} = \frac{k_p\, k(s+a)}{s(s+p)} \tag{6.35}$$

Letting $a = p$:

$$G(s) = \frac{k_p\, k}{s} \tag{6.36}$$

where $k = 1/\sigma(L_{lr}+L_m)$.

The closed loop transfer function:

$$\frac{G(s)}{1+G(s)} = \frac{k_p\, k}{s + k_p\, k} \tag{6.37}$$

This is a first order system, the bandwidth is thus:

$$\omega_n = k_p\, k \tag{6.38}$$

There is a relationship between the rise-time (10%-90%) and bandwidth for a first order system and this can be expressed as $\omega_n = \frac{\ln 9}{t_R}$.

The rise time of the system step response is therefore $t_R = \frac{\ln 9}{k_P k}$.

Thus the proportional gain of the current controller k_p can be deduced as:

$$k_p = \frac{\ln 9}{k\, t_R}(1 + d\%) \tag{6.39}$$

Where $d\%$ is added to ensure the required rise time will be obtained.

The active and reactive power loop transfer functions can be obtained from equations (6.13) and (6.14) with SVO as:

$$\frac{P_s}{i_{dr}^e} = -\frac{3\,L_m}{2\,L_s} v_{ds}^e \tag{6.40}$$

$$\frac{Q_s}{i_{qr}^e} = -\frac{3\,L_m}{2\,L_s} v_{ds}^e \tag{6.41}$$

Assuming ideal decoupling between the *d*-axis and *q*-axis currents, the cascade control scheme with the power loop (real and reactive power) is shown along with the inner current control loop in Figure 6.4, where K_1 represents the power control loop plant:

$$k_1 = -\frac{3\,L_m}{2\,L_s} v_s \tag{6.42}$$

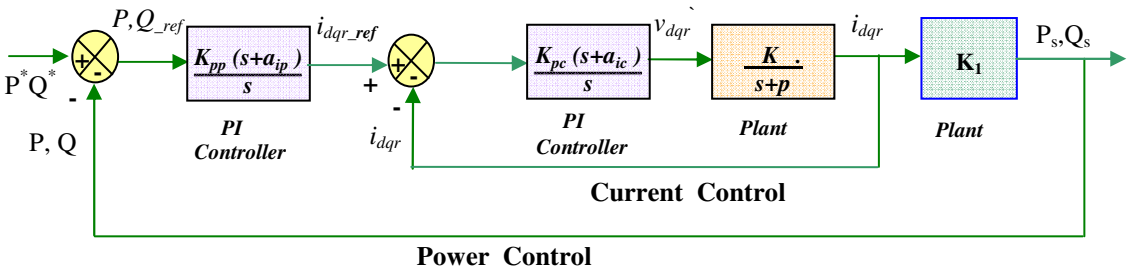

Figure 6.4 Cascade control structure

With the closed-loop transfer function of the current control loop expressed as equation (6.37), the control scheme shown in Figure 6.4 may be simplified as shown in Figure 6.5.

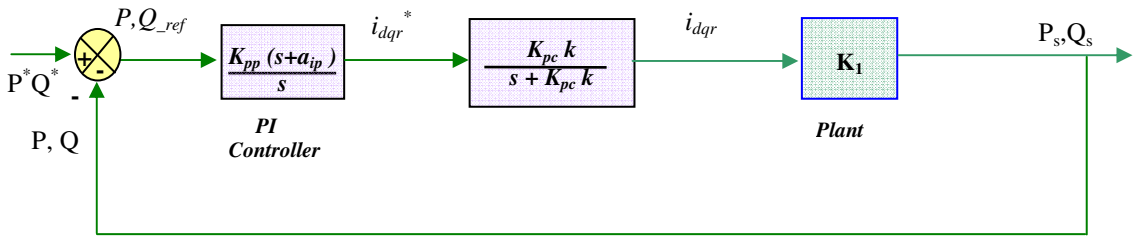

Figure 6.5 Cascade control structure

The PI-controllers in the power control loops can be designed in a similar way to the design of the PI-controllers in the current control loops. Controller gains can be obtained as:

$$a_{ip} = k_{pc}k \tag{6.43}$$

$$k_{Pp} = \frac{\ln 9}{k_{pc}k\,k_1\,t_{R2}}(1+m\%) \tag{6.44}$$

where t_{R2} is the rise time of the power control loop step response (s), and m is the design margin.

The DFIG test-rig PI control parameters are obtained using the parameters of the induction machine as tabulated in Table A1 in Appendix A. For the induction machine plant, the value of k is:

$k = 1/\sigma(L_{lr}+L_m) = 1/((0.054676)(0.031164))$ and thus:

$$G(s) = \frac{k}{p+s} = \frac{586.8}{86+s} \tag{6.45}$$

For a rise-time of 0.01s (Appendix I) the gains of the current controller are:

$$a_{ic} = p = 86 \tag{6.46}$$

$$k_{Pc} = \frac{\ln 9}{k\, t_R}(1+m\%) = 0.412 \quad (6.47)$$

The integral gain can be obtained as:

$$K_{ic} = a_{ic}\, k_{pc} = 86 \,.\, 0.412 = 35.42 \quad (6.48)$$

The gains of the power controllers are (for a rise time of 0.1s):

$$a_{ip} = k_{pc}\, k = 242.76 \quad (6.49)$$

From (6.42), $k_1 = 1.458$ and the proportional power gain is:

$$k_{Pp} = \frac{\ln 9}{k_{pc} k\, k_1\, t_{R2}}(1+d\%) = 0.0623 \quad (6.50)$$

The integral gain can be obtained as:

$$K_{ip} = a_{ip}\, k_{pp} = 242.76 \,.\, 0.0623 = 15.13 \quad (6.51)$$

6.3.2.1 Grid Side Converter Control Scheme

The control structure for the grid-side converter is based on decoupled *d-q* vector control methods as previously outlined for the rotor-side converter. The grid-side converter control scheme has been investigated in [73], [92]. The grid-side converter controls the DC-link voltage and reactive power. The main objective of the grid-side converter is to control the DC-link voltage regardless of the magnitude and direction of the slip power [89]. In the vector-control scheme of the grid-side PWM voltage source converter, the *d* and *q*-axis line currents are decoupled for controlling the DC-link voltage and the reactive power flow between the grid and the grid-side converter respectively.

To maintain a constant DC-link voltage, a power balance is desirable between the rotor-side converter and the grid-side converter neglecting converter losses. In super-synchronous mode of operation DFIG real power flows from the rotor windings to the

rotor-side converter, through the DC-link to the grid-side converter and into the supply grid. The grid-side converter thus operates as an inverter.

However in sub-synchronous mode of operation real power flows from the grid, through the grid-side converter, DC-link and rotor-side converter through to the rotor windings. During this mode of operation the grid-side converter operates as a rectifier. Figure 6.6 shows a schematic diagram of the grid-side converter .

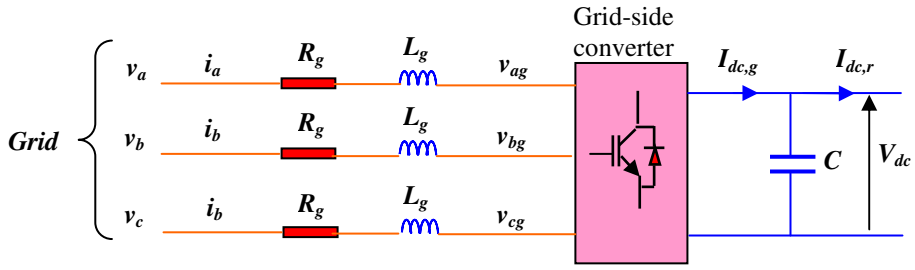

Figure 6.6 Grid-side converter schematic

Power flow in the grid-side front-end PWM converter is controlled by adjusting the phase shift angle δ between the source voltage v and the respective converter reflected input voltage v_g. When grid voltage v leads v_g the real power flows from the ac grid source into the grid-side converter (and thus dc bus). Conversely, if v lags v_g, power flow is from the converter (i.e., dc bus) into the grid.

Power flow in the grid side converter is determined by the load. When the DFIG operates in the super-synchronous mode the magnitude of the output current i is positive, and real power flows from the DC bus into the grid. Conversely during sub-synchronous mode of operation i is negative and real power flows through the grid-side converter and into the DC-link to the rotor-side converter.

The voltage balance across the grid-side inductors is:

$$v_a = i_{ag} R_g + L_g \frac{di_{ag}}{dt} + v_{ag} \qquad (6.52)$$

$$v_b = i_{bg} R_g + L_g \frac{di_{bg}}{dt} + v_{bg} \quad (6.53)$$

$$v_c = i_{cg} R_g + L_g \frac{di_{cg}}{dt} + v_{cg} \quad (6.54)$$

where: R_g is the filter resistance

L_g is the filter inductance

The *d-q* voltage equations can be obtained in the grid voltage reference frame with the d_{axis} aligned with the grid voltage. Aligning the d_{axis} with the grid voltage and applying the transform rotation to the equations (6.52) to (6.54) will yield:

$$v_d^e = i_{dg}^e R_g + L_g \frac{di_{dg}^e}{dt} - \omega_e L_g \, i_{qg}^e + v_{dg}^e \quad (6.55)$$

$$v_q^e = i_{qg}^e R_g + L_g \frac{di_{qg}^e}{dt} + \omega_e L_g \, i_{dg}^e + v_{qg}^e \quad (6.56)$$

When the *d-axis* is aligned with the grid voltage, the *q-axis* voltage is forced to zero i.e. v_q is zero. Grid-side decoupled vector control is normally implemented, with i_q controlling DC-link voltage and i_d controlling reactive power [75]. The control strategy for decoupled control of the grid-side converter is shown in Figure 6.7.

The *d-q* axis has the same speed as that of the grid voltage and therefore $\theta_e = \omega_e t$ in Figure 6.7. The reference voltages v_{d1}^* *and* v_{q1}^* are computed from the errors between reference current set-points i_{dg}^* and i_{qg}^* and measured grid currents i_{dg} and i_{qg} . The voltages $v_{\alpha 1}^*$ and $v_{\beta 1}^*$ are obtained using the calculated value for θ_e and the rotation transformation $e^{-j\theta e}$. The reference values v_a^*, v_b^* and v_c^* are thus obtained for the PWM

block. The actual rotor voltages v_a, v_b and v_c are supplied by the power electronics grid-side converter, using space vector modulation.

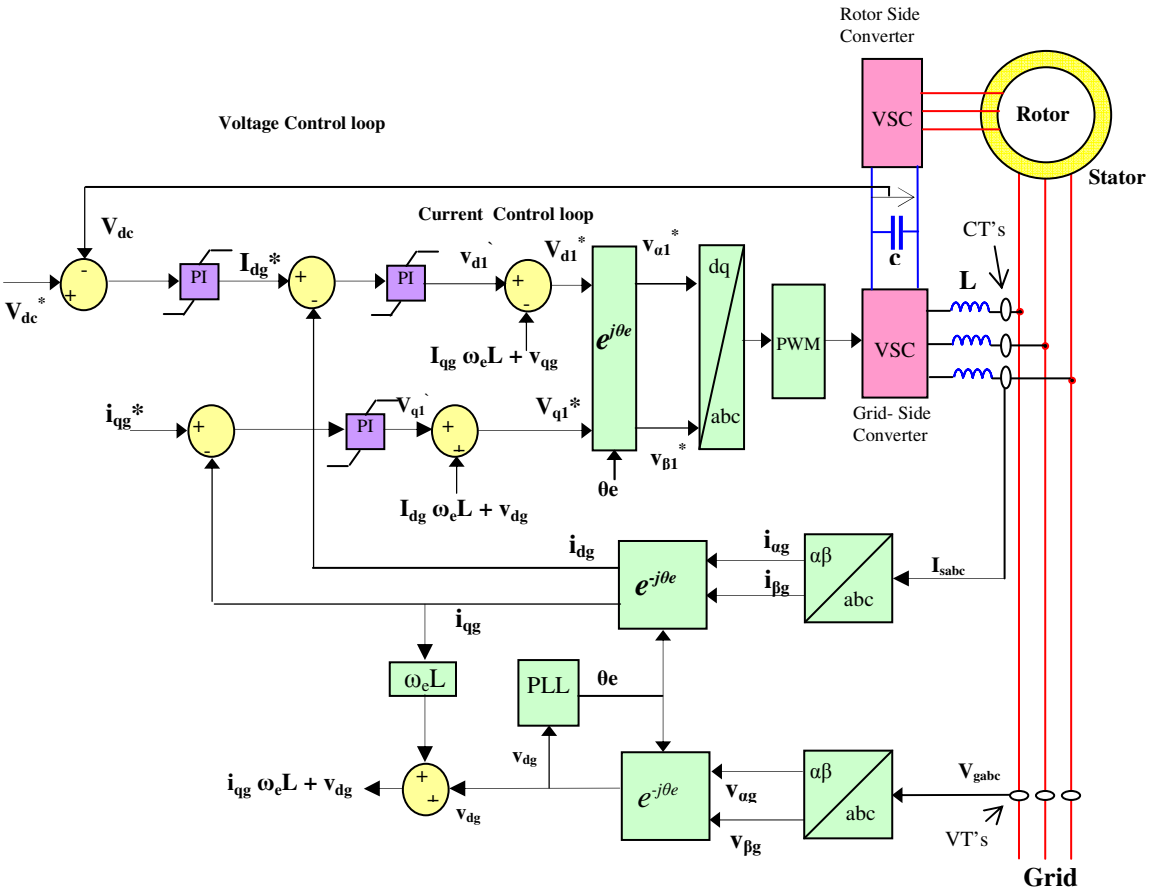

Figure 6.7 Grid-side converter d-q vector control scheme in grid (stator) voltage orientation.

Observing equations (6.55 and 6.56), the reference values $v_{dg}^{ref,e}$, *and* $v_{qg}^{ref,e}$ can be obtained as:

$$v_{dg}^{ref,e} = -i_{dg}^e R_g - L_g \frac{di_{dg}^e}{dt} + \omega_e L_g\, i_{qg}^e + v_d^e \qquad (6.57)$$

$$v_{qg}^{ref,e} = -i_{qg}^e R_g - L_g \frac{di_{qg}^e}{dt} - \omega_e L_g\, i_{dg}^e + v_q^e \qquad (6.58)$$

And the decoupling terms are:

$$\omega_e L_g \; i_{qg}^e \quad and \quad \omega_e L_g \; i_{dg}^e \tag{6.59}$$

If the losses associated with the converter and inductor are neglected and neglecting harmonics due to switching, the following equations associated with the DC link can be obtained [89]:

$$V_{dc} I_{dcg} = \frac{3}{2} v_d^e \; i_d^e \tag{6.60}$$

$$v_d^e = \frac{M_1}{2\sqrt{2}} V_{dc} \tag{6.61}$$

$$I_{dc,g} = \frac{3}{4\sqrt{2}} M_1 \, i_d^e \tag{6.62}$$

$$C \frac{dV_{dc}}{dt} = I_{dc,g} - I_{dc,r} \tag{6.63}$$

where V_{dc} is the DC-link voltage, $I_{dc,g}$ is the grid-side dc current, $I_{dc,r}$ is the rotor-side dc current (schematic, Figure 6.6), and M_1 is the grid-side modulation index.

Normally the stator to rotor turns ratio n_s is less than 1 for induction machines designed as wind generators. The rotor circuit will thus present a higher rated voltage level than the stator so that the maximum modulation index over the controlled speed range is not so different to that of the grid side converter [128]. The laboratory induction machine however has a stator to rotor turns ratio of 2:1 and thus for the rotor side converter the maximum modulation index is usually smaller than that of the grid side converter.

6.3.2.1 Grid Side Current PI Controller

For its straightforwardness and simplicity, the pole-placement method is applied for designing PI-controllers in current control loops and power control loops. PI controllers are used to obtain reference voltages v_{d1}` and $v_{q1}$` from the reference currents in the current loops. The gains of the proportional and integral parameters of the PI controllers are computed assuming that compensation is perfect [67]. Equations (6.57) and (6.58) can be written as:

$$v_{dg}^{ref,e} = -i_{dg}^{e} R_g - L_g U_{dg} + \omega_e L_g i_{qg}^{e} + v_d^{e} \tag{6.64}$$

$$v_{qg}^{ref,e} = -i_{qg}^{e} R_g - L_g U_{qg} - \omega_e L_g i_{dg}^{e} \tag{6.65}$$

where:

$$U_{dg} = k_p\left(i_{dg}^{e*} - i_{dg}^{e}\right) + k_i \int \left(i_{dg}^{e*} - i_{dg}^{e}\right) dt \tag{6.66}$$

$$U_{qg} = k_p\left(i_{qr}^{e*} - i_{qr}^{e}\right) + k_i \int \left(i_{qr}^{e*} - i_{qr}^{e}\right) dt \tag{6.67}$$

The i_{dg} and i_{qg} errors are processed by the PI controllers to give v_{d1}^{*} and v_{q1}^{*} shown in Figure 6.7. Considering the compensation terms as a disturbance the transfer function of the plant current control loop is [78], [89]:

$$G_g(s) = \frac{i_{dqg}^{e}(s)}{v'^{e}_{dqg}(s)} = \frac{1}{R_g + sL_g} \tag{6.68}$$

Damping of the grid filter is given by:

$$\left|G_g(j\omega)\right| = \frac{1}{\sqrt{\omega^2 L_g^2 + R_g^2}} \tag{6.69}$$

The grid side converter can be controlled by considering a cascade control structure with a current control loop inside the dc voltage control loop as illustrated in Figure 6.8.

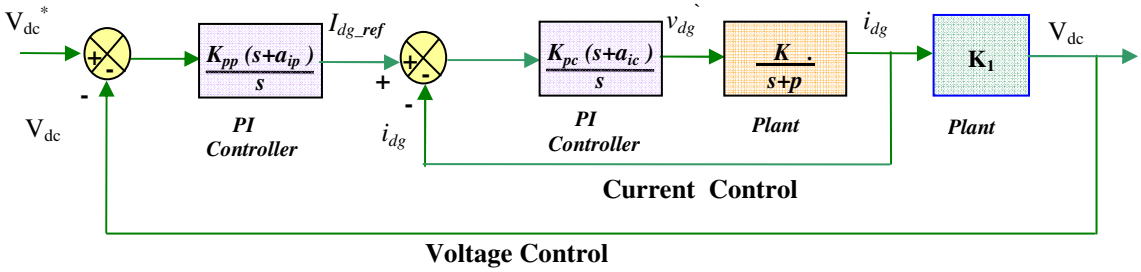

Figure 6.8 Grid-side converter current and voltage control loops

Similar to the rotor-side converter, the grid-side converter has a cascade control loop; a current loop inside the DC link voltage control loop. Assuming ideal decoupling between the *d* and *q*-axis currents, the current control loop is shown in Figure 6.9. The i_{dr} and i_{qr} errors are processed by the PI controllers to give v_{dr}` and $v_{qr}$`.

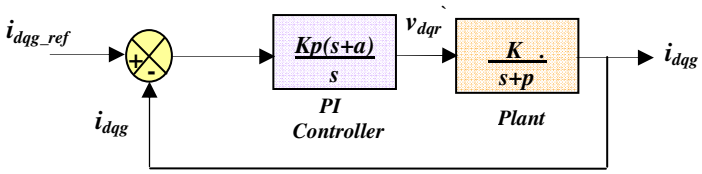

Figure 6.9 Grid Side converter current-control loop

The grid-side plant equation is:

$$G_g(s) = \frac{k}{p+s} = = \frac{1562.5}{8.5469+s} \qquad (6.70)$$

where k = $1/L_g$ = 1562.5, and p = R_g/L_g = 8.5469 (Details of parameters are included in Appendix A).

The open loop transfer function including the *PI* regulator is:

$$G_g(s) = \frac{i^e_{dqg}(s)}{i^e_{dqg-ref}(s)} = \frac{k_{pg}\,k(s+a)}{s(s+p)} \qquad (6.71)$$

If $p = a$:

$$G_g(s) = \frac{k_{pg}\, k}{s} \tag{6.72}$$

Thus the proportional gain of the DC link current controller k_{pg} can be deduced for a rise-time of 0.01s as:

$$k_{pg} = \frac{\ln 9}{k\, t_R}(1 + m\%) = 0.1547 \tag{6.73}$$

where $m\%$ is a design margin which guarantees the required rise time will be obtained.

$$a_{ic} = p = 8.547 \tag{6.74}$$

The integral gain is:

$$K_{ic} = a_{ic}\, k_{pg} = 8.547 \,.\, 0.1547 = 1.322 \tag{6.75}$$

Fine tuning in Matlab of the proportional gain k_{pg} ensured a satisfactory performance as observed in Appendix I.

6.3.3 Rotor side and Grid side converter parameters.

PI control parameters for the current, power and voltage control loops for the rotor side and grid side converters are obtained based on the information provided in Appendix A. Values obtained for PI parameters of the DFIG laboratory controllers are tabulated in Table 5.

Table 5 Converter gains

	Rotor Side Converter		Grid Side Converter	
	Power Control	Current Control	Current Control	V_{dc} control
K_p Proportional Gain	0.062	0.412	0.1547	0.0505
K_i Integral Gain	15.1	35.42	1.322	21.972

6.4 Phase Locked Loop (PLL)

Methods to obtain phase angle (θ_e) of stator or grid voltages are predominately the PLL technique. The PLL is normally implemented in the *dq* synchronous reference frame. A schematic of a PLL in a *dq* synchronous reference frame is shown in Fig. 6.10.

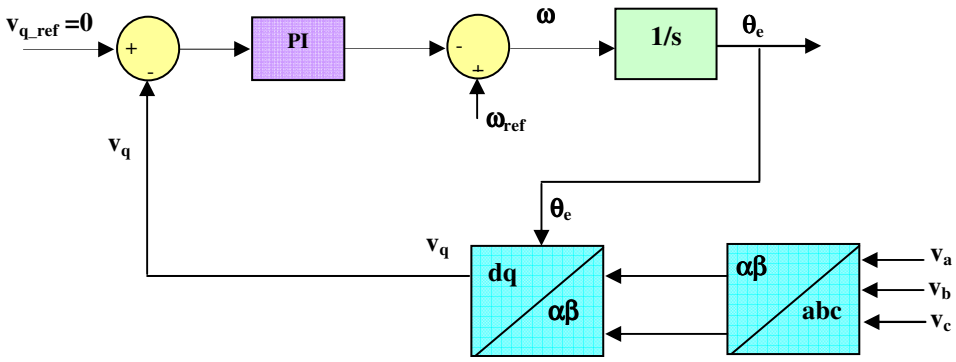

Figure 6.10 Phase Locked Loop, PLL to obtain θ_e

The inputs to the PLL model are the grid phase voltages and the output is the tracked phase angle θ_e. The grid quadrature component v_q is the locking reference, and when set to zero reference the PLL locks *vq* to zero. The PLL model is implemented in *dq* synchronous reference frame requiring a Park transform from *abc* to *dq* reference frame. The Park transform requires the output angle of the PLL to synchronize the *dq* reference frame.

A PI controller is used to control the v_q variable and the output of this regulator is the grid frequency. Integrating the grid frequency the utility voltage angle is obtained, which is fed back into the $\alpha\beta$ to *dq* transformation module. Therefore the value of V_q is maintained at zero and V_d is the positive voltage magnitude. The magnitude of the controlled variable V_q determines the phase difference between the grid voltage and the converter phase angle. Hence the PI controller input is V_q.

Additional improvements are required to alleviate the problems of voltage unbalance. The PLL system can be designed to filter out the negative sequence producing a clean synchronisation signal. During conditions of grid voltage unbalance, negative sequence voltage can introduce double frequency oscillations on θ_e. If the three-phase PLL system is not designed to be robust to asymmetrical grid voltage, second-harmonic oscillations will appear in the phase angle signal and therefore in the current reference [90]. Low pass or band stop filters tuned to 100Hz at the output of the PLL can can eliminate the double frequency oscillations on θ_e and as a consequence the three-phase *dq* PLL structure can estimate the phase angle of the positive sequence of the grid voltages.

6.5 Switching Patterns

Switching patterns are required for the operation of both the rotor-side and grid-side converters. A general scheme is outlined, which can then be interpreted for both the rotor-side or grid-side converters. For each converter there are eight possible combinations of on and off states for the transistors. There are six transistors on each of the rotor-side and grid-side converter banks, observed in Figure 6.11.

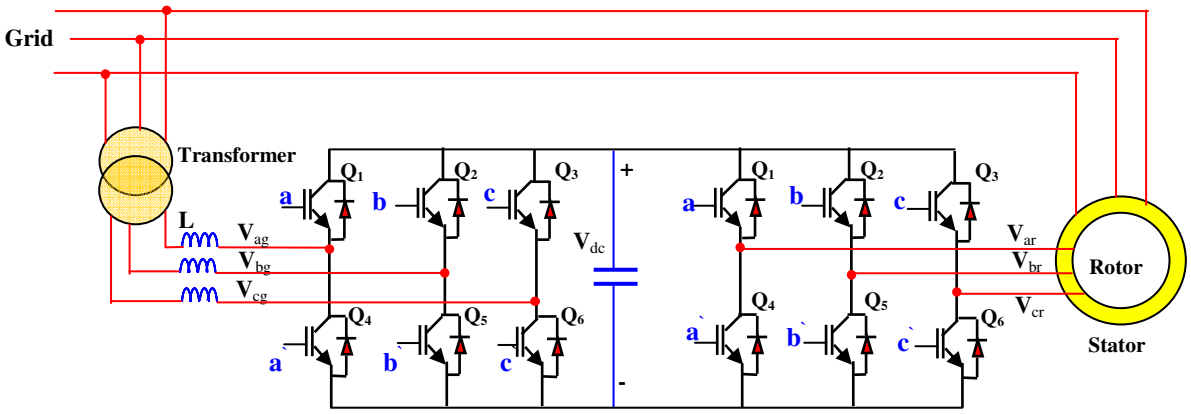

Figure 6.11 IGBT transistors on rotor side and grid side converters

With respect to the rotor-side converter when an upper IGBT of a leg is on (*a* or *b* or *c* = 1), the voltage V_{ar}, V_{br} or V_{cr} applied by the leg to the corresponding motor winding is the DC link voltage V_{dc}. When the switch is off (*a* or *b* or *c* = 0), the voltage applied to the windings is zero. The on and off switching of the upper IGBTs Q_1, Q_2 or Q_3 have eight possible combinations. Expressing V_{ar}, V_{br} or V_{cr} as functions of Q_1, Q_2 or Q_3, respectively:

$$\begin{aligned} V_{ar} &= Q_1 V_{dc} \\ V_{br} &= Q_2 V_{dc} \\ V_{cr} &= Q_3 V_{dc} \end{aligned} \tag{6.76}$$

A similar analysis holds true for the grid side converter with voltages (V_{ag}, V_{bg} or V_{cg}) substituted for (V_{ar}, V_{br} or V_{cr}).

If the Park transformation is applied to equation (6.76) in the two-phase stationary reference frame the following vector is obtained:

$$V_s = \frac{2}{3}\left(V_{ar} + V_{br} e^{j\frac{2}{3}\pi} + V_{cr} e^{j\frac{4}{3}\pi} \right) \tag{6.77}$$

Introducing the switching functions equation (6.76) into equation (6.77):

$$V_s = \frac{2}{3} V_{dc}\left(Q_1 + Q_2 e^{j\frac{2}{3}\pi} + Q_3 e^{j\frac{4}{3}\pi} \right) \tag{6.78}$$

Eight combinations of on and off states are possible for the upper power transistors, therefore eight combinations can be obtained for the derived output line-to-line voltages in terms of the DC-link voltage V_{dc}. Equations (6.79) and (6.80) establish the relationship between the dc voltage and the line and phase voltages [67], [69].

$$\begin{bmatrix} v_{ab} \\ v_{bc} \\ v_{ca} \end{bmatrix} = V_{dc} \begin{bmatrix} 1 & -1 & 0 \\ 0 & 1 & -1 \\ -1 & 0 & 1 \end{bmatrix} \begin{bmatrix} a \\ b \\ c \end{bmatrix} \tag{6.79}$$

$$\begin{bmatrix} v_{ar} \\ v_{br} \\ v_{cr} \end{bmatrix} = \frac{1}{3} V_{dc} \begin{bmatrix} 2 & -1 & -1 \\ -1 & 2 & -1 \\ -1 & -1 & 2 \end{bmatrix} \begin{bmatrix} a \\ b \\ c \end{bmatrix} \tag{6.80}$$

The switching patterns described in equations (6.79) and (6.80) are outlined in Table 6.2 [69].

Table 6 Switching patterns and output voltages of converter

Switching State	a	b	c	V_a	V_b	V_c	V_{ab}	V_{bc}	V_{ca}
S_0	0	0	0	0	0	0	0	0	0
S_1	1	0	0	2/3	-1/3	-1/3	1	0	-1
S_2	1	1	0	1/3	1/3	-2/3	0	1	-1
S_3	0	1	0	-1/3	2/3	-1/3	-1	1	0
S_4	0	1	1	-2/3	1/3	1/3	-1	0	1
S_5	0	0	1	-1/3	-1/3	2/3	0	-1	1
S_6	1	0	1	1/3	-2/3	1/3	1	-1	0
S_7	1	1	1	0	0	0	0	0	0

Three-phase rotor winding orientation in space is given by Figure 5.12 (Chapter 5). Six switching states S_1, S_2, S_3, S_4, S_5 and S_6 (Table 6) result in the voltage space vectors V_1, V_2, V_3, V_4, V_5 and V_6 at any instant in time observed in Figure 6.12 [106]. The switching states S_0 and S_7 are null states and give a zero output.

The space phasor plane is subdivided into six 60° sectors; sector 1 to sector 6. The eight vectors are called the basic space vectors. The magnitude and angular velocity of the rotor voltage is controlled by selecting a particular voltage vector depending on its

current location. The binary representation of two adjacent basic vectors is different in only one bit. For example only one of the upper IGBT's is switched on when the switching pattern switches from V_1 to V_1+60^0. Anti clockwise direction of rotation of the flux vectors is normally considered the positive direction and the rotor flux ψ_r will lead the stator flux ψ_s in super-synchronous mode of operation. This is illustrated in Figure 6.12.

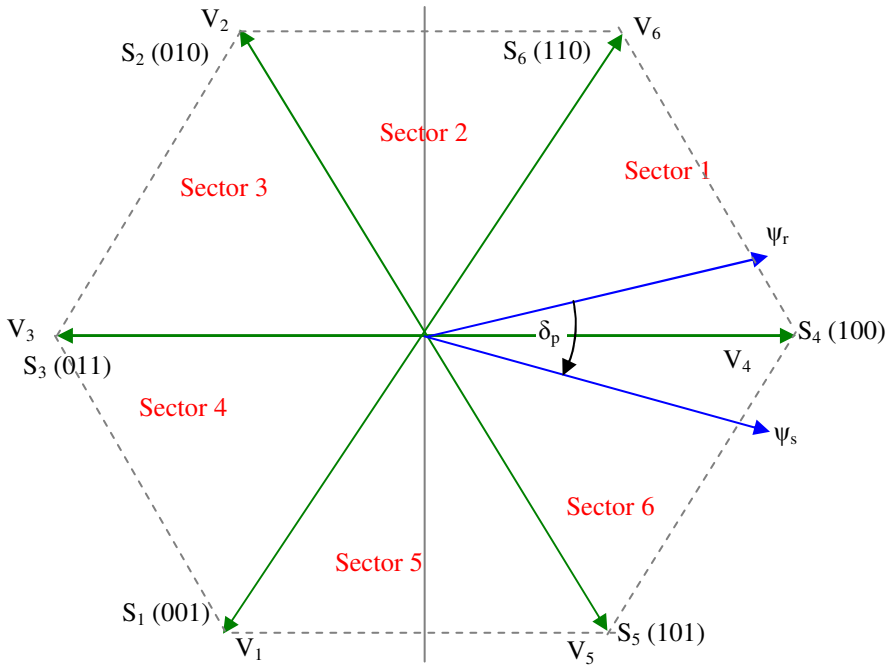

Figure 6.12 Voltage space vectors

If the rotor flux ψ_r is located in sector one, application of vectors V_2 and V_6 accelerates ψ_r in the positive direction. When in the generating mode of operation, application of vectors V_2 and V_6 result in an increase in angular separation between the fluxes ψ_r and ψ_s resulting in an increase in active power generated by the stator. Conversely the application of vectors V_1 and V_5 have the opposite effect and decrease the active power [106].

With reference to the phasor diagrams in Chapter 5 (Figures 5.25 and 5.26) repeated in Figure 6.13, active and reactive power can be controlled by i_{qs} and i_{ds} respectively. This

is achieved by controlling the rotor currents i_{qr} and i_{dr}. The variation in rotor flux with variations in the real and reactive power demand is shown in Figure 6.13. If for example i_{dr} is set to zero, reactive power is fed entirely from the stator side, Figure 6.13(a). In this condition if i_{qr} is varied from zero to full rated power, the locus of ψ_r varies along A-B, and ψ_r does not change appreciably.

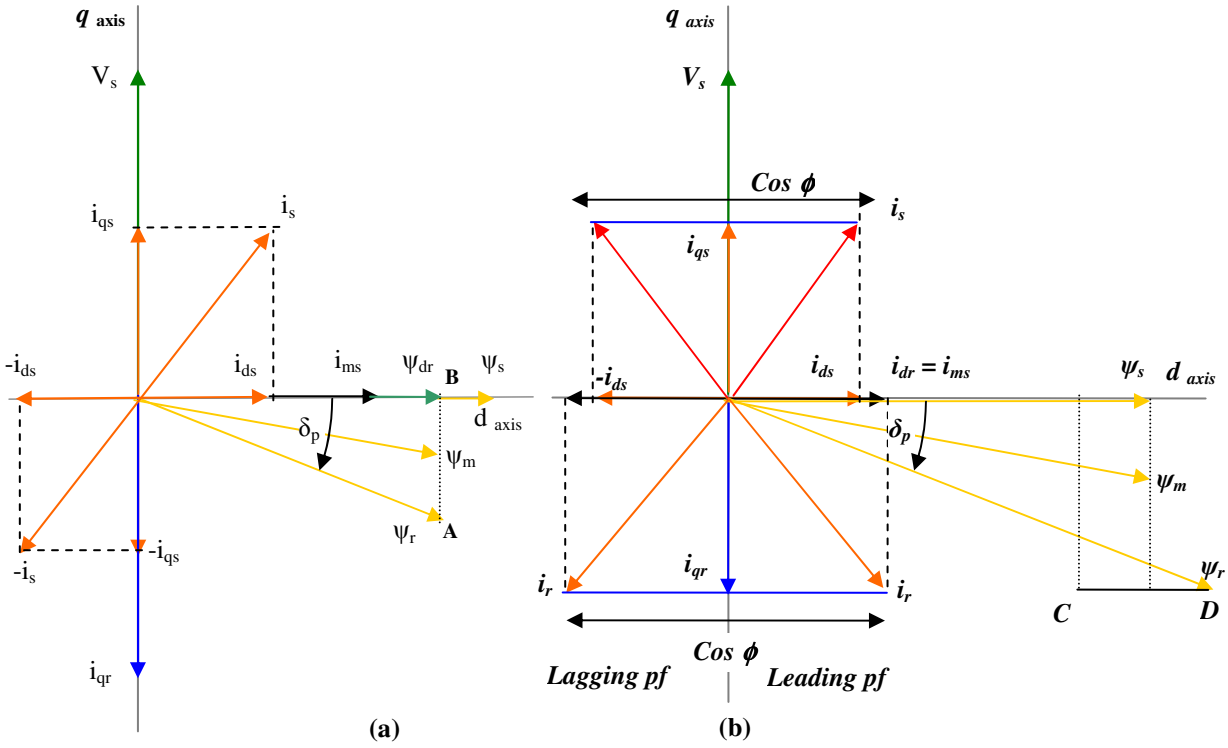

Figure 6.13 Phasor diagram active and reactive power control

In the phasor diagrams of Figure 6.13 (a) and Figure 6.13 (b), reactive power taken by the stator depends on the component of ψ_r that is along ψ_s i.e. ψ_{dr}. When the angle between ψ_s and ψ_r, (δ_p) is very small, the magnitude of ψ_r is approximately equal to ψ_{dr} [106]. Therefore when the rotor flux vector is located in Sector 1, (Figure 6.12) voltage vectors V_4, V_5 and V_6 increase the magnitude of ψ_r, and V_1, V_2 and V_3 reduce the magnitude. An increase in the magnitude of ψ_r increases the reactive power being fed from the rotor side, and therefore reduces the reactive power taken by the stator. This

improves the power factor. Conversely a decreases in the magnitude of ψ_r, has the effect of decreasing the stator power factor.

6.5.1 Voltage Space Vectors with d-q axis

Voltages can be represented in *dq* coordinates and represent the spatial vector sum of the three-phase voltage [69] as:

$$\begin{bmatrix} v_q \\ v_d \end{bmatrix} = \frac{2}{3}\begin{bmatrix} 1 & -\frac{1}{2} & -\frac{1}{2} \\ 0 & -\frac{\sqrt{3}}{2} & \frac{\sqrt{3}}{2} \end{bmatrix}\begin{bmatrix} v_a \\ v_b \\ v_c \end{bmatrix} \tag{6.81}$$

The voltages corresponding to the eight combinations of switching patterns can be mapped into the *dq* plane, shown in Table 7. This mapping results in six non-zero vectors, which form the axis of a hexagonal and two zero vectors located at the centre, illustrated in Figure 6.14.

Table 7 Switching patterns and output voltages of converter - *dq* axis

Switching State	a	b	c	V_q	V_d	V_{dq}
S_0	0	0	0	0	0	$V_0 = 0$
S_1	0	0	1	-1/3 V_{dc}	1/√3 V_{dc}	V_1= 2/3 V_{dc}
S_2	0	1	0	-1/3 V_{dc}	-1/√3 V_{dc}	V_2= 2/3 V_{dc}
S_3	0	1	1	-1/3 V_{dc}	0	V_3= 2/3 V_{dc}
S_4	1	0	0	2/3 V_{dc}	0	V_4= 2/3 V_{dc}
S_5	1	0	1	1/3 V_{dc}	1/√3 V_{dc}	V_5= 2/3 V_{dc}
S_6	1	1	0	1/3 V_{dc}	-1/√3 V_{dc}	V_6= 2/3 V_{dc}
S_7	1	1	1	0	0	$V_7 = 0$

The angle between any two adjacent non-zero vectors is 60°. The two zero vectors are positioned at the origin and apply zero voltage to the converter. The group of eight vectors are referred to as the basic space vectors and are denoted by V_o to V_7. The *d-q*

transformation can be applied to the reference a, b, and c voltages to obtain the reference V_{out} on the *d-q* plane as shown in Figure 6.14.

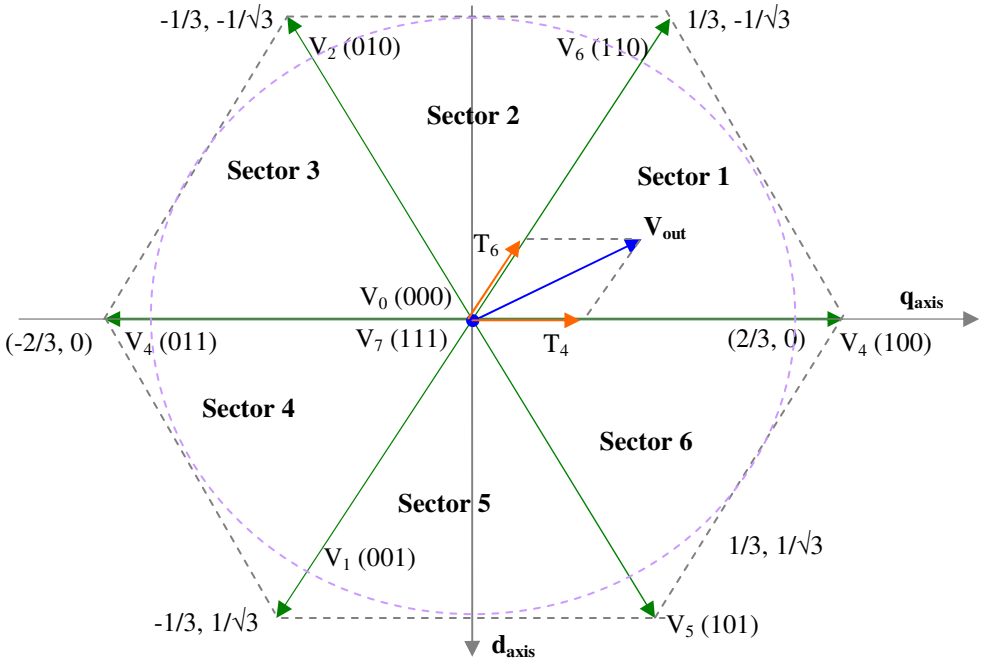

Figure 6.14 Voltage dq space vectors

The envelope of the hexagon formed by the basic space vectors Figure 6.14 is the locus of maximum V_{out}. This is a rotating vector and so the maximum is $(1/\sqrt{3})\ V_{dc}$ for V_{out}.

The objective of the space vector PWM technique is to approximate the reference voltage V_{out}, by a combination of the eight switching patterns. Each of the vectors V_1 – V_6 in Figure 6.14 represents the six voltage steps developed by the inverter with the zero voltages 000 and 111 located at the origin. Observing Figure 6.14 a space vector V_{out} located in the sector defined by V_4 and V_6 can be approximated by applying V_4 for a time period (T_4), and V_6 for a time period (T_6), such that:

$$T_4.V_4 + T_6.V_6 = T_{PWM}\,V_{out} \tag{6.82}$$

$$\frac{1}{T}\int_{nT}^{(n+1)T} V_{out}\,dt = \frac{1}{T}(T_4V_4 + T_6V_6) \tag{6.83}$$

where: n = 1,2,..6 and $T_4 + T_6 \leq T$

If $T = T_{PWM}$, can obtain [69]:

$$\int_{nT_{PWM}}^{(n+1)T_{PWM}} V_{out}\,dt = T_{PWM}\,V_{out} = (T_4V_4 + T_6V_6) \qquad (6.84)$$

where: n = 1,2,..6, and $T_4 + T_6 \leq T_{PWM}$

In equation (6.84) the required reference voltage V_{out} can be approximated by a switching pattern of V_4 for a period of time T_4 and V_6 for a period of time T_6. The sum of T_4 and T_6 can be less or equal to T_{PWM}. If it is less a zero (000) V_0 is required i.e. all inverter switches are tied to the zero rail or (111) V_7, all switches tied to the positive rail for the remainder of the period. This is illustrated in Figure 6.15.

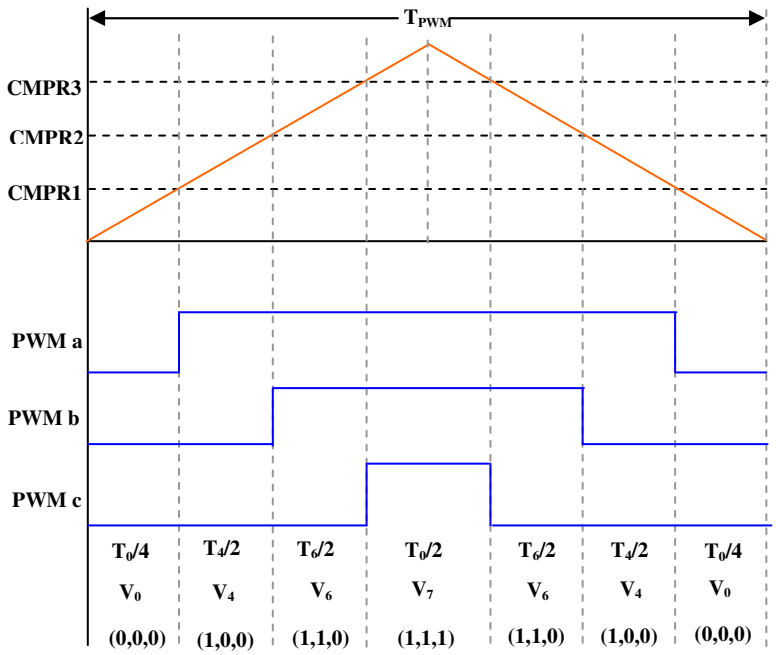

Figure 6.15 Symmetric space vector PWM waveform

Therefore equation (6.84) is modified as:

$$T_{PWM}\,V_{out} = T_4V_4 + T_6V_6 + T_0(V_0 \text{ or } V_7) \qquad (6.85)$$

where: $T_4 + T_6 + T_0 = T_{PWM}$

Figure 6.16 is an example of a symmetric space vector PWM waveform with reference V_{out} in Sector 1 bordered by vectors V_4 and V_6 [69]. Included in Figure 6.16 are the zero and non-zero vectors for each PWM period in a symmetric switching scheme.

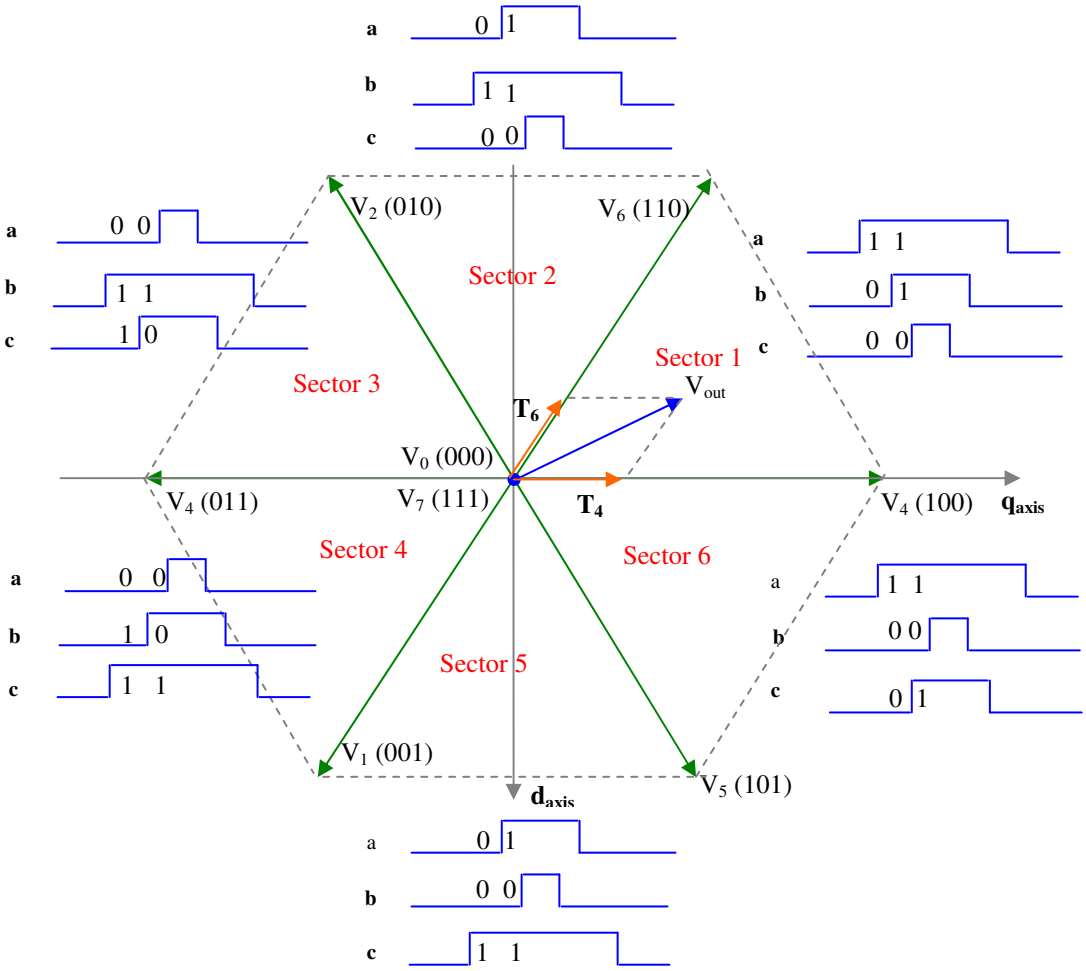

Figure 6.16 Voltage dq space vectors

6.6 Modelling in Simulink/Matlab.

Development of wind turbine models is advantageous in studies of power systems. To determine the performance of wind turbines under various operating and control strategies simulation models are an important part of the analysis. For example the behaviour of and effects of wind turbines to power quality issues on the grid can be

studied using simulation models in the more common software packages of PSCAD/EMTDC, PSS/E, Simpow, DigSilent, Matlab/Simulink, VisSim [69], [70]. Matlab/Simulink Power System Blockset was chosen because it provides a powerful graphical platform to investigate a range of complicated issues in electrical systems such as transients, unbalanced networks, harmonics etc.

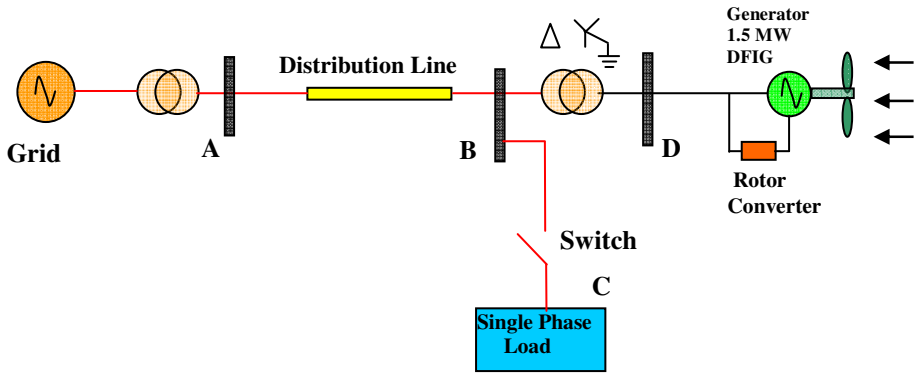

Figure 6.17 DFIG and network model

The simple network model in Figure 6.17 was developed and implemented in Matlab/Simulink [61]. In the model of Figure 6.17 a single-phase load is supplied at bus B through a switch. This single-phase load (when connected) decreases the voltage magnitude of phase C. The other two phase voltages remain at rated voltage magnitude and thus a magnitude voltage unbalance is introduced at bus B. Voltage unbalance is expressed as the ratio of the negative sequence voltage to the positive sequence voltage [4].

Control schemes for the DFIG as outlined in Sections 6.2 and 6.3 are implemented in the grid-connected wind turbine model in Matlab/Simulink. The control blocks designed in Matlab/Simulink incorporate the mathematical equations described in this chapter; these blocks include PI control, PLL bocks, reference frames, Clarke and Park models, space vector control and PWM. Vector-control schemes are designed respectively for the rotor-side and grid-side PWM voltage source converters.

6.7 Results

6.7.1 Voltage and Current Distortion

Problems associated with the response of a DFIG to network voltage unbalance are analysed using simulations in Matlab/Simulink and results can be observed in Figures (6.18-6.31). The Simulink model when simulated took approximately 0.2 seconds to settle to steady-state values, so timed delay switching requirements in the model were initiated with a time delay in excess of 0.2 seconds. To observe the effects of network voltage unbalance on the DFIG model, it was necessary to introduce voltage unbalance to the three line voltages close to the terminal connections of the DFIG. To achieve this a single-phase load was inserted between the distribution line and the distribution transformer (Figure 6.17). A timed switch in the Simulink model connected the single-phase load and initiated the required level of voltage unbalance at the DFIG terminals.

The network to which the DFIG is connected is represented by a constant voltage and a distribution line with a length of 30 km. The line series resistance is 0.115 Ω/km and the reactance is 0.33 Ω/km. The distribution line is operated at a voltage of 25kV. The fault level at bus A in Figure 6.17 is 30 MVA. The DFIG is connected via a 25kV/690V three-phase transformer. The generator rotor is connected to the grid side via a rotor converter, a DC bus (1.2 kV) and a grid side converter. The DFIG model has a total rating of 1.5 MVA and for a speed variation of 30% the rotor converter has a rating 30% of the capacity of the induction genertor.

A single-phase load (C in Figure 6.17) was timed to switch-in at 0.3 seconds. Initially the effect of the voltage unbalance on the stator of the generator is considered. During network asymmetrical voltage conditions a negative phase sequence component occurs.

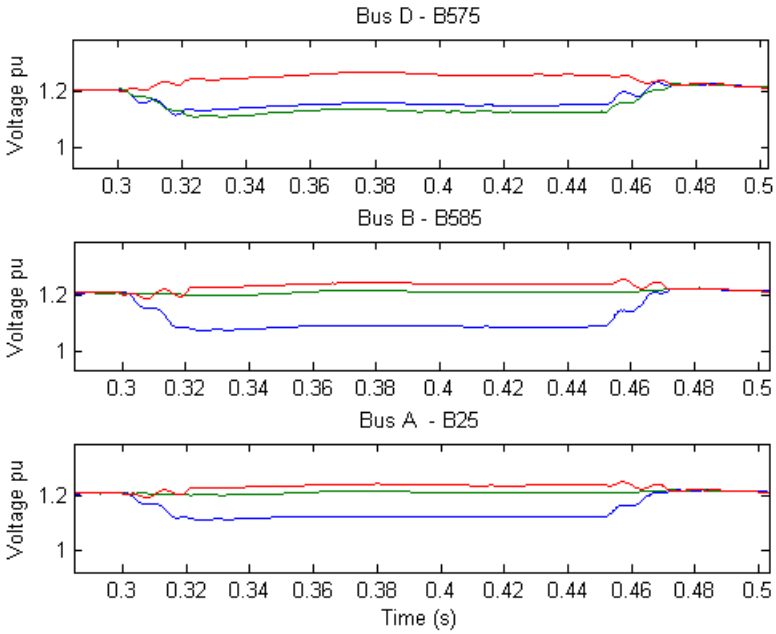

Figure 6.18 Voltage profile of network busses

The effects on bus voltages on the introduction of a large single-phase load into the network in Figure 6.17 at bus B can be observed in Figure 6.18. A noticeable observation is the voltage profile at bus D is different to the voltage profiles at buses A and B. The reason for the difference in the voltage profile at bus D is due to the influence the star-delta transformer (between busses B and D in Figure 6.17) has on voltage dips and voltage unbalance as outlined in Chapter 4, Section 4.15.

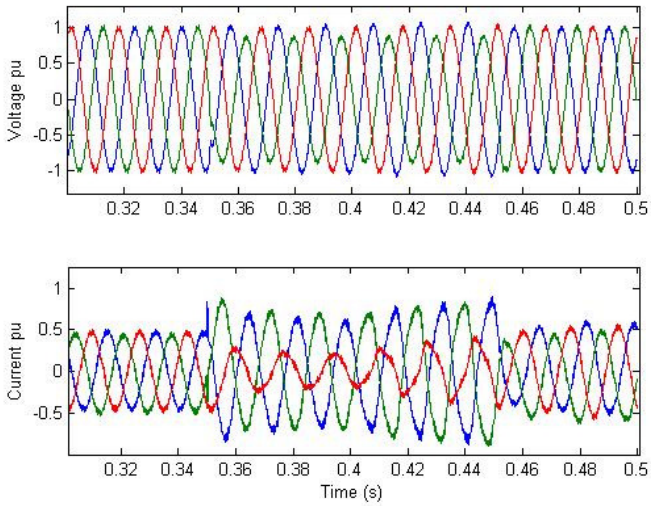

Figure 6.19 DFIG Stator Voltage and Current

Figure 6.19 shows the instantaneous voltage and generated current at the terminals of the DFIG predicted by the Matlab/Simulink simulation [104], [105]. The single-phase load is switched-in at 0.35 seconds and introduces a voltage unbalance factor of 9%. The DFIG stator current is significantly distorted at 0.35 seconds.

Figure 6.20 is a plot of the voltage unbalance factor (VUF) and current unbalance factor (CUF) at the terminals of the DFIG. The network VUF rises to a value of 9% as measured at the terminals of the DFIG.

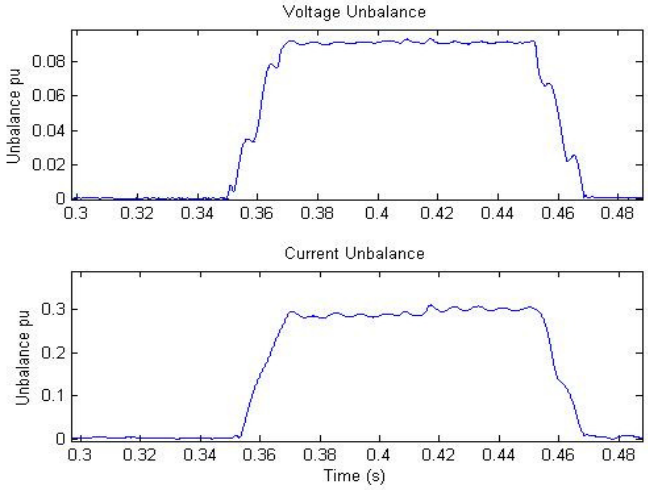

Figure 6.20 Percentage voltage and current unbalance at DFIG terminals

Although the VUF is approximately 9%, the corresponding CUF is 30%, as shown in Figure 6.20. Described in [1], this is because the negative sequence impedance of an induction generator is considerably lower than the positive sequence impedance at normal operating slip speeds, resulting in larger stator currents (Chapter 4, Section 4.4).

Investigations into voltage unbalance and voltage dip conditions in a variable speed drive incorporating a PWM converter was evaluated in [37]. Some of the conclusions reached by the authors are that current unbalance can be up to 100% for an input voltage unbalance of only 5%. The stator and rotor currents of the DFIG model simulated in Simulink are illustrated in Figure 6.21 [104].

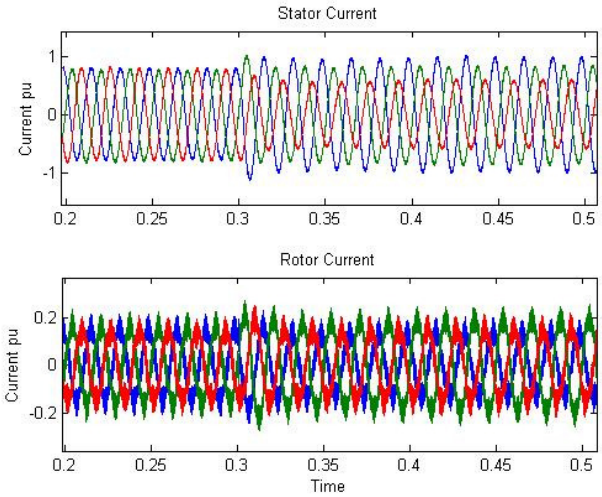

Figure 6.21 DFIG stator and rotor currents

During network voltage unbalance conditions a negative phase voltage sequence occurs, resulting in power and torque oscillations. The product of positive and negative sequence components of voltage and current generate a double frequency (100 Hz) power ripple, causing DC-link voltage and current ripple [36], [103].

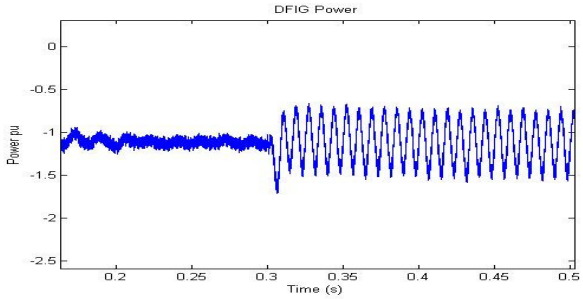

Figure 6.22 DFIG Power

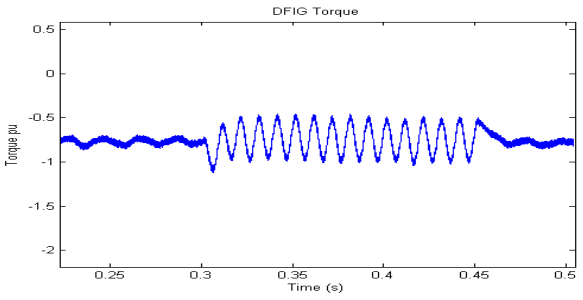

Figure 6.23 DFIG Torque

Figures 6.22 and 6.23 show the results of the Matlab/Simulink simulation on a 1.5 MW DFIG with network voltage unbalance occurring at 0.3 seconds. Power and torque

pulsations are observed due to network voltage unbalance of 9%. Figure 6.24 is a plot of the DC-link voltage pulsations in the converter of a DFIG due to the same level of voltage unbalance.

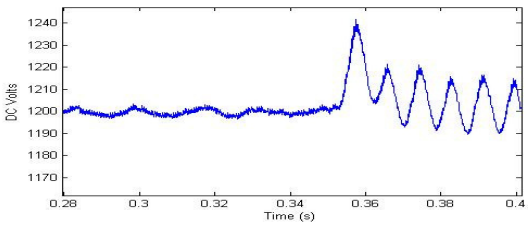

Figure 6.24 DFIG DC link voltage, V_{dc}

The Matlab/Simulink model used in the simulation is controlled in the *d-q* reference frame with the d-axis aligned with the stator voltage vector (SVO). Under the influence of voltage unbalance the stator i_d and i_q currents will oscillate at twice the network frequency [36], [104] shown in Figure 6.25. This result is similar to that discussed in Chapter 4, Section 4.7.

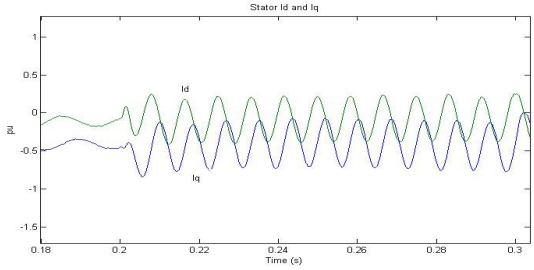

Figure 6.25 Stator i_d and i_q currents

By using a band-pass filter to isolate $\tilde{i}_d$ and $\tilde{i}_q$ (where $\tilde{i}_d$ and $\tilde{i}_q$ are the double frequency terms produced by the network voltage unbalance), the voltage unbalance factor can be obtained as [104]:

$$\text{VUF} = \sqrt{\tilde{i}_d^{\,2} + \tilde{i}_q^{\,2}} \qquad (6.86)$$

A comparison of VUF's obtained using stator symmetrical components and equation (6.86) is shown in Figure 6.26. It can be observed that both methods produce a voltage unbalance measurement of approximately 9%.

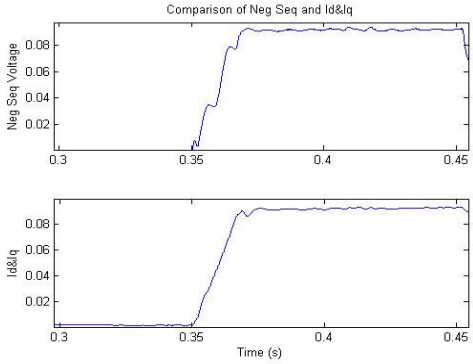

Figure 6.26 Voltage unbalance factor

The variation in speed of a DFIG during voltage unbalance conditions is illustrated in Figure 6.27.

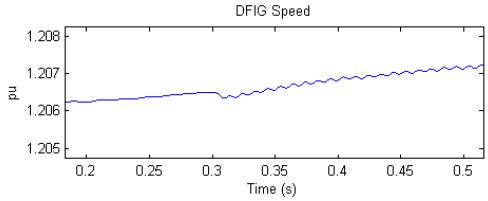

Figure 6.27 DFIG Speed

6.7.2 Third Harmonic Voltage and Current Distortion

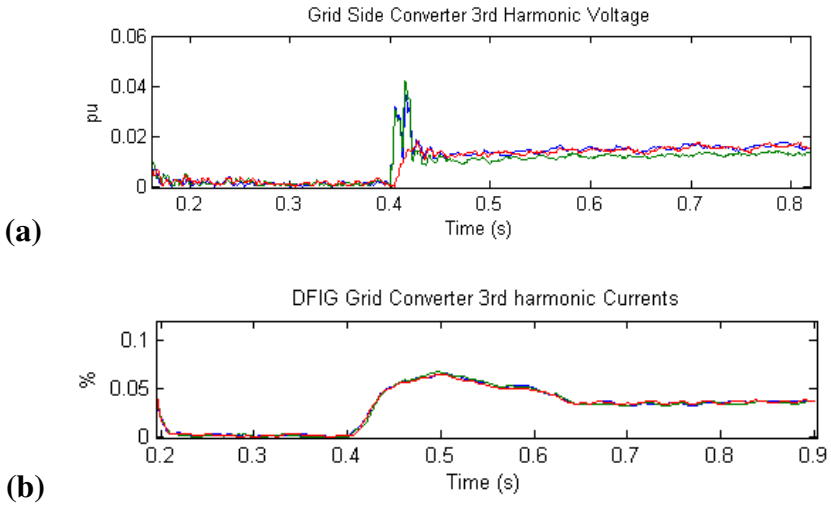

Figure 6.28 Grid-side converter ac side input third harmonic voltages (a) and third harmonic currents (b) – Subsynchronous mode of operation.

The level of third harmonic voltage and current at the ac side of the grid-side converter when a network voltage unbalance of 7.5% is introduced at 0.4 seconds is illustrated in Figure 6.28. In Figure 6.28(a) the 3rd harmonic voltage rises to 1.8 %, and in Figure 6.28(b) the 3rd harmonic currents rise to a steady state level of 4%.

Third-harmonic voltages and currents at the DFIG stator terminals are plotted in Figure 6.29. At the onset of Voltage unbalance at 0.4 seconds stator 3rd harmonic voltage rises to 2% and stator third harmonic currents after an initial increase in value return to the prefault value close to zero.

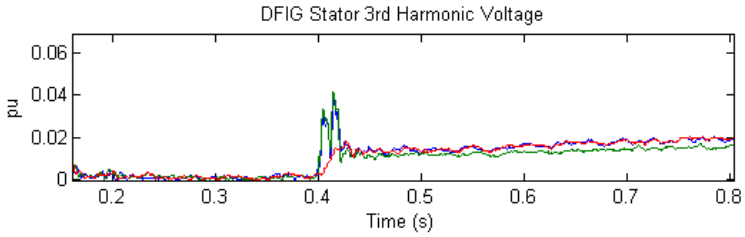

(a) Stator third-harmonic voltages – full power super-synchronous operation

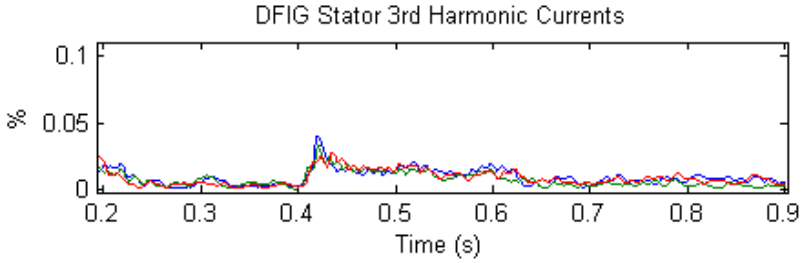

(b) Stator third-harmonic currents – full power, super-synchronous operation

Figure 6.29 DFIG stator third harmonic voltages and currents

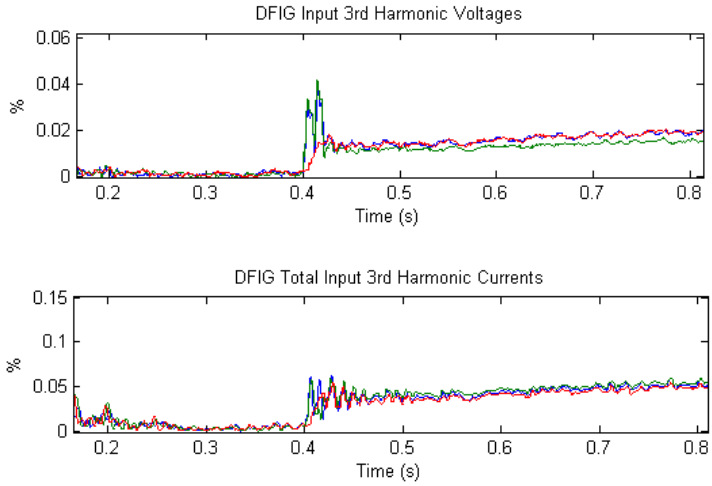

Figure 6.30 DFIG Total Input 3rd harmonic voltages and currents – full power

The third-harmonic voltages and currents measured at the DFIG terminals (i.e. total input to stator and grid converter) are plotted in Figure 6.30 [116]. Voltage unbalance in the model Figure 6.17, was introduced at 0.4 seconds, and the stator voltage 3rd

harmonic rises to 2% and the third harmonic currents rise to 5%. Observing the voltage and current traces in Figures 6.28-6.30, they indicate that when the DFIG is operating in super-synchronous mode, the grid-side converter has a greater influence on the level of generated third harmonic currents.

Figure 6.31 is a plot of the THD of the voltage and currents measured at the terminals of the DFIG. It is evident that when voltage unbalance is introduced at 0.4 seconds the THD of the voltage at input to the DFIG increases from 2% to 2.4%. However the THD of the current has a larger percentage increase, from 7% to 14%.

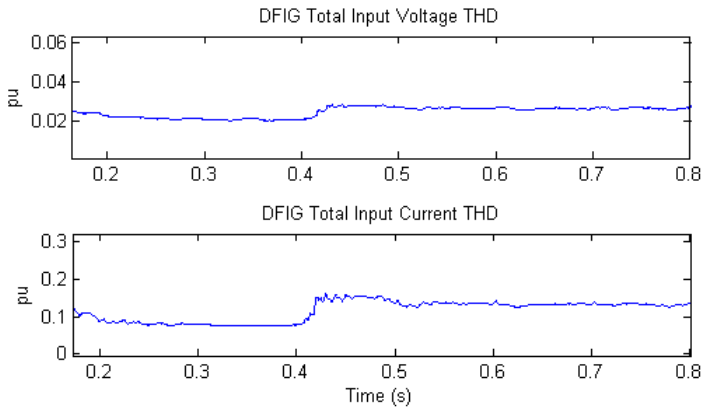

Figure 6.31 DFIG terminal voltage THD and current THD – full power

6.6.2 Conclusions from simulation results

Results of simulations conducted with an asymmetrical grid supply identified key problem areas for grid connected DFIG's. The problems include:

- Rotor current unbalance and over current
- Stator current unbalance and over current
- Rotor speed deviation
- DC link voltage oscillations
- Power oscillations
- Torque pulsations
- Increase in harmonic current generation

Chapter 7 Voltage Unbalance Compensation Techniques

Issues associated with the operation of wind turbines and DFIG's connected to network grids and independent loads during asymmetric voltage conditions, has been investigated in ([24], [36], [56], [71], [95], [96], [97], [103], [107], [110], [111], [113], [117], [120], [121], [122], [123], [124], [125], [129], [130], [131], [132], [134], [135]). This list of previous published work provides the basis for this thesis.

Network voltage unbalance can lead to asymmetry within the DFIG system's three phase voltages [82]. Using sequence component theory, under network voltage unbalance conditions the three-phase voltages, currents and fluxes can be decomposed into positive, negative and zero sequence components as outlined in Chapter 4. The stator and rotor windings of a DFIG are usually connected in star; with the star point isolated, therefore normally there are no zero sequence components.

The vector control schemes employed in the models in Chapter 6 assumed balanced conditions at the terminals of the DFIG. The aforementioned control schemes cannot control the double frequency currents generated during grid voltage unbalance conditions, resulting in the problems outlined in Chapter 4, including unwanted power and torque oscillations. Compensation schemes for improving machine control, under both balanced and unbalanced conditions, make allowance for the sequence components in the control software in a number of ways. This has the advantage of requiring no hardware upgrade. The main disadvantage is in the increased computational requirements.

During network asymmetric voltage conditions there are two dominant frequency components present within the frequency spectrum of the rotor current. There is a

positive sequence component driven by the source voltage, and a negative sequence component as a result of negative sequence impedance of the generator [1].

Unbalanced faults introduce a negative sequence component to the stator voltages and consequently to the rotor currents due to the impedance of the induction machine. Methods to alleviate the problem of voltage unbalance have been investigated in the literature as indicated above. The main theme among many of the authors is essentially to extract and control the positive and negative sequence components in the controllers of the rotor side and grid side converters. Thus the following sections describe methods incorporating positive and negative sequence control structures implemented in the laboratory based test rig.

7.1 Control of DFIG Under Network Voltage Unbalance Conditions

If the voltage in a grid network system is unbalanced, and assuming there are no zero sequence components, the three-phase quantities, (voltages, currents and fluxes) can be described by using positive and negative sequence components described in Chapter 4, [71], [96].

In the stationary reference frame, α and β voltages, currents and fluxes can be decomposed into positive and negative sequence components as:

$$\begin{aligned} F_{\alpha\beta}(t) &= F_{\alpha\beta+}(t) + F_{\alpha\beta-}(t) \\ &= \left|F_{\alpha\beta+}\right|.e^{j(\omega_s t+\phi_+)} + \left|F_{\alpha\beta-}\right|.e^{-j(\omega_s t+\phi_-)} \\ &= \left(F_{\alpha+} + jF_{\beta+}\right).e^{j(\omega_s t+\phi_+)} + \left(F_{\alpha-} + jF_{\beta-}\right).e^{j(\omega_s t+\phi_-)} \end{aligned} \quad (7.1)$$

where subscripts + and – are positive and negative sequence components respectively and ϕ_+ and ϕ_- are the positive and negative sequence phase shifts.

The relationship between the positive and negative sequence components in the *dq* reference frames can be observed in stator flux oriented (SFO) reference frame Figure 7.1(a) or in stator voltage oriented (SVO) reference frame Figure 7.1(b).

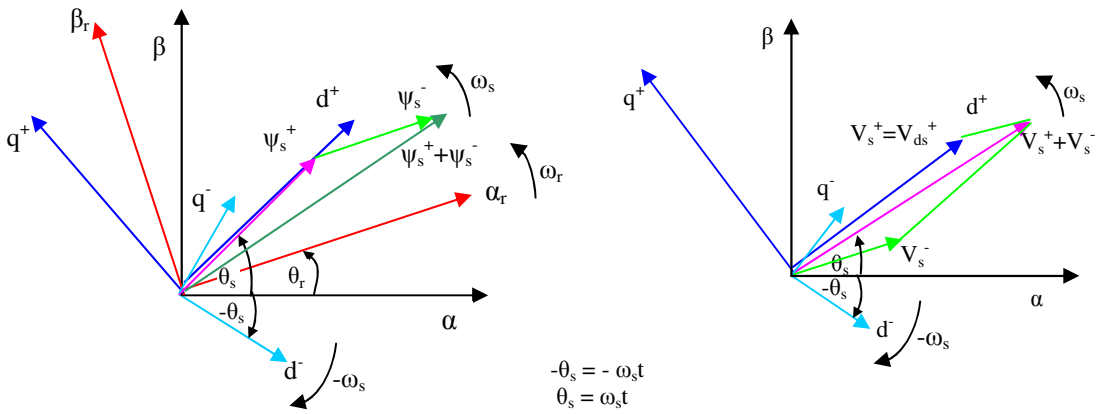

(a) Stator Flux Orientation SFO **(b) Stator VoltageOrientation SVO**

Figure 7.1 Reference frame orientation.

In Figure 7.1(a) stator flux orientation, the d^+ axis is fixed to the positive sequence stator flux rotating at a speed of ω_s, whereas for the negative sequence dq^- components the d^- axis is rotating at the speed of $-\omega_s$ with a phase angle to the α axis of $-\theta_s$. A similar analysis can be performed on Figure 7.1(b) in stator voltage orientation (SVO) (Chapter 5 section 5.3.3.1). Observing Figure 7.1 the transformation between $\alpha\beta$, dq^+ and dq^- reference frames is obtained as [71], [76], [96]:

$$F_{dq}^{+} = F_{\alpha\beta} e^{-j\omega_s t}, \qquad F_{dq}^{-} = F_{\alpha\beta} e^{j\omega_s t} \tag{7.2}$$

$$F_{dq}^{+} = F_{dq}^{-} e^{-2j\omega_s t}, \qquad F_{dq}^{-} = F_{dq}^{+} e^{2j\omega_s t} \tag{7.3}$$

where superscripts (+) and (–) represent the positive and negative sequence reference frames respectively.

The relationship between positive and negative sequence reference frames (Figure 7.1) and equations (7.1), (7.2) and (7.3), can be used to express the stator and rotor voltage, current and flux vectors using their respective positive and negative sequence components as [76], [95], [96]:

$$\left.\begin{aligned}
v^{+}_{dqs} &= v^{+}_{dqs+} + v^{+}_{dqs-} = v^{+}_{dqs+} + v^{-}_{dqs-}.e^{-2j\omega_s t} \\
i^{+}_{dqs} &= i^{+}_{dqs+} + i^{+}_{dqs-} = i^{+}_{dqs+} + i^{-}_{dqs-}.e^{-2j\omega_s t} \\
\psi^{+}_{dqs} &= \psi^{+}_{dqs+} + \psi^{+}_{dqs-} = \psi^{+}_{dqs+} + \psi^{-}_{dqs-}.e^{-2j\omega_s t} \\
v^{+}_{dqr} &= v^{+}_{dqr+} + v^{+}_{dqr-} = v^{+}_{dqr+} + v^{-}_{dqr-}.e^{-2j\omega_s t} \\
i^{+}_{dqr} &= i^{+}_{dqr+} + i^{+}_{dqr-} = i^{+}_{dqr+} + i^{-}_{dqr-}.e^{-2j\omega_s t} \\
\psi^{+}_{dqr} &= \psi^{+}_{dqr+} + \psi^{+}_{dqr-} = \psi^{+}_{dqr+} + \psi^{-}_{dqr-}.e^{-2j\omega_s t}
\end{aligned}\right\} \qquad (7.4)$$

where subscripts (+) and (-) represent positive and negative sequence components respectively.

The DFIG equivalent circuit, Figure 5.14 (Chapter 5) can be redrawn for both positive and negative sequence conditions in the synchronous reference frames as Figure 7.2 and Figure 7.3.

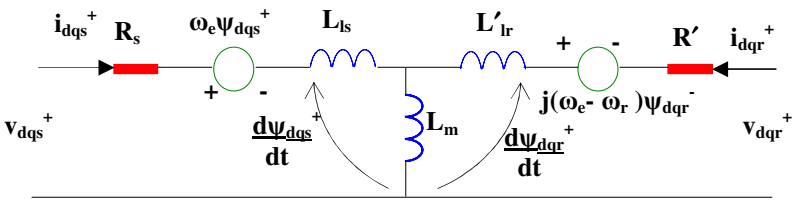

Figure 7.2 Positive sequence reference frame equivalent circuit

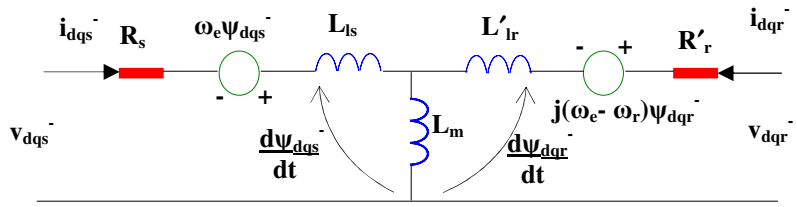

Figure 7.3 Negative sequence reference frame equivalent circuit

The dynamic model for a DFIG can be analysed in the positive and negative sequence reference frames. In the positive sequence representation of a DFIG rotating at a speed of ω_e (synchronous reference frame), the stator and rotor flux linkages can be given as:

$$\psi^+_{dqs} = L_s i^+_{dqs} + i^+_{dqr} L_m \tag{7.5}$$

$$\psi^+_{dqr} = L_r i^+_{dqr} + i^+_{dqs} L_m \tag{7.6}$$

Observing Figure 7.2 positive sequence stator and rotor voltage equations are [96]:

$$v^+_{dqs} = i^+_{dqs} R_s + \omega_e \psi^+_{dqs} + \frac{d\psi^+_{dqs}}{dt} \tag{7.7}$$

$$v^+_{dqr} = i^+_{dqr} R_r + (\omega_e - \omega_r)\psi^+_{dqr} + \frac{d\psi^+_{dqr}}{dt} \tag{7.8}$$

where:

$v_{dqs}{}^+$ are the stator positive sequence *d-q* voltages

$v_{dqr}{}^+$ are the rotor positive sequence *d-q* voltages

$i_{dqs}{}^+$ are the stator positive sequence *d-q* currents

$\psi_{dqr}{}^+$ are the rotor positive sequence *d-q* flux linkages

The stator and rotor positive sequence *dq* voltage equations in matrix form are:

$$\begin{bmatrix} v^+_{ds} \\ v^+_{qs} \end{bmatrix} = R_s \begin{bmatrix} i^+_{ds} \\ i^+_{qs} \end{bmatrix} + \frac{d}{dt}\begin{bmatrix} \psi^+_{ds} \\ \psi^+_{qs} \end{bmatrix} + j\omega_e \begin{bmatrix} 0 & -1 \\ 1 & 0 \end{bmatrix}\begin{bmatrix} \psi^+_{ds} \\ \psi^+_{qs} \end{bmatrix} \tag{7.9}$$

$$\begin{bmatrix} v^+_{dr} \\ v^+_{qr} \end{bmatrix} = R_r \begin{bmatrix} i^+_{dr} \\ i^+_{qr} \end{bmatrix} + \frac{d}{dt}\begin{bmatrix} \psi^+_{dr} \\ \psi^+_{qr} \end{bmatrix} + j\omega_e \begin{bmatrix} 0 & -1 \\ 1 & 0 \end{bmatrix}\begin{bmatrix} \psi^+_{dr} \\ \psi^+_{qr} \end{bmatrix} \tag{7.10}$$

Substituting equations (7.5) and (7.6) into equations (7.9) and (7.10) respectively yields:

$$\begin{bmatrix} v_{ds}^{+} \\ v_{qs}^{+} \end{bmatrix} = R_s \begin{bmatrix} i_{ds}^{+} \\ i_{qs}^{+} \end{bmatrix} + L_s \frac{d}{dt} \begin{bmatrix} i_{ds}^{+} \\ i_{qs}^{+} \end{bmatrix} + L_m \frac{d}{dt} \begin{bmatrix} i_{dr}^{+} \\ i_{qr}^{+} \end{bmatrix} + j\omega_e \begin{bmatrix} 0 & -1 \\ 1 & 0 \end{bmatrix} \begin{bmatrix} \psi_{ds}^{+} \\ \psi_{qs}^{+} \end{bmatrix} \quad (7.11)$$

$$\begin{bmatrix} v_{dr}^{+} \\ v_{qr}^{+} \end{bmatrix} = R_r \begin{bmatrix} i_{dr}^{+} \\ i_{qr}^{+} \end{bmatrix} + L_r \frac{d}{dt} \begin{bmatrix} i_{dr}^{+} \\ i_{qr}^{+} \end{bmatrix} + L_m \frac{d}{dt} \begin{bmatrix} i_{dS}^{+} \\ i_{qS}^{+} \end{bmatrix} + j\omega_e \begin{bmatrix} 0 & -1 \\ 1 & 0 \end{bmatrix} \begin{bmatrix} \psi_{dr}^{+} \\ \psi_{qr}^{+} \end{bmatrix} \quad (7.12)$$

The negative sequence stator and rotor *dq* fluxes in the synchronous reference frame (similar to equations (7.5) and (7.6) for positive sequence) are:

$$\psi_{dqs}^{-} = L_s i_{dqs}^{-} + i_{dqr}^{-} L_m \quad (7.13)$$

$$\psi_{dqr}^{-} = L_r i_{dqr}^{-} + i_{dqs}^{-} L_m \quad (7.14)$$

The negative sequence stator and rotor voltage equations can be described as [96]:

$$v_{dqs}^{-} = i_{dqs}^{-} R_s + \omega_e \psi_{dqs}^{-} + \frac{d\psi_{dqs}^{-}}{dt} \quad (7.15)$$

$$v_{dqr}^{-} = i_{dqr}^{-} R_r + (\omega_e - \omega_r) \psi_{dqr}^{-} + \frac{d\psi_{dqr}^{-}}{dt} \quad (7.16)$$

where: v_{dqs}^{-} are the stator negative sequence *d-q* voltages

v_{dqr}^{-} are the rotor negative sequence *d-q* voltages

i_{dqs}^{-} are the stator negative sequence *d-q* currents

ψ_{dqr}^{-} are the rotor negative sequence *d-q* flux linkages.

The stator and rotor negative sequence *dq* voltage equations in matrix form are:

$$\begin{bmatrix} v_{ds}^{-} \\ v_{qs}^{-} \end{bmatrix} = R_s \begin{bmatrix} i_{ds}^{-} \\ i_{qs}^{-} \end{bmatrix} + \frac{d}{dt} \begin{bmatrix} \psi_{ds}^{-} \\ \psi_{qs}^{-} \end{bmatrix} + j\omega_e \begin{bmatrix} 0 & -1 \\ 1 & 0 \end{bmatrix} \begin{bmatrix} \psi_{ds}^{-} \\ \psi_{qs}^{-} \end{bmatrix} \quad (7.17)$$

$$\begin{bmatrix} v_{dr}^{-} \\ v_{qr}^{-} \end{bmatrix} = R_r \begin{bmatrix} i_{dr}^{-} \\ i_{qr}^{-} \end{bmatrix} + \frac{d}{dt}\begin{bmatrix} \psi_{dr}^{-} \\ \psi_{qr}^{-} \end{bmatrix} + j\omega_e \begin{bmatrix} 0 & -1 \\ 1 & 0 \end{bmatrix}\begin{bmatrix} \psi_{dr}^{-} \\ \psi_{qr}^{-} \end{bmatrix} \qquad (7.18)$$

7.2 Control of Rotor Side Converter – Parallel Control Scheme

The function of the rotor-side converter controller in a DFIG is to control the active and reactive power [73] and is normally comprised of a parallel two stage controller with active and reactive powers controlled independently [75]. The controller can operate either in stator flux reference orientation (SFO) or stator voltage orientation (SVO). In the SFO reference frame the quadrature (q_{axis}) current signal controls active power and the direct (d_{axis}) current signal controls reactive power, whereas implementation in the SVO reference frame the d_{axis} current signal controls active power and the q_{axis} current signal controls reactive power. Decoupled control between the stator-side active and reactive powers can be obtained, providing the generator with a wide operating speed-range [65].

When the stator voltage is unbalanced it can still be regarded as constant [71], and differentiating the flux linkages will equal zero:

$$\frac{d\psi_{dqs+}^{+}}{dt} = 0 \quad and \quad \frac{d\psi_{dqs-}^{-}}{dt} = 0 \qquad (7.19)$$

If stator resistance is neglected, substituting equation (7.5) into equation (7.7) and taking into consideration equation (7.4):

$$V_{dqs}^{+} = j\omega_e \left(\psi_{dqs+}^{+} + \psi_{dqs-}^{-}.e^{-2j\omega_s t}\right)$$

$$= j\omega_e \left(L_s i_{dqs+}^{+} + L_m i_{dqr+}^{+}\right) + j\omega_e \left(L_s i_{dqs-}^{-} + L_m i_{dqr-}^{-}\right)e^{-2j\omega_s t} \qquad (7.20)$$

7.2.1 Stator Power Equations

In unbalanced networks DFIG stator apparent power can be expressed in terms of positive and negative sequence components [71], [76], [95]. Using developed equations for positive and negative sequence voltages and currents, apparent power of a DFIG can be determined, to observe the effects that grid voltage unbalance has on the system.

The stator power in the positive sequence reference frame is (equation (6.11) in Chapter 6):

$$S = P_s + jQ_s = -\frac{3}{2} v^{+}_{dqs} i^{+*}_{dqs} \tag{7.21}$$

Stator active and reactive powers can be described as:

$$P_s = \frac{3}{2} R_e\left(v^{+}_{dqs}.i^{+*}_{dqs}\right) \tag{7.22}$$

$$Q_s = \frac{3}{2} I_m\left(v^{+}_{dqs}.i^{+*}_{dqs}\right) \tag{7.23}$$

Manipulating equation (7.5) yields:

$$i^{+}_{dqs} = \frac{1}{L_s}\left(\psi^{+}_{dqs} - i^{+}_{dqr} L_m\right) \tag{7.24}$$

Inserting (7.4) into (7.24):

$$i^{+}_{dqs} = \frac{1}{L_s}\left(\psi^{+}_{dqs+} + \psi^{-}_{dqs-}.e^{-2j\omega_s t}\right) - \frac{L_m}{L_s}\left(i^{+}_{dqr+} + i^{-}_{dqr-}.e^{-2j\omega_s t}\right) \tag{7.25}$$

Substituting (7.4) for V_{dqs}^{+} and substituting (7.25) in (7.21) yields:

$$S = -\frac{3}{2L_s}.\begin{pmatrix}\left(v^{+}_{dqs+}+v^{-}_{dqs-}.e^{-j2\omega_e t}\right)\left(\psi^{+*}_{dqs+}+(\psi^{-}_{dqs-}.e^{-j2\omega_e t})^{*}\right)\\ -L_m.\left(v^{+}_{dqs+}+v^{-}_{dqs-}.e^{-j2\omega_e t}\right)\left(i^{+*}_{dqr+}+(i^{-}_{dqr-}.e^{-j2\omega_e t})^{*}\right)\end{pmatrix} \quad (7.26)$$

Multiplying the terms in (7.26) and then substituting the real and imaginary components for v^{+}_{dqs+}, v^{-}_{dqs-}, i^{+}_{dqs+}, i^{-}_{dqs-}, i^{+}_{dqr+}, i^{-}_{dq-}, ψ^{+}_{dqs+} and ψ^{-}_{dqs-} yields:

$$\begin{aligned}S = & -\frac{3}{2L_s}.\begin{Bmatrix}\left(v^{+}_{ds+}.\psi^{+}_{ds+}-v^{+}_{ds+}.j\psi^{+}_{qs+}+jv^{+}_{qs+}.\psi^{+}_{ds+}+v^{+}_{qs+}.\psi^{+}_{qs+}\right)\\ +\left(v^{+}_{ds+}.\psi^{-}_{ds-}-v^{+}_{ds+}.j\psi^{-}_{qs-}+jv^{+}_{qs+}.\psi^{-}_{ds-}+v^{+}_{qs+}.\psi^{-}_{qs-}\right)e^{j2\omega_e t}\\ +\left(v^{-}_{ds-}.\psi^{+}_{ds+}-jv^{-}_{ds-}.\psi^{+}_{qs+}+jv^{-}_{qs-}.\psi^{+}_{ds+}+v^{-}_{qs-}.\psi^{+}_{qs+}\right)e^{-j2\omega_e t}\\ +\left(v^{-}_{ds-}.\psi^{-}_{ds-}-v^{-}_{ds-}.j\psi^{-}_{qs-}+jv^{-}_{qs-}.\psi^{-}_{ds-}+v^{-}_{qs-}.\psi^{-}_{qs-}\right)\end{Bmatrix}\\ & +\frac{3L_m}{2L_s}.\begin{Bmatrix}\left(v^{+}_{ds+}.i^{+}_{dr+}-v^{+}_{ds+}.ji^{+}_{qr+}+jv^{+}_{qs+}.i^{+}_{dr+}+v^{+}_{qs+}.i^{+}_{qr+}\right)\\ +\left(v^{+}_{ds+}.i^{-}_{dr-}-v^{+}_{ds+}.ji^{-}_{qr-}+jv^{+}_{qs+}.i^{-}_{dr-}+v^{+}_{qs+}.i^{-}_{qr-}\right)e^{j2\omega_e t}\\ +\left(v^{-}_{ds-}.i^{+}_{dr+}-v^{-}_{ds-}.ji^{+}_{qr+}+jv^{-}_{qs-}.i^{+}_{dr+}+v^{-}_{qs-}.i^{+}_{qr+}\right)e^{-j2\omega_e t}\\ +\left(v^{-}_{ds-}.i^{-}_{dr-}-v^{-}_{ds-}.ji^{-}_{qr-}+jv^{-}_{qs-}.i^{-}_{dr-}+v^{-}_{qs-}.i^{-}_{qr-}\right)\end{Bmatrix}\end{aligned} \quad (7.27)$$

The terms for active and reactive power in equation (7.27) can be equated to equation (7.28) ([95], [96], [97], [107], [108]):

$$\begin{aligned}S = P+jQ = & \left(P_{s\_av}+P_{s\_\sin 2}\sin(2\omega_e t)+P_{s\_\cos 2}\cos(2\omega_e t)\right)\\ & +j\left(Q_{s\_av}+Q_{s\_\sin 2}\sin(2\omega_e t)+Q_{s\_\cos 2}\cos(2\omega_e t)\right)\end{aligned} \quad (7.28)$$

where $P_{s\text{-}av}$ can be described as the dc average value of the real power, and $P_{s\text{-}sin2}$, and $P_{s\text{-}cos2}$ the sine and cosine terms of instantaneous real power at double the network frequency.

Similarly $Q_{s\text{-}av}$ can be described as the dc average value of the instantaneous reactive power, and $Q_{s\text{-}sin2}$, and $Q_{s\text{-}cos2}$ the sine and cosine terms of reactive power at double the network frequency. The active and reactive powers can thus be described as:

$$\begin{bmatrix} P_{s\_av} \\ Q_{s\_av} \\ P_{s\_\sin 2} \\ P_{s\_\cos 2} \\ Q_{s\_\sin 2} \\ Q_{s\_\cos 2} \end{bmatrix} = -\frac{3}{2L_s} \begin{bmatrix} v_{ds+}^{+} & v_{qs+}^{+} & v_{ds-}^{-} & v_{qs-}^{-} \\ v_{qs+}^{+} & -v_{ds+}^{+} & v_{qs-}^{-} & -v_{ds-}^{-} \\ v_{qs-}^{-} & -v_{ds-}^{-} & -v_{qs+}^{+} & v_{ds+}^{+} \\ v_{ds-}^{-} & v_{qs-}^{-} & v_{ds+}^{+} & v_{qs+}^{+} \\ -v_{ds-}^{-} & -v_{qs-}^{-} & v_{ds+}^{+} & v_{qs+}^{+} \\ v_{qs-}^{-} & -v_{ds-}^{-} & v_{qs+}^{+} & -v_{ds+}^{+} \end{bmatrix} \begin{bmatrix} \psi_{ds+}^{+} \\ \psi_{qs+}^{+} \\ \psi_{ds-}^{-} \\ \psi_{qs-}^{-} \end{bmatrix}$$

$$+\frac{3L_m}{2L_s} \begin{bmatrix} v_{ds+}^{+} & v_{qs+}^{+} & v_{ds-}^{-} & v_{qs-}^{-} \\ v_{qs+}^{+} & -v_{ds+}^{+} & v_{ds-}^{-} & -v_{qs-}^{-} \\ v_{qs-}^{-} & -v_{ds-}^{-} & -v_{qs+}^{+} & v_{ds+}^{+} \\ v_{ds-}^{-} & v_{qs-}^{-} & v_{ds+}^{+} & v_{qs+}^{+} \\ -v_{ds-}^{-} & -v_{qs-}^{-} & v_{ds+}^{+} & v_{qs+}^{+} \\ v_{qs-}^{-} & -v_{ds-}^{-} & v_{qs+}^{+} & v_{ds+}^{+} \end{bmatrix} \begin{bmatrix} i_{dr+}^{+} \\ i_{qr+}^{+} \\ i_{dr-}^{-} \\ i_{qr-}^{-} \end{bmatrix} \quad (7.29)$$

Transformation to synchronous coordinates implies that the variables will be dc quantities in the steady state. Observing equation (7.7) and neglecting the stator resistance, with $v_{dqs} = \omega_e . j\psi_{dqs}$ in steady state, equation (7.29) can be written as [76]:

$$\begin{bmatrix} P_{s\_av} \\ Q_{s\_av} \\ P_{s\_\sin 2} \\ P_{s\_\cos 2} \\ Q_{s\_\sin 2} \\ Q_{s\_\cos 2} \end{bmatrix} = -\frac{3}{2L_s\omega_e} \begin{bmatrix} v_{ds+}^{+} & -v_{qs+}^{+} & -v_{ds-}^{-} & v_{qs-}^{-} \\ v_{qs+}^{+} & v_{ds+}^{+} & -v_{qs-}^{-} & -v_{ds-}^{-} \\ v_{qs-}^{-} & v_{ds-}^{-} & v_{qs+}^{+} & v_{ds+}^{+} \\ v_{ds-}^{-} & -v_{qs-}^{-} & -v_{ds+}^{+} & v_{qs+}^{+} \\ -v_{ds-}^{-} & -v_{qs-}^{-} & v_{ds+}^{+} & v_{qs+}^{+} \\ v_{qs-}^{-} & -v_{ds-}^{-} & v_{qs+}^{+} & -v_{ds+}^{+} \end{bmatrix} \begin{bmatrix} v_{qs+}^{+} \\ v_{ds+}^{+} \\ v_{qs-}^{-} \\ v_{ds-}^{-} \end{bmatrix}$$

$$+\frac{3L_m}{2L_s} \begin{bmatrix} v_{ds+}^{+} & v_{qs+}^{+} & v_{ds-}^{-} & v_{qs-}^{-} \\ v_{qs+}^{+} & -v_{ds+}^{+} & v_{ds-}^{-} & -v_{qs-}^{-} \\ v_{qs-}^{-} & -v_{ds-}^{-} & -v_{qs+}^{+} & v_{ds+}^{+} \\ v_{ds-}^{-} & v_{qs-}^{-} & v_{ds+}^{+} & v_{qs+}^{+} \\ -v_{ds-}^{-} & -v_{qs-}^{-} & v_{ds+}^{+} & v_{qs+}^{+} \\ v_{qs-}^{-} & -v_{ds-}^{-} & v_{qs+}^{+} & v_{ds+}^{+} \end{bmatrix} \begin{bmatrix} i_{dr+}^{+} \\ i_{qr+}^{+} \\ i_{dr-}^{-} \\ i_{qr-}^{-} \end{bmatrix} \quad (7.30)$$

Equation (7.30) is a matrix of the real and reactive powers developed in the DFIG generator, including negative sequence components and oscillating terms as a result of

network voltage unbalance. To enable a reduction in the torque and power oscillations as a result of asymmetrical grid voltage, it is necessary to control the positive and negative sequence rotor currents i_{dr+}^{+}, i_{qr+}^{+}, i_{dr-}^{-} and i_{qr-}^{-} in equation (7.30). The terms for oscillating active powers $P_{s\text{-}sin2}$ and $P_{s\text{-}cos2}$ and for oscillating reactive powers $Q_{s\text{-}sin2}$ and $Q_{s\text{-}cos2}$ are required to go to zero. Thus:

$$P_{s\text{-}sin2} = P_{s\text{-}cos2} = Q_{s\text{-}sin2} = Q_{s\text{-}cos2} = 0. \qquad (7.31)$$

As expanded upon in Chapter 5, in *dq* coordinates the *d*-axis can be aligned with the positive sequence voltage vector or the positive sequence flux vector. When the positive sequence *d*-axis is aligned with the positive sequence voltage vector, the *q*-axis component V_{qs+}^{+} can be regarded as being equal to zero. Equation (7.31) can now be resolved to obtain the required reference currents to control the power oscillations as:

$$P_{s\_\sin 2} = -\frac{3}{2\omega_e L_s}\left(0 + v_{ds-}^{-}v_{ds+}^{+} + 0 + v_{ds+}^{+}v_{ds-}^{-}\right) + \frac{3L_m}{2L_s}\left(v_{qs-}^{-}i_{dr+}^{+} - v_{ds-}^{-}i_{qr+}^{+} + 0 + v_{ds+}^{+}i_{qr-}^{-}\right) = 0 \qquad (7.32)$$

Solving for i_{qr}^{-}:

$$i_{qr-}^{-} = \frac{2.v_{ds-}^{-}}{\omega_e L_m} + \frac{1}{V_{ds+}^{+}}\left(v_{ds-}^{-}i_{qr+}^{+} - v_{qs-}^{-}i_{dr+}^{+}\right) \qquad (7.33)$$

Similarly P_{s_cos2} can be solved as:

$$P_{s\_\cos 2} = -\frac{3}{2\omega_e L_s}\left(0 + v_{qs-}^{-}v_{ds+}^{+} + v_{ds+}^{+}v_{qs-}^{-} + 0\right) + \frac{3L_m}{2L_s}\left(v_{ds-}^{-}i_{dr+}^{+} - v_{qs-}^{-}i_{qr+}^{+} + v_{ds+}^{+}i_{dr-}^{-} + 0\right) = 0 \qquad (7.34)$$

Solving for i_{dr}^{-}:

$$i_{dr-}^{-} = \frac{2.v_{qs-}^{-}}{\omega_e L_m} - \frac{1}{v_{ds+}^{+}}\left(v_{ds-}^{-} i_{dr+}^{+} - v_{qs-}^{-} i_{qr+}^{+}\right) \quad (7.35)$$

The positive reference control current for the DFIG power is obtained as:

$$i_{dr+}^{+} = -\frac{P_{s\_av}\, 2L_s}{3L_m v_{ds+}^{+}} - \frac{1}{v_{ds+}^{+}\omega_e L_m}\left(\left(v_{ds+}^{+}\right)^2 + \left(v_{ds-}^{-}\right)^2 + \left(v_{qs-}^{-}\right)^2\right) + \frac{1}{v_{ds+}^{+}}\left(v_{ds-}^{-} i_{dr-}^{-} - v_{qs-}^{-} i_{qr-}^{-}\right) \quad (7.36)$$

The double frequency reactive sine and cosine compensation terms can be determined in a similar way for reactive powers.

7.2.2 DFIG Torque Equations

The electromechanical torque of a DFIG can be described as [76]:

$$T_e = \frac{3}{2}\left(\frac{p}{2}\right) Im\left(\psi_{dqs}^{+} . i_{dqs}^{+*}\right) \quad (7.37)$$

Substituting equation (7.24) into (7.37) yields:

$$T_e = \frac{3}{2L_s}\left(\frac{p}{2}\right) Im\left(\psi_{dqs}^{+} \psi_{dqs}^{+*} - \psi_{dqs}^{+}\, i_{dqr}^{+*} L_m\right) \quad (7.38)$$

Implementing equation (7.4) in (7.38) yields:

$$T_e = \frac{3}{2L_s}\left(\frac{p}{2}\right) Im. \begin{pmatrix} \left(\psi_{dqs+}^{+} + \psi_{dqs-}^{-} . e^{-j2\omega_e t}\right)\left(\psi_{dqs+}^{+*} + \left(\psi_{dqs-}^{-} . e^{-j2\omega_e t}\right)^*\right) \\ - L_m\left(\psi_{dqs+}^{+} + \psi_{qds-}^{-} . e^{-j2\omega_e t}\right)\left(i_{dqr+}^{+*} + (i_{dqr-}^{-} . e^{-j2\omega_e t})^*\right) \end{pmatrix} \quad (7.39)$$

Similar to the analysis of the apparent power in Section 7.2.1, multiplying the terms in brackets, and knowing $\psi^{+}_{dqs+} = \psi^{+}_{ds+} + j\psi^{+}_{qs+}$ equation (7.39) can be developed as:

$$T_e = -\frac{3L_m}{2L_s}\left(\frac{p}{2}\right).\begin{Bmatrix} -\psi^+_{qs+}.i^+_{dr+} + \psi^+_{ds+}.i^+_{qr+} - \psi^-_{ds-}.i^-_{qr-} + \psi^-_{qs-}.i^-_{dr-} \\ \left(-\psi^+_{ds+}.i^-_{qr-} + \psi^+_{qs+}.i^-_{dr-} - \psi^-_{ds-}.i^+_{qr+} + \psi^-_{qs-}.i^+_{dr+}\right)\cos(2\omega_e t) \\ \left(\psi^+_{ds+}.i^-_{dr-} + \psi^+_{qs+}.i^-_{qr-} - \psi^-_{ds-}.i^+_{dr+} - \psi^-_{qs-}.i^+_{qr+}\right)\sin(2\omega_e t) \end{Bmatrix} \quad (7.40)$$

Equation (7.40) can be equated to [71], [76]:

$$T_e \quad = \quad T_{e\_av} + T_{e\_sin}\sin(2\omega_e t) + T_{e\_cos}\cos(2\omega_e t) \quad (7.41)$$

where T_{e_av}, T_{e_sin}, and T_{e_cos} are:

$$\begin{bmatrix} T_{e\_av} \\ T_{e\_\sin} \\ T_{e\_\cos} \end{bmatrix} = \frac{-3L_m}{2.L_s}\left(\frac{p}{2}\right)\begin{bmatrix} -\psi^+_{qs+} & \psi^+_{ds+} & \psi^-_{qs-} & -\psi^-_{ds-} \\ -\psi^-_{ds-} & -\psi^-_{qs-} & \psi^+_{ds+} & \psi^+_{qs+} \\ \psi^-_{qs-} & -\psi^-_{ds-} & \psi^+_{qs+} & -\psi^+_{ds+} \end{bmatrix}\begin{bmatrix} i^+_{dr+} \\ i^+_{qr+} \\ i^-_{dr-} \\ i^-_{qr-} \end{bmatrix} \quad (7.42)$$

Using equations ((7.9) to (7.12), (7.15) and (7.16)) in the steady state and neglecting the stator resistance equation (7.42) can be rewritten as:

$$\begin{bmatrix} T_{e\_av} \\ T_{e\_\sin} \\ T_{e\_\cos} \end{bmatrix} = \frac{-3L_m}{2.L_s\omega_e}\left(\frac{p}{2}\right)\begin{bmatrix} -v^+_{ds+} & -v^+_{qs+} & v^-_{ds-} & -v^-_{qs-} \\ v^-_{qs-} & -v^-_{ds-} & v^+_{qs+} & -v^+_{ds+} \\ v^-_{ds-} & v^-_{qs-} & -v^+_{ds+} & -v^+_{qs+} \end{bmatrix}\begin{bmatrix} i^+_{dr+} \\ i^+_{qr+} \\ i^-_{dr-} \\ i^-_{qr-} \end{bmatrix} \quad (7.43)$$

To control the torque pulsations it is necessary to control $T_{e\_sin} = T_{e\_cos} = 0$ in equation (7.43). Considering that in SVO control, $V_{qs+}{}^+ = 0$, T_{e_sin} can be written as:

$$T_{e\_\sin} = \frac{-3L_m}{2.L_s\omega_e}\left(\frac{p}{2}\right)\left[v^-_{qs-}.i^+_{dr+} - v^-_{ds-}.i^+_{qr+} + 0 - v^+_{ds+}.i^-_{qr-}\right] = 0 \quad (7.44)$$

To obtain the reference negative sequence current required, it is necessary to extract i^-_{qr-} in (7.44) as:

$$i_{qr-}^{-} = \frac{1}{v_{ds+}^{+}} \left[v_{qs-}^{-} . i_{dr+}^{+} - v_{ds-}^{-} . i_{qr+}^{+} \right] \tag{7.45}$$

Similarly the reference current i^{-}_{qr-} can be obtained setting T_{e_cos} equal to zero as:

$$T_{e\_\cos} = \frac{-3L_m}{2.L_s \omega_e} \left(\frac{p}{2} \right) \left[v_{ds-}^{-} . i_{dr+}^{+} + v_{qs-}^{-} . i_{qr+}^{+} - v_{ds+}^{+} . i_{dr-}^{-} + 0 \right] = 0 \tag{7.46}$$

The reference current i^{-}_{dr-} is obtained as:

$$i_{dr-}^{-} = \frac{1}{v_{ds+}^{+}} \left[v_{ds-}^{-} . i_{dr+}^{+} + v_{qs-}^{-} . i_{qr+}^{+} \right] \tag{7.47}$$

The positive torque reference is obtained as:

$$i_{dr+}^{+} = \frac{T_{e\_av} 2L_s \omega_e}{v_{ds+}^{+} 3.L_m} \left(\frac{2}{p} \right) - \frac{1}{v_{ds+}^{+}} \left[v_{ds-}^{-} . i_{dr-}^{-} + v_{qs-}^{-} . i_{qr-}^{-} \right] \tag{7.48}$$

From (7.2) and (7.3), in the dq^{+} reference frame, positive sequence components appear as dc values while the negative sequence components oscillate at $2\omega_e$. Whereas in the negative dq^{-} reference frame negative sequence components appear as dc values while the positive sequence components oscillate at $2\omega_e$. Observing Figure 7.4, the stator voltages and currents and the rotor currents are converted to the $\alpha\beta$ reference frame. The stator voltages and currents are then transformed into the positive sequence dq^{+} and negative dq^{-} sequence reference frames using the voltage angle θ_e (Figure 7.1), obtained with a PLL. The PLL operates by controlling the q-axis component to zero and therefore all the voltage is manifested through the d-axis. The slip angle θ_{sl} is obtained to transform the rotor values to the positive and negative sequence rotor reference frames. Band-stop (notch) filters tuned at $2\omega_e$ are then implemented to remove the oscillating terms, thus obtaining the respective positive and negative sequence dq^{+}_{+} and dq^{-}_{-} components.

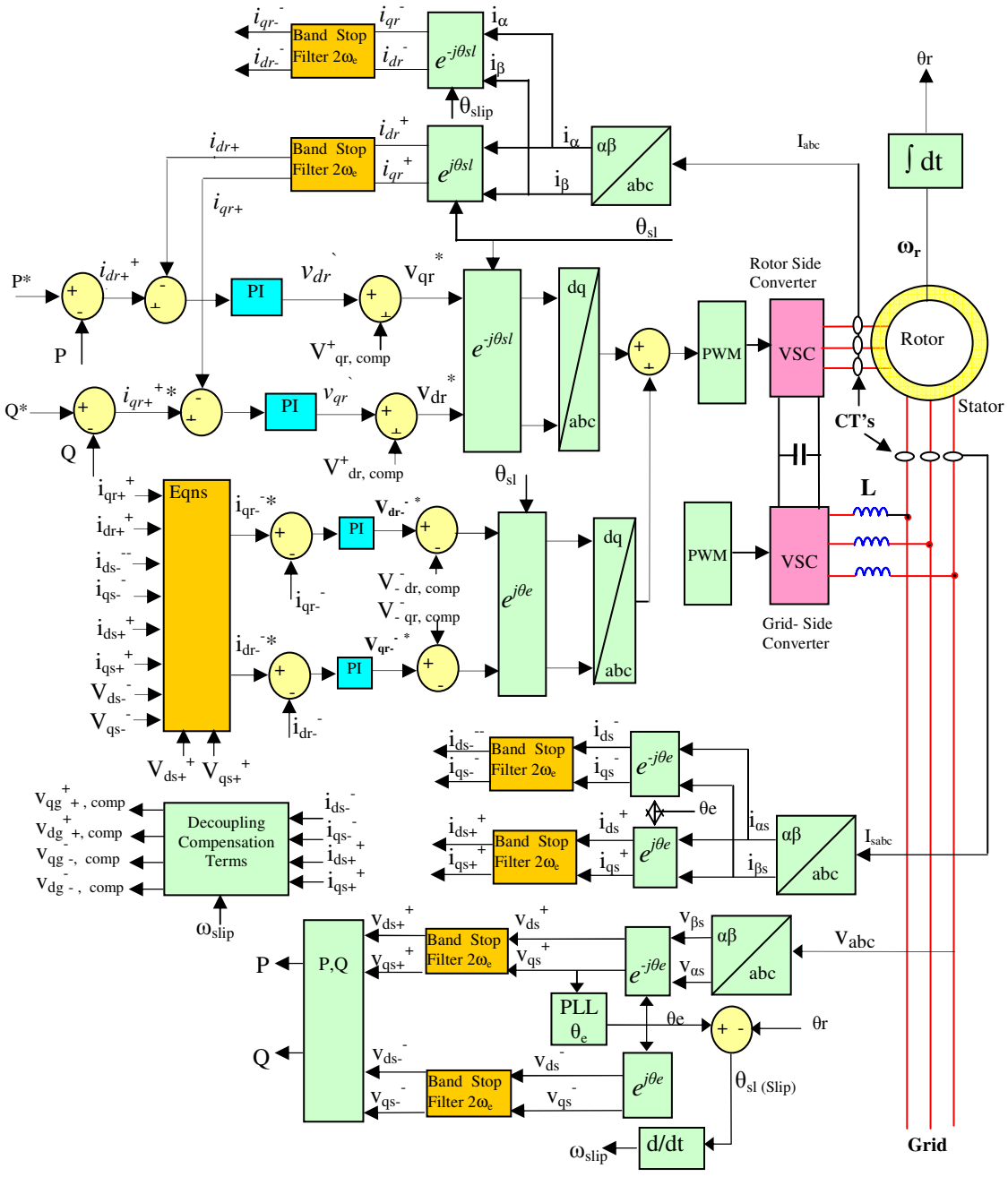

Figure 7.4 DFIG rotor side converter control including compensation scheme

The positive and negative sequence control voltages v_{dqs+}^{+} and v_{dqs-}^{-}, and the positive and negative sequence control currents i_{dqs+}^{+} and i_{dqs-}^{-} are thus obtained. Similarly the rotor currents are transformed into the positive sequence dq^{+} and negative dq^{-} sequence reference frames, using the slip angle θ_{sl}. The slip angle θ_{sl} is obtained by subtracting the grid angle θ_e form the actual rotor position angle θ_r. Band-stop (notch) filters tuned at

$2\omega_e$ are then used to remove the oscillating terms, thus obtaining the respective positive and negative sequence $i_{dqr}^{+}{}_{+}$ and $i_{dqr}^{-}{}_{-}$ control currents.

It is also necessary to incorporate positive and negative sequence components, $i_{dqs}^{+}{}_{+}$ and $i_{dqs}^{-}{}_{-}$ respectively to obtain the necessary decoupling terms, $V_{d\text{-}comp}$ and $V_{q\text{-}comp}$. The positive and negative sequence control components are regulated independently before being transformed into the positive sequence reference frame and then summed to form a reference for the PWM controller.

Figure 7.5 [105] illustrates the effect of the extraction process to obtain the negative sequence component from the negative sequence reference frame. Figure 7.5 (a) shows the rotor control current i_{dr}^{-} (in the negative sequence reference frame) after *dq* transformation and Figure 7.5 (b) is the negative sequence component i_{dr-}^{-} with the positive sequence component removed with a notch filter.

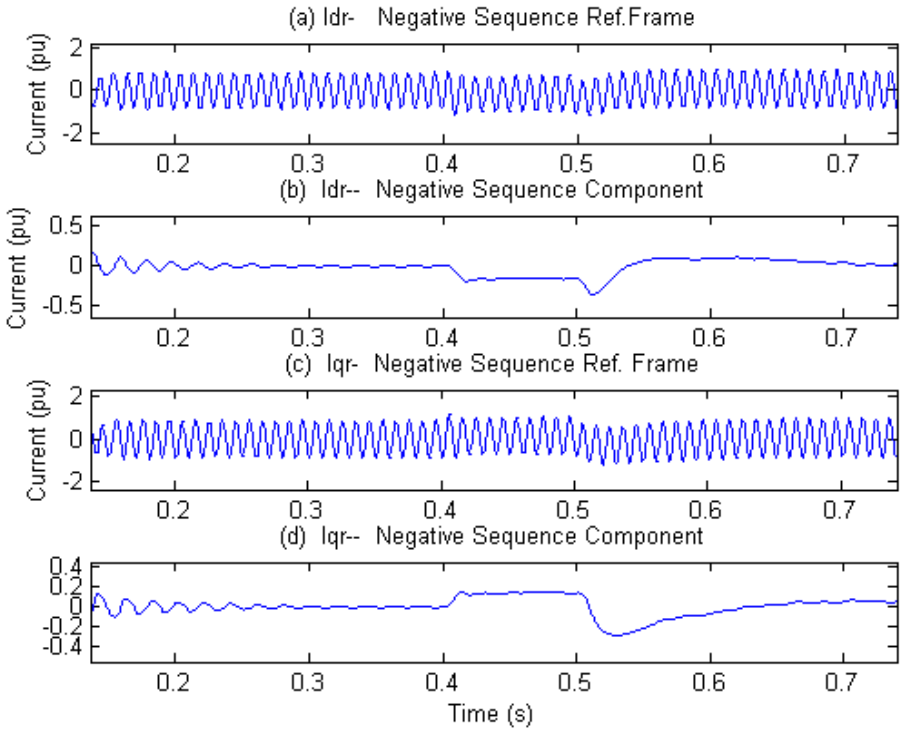

Figure 7.5 Negative sequence reference frames and components

Figures 7.5 (c) and (d) show a similar result for the rotor q-axis negative sequence reference frame i_{qr}^{-}, to obtain the negative sequence reference current I_{qr-}^{-}.

The stator power and torque pulsations in the DFIG are controlled using the control scheme as described in Figure 7.4, incorporating equations (7.33) and (7.35) to control stator power oscillations and incorporating equations (7.45) and (7.47) to control the torque pulsations. The scheme was implemented in the toolbox "SimpowerSystems" in Matlab/Simulink and the simple model and parameters are illustrated in Figure 6.21 (Chapter 6). Chapter 6, Section 6.7 illustrates the effects of network voltage unbalance on a DFIG predicted by Matlab/Simulink simulations. This model in Matlab/Simulink is also implemented here to demonstrate the efficacy of the compensation techniques in the rotor side converter described in this chapter.

The network is represented by a constant voltage source and a distribution line with a length of 30 km. The line series resistance is 0.115 Ω/km and the reactance is 0.33 Ω/km. The distribution line is operated at a voltage of 25kV, and the fault level at Bus A in Figure 6.21 is 30 MVA. The DFIG is connected via a 25kV/690V three-phase transformer. The generator rotor is connected to the grid via a rotor converter, a DC bus (1.2 kV), and a grid side converter. As shown in Figure 6.21 a single-phase load of 4 MVA is supplied at bus B, and this load introduces a three-phase voltage unbalance factor of 7% at Bus B.

It can be observed in Figure 7.6 [105] power oscillations developed as a result of grid voltage unbalance. The steady state power reference is set at (-1.0) pu, and as observed in Figure 7.6, when grid voltage unbalance is instigated, stator power oscillates at twice the network frequency (100 Hz), with peak values between -0.5 pu and -1.5 pu. The compensation control scheme was initiated through a timer and switched-in at 0.5 seconds, with the negative sequence currents controlled according to the requirement to

minimise power oscillations, i.e. the implementation of (7.33) and (7.35) in Figure 7.4. It can be observed that when the voltage unbalance compensation technique is switched in at 0.5 seconds the power oscillations are practically eliminated at 0.55 seconds. Although the voltage unbalance factor is approximately 7%, the accompanying negative sequence current unbalance factor is in the region of 28%, (Chapter 2, Section 2.8, and Chapter 6 Section 6.7). As described in [1] this is because the negative sequence impedance of an induction generator is considerably lower than the positive sequence impedance at normal operating slip speeds.

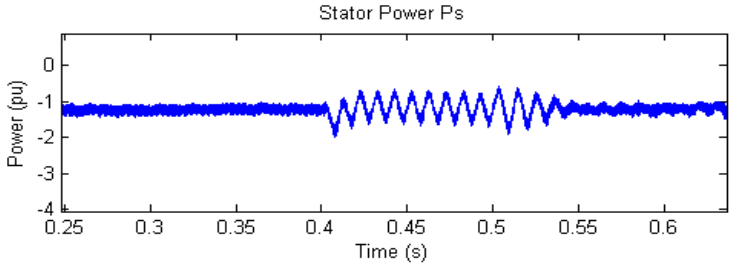

Figure 7.6 DFIG stator power

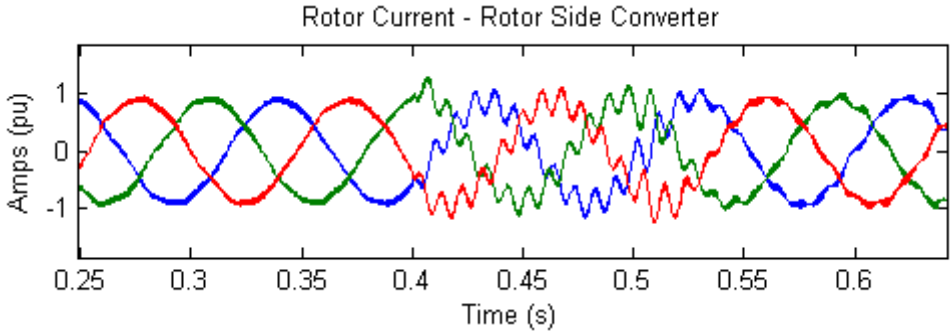

Figure 7.7 DFIG rotor side converter rotor currents

Figure 7.7 [105] shows the rotor currents measured at the rotor-side converter terminals. At time 0.4 seconds it can be observed that oscillations are superimposed on the rotor currents at slip frequency of 10 Hz (rotor speed – network frequency, (60Hz-50Hz = 10Hz)). Due to the negative sequence rotation, the induced oscillations have a

frequency of 110 Hz (60 Hz + 50 Hz). The compensation scheme is introduced at 0.5 seconds and the current profile is greatly improved with a good reduction in current oscillations at 0.55 seconds. The control currents I_{dr}^{+} and I_{qr}^{+} can be observed in Figure 7.8 [115].

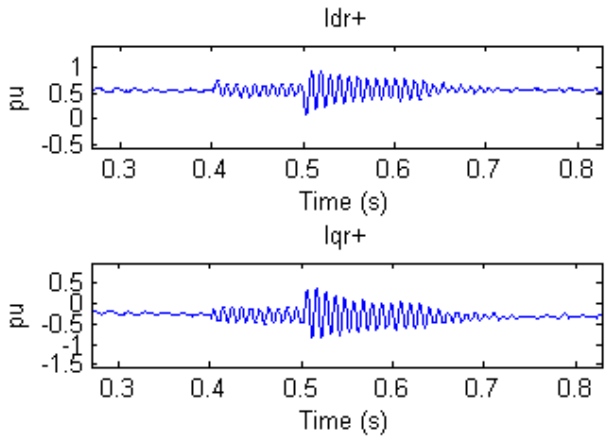

Figure 7.8 DFIG positive sequence rotor side control currents I_{dr} and I_{qr}

Torque pulsations can be controlled by implementing equations (7.45) and (7.47) in the control loop in Figure 7.4 [105]. When the negative sequence torque control scheme is applied, torque pulsations are reduced as shown in Figure 7.9.

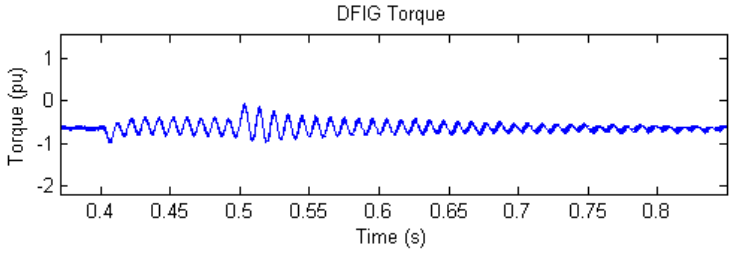

Figure 7.9 DFIG torque

7.3 Grid-Side Converter Compensation Techniques

Control of the grid-side converter is usually defined in the synchronous reference frame fixed to the grid voltage [73], [96], and is similar to that required for front end PWM converters. Voltage unbalance techniques have been investigated for PWM converters

[107], [108]. Rioual et al [41] derived voltage equations for both negative and positive-sequence components, and obtained positive and negative-sequence control commands to reduce the pulsations on the DC-link bus of a PWM rectifier.

Figure 6.8 is repeated here in Figure 7.10 to assist in developing equations to control the converter under the influence of network voltage unbalance.

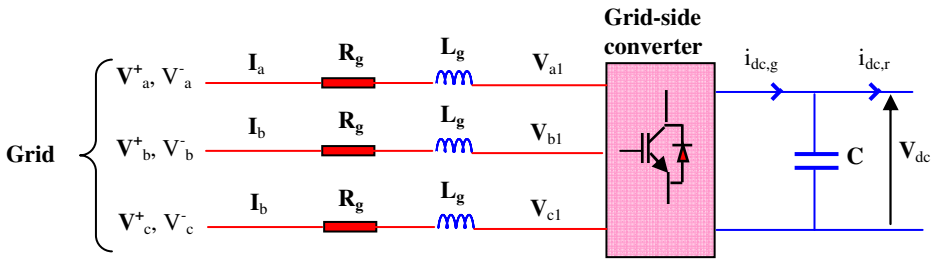

Figure 7.10 Grid-side converter schematic when network supply is unbalanced

Dq voltage equations can be obtained as outlined in Chapter 6 with the reference frame aligned with the grid voltage. Song et al [107] used two synchronous reference frames, obtaining the positive sequence components in the positive SRF (synchronous reference frame) by eliminating the negative sequence components with a notch filter tuned to double grid frequency. They also obtained negative sequence components in the negative sequence SRF by eliminating the positive sequence components with a notch filter tuned to twice grid frequency. Two parallel feedback *PI* (proportional-integral) controllers are incorporated to separately control the positive and negative signals for the space vector PWM converter. Grid-side decoupled vector control schemes are normally incorporated with quadrature axis current i_q implemented to control DC link voltage and direct axis current i_d controlling reactive power [75].

Equations 6.59 and 6.60 are repeated here in the synchronous grid reference frame as:

$$v_{dg}^{e} = i_{dg}^{e} R_g + L_g \frac{di_{dg}^{e}}{dt} - \omega_e L_g \, i_{qg}^{e} + v_{dg1}^{e} \tag{7.49}$$

$$v_{qg}^{e} = i_{qg}^{e} R_g + L_g \frac{di_{qg}^{e}}{dt} + \omega_e L_g \, i_{dg}^{e} + v_{qg1}^{e} \tag{7.50}$$

Under voltage unbalance conditions, not only are there positive sequence dq^+ components there is also negative sequence dq^- components. Equations (7.51)-(7.54) include positive and negative sequence components.

$$v_{dg+}^{+} = i_{dg+}^{+} R_g + L_g \frac{di_{dg+}^{+}}{dt} - \omega_e L_g \, i_{qg+}^{+} + v_{dg1+}^{+} \tag{7.51}$$

$$v_{qg+}^{+} = i_{qg+}^{+} R_g + L_g \frac{di_{qg+}^{+}}{dt} + \omega_e L_g \, i_{dg+}^{+} + v_{qg1+}^{+} \tag{7.52}$$

$$v_{dg-}^{-} = i_{dg-}^{-} R_g + L_g \frac{di_{dg-}^{-}}{dt} - \omega_e L_g \, i_{qg-}^{-} + v_{dg1-}^{-} \tag{7.53}$$

$$v_{qg-}^{-} = i_{qg-}^{-} R_g + L_g \frac{di_{qg-}^{-}}{dt} + \omega_e L_g \, i_{dg-}^{-} + v_{qg1-}^{-} \tag{7.54}$$

where (+) and (-) indicate positive and negative sequence components respectively.

Voltage equations (7.53)-(7.54) for the grid side converter now include negative sequence *dq* components. The effects of asymmetric grid voltage on the grid-side converter can be analysed by obtaining the apparent power of the converter using equations for positive and negative sequence voltages and currents. The grid-side converter apparent power can be described as [107], [108], [115]:

$$S = P_g + jQ_g = \frac{3}{2} v_{dqg}^{+} i_{dqg}^{+*} \tag{7.55}$$

Substituting equation (7.4) into (7.55) yields:

$$S = \frac{3}{2}.\left(\left(v^{+}_{dqg+} + v^{-}_{dqg-}.e^{-j2\omega_e t}\right).\left(i^{+*}_{dqg+} + (i^{-}_{dqg-}.e^{-j2\omega_e t})^{*}\right)\right) \quad (7.56)$$

Similar to the analysis of the rotor side converter, multiplying the terms in (7.56) and knowing $v^{+}_{dqs+} = v^{+}_{ds+} + jv^{+}_{qs+}$ equation (7.56) can be expanded as:

$$S = \frac{3}{2}\left\{\begin{array}{l} \left(v^{+}_{dg+}.i^{+}_{dg+} - jv^{+}_{dg+}.i^{+}_{qg+} + jv^{+}_{qg+}.i^{+}_{dg+} + v^{+}_{qg+}.i^{+}_{qg+}\right) \\ + \left(v^{+}_{dg+}.i^{-}_{dg-} - v^{+}_{dg+}.ji^{-}_{dg-} + jv^{+}_{qg+}.i^{-}_{dg-} + v^{+}_{qg+}.i^{-}_{qg-}\right)\cos 2\omega_e t \\ + \left(jv^{+}_{dg+}.i^{-}_{dg-} + v^{+}_{dg+}.i^{-}_{dg-} - v^{+}_{qg+}.i^{-}_{dg-} + jv^{+}_{qg+}.i^{-}_{qg-}\right)\sin 2\omega_e t \\ + \left(v^{-}_{dg-}.i^{+}_{dg+} - jv^{-}_{dg-}.i^{+}_{qg+} + jv^{-}_{qg-}.i^{+}_{dg+} + v^{-}_{qg-}.i^{+}_{qg+}\right)\cos 2\omega_e t \\ + \left(-jv^{-}_{dg-}.i^{+}_{dg+} - v^{-}_{dg-}.i^{+}_{qg+} + v^{-}_{qg-}.i^{+}_{dg+} - jv^{-}_{qg-}.i^{+}_{qg+}\right)\sin 2\omega_e t \\ + \left(v^{-}_{dg-}.i^{-}_{dg-} - v^{-}_{dg-}.ji^{-}_{dg-} + jv^{-}_{qg-}.i^{-}_{dg-} + v^{-}_{qg-}.i^{-}_{qg-}\right) \end{array}\right\} \quad (7.57)$$

Apparent power of the grid-side converter is $S = P_g + jQ_g$ and from equation (7.57), the instantaneous active and reactive powers at the input to the grid-side converter can be expressed as [96], [107], [108] and [115]:

$$P_g = P_{og} + P_{c2g}\cos(2\omega_s t) + P_{s2g}\sin(2\omega_s t) \quad (7.58)$$

$$Q_g = Q_{og} + Q_{c2g}\cos(2\omega_s t) + Q_{s2g}\sin(2\omega_s t) \quad (7.59)$$

where:
$$\begin{bmatrix} P_{og} \\ Q_{og} \\ P_{c2g} \\ P_{s2g} \\ Q_{c2g} \\ Q_{s2g} \end{bmatrix}_o = \frac{3}{2}\begin{bmatrix} v^{+}_{dg+} & v^{+}_{qg+} & v^{-}_{dg-} & v^{-}_{qg-} \\ v^{+}_{qg+} & -v^{+}_{dg+} & v^{-}_{qg-} & -v^{-}_{dg-} \\ v^{-}_{dg-} & v^{-}_{qg-} & v^{+}_{dg+} & v^{+}_{qg+} \\ v^{-}_{qg-} & -v^{-}_{dg-} & -v^{+}_{qg+} & v^{+}_{dg+} \\ v^{-}_{qg-} & -v^{-}_{dg-} & v^{+}_{qg+} & -v^{+}_{dg+} \\ -v^{-}_{dg-} & -v^{-}_{qg-} & v^{+}_{dg+} & v^{+}_{qg+} \end{bmatrix}\begin{bmatrix} i^{+}_{dg+} \\ i^{+}_{qg+} \\ i^{-}_{dg-} \\ i^{-}_{qg-} \end{bmatrix} \quad (7.60)$$

Eliminating DC-link voltage oscillations requires double frequency power terms in equation (7.60) to be equated to zero as:

$$P_{c2g} = \frac{3}{2}\left[v^{-}_{dg-}.i^{+}_{dg+} + v^{-}_{qg-}.i^{+}_{qg+} + v^{+}_{dg+}.i^{-}_{dg-} + v^{+}_{qg+}.i^{-}_{qg-}\right] = 0 \qquad (7.61)$$

$$P_{s2g} = \frac{3}{2}\left[v^{-}_{qg-}.i^{+}_{dg+} - v^{-}_{dg-}.i^{+}_{qg+} - v^{+}_{qg+}.i^{-}_{dg-} + v^{+}_{dg+}.i^{-}_{qg-}\right] = 0 \qquad (7.62)$$

In SVO reference frame $v_{qg}{}^{+}{}_{+}$ is zero and reference current i^{-}_{dg-} is be obtained from equation (7.61) as:

$$i^{-}_{dg-} = \frac{1}{v^{+}_{dg+}}\left[v^{-}_{dg-}.i^{+}_{dg+} + v^{-}_{qg-}.i^{+}_{qg+}\right] \qquad (7.63)$$

Also from equation (7.62) the reference current i^{-}_{qg-} is obtained as:

$$i^{-}_{qg-} = \frac{1}{v^{+}_{dg+}}\left[v^{-}_{qg-}.i^{+}_{dg+} - v^{-}_{dg-}.i^{+}_{qg+}\right] \qquad (7.64)$$

The positive reference currents i^{+}_{qg+} and i^{+}_{dg+} are also obtained from equation (7.60) as:

$$i^{+}_{dg+} = \frac{1}{v^{+}_{dg+}}\left[\frac{2}{3}P_o - v^{-}_{dg-}.i^{-}_{dg-} - v^{-}_{qg-}.i^{-}_{qg-}\right] \qquad (7.65)$$

$$i^{+}_{qg+} = -\frac{1}{v^{+}_{dg+}}\left[\frac{2}{3}Q_o - v^{-}_{qg-}.i^{-}_{dg-} + v^{-}_{dg-}.i^{-}_{qg-}\right] \qquad (7.66)$$

Equations (7.63) - (7.66) are implemented into a parallel control loop in the grid side converter as illustrated in Figure 7.11, (similar to those described for the rotor-side converter) where positive sequence and negative sequence functions are controlled separately.

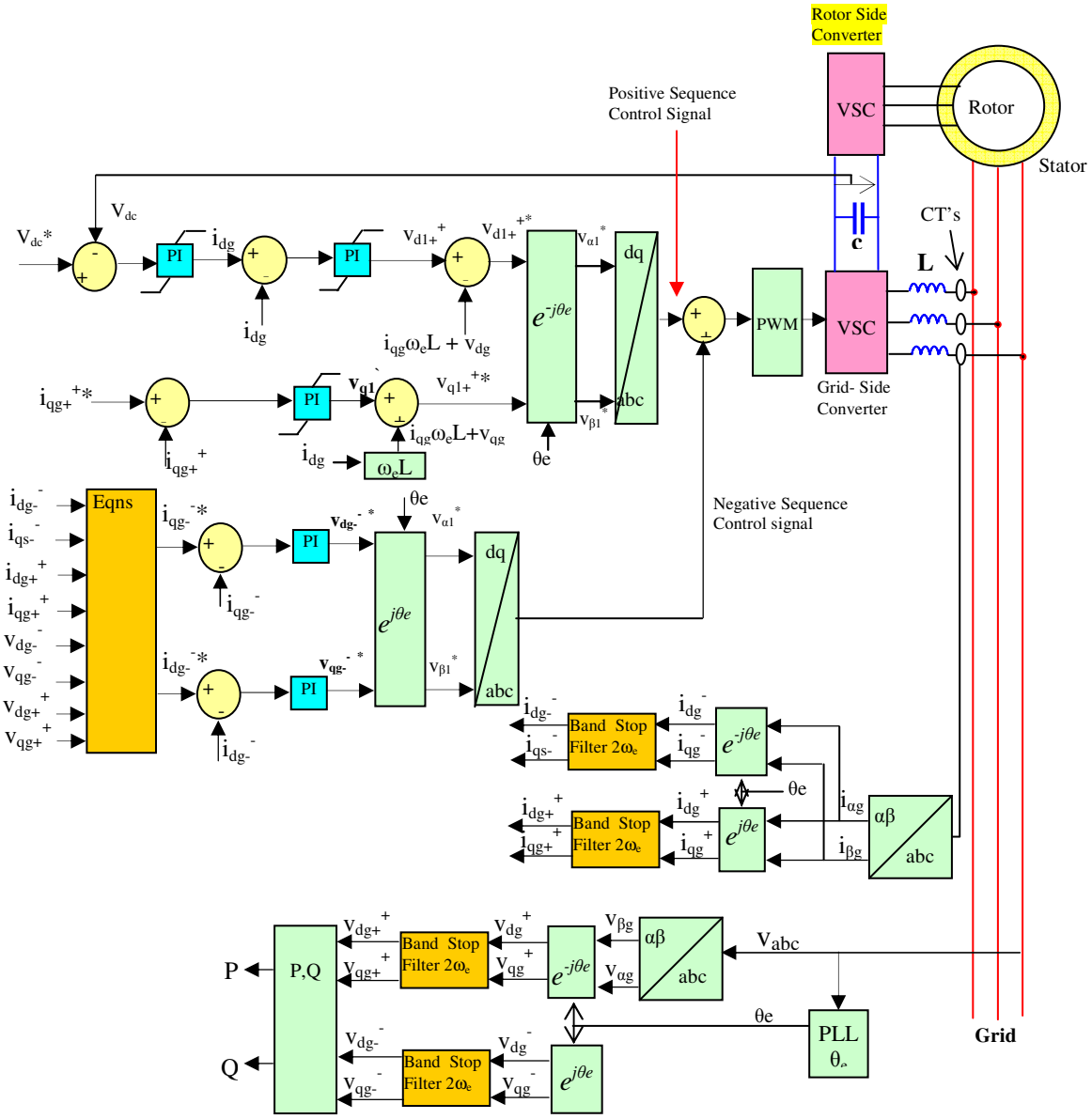

Figure 7.11 Grid side converter contro1 scheme including parallel negative sequence compensation

The positive sequence controller regulates the control signal in the positive synchronous reference frame, whereas the negative sequence controller regulates the control signal in the negative sequence reference frame. Implementation in the negative sequence reference frame facilitates the grid-side converter negative-sequence current controlled as a dc signal.

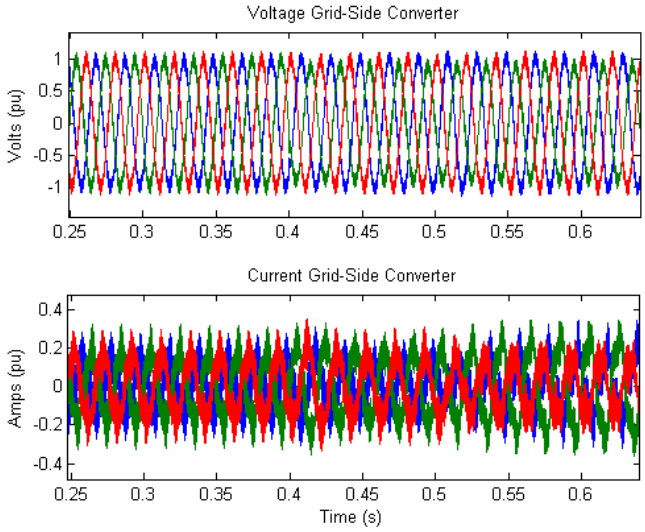

Figure 7.12 Grid side voltage and current plots

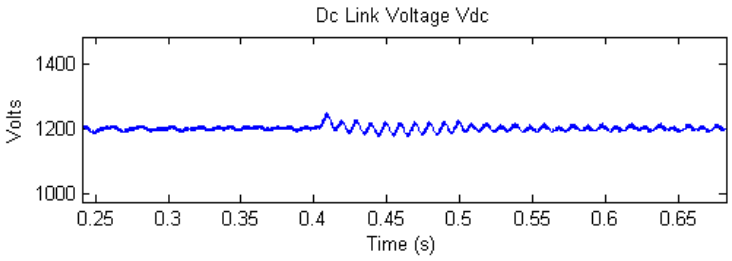

Figure 7.13 DC link voltage V_{dc}

The control structure for the grids side converter as outlined was implemented in the model described in Chapter 6. The model (Figure D3 Appendix D) was simulated in Matlab/Simulink. In the Matlab/Simulink model voltage unbalance was introduced at 0.4 seconds and the voltage unbalance correction technique as described by equations (7.65) and (7.66) was introduced at 0.5 seconds. Results of simulations include the grid-side voltage and current waveforms and these are observed in Figure 7.12. The DC-link voltage is plotted in Figure 7.13 and voltage oscillations are reduced when the compensation technique is implemented. When the compensation technique in the form of equations (7.63) – (7.66) is introduced the higher order coefficients P_{c2g} and P_{s2g} are reduced resulting in a reduction in grid-side power oscillations as indicated in Figure 7.14.

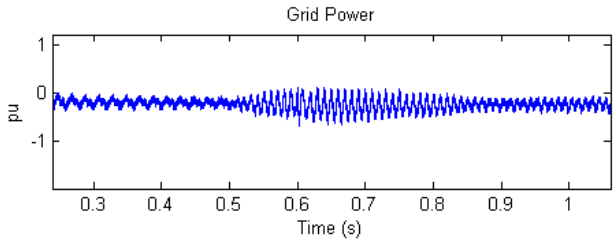

Figure 7.14 Grid-side real power

Assuming no losses in the grid-side converter, the power flowing from the grid into the converter and into the DC-link, (subsynchronous mode), or the power flowing out of the converter from the DC-link (super-synchronous mode), will equal the DC- link power. Therefore by using the power balancing equation, the power equation for the rotor converter can be expressed as:

$$P_{ac} = P_g = V_{dc}.I_{dc} = P_r \tag{7.67}$$

Where P_{ac} is the ac side instantaneous active power,

P_g is the grid-side converter instantaneous active power,

$V_{dc}.I_{dc}$ is the DC link power and

P_r is the rotor converter instantaneous active power.

7.4 Coordinated Control of Both Power and Torque Pulsations

In section 7.2 the control of the rotor side converter was configured to control either the torque pulsations or the stator power oscillations. It was not possible to reduce both the stator power and torque pulsations simultaneously, due to the limitations of the control variables. However by analysing both converters with respect to the total power supplied by the DFIG, it is possible to reduce both the total power and torque oscillations. The idea is to integrate the control variables of both the rotor-side and grid-side converters in a coordinated method [113], [115].

Previously it was observed that the stator power oscillations can be improved by controlling the negative sequence control currents as in equations (7.33) and (7.35) was 7.36 to control $P_{s\_sin2} = P_{s\_cos2} = 0$. The torque pulsations were controlled using equations (7.45) to control the double frequency torque pulsations T_{e_sin2} and T_{e_cos2}. However it can be observed in these four equations that it is not possible to control both the power and torque pulsations simultaneously. Xu [113] investigates a method to control both the stator power oscillations and the torque pulsations in a DFIG, by analysing the rotor side converter which controls the stator power in the stator flux oriented reference frame and the control of the grid side converter in the grid voltage reference frame.

In this thesis the rotor side converter and the grid side converter are controlled using the stator or grid voltage reference frame, illustrated in Figure 7.14. Observing Figure 7.14, it shows that to align the negative sequence frame onto the positive sequence frame requires a rotation of $2\theta_e$.

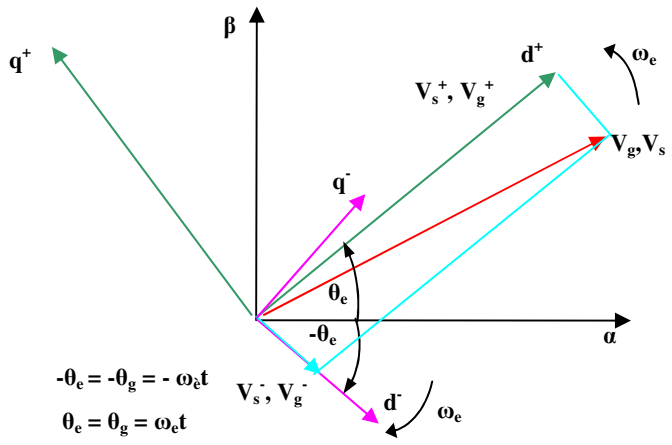

Figure 7.14 D-Q reference frame orientation.

The total apparent power of a DFIG is [95]:

$$S = P_T + jQ_T = -\frac{3}{2}\left(v^+_{dqs} i^*_{dqs} + v^+_{dqr} i^*_{dqr}\right) \quad (7.68)$$

The total real power in equation (7.68) is $P_T = Ps + P_g$. From equation (7.29) and knowing that grid side power $S_g = P_g + jQ_g$, the total real power can be described as:

$$P_T = P_s + P_g = \left(P_{s\_av} + P_{s\_\sin 2}\sin(2\omega_e t) + P_{s\_\cos 2}\cos(2\omega_e t)\right) + \left(P_{og} + P_{s2g}\sin(2\omega_e t) + P_{c2g}\cos(2\omega_e t)\right) \quad (7.69)$$

$$P_T = \left(P_{s\_av} + P_{og}\right) + \left(P_{s\_\sin 2} + P_{s2g}\right)\sin(2\omega_e t) + \left(P_{s\_\cos 2} + P_{c2g}\right)\cos(2\omega_e t) \quad (7.70)$$

If in equation (7.70) P_{s_sin2} is made equal to $-P_{s2g}$ and P_{c_cos2} is made equal to $-P_{c2g}$ then the total real power becomes $P_T = (P_{s\_av}+P_{og})$.

If $-P_{s\_sin2} = P_{s2g}$ from equations (7.31) and (7.62):

$$P_{s2g} = \frac{3}{2}\left(v^-_{qg-}i^+_{dg+} - v^-_{dg-}i^+_{qg+} - 0 + v^+_{dg+}i^-_{qg-}\right) =$$

$$-P_{s\_\sin 2} = \frac{3}{2\omega_e L_s}\left(v^-_{qs-}v^+_{ds+} + 0 + 0 + v^+_{ds+}v^-_{qs-}\right) - \frac{3L_m}{2L_s}\left(v^-_{qs-}i^+_{dr+} - v^-_{ds-}i^+_{qr+} + 0 + v^+_{ds+}i^-_{qr-}\right) \quad (7.71)$$

And solving, the negative-sequence *q*-axis reference current can be obtained as:

$$i^-_{qg-} = \frac{1}{v^+_{dg+}}\left[-v^-_{qg-}i^+_{dg+} + v^-_{dg-}i^+_{qg+}\right] + \frac{2}{v^+_{dg+}\omega_e L_s}\left(v^-_{qs-}v^+_{ds+}\right) - \frac{L_m}{v^+_{dg+}L_s}\left(v^-_{qs-}i^+_{dr+} - v^-_{ds-}i^+_{qr+} + v^+_{ds+}i^-_{qr-}\right) \quad (7.72)$$

Also equating $P_{s\_cos2} = -P_{c2g}$, a similar analysis is performed to obtain the *d-axis* reference negative sequence current i_{dg}^- as:

$$i^-_{dg-} = -\frac{1}{v^+_{dg+}}\left[v^-_{qg-}.i^+_{qg+} + v^-_{dg-}.i^+_{dg+}\right] + \frac{2}{v^+_{dg+}\omega_e L_s}\left(v^+_{ds+}v^-_{ds-}\right) - \frac{L_m}{v^+_{dg+}L_s}\left(v^-_{ds-}i^+_{dr+} + v^-_{qs-}i^+_{qr+} + v^+_{ds+}i^-_{dr-}\right) \quad (7.73)$$

7.4.1 Simulations Results – Parallel Control Scheme

The grid side converter control scheme illustrated in Figure 7.1 was implemented in a model (Figure 6.16) in the software program Matlab/Simulink. In the Simulink model a single-phase load is introduced on one of the three line voltages at 0.4 seconds creating a

VUF of 5% at Bus B (Figure 6.16). Figure 7.15 shows plots of the stator power and DFIG torque when compensation control is applied to the rotor side converter to control power oscillations only [115].

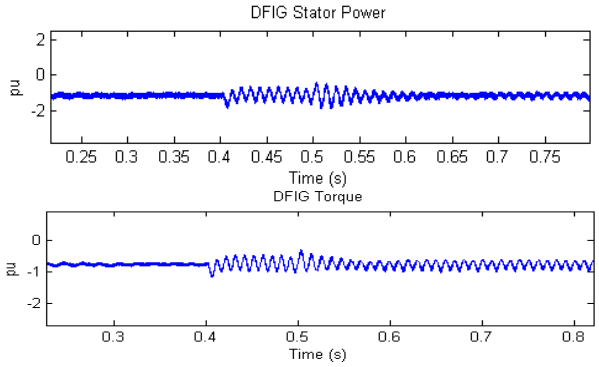

Figure 7.15 DFIG stator power and torque – stator power compensation

Steady-state power is -1.0 pu and as observed in Figure 7.15. A single phase load is introduced 0.4s introducing VUF of 5% and immediately power oscillations occur at twice the network frequency (100 Hz). In the model the compensation control scheme was timed to start at 0.5 seconds, with negative sequence currents controlled according to the requirement to minimise power pulsations. It can be observed in Figure 7.15 (DFIG Stator Power) that at 0.6 seconds the power oscillations are practically eliminated, however there is still a reasonable magnitude of torque pulsations (DFIG Torque).

Figure 7.16 is a plot of stator power and torque when the control compensation scheme is implemented in the rotor side converter to control torque pulsations only. When voltage unbalance is introduced at 0.4s, stator power oscillations and torque pulsations occur at twice the network frequency. At 0.5s when torque control compensation is introduced, the torque pulsations decay substantially, however stator power still has appreciable oscillations [115].

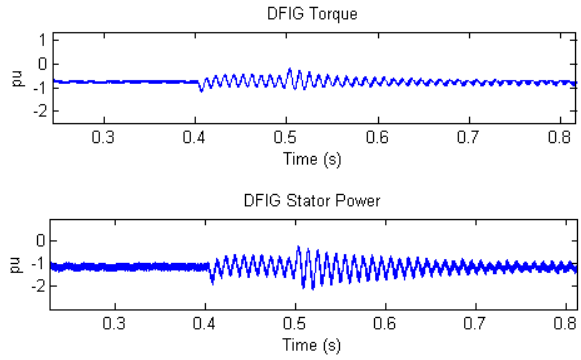

Figure 7.16 DFIG stator power and torque – Torque Compensation

The total power (sum of stator power and grid-side converter power) supplied by the DFIG is plotted in Figure 7.17. The DFIG in this case is controlled to reduce the torque pulsations (rotor-side converter only). When torque compensation is applied at 0.5s only a slight decrease in the total power oscillations is discernable [115].

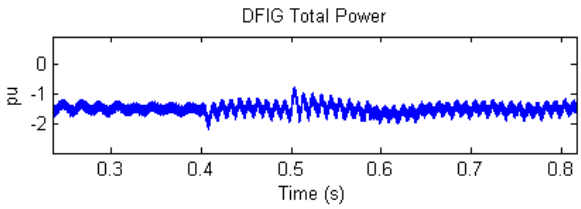

Figure 7.17 DFIG total power – no grid side compensation

Figure 7.18 is a plot of the total power supplied by the DFIG with the rotor-side converter configured to control torque and grid-side converter configured to control total power oscillations, i.e. implementing equations (7.71) and (7.72). There is good improvement in the reduction of power oscillations.

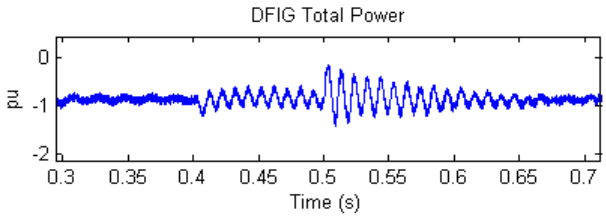

Figure 7.18 DFIG total power – grid side compensation

The total current supplied by the DFIG is shown in Figure 7.19. With the introduction of voltage unbalance at 0.4s current unbalance is significant. At 0.5s when the compensation schemes are implemented the current unbalance decreases and is significantly reduced at 0.8s [115]. The reduction in distortion of the total current leads to a reduction in distortion of the total power.

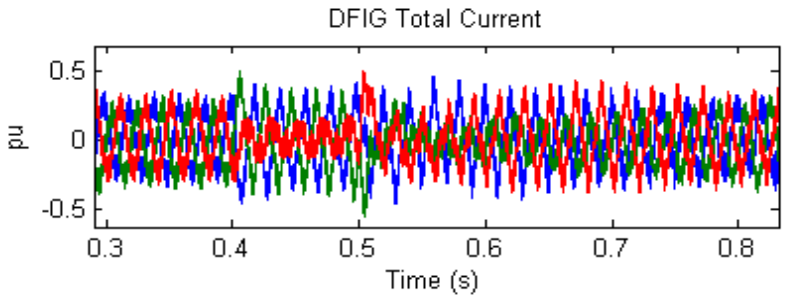

Figure 7.19 DFIG total current

Similarly the stator current waveforms are also improved as observed in Figure 7.20. The improvement of stator current distortion results in a reduction in distortion of the stator power.

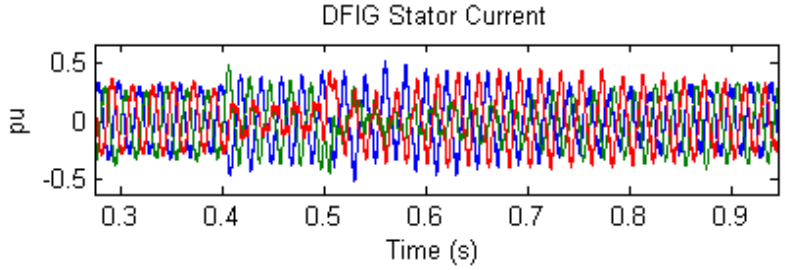

Figure 7.20 Stator Current

7.5 Resonant Control of Rotor Side Converter

An alternative approach to control a DFIG during voltage unbalance conditiions (as opposed to the methods described in Section 7.2 and 7.3) is to use a resonant (*R*) controller in parallel with the *PI* current controllers in either or both of the rotor-side and grid-side converters. Resonant controllers for wind turbine applications have been investigated in [116], [125], [126], [129], [130], [131], [132], [133], [134]. Resonant

controllers are normally tuned to the required harmonic frequency to be controlled, i.e. to control double frequency current oscillations resulting from asymmetric grid voltage the resonant controller is tuned to twice the network frequency 2ω or to control third harmonic currents it is tuned to 3ω. The idea is that at the resonant frequency the controller has infinite gain to eliminate the steady-state error at that frequency [125]. The *R* controller requires less positive and negative sequence decomposition and thus less time delay and errors [117].

Negative sequence currents i_{dqr}^{-} have a frequency of $2\omega_e$ (100 Hz), therefore to control these currents it is necessary to use a controller tuned to 100 Hz. The voltage reference output of the *PI&R* controller can be described as:

$$V_{dqr}^{e+`} = \left(I_{dqr}^{e+*} - I_{dqr}^{e+}\right)\left\{k_p + \frac{k_i}{s} + k_{iR}\left(\frac{s}{s^2 + s2\omega_c + (2\omega_e)^2}\right)\right\} \qquad (7.74)$$

A control scheme incorporating a *PI* controller in parallel with a resonant (*R*) controller tuned to twice the network frequency (100 Hz) is implemented in discrete form in Figure 7.21.

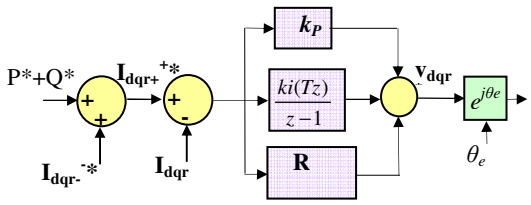

Figure 7.21 Rotor Side PI and Resonant Controller

The *PI&R* controller shown in Figure 7.21 is implemented in the SVO dq^+ reference frame. The rotor currents are transformed into the positive sequence dq^+ reference frame and the negative sequence dq^- reference frame using the slip angle θ_{sl}. Band-stop (notch) filters, tuned at $2\omega_e$ are used to remove the oscillating terms and leave the respective

positive and negative sequence control currents $i_{dqr}^{+}{}_{+}$ and $i_{dqr}^{-}{}_{-}$. The *PIR* control method incorporates the negative sequence components into the positive sequence control loop.

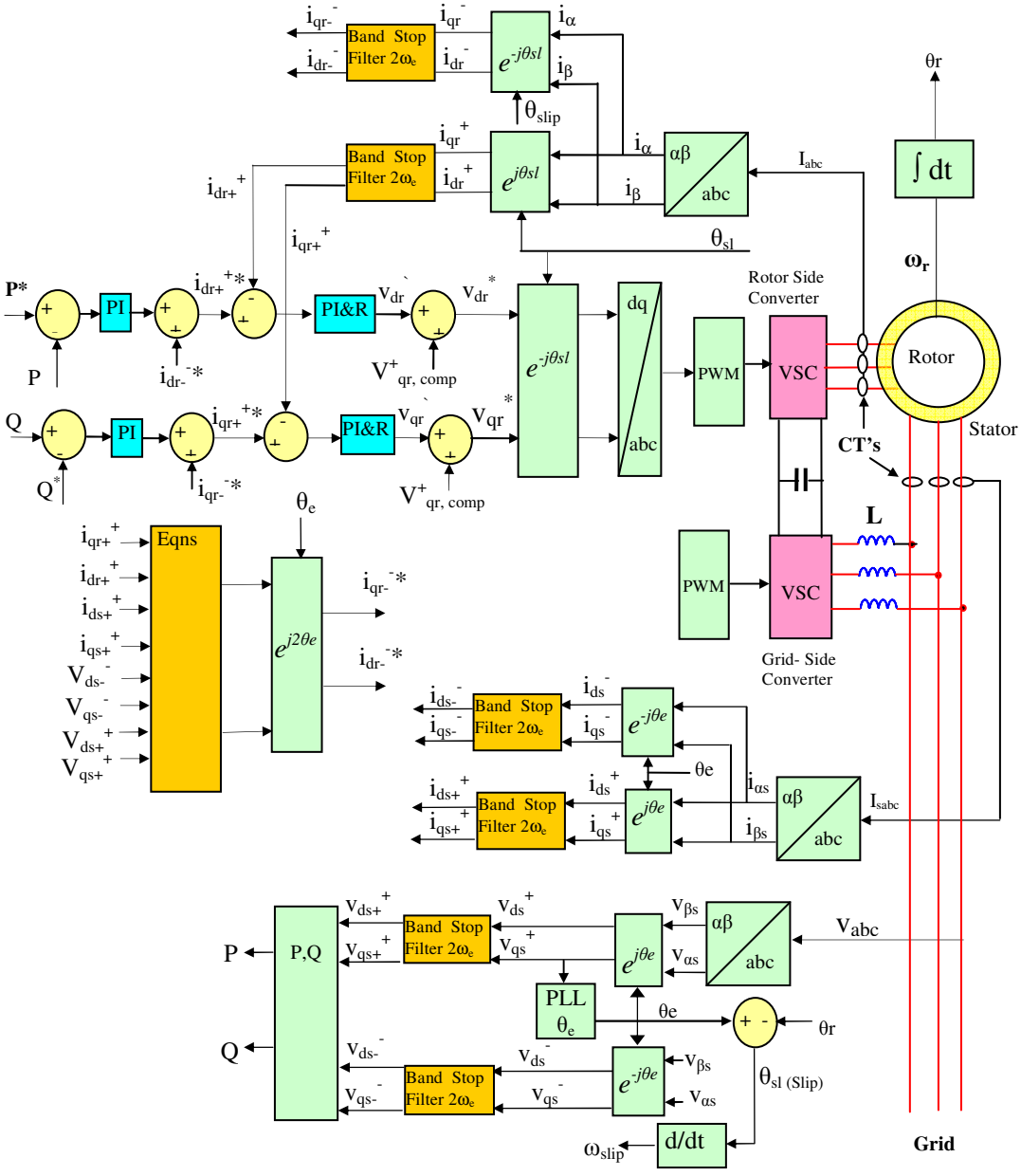

Figure 7.22 DFIG rotor side converter control including compensation scheme

In the rotor side converter the negative sequence compensation components required to control the torque pulsations are as equations (7.45) and (7.47). If it is required to reduce the stator power oscillations it is necessary to use equations (7.33) and (7.35) in the control loop of Figure 7.22.

7.6 Resonant Control of Grid Side Converter

Resonant controllers can also be used to control grid-side converters in DFIG's to improve performance during grid voltage unbalance conditions. In the grid-side converter, the negative sequence compensation components required to control the DC link voltage oscillations, are derived as equations (7.65) and (7.66).

The voltage reference output of the *PI&R* controller can be described as:

$$V_{dqg}^{e+`} = \left(i_{dqg}^{e+*} - i_{dqg}^{e+}\right)\left\{k_p + \frac{k_i}{s} + k_{iR}\left(\frac{s}{s^2 + s2\omega_c + (2\omega_e)^2}\right)\right\} \tag{7.75}$$

Voltage equations (7.65) and (7.66) can be incorporated into the vector control scheme shown in Figure 7.23 where *PIR* controllers are applied as in equation (7.75) to control the DC-link voltage and reactive power.

7.6.1 Resonant Control Scheme – Third Harmonic Compensation

Third harmonic currents at the grid side converter can also be controlled using a resonant controller tuned to $3\omega_e$ (150Hz) [116], [125]. The voltage reference output of the *PI&R* controllers will then be as:

$$V_{dqr}^{e+`} = \left(i_{dqr}^{e+*} - i_{dqr}^{e+}\right)\left\{\begin{array}{l} k_p + \frac{k_i}{s} + k_{iR}\left(\frac{s}{s^2 + s2\omega_c + (2\omega_e)^2}\right) \\ + k_{iR}\left(\frac{s}{s^2 + s2\omega_c + (3\omega_e)^2}\right) \end{array}\right\} \tag{7.76}$$

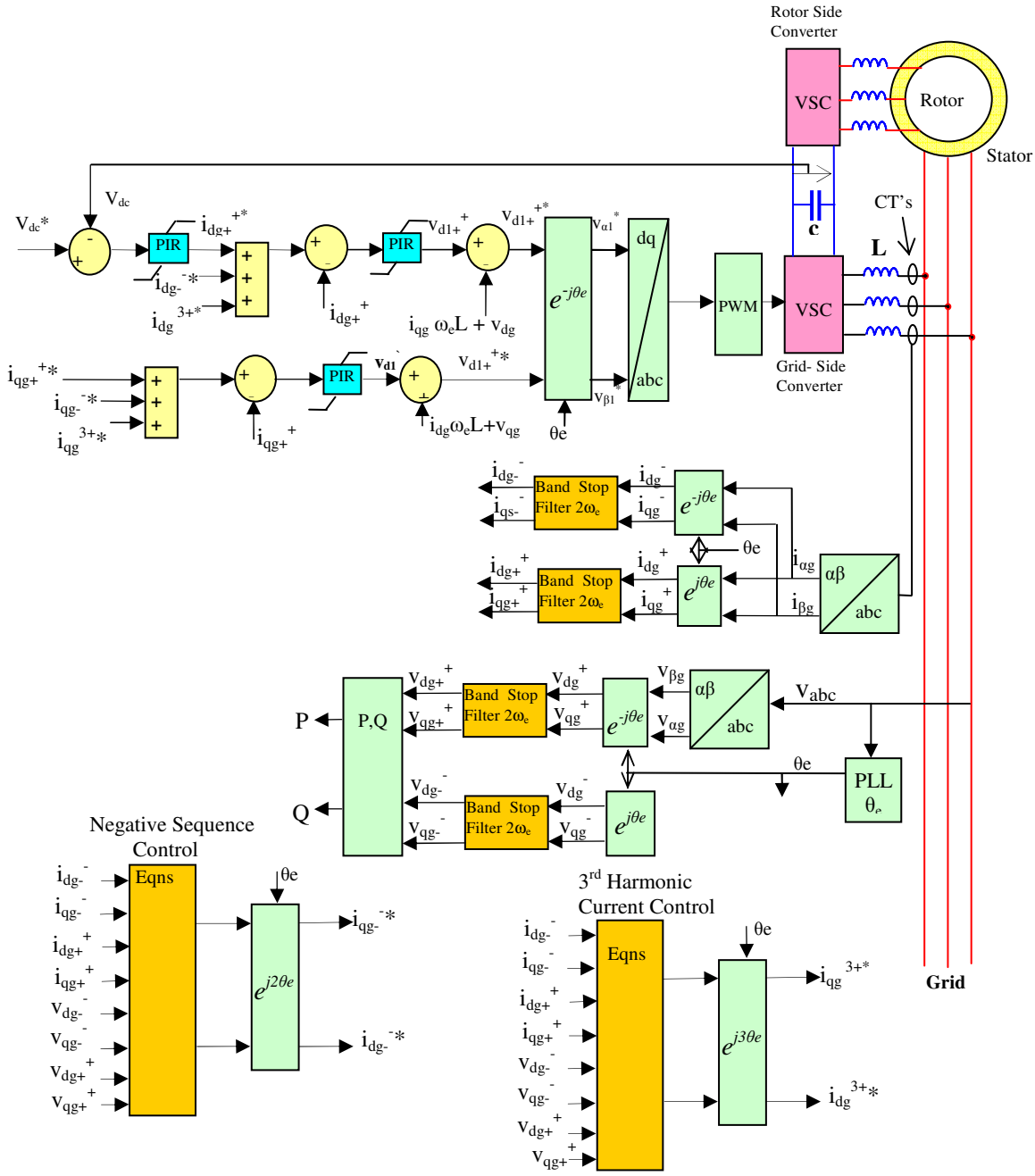

Figure 7.23 Grid side converter contro1 including PIR negative sequence compensation

The rotor-side and grid-side converters are controlled using the stator/grid voltage reference frame. Observing Figure 7.24 [116], it shows that to align the third harmonic reference frame onto the positive sequence frame requires a rotation of $3\theta_e$.

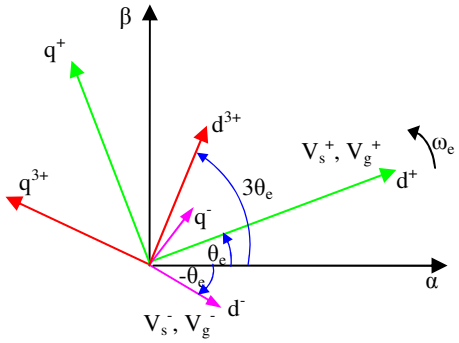

Figure 7.24 DQ positive, negative and 3rd harmonic reference frames.

7.7 Simulations Results – Resonant Control Scheme

The previously developed Matlab/Simulink model was configured to include PIR control structures in the rotor-side and grid-side converters, as shown in Figure 7.22 and Figure 7.23. The grid side converter was configured to control the DC link voltage at 1200V and coordinated with the rotor side converter to control the DFIG total power oscillations.

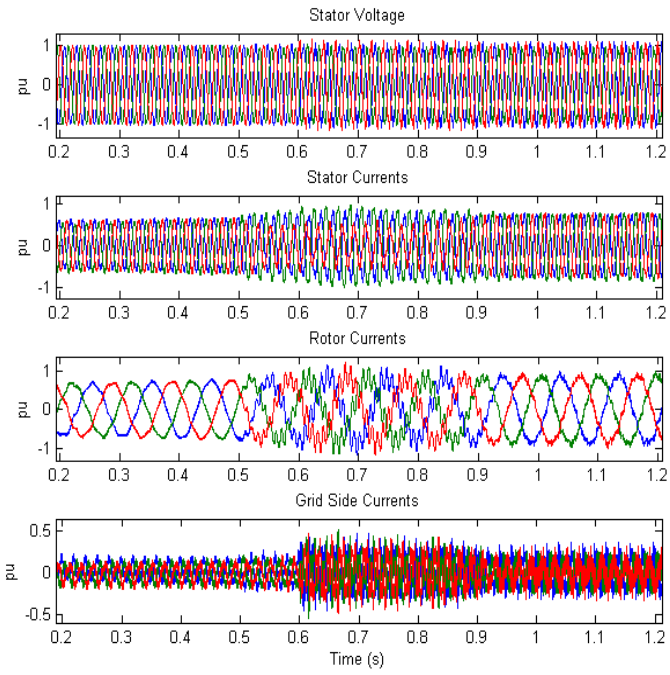

Figure 7.25 Results for PIR Control Scheme

The stator voltage and the stator, rotor and grid side currents can also be observed in Figure 7.25 [116]. In the Simulink model a large single-phase load is timed to switch-in

at 0.5s, introducing a VUF of 6%. The stator and rotor currents become unbalanced at 0.5s and when rotor side converter compensation (PIR control) is introduced at 0.6s the current oscillations reduce and are eliminated at 0.9s. The rotor currents have a frequency of 10Hz (rotor speed 60Hz minus grid frequency 50Hz). Due to the negative sequence rotation as a result of grid voltage unbalance, the induced negative sequence oscillations in the rotor have a frequency of 110 Hz, (60 Hz + 50 Hz), and oscillations are clearly visible starting at 0.5s in Figure 7.25 [116].

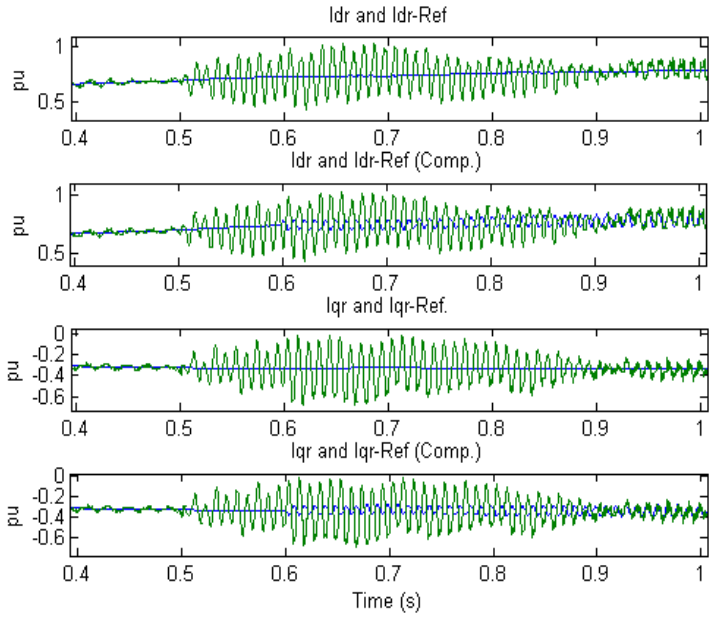

Figure 7.26 Rotor Side Converter Idr and Iqr currents

The measured three-phase rotor currents are transformed into the positive sequence (dq^+) reference frame, and when subjected to network voltage unbalance conditions will result in a negative sequence ac component at twice the network frequency super-imposed on the dc component of the positive sequence. The rotor-side converter reference currents $I_{dr\text{-}Ref}$, and $I_{qr\text{-}Ref}$, and the actual currents I_{dr}- and I_{qr}-, before and after negative sequence compensation is applied, are plotted in Figure 7.26. The plots demonstrate that when compensation is introduced the actual currents I_{dr} and I_{qr} follow the reference currents $I_{dr\text{-}Ref}$, and $I_{qr\text{-}Ref}$ closely.

Figure 7.27(a) shows the stator power plot with stator power oscillations when unbalance is introduced at 0.5s, and Figure 7.27(b) shows the results when negative-sequence compensation is introduced. Due to the step nature of the introduction of the single-phase load there is a period of about 0.2s before the DFIG system reaches a steady state with constant power oscillations. When the compensation scheme is introduce at 0.6s the oscillations start to reduce and are significantly lower at 0.8 s, Figure 7.27(b), when compared to the standard control technique illustrated in Figure 7.27(a) [116].

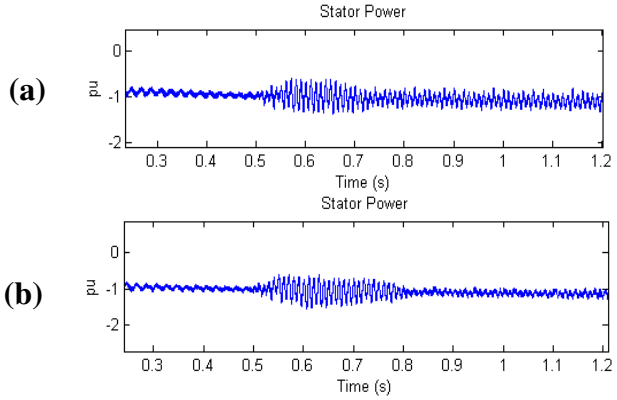

Figure 7.27 Stator Power ((a)-Standard Control- (b) PIR Compensation)

Figure 7.28 is a plot of the DFIG torque. The DFIG input torque set-point is 0.8 pu, and grid voltage unbalance introduced at 0.5s and torque pulsations occur as indicated in Figure 7.28(a).

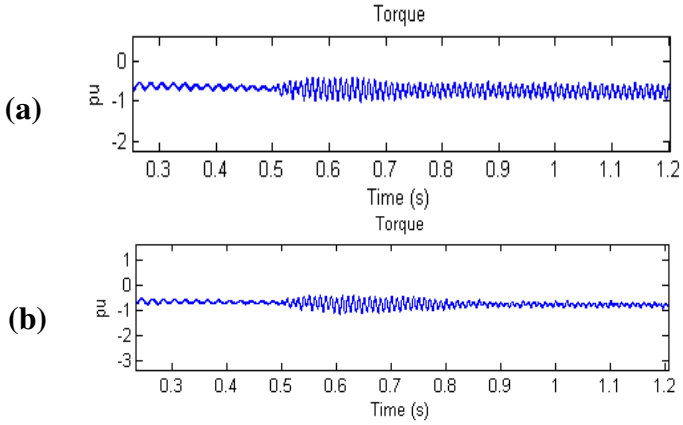

Figure 7.28 DFIG Torque (a) no compensation (b) compensation

Torque pulsations occur at the onset of grid voltage unbalance, however when negative-sequence voltage compensation is introduced at 0.6s, torque pulsations are reduced as illustrated in Figure 7.28(b).

Plots of the grid-side converter power are shown in Figure 7.29. The grid side converter is controlled to reduce the total power oscillations at the DFIG terminals. There is good reduction of the grid side converter power oscillations.

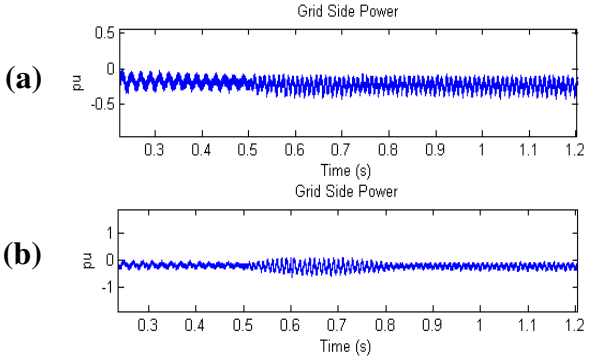

Figure 7.29 Grid Side Power (a) no compensation (b) compensation

The total power delivered by the DFIG to the grid from both the stator and rotor is plotted in Figure 7.30. The rotor-side converter is configured to control the DFIG torque pulsations as observed in Figure 7.28 and the grid-side converter configured to control total power oscillations at the DFIG terminals. The total power supplied by the DFIG can be observed in Figure 7.30(a) and the resulting oscillations when grid voltage unbalance is introduced at 0.5s.

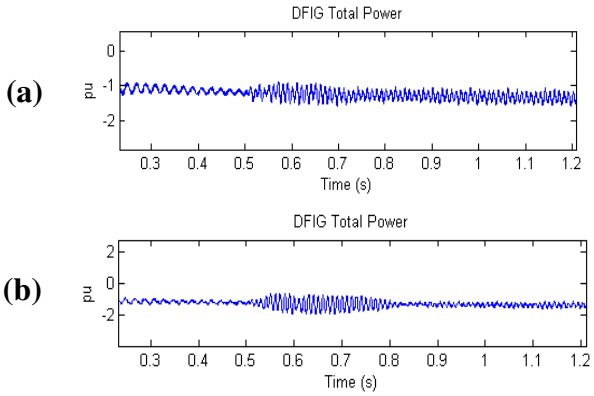

Figure 7.30 DFIG Total Power (a) no compensation (b) compensation

Figure 7.30(b) shows a good reduction in the power oscillations as a result of the grid-side converter configured to assist in reducing the overall power oscillations.

7.8 Resonant Control of Synchronous Generator System

Typically in synchronous generator converter systems the grid-side converter controls the real power delivered to the grid by maintaining adequate DC link voltage. The grid-side converter can also control reactive power. A resonant (*R*) controller can be used in parallel with the *PI* current controller in the grid side converter of a synchronous generator converter system, similar to operation in a DFIG. A proportional, integral plus resonant (*PI*+*R*) grid-side converter current controller can be implemented for directly controlling both the positive and negative sequence components of real power [134].

A model of a synchronous generator converter system was configured in Matlab/Simulink to investigate issues associated with the performance of the system to grid network problems. A generic synchronous generator converter system as described by Figure 7.32 was implemented in a similar model as previously configured for a DFIG (Figure 6.19) as shown in Figure 7.31.

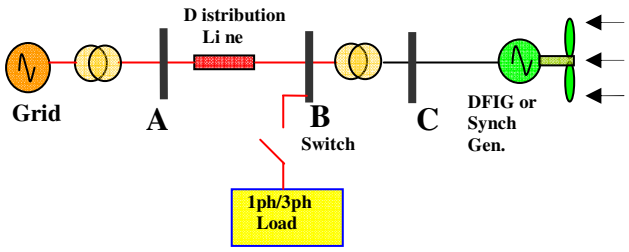

Figure 7.31 Synchronous Generator Network Model

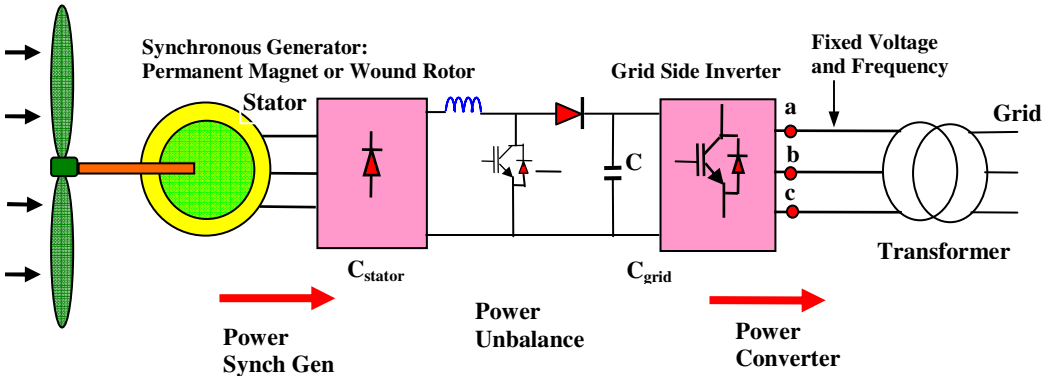

Figure 7.32 Synchronous Generator System

The synchronous generator system illustrated in Figure 7.32 comprises of a synchronous generator connected to a three-phase rectifier, DC-link boost converter and grid-side inverter. A control scheme for the converter connected synchronous generator is illustrated in Figure 7.33 [134]. The model included an improved control scheme of the grid side converter (similar to improved control structure of DFIG grid side converter), to reduce grid power oscillations due to grid voltage unbalance.

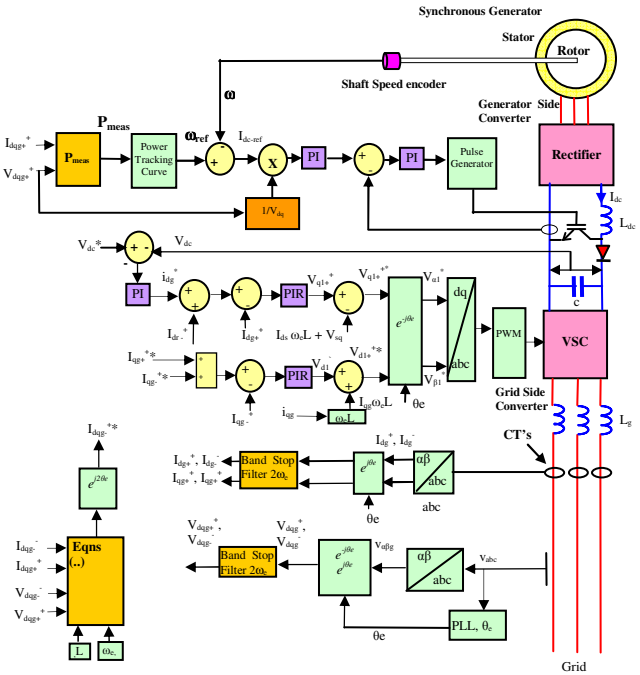

Figure 7.33 Synchronous Generator Control Scheme

Figure 7.34 shows the grid-side power oscillations measured at the of terminals of the inverter (a, b, c in Figure 7.32), occurring at 1.5s in the simulation when the grid voltage unbalance is introduced at the grid-side converter of the synchronous generator. When voltage unbalance compensation using a PIR resonant controller is introduced in the grid-side converter at 1.9s the power oscillations are eliminated.

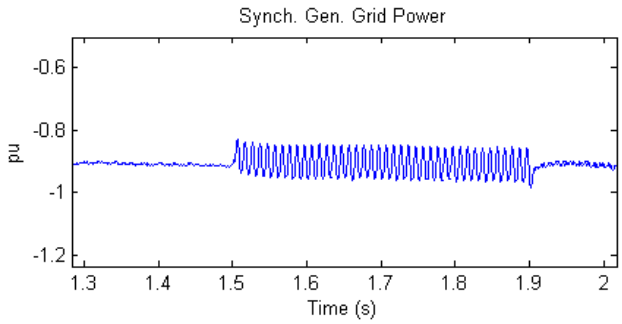

Figure 7.34 Synchronous Generator System Grid Power

7.9 Conclusion

Investigative studies were undertaken to establish the most appropriate methods of controlling DFIG's when subjected to grid voltage unbalance conditions. Control structures in the rotor-side and grid-side converters in a DFIG model were modified to improve the performance during network voltage unbalance conditions. In particular modifications to the control structures to decrease power and torque oscillations and 3rd harmonic currents were investigated. A model of a DFIG was implemented in Matlab/Simulink with proportional resonant (PIR) controller incorporated in the rotor-side and grid-side converters. Simulation results demonstrate the reduction in torque and power oscillations and 3rd harmonic currents.

Also investigated was a model of a synchronous generator system. Improvements in the performance of the synchronous generator was shown.

Chapter 8 Laboratory Test Rig

8.1 Laboratory Test Rig

This chapter describes in detail the realised test rig. A laboratory based test facility was designed and constructed to implement the control schemes described in Chapters 6 and 7. A DSP based digital microcontroller and interfacing hardware has been developed for a 5kVA DFIG laboratory based system. The system comprises of a machine set; a dc machine with common shaft coupling to a three-phase wound-rotor induction machine. The dc machine is rated 5kW and the induction machine is rated at 5kVA. The dc machine emulates a wind turbine, and drives the induction machine in response to required speed.

A back-to-back PWM dual converter has been constructed by the author to control the rotor power of the induction machine. Interfacing schemes for the required feedback signals including voltage and current transducers and speed measurement were designed to enable control of both the rotor-side and grid-side converters of the DFIG. A Texas Instruments TMS320F2812 microprocessor is configured to implement the control techniques developed for control of the rotor and grid converters (details of switchgear are included in Appendix A). The equipment is located in the Electrical Energy Laboratory, DIT Kevin Street. An incremental shaft encoder is fixed to the shaft of the induction machine. The electrical control panel incorporates the IGBT power electronics, associated protection devices, voltage and current transformers, interface analogue conditioning boards, and the DSP microcontroller. A schematic of the DFIG system in Figure 8.1 illustrates the main components and connection requirements.

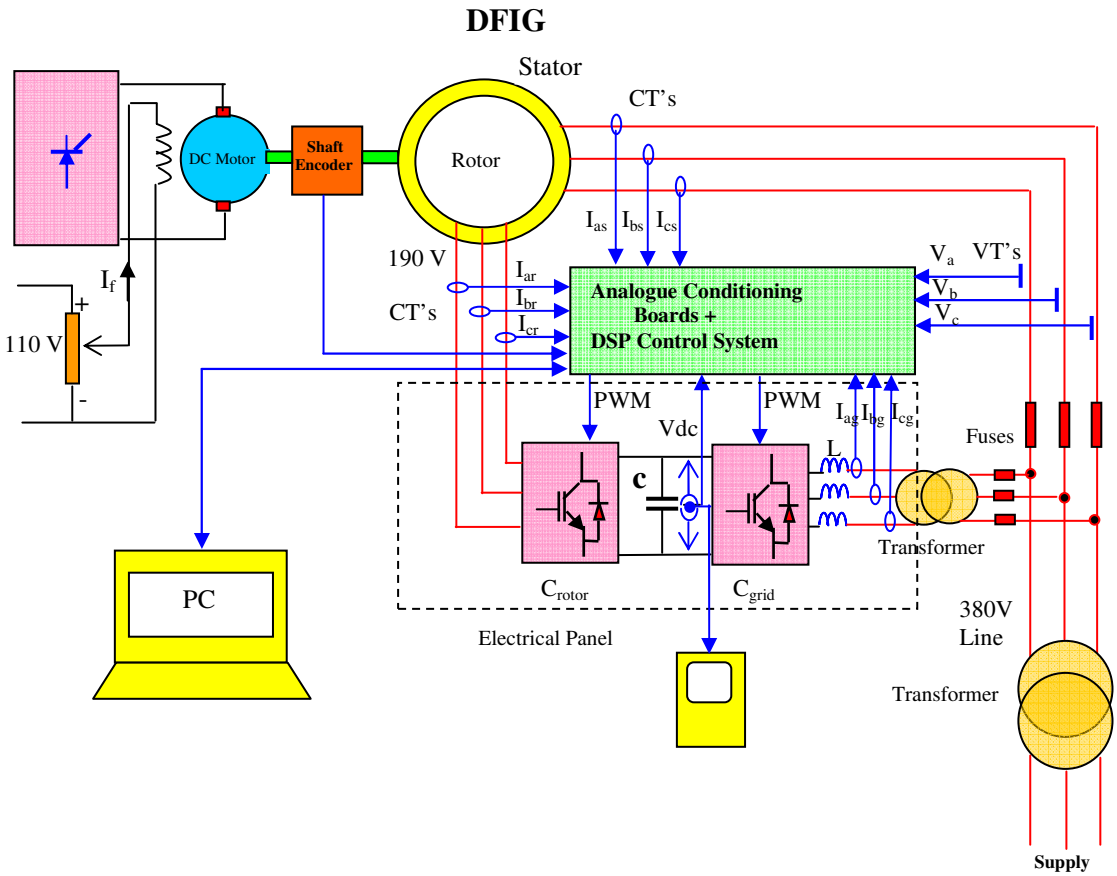

Figure 8.1 Double-Fed Induction Machine

Control of the DFIG was designed and complied using Code Composer Studio (CCS), a C^{++} platform for the development and debugging of software program code for the TMS320F2812 microprocessor. The back-to-back bridge circuits use voltage-source converters incorporating Semikron IGBT's. The Texas Instruments microcontroller generates six pulse-width-modulation (PWM) signals by means of space vector PWM technique for each of six power IGBT switching devices in both the rotor and grid side converters.

The test system consists of the following components:

- Induction machine
- DC Shunt machine

- Back-to-back converter in the rotor of the induction machine incorporating a rotor-side converter (C_{rotor}) a DC link and a grid-side converter (C_{grid}).
- Texas Instruments (TI) D.S.P microcontroller (TMS320F2812).
- PC to program the TMS320F2812.
- LEM current and voltage transformers.
- Analogue conditioning boards
- Power supplies: 5V, 12V, 15V.
- Optical incremental shaft encoder.
- Panel meters – voltage and current meters.

8.2 The eZdsp TMS320F2812 Board

The control complexity of a DFIG requires a powerful microcontroller or a digital signal processor be applied for the purpose. A DSP based digital controller is preferable because of its high-speed and on-board peripherals. A Texas Instrument (TI) DSP based eZdspTMF2812 development kit evaluation module (Appendix F) was chosen for the control of the DFIG. An eZdspTMS320F2812 development kit is based on TI's TMS320F2812 DSP.

The development board has an operating speed of 150 MIPS. The DSP controller is suitable for machine control applications, as it contains 16, 12-bit ADC channels, 56 General Purpose Digital Input/Output (GPIO) ports of which 12 can also act as inbuilt PWM channels. There is also on-chip memory as well as external on-board memory. A more detailed description of the DSP functionalities is provided in Appendix F. The ADC channels offer a fast conversion rate of 80ns at 25 MHz clock speed. The 16 ADC channels can be either operated as an auto-sequenced single sequencer or two independent dual sequencers (8 in a group). The ADC conversion can be triggered by a

variety of sources including hardware, software and a number of timer events in the DSP. Therefore, synchronization of the ADC with different events can be achieved very easily. The inbuilt PWM channels are another advantage of the DSP board. A total of 16 PWM pulses are available, (8 in Event Manager A (EVA) and 8 in Event Manager B (EVB) either independently or synchronized to each other. The PWM pulses generated by the compare units (3 pairs) on each module are suitable for control of two full bridge converters simultaneously. Also a suitable dead-time can be introduced for the PWM pulses on the rising edge.

Setting of suitable interrupts and clock speeds on both peripherals can easily synchronize the Event Managers and ADC. More details on these peripherals can be found in Appendix F. The control software is developed in C++, using Code Composer Studio (CCS) environment for TI DSP's.

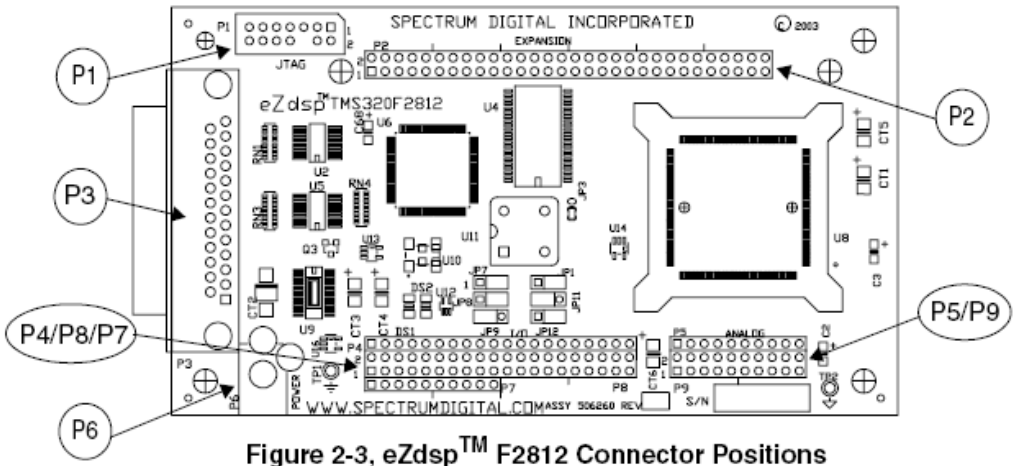

Figure 2-3, eZdsp™ F2812 Connector Positions

Figure 8.2 eZdsp™ TMS320F2812 PCB connector positions

The eZdsp DSP is a standalone circuit board, incorporating a TI TMS320F2812 microcontroller, associated hardware necessary to interface it with a PC, plus additional electrical hardware interfaces. Software programs are directly downloaded to the eZdsp

circuit board through a direct connection to a PC. The eZdsp circuit board is supplied by a dedicated external 5 V power supply.

The main features of the EZdsp DSP are:

- TMS320F2812 Digital Signal Processor
- 150 MIPS operating speed
- 18K words on-chip RAM
- 128K words on-chip Flash memory
- 64K words off-chip, on board SRAM memory
- 30 MHz clock
- 2 Expansion Connectors (analogue, I/O)
- 5 volt only operation with supplied ac adapter
- TI TMS320F2812 Code Composer Studio tools driver

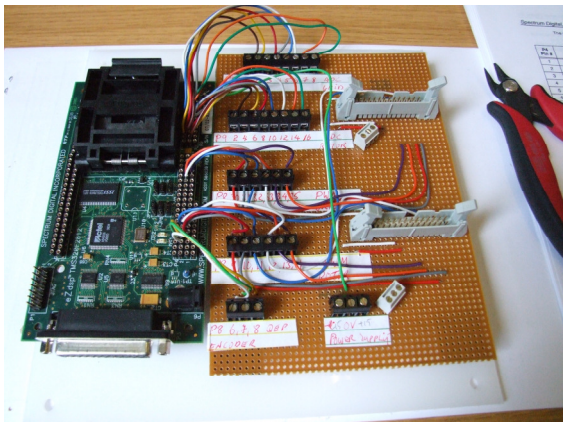

Figure 8.3 eZdsp™ TMS320F2812 and interface connector board

8.2.1 Fixed-point arithmetic and representation of numbers

All numbers are represented in fixed-point representation numbers for accuracy. To represent real numbers on this fixed-point architecture, a *Qk* format was chosen. *Qk* numbers can be represented by the following general formula:

$$Z = b_{31-k} * 2^{31-k} + b_{30-k} * 2^{30-k} + ...b_0 + b_1 * 2^{-1} + b_2 * 2^{-2} + ...b_k * 2^{-k}$$

An implied dot separates the integer part from the fractional part of the *Qk* number where k represents the quantity of fractional bit. For instance, the real number π (3.14159) can be represented in Q13 (16 bit) with finite precision as follows:

$$011.0010010000111 = 0*2^{2} +1* 2^{1} +1* 2^{0} + 0* 2^{-1}+0* 2^{-2}+1* 2^{-3}\ 0* 2^{-4}+0* 2^{-5}+1* 2^{-6}+0* 2^{-7}+0* 2^{-8} + 0* 2^{-9}+0* 2^{-10}+1* 2^{-11} + 1* 2^{-12}+ 1* 2^{-13}$$

The *Qk* format offers a compromise between dynamic range and precision. In this project the Q24 numeric format is used in the major parameters: 8 bits are dedicated to the integer part and 24 bits are dedicated to the fractional part. The precision of this format is 2^{-24} (0.0000000596046). The represented numbers are in the range of [-128 to 128] to ensure that values can handle the DFIG control quantity, not only during steady state operation but also during transient operation.

8.3 Rotor Side Converter

The rotor-side and grid-side converters are both controlled by a space vector PWM technique. Space vector PWM refers to the technique of determining the switching sequence of the upper three power transistors of a three-phase voltage source inverter (VSI). The structure of the rotor-side converter is illustrated in Figure 8.4.

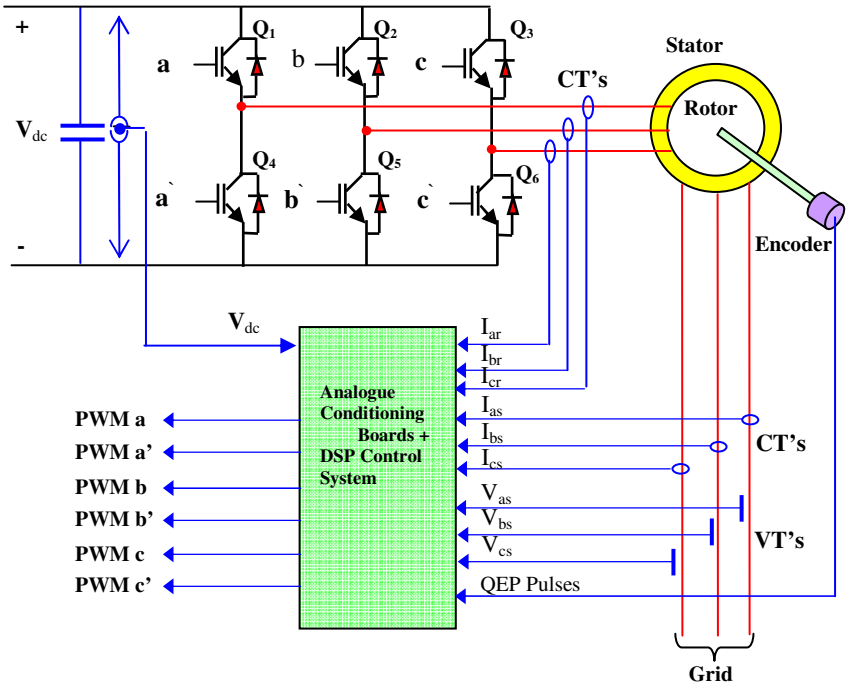

Figure 8.4 Rotor side converter

In Figure 8.4 the voltages V_{as}, V_{bs} and V_{cs} are the supply voltages obtained through LEM voltage transformers (LEM 25V-600). These voltages are then passed through an analogue conditioning board and connected to the ADC of the DSP through the input connector P5 (Pins 1, 2 and 3), listed in Table 10. The rotor currents are measured using LEM current transformers (LA 55P). The output signals of the LEM current transducers are connected to an analogue conditioning board and are then applied to the DSP P9 connector (pins 2, 4 and 6). Q_1 to Q_6 in Figure 8.4 represent the six Semikron IGBT power transistors, controlled by the PWM gating signals *a, a`, b, b`, c* and *c`*, and these signals determine the shape of the output voltages supplied to the rotor windings [69]. The PWM gating signals (*a, a', b, b', c, c'*) are the outputs from the 3V to 15V level-shift conditioning PCB. The inputs signals to the level shifting PCB are the 3V outputs from the DSP P8 output connector (pins 9-14), listed in Table 11. The 3V PWM output pattern from the DSP chip depends on the control algorithms developed in Chapter 7.

The 3V PWM output signals are level shifted to 15V as required to drive the Semikron IGBT's. When the upper transistors (IGBT's) are switched on, i.e. if *a*, *b,* or *c* is equal to 1, the corresponding lower transistors are switched off, i.e. $a`$, $b`$ or $c`$ is set to 0.

8.4 Grid Side Converter

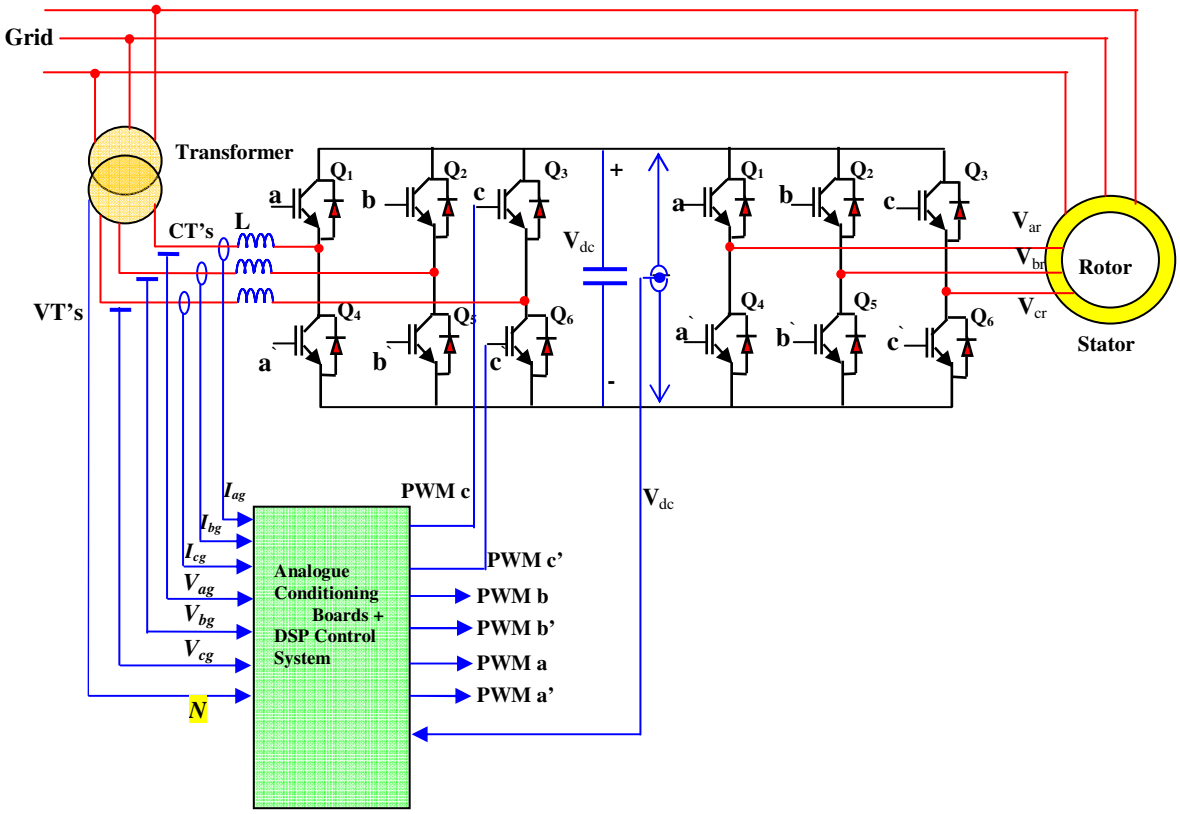

Figure 8.5 Grid side converter

The grid-side interface scheme to collect voltage and current measurements is shown in Figure 8.5. Voltages V_{ag}, V_{bg} and V_{cg} are the measured grid supply voltages obtained through VT's (LEM), modulated through an analogue conditioning board and then connected to the ADC of the DSP through the input connector P5 (Pins 1, 2, 3 – listed in Table 8.1 (Table 10)). Grid-side currents, I_{ag}, I_{bg} and I_{cg} are measured with current transformers (LEM LA 55P), and the outputs from these C.T.'s are connected to an analogue conditioning PCB and subsequently applied to the DSP P5 connector, (pins 4,

5, 6 – listed in Table 10). The grid-side converter power devices in Figure 8.5, Q_1 to Q_6, represent the six IGBT power transistors, controlled by the PWM gating signals *a, a`, b, b`, c* and *c`*. The PWM gating signals (*a, a', b, b', c, c'*) are the output signals from the 3V to 15V level shift conditioning PCB and these signals determine the power supplied to the DC link [69]. The PWM output signals emanate from pins 30-36 on the P8 connector of the DSP listed in Table 11.

The DSP will create the desired symmetrical synchronized PWM signals, and these signals are applied to the rotor side and grid side Semikron IGBT converters. The frequency of the PWM triangular carrier wave is 2.5 kHz. and this is compatible for use with the IGBT's. In spite of this, because of the finite turn-on and turn-off times associated with any type of switch, the design requires the inclusion of slight time delays (dead band), when the IGBT's are switching.

8.5 Semikron IGBT Modules.

The converter modules employed are SkiiPPack manufactured by Semikron (Appendix G). Each Semikron module (rotor-side and grid-side) incorporates three half-bridge circuits, combined to form a back-to-back full-bridge converter. The semi-conductor switches are high quality IGBT's, that feature sufficient switching efficiency and blocking voltage for applications of this nature. The Semikron IGBT's also have integrated gate drivers. Within the DSP controller, the software generates the required control signals at 3V, and these are then level shifted to 15V as required by the Semikron modules.

The Semikron IGBT's are designed with large attached heat sinks and are rated at 150A. Due to the high current rating of the IGBT's forced cooling of the heat sinks is not

required. The gate drivers are built on to the IGBT's, and have short circuit and over current protection (OCP), illustrated in Figure 8.6.

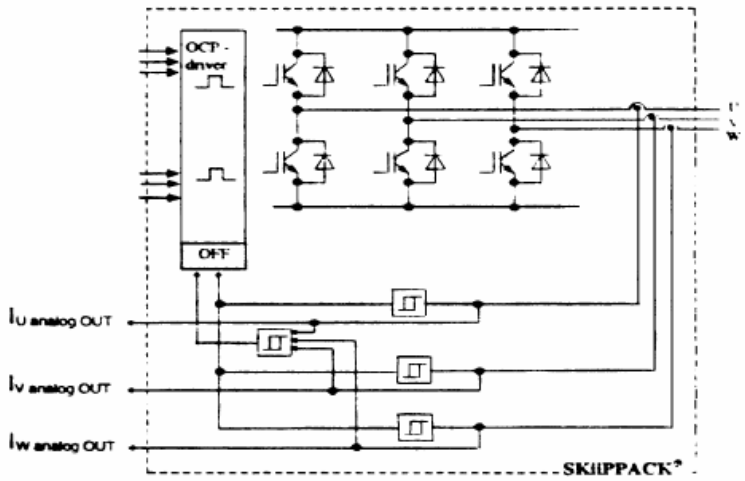

Figure 8.6 IGBT over current protection

If the voltage supply drops below 13.5V using regulated 15V supply (regulated 15V is used and high control signals must have a value of 15V), the IGBT's are immediately switched off and switching pulses from the controller are ignored and the error latch is set. The output (ERROR OUT) is in high state.

To reduce the possibility of shoot-through current, the gate drivers generate a dead-band time of 2.3μs. There is also a software dead-band time programmed in the DSP and therefore the total dead-band is the sum of both the software dead-band and hardware dead-band. The current total dead-band time is 2.3μs + 3.2 μs = 5.5 μs.

8.6 Base Values of Voltage and Current

It is normally more beneficial to express machine parameters and associated variables in the per-unit (pu) format. The pu implementation reduces the range of variables. The software modules in the software program require that the line current and voltage variables be normalized with respect to their individual instantaneous maximum values,

and expressed as fractional numbers (i.e., Q24 format). The TMS320F2812 is a fixed-point DSP, and the greatest precision is obtained in Q^{31} format, but the dynamic range of this format is small: the dynamic range is between –1 and +1 only. With fixed-point DSP's, the amplitude of the variables must be reduced to get a fractional part with maximum precision [69]. The per-unit (pu) format used complements the fixed-point feature and is associated with the base values of the machine. Voltage and current are thus controlled between 0-1pu.

Some of the variable parameters may reach in excess of their rated values; e.g. the pu value for the speed at 1500 rev/min (314 rad/sec) is 1pu, however during supersynchronous operation the speed may reach 1800 rev/min., and the pu value is greater than one. Transient currents may also reach in excess of 1 pu. For these reasons the numerical format in the DSP is set at Q^{24}. The extended dynamic range is then ±127. The global fixed point format in the software program is Q^{24}.

The choice of maximum line current and voltage depends on maximum machine and system ratings. The base value of the voltage is based on the maximum rated rotor voltage of 190V and the value of rated stator current (Table 15, Appendix A) is 11.7A. To obtain a suitable base current to use in the DSP for both the rotor-side and grid-side converters, it is necessary to determine the speed range over which the DFIG will operate. The reason for this is that the rotor converter current is dependent on the speed at any instant. For example if the speed range required is ± 0.2 above and below synchronous speed, not untypical for DFIG's, then the real power transferred across the rotor-side and grid-side converters is 0.2 multiplied by the rated power of the induction generator. The induction machine has four poles (2 pairs) and therefore the synchronous speed is:

$$60 \,.\, f/2 \quad = \quad 1500 \; rev/min. \tag{8.1}$$

where f is the supply frequency of 50 Hz.

The speed range at ±0.2 of rated speed is thus 1500 rev/min. ± 300 rev/min., resulting in a speed range of 1200 rev/min to 1800 rev/min. Thus when the speed is 1200 rev/min. the induction machine is operating in the sub-synchronous region and the slip s is:

$$s \quad = \quad \frac{1500-1200}{1500} \quad = \quad +0.2 \tag{8.2}$$

If the speed of the DFIG is 1800 rev/min. the induction machine is operating in the super-synchronous region and the slip s is:

$$s \quad = \quad \frac{1500-1800}{1500} \quad = \quad -0.2 \tag{8.3}$$

The rotor power P_r is equal to $s.P_s$ so the maximum power in the rotor for a speed range of ± 20% of rated speed is (P_s =5kVA):

$$P_r \; = \; s \,.\, P_s = \; 0.2 \,.\, 5 \; kVA \; = 1 \; kVA \tag{8.4}$$

The test induction machine is rated at 5kVA, and the rotor and grid-side converters are thus required to transfer one fifth of this power, 1 kVA for maximum power transfer.

The maximum rated voltage of the rotor is normally induced when the machine is at standstill, i.e. starting when the slip s = 1. As the DFIG is designed to operate with a limited speed range (1200 rev/min. – 1800rev/min.) the slip s will range between $-0.2 < s < 0.2$. The maximum required rotor voltage is thus:

$$V_s/a \,.\, s \; = \; 380/2 \,.\, 0.2 \quad = \quad 38V \tag{8.5}$$

where a is the turns ratio.

The peak value is $38.\sqrt{2} = 53.74$ V. Figure 5.9 illustrates the effect of developed power versus slip for five different values of injected rotor voltage.

Inductors rated at 27mH and 7.5A were obtained, and with operation of the DFIG based on the control of the rotor currents, an appropriate base current for the control of the rotor-side and grid-side converters is selected at 10A.

The maximum power of the induction machine available at the stator is 5kVA and the maximum designed power in the rotor is calculated at 1 kVA. The total designed available minimum power of the DFIG (in sub-synchronous mode) is thus 5 kVA – 1 kVA = 4 kVA and the total designed maximum available power (in super-synchronous mode) is 5kVA + 1 kVA = 6kVA. Thus for a speed range of 1200 rev/min to 1800 rev/min the operating power range is 4 kVA – 6 kVA.

Table 6 Base values

Base Values – Peak	
Voltage (AC)	190 V
Voltage (DC)	100 V
Current	10 A
Power	5 kVA

8.7 Current and Voltage Transducers and Signal Conditioning

8.7.1 Current Transducers

The currents and voltages associated with the stator and rotor-side and grid-side converters of the DFIG are measured for use in the control algorithms in the DSP controller. LEM current transformers (C.T.'s) are connected to the stator and rotor circuits of the induction machine to measure the stator and rotor currents. It is recommended that the rated value of LEM C.T.'s be a multiple of the rated peak value of

current. The base value of converter currents is 10A, and so LEM 55P C.T.'s are used (50A capacity, Appendix C) in the rotor-side and grid-side converters. The secondary circuit of the C.T.'s are connected to an analogue conditioning PCB and then to the ADC (analogue to digital) inputs of t

he DSP chip.

LEM voltage transformers are used to measure the grid voltage and DC link voltage of the converter.

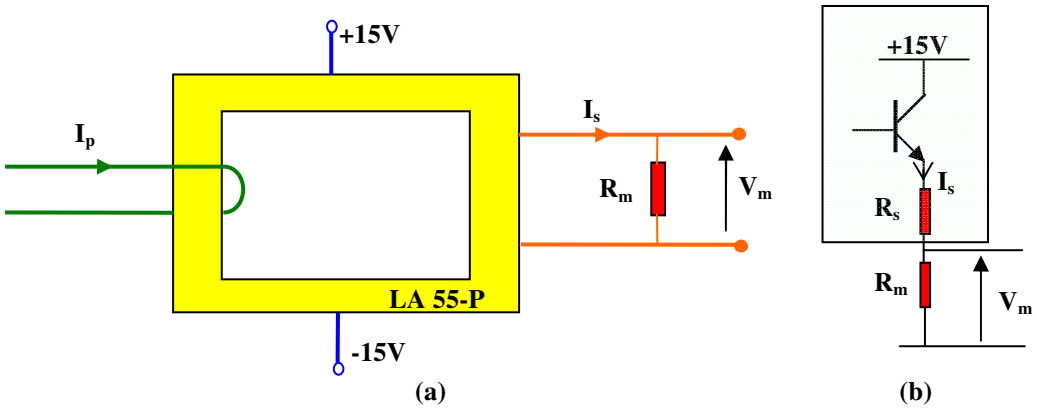

Figure 8.7 Connection of current transducer LA 55-P

In Figure 8.7, I_p is the primary current to be measured, I_s is the secondary or output current, R_m is the output resistor and V_m is the output voltage of the transducer. The output signal is the voltage drop across the resistor R_m resulting from the secondary current I_s. Figure 8.7 (b) illustrates how the output voltage is obtained from the emitter of the transistor, on the LEM device.

The current transformer LEM LA 55-P has a maximum value of 50A for one primary turn, corresponding to a secondary current value of 100mA (conversion ratio is 2/1000); further details can be found in Appendix C. The value of the measuring resistor R_m can be determined using the peak or rms value of current required. The maximum voltage level allowed at the input to the ADC on the DSP is 3V, therefore the input voltage for

all transducers is scaled in the range 0-3V (1.5V = 0 i.e. ± 1.5V (section 8.8)). To get a reasonable scaleable input into the DSP, two primary turns are used on the LEM C.T. Therefore to obtain the required value of the measuring resistor R_m:

$$R_m = \frac{V}{I_{pn} k_N} = \frac{1.5V}{10.\left(2/1000\right)mA} = 50\Omega \qquad (8.6)$$

where I_{pn} is the rms measured current and k_n is the C.T. turns ratio.

The value chosen for the measuring resistor R_m is 47Ω (closest component resistance value to 50 Ω). The recommended maximum value of measuring resistor R_m is 164.51Ω as determined in Appendix C. The voltage across the measuring resistance R_m can be obtained as:

$$V_m = R_m I_p \frac{2}{1000} \qquad (8.7)$$

The following table lists the expected output voltage versus the input current. The measuring resistor R_m is calculated to obtain 0-3 V_{pp} for a current of 0-10 A rms (peak-peak current of 28.28 A).

Table 7 LEM LA 55P measurements

Measured Current I (A rms)	Calculated Voltage V_m (V rms)	Actual Measured Voltage from PCB V_m (V rms)	DC Offset
1	0.09	0.1	1.5V
2	0.18	0.15	1.5V
3	0.28	0.27	1.5V
4	0.37	0.36	1.5V
5	0.46	0.46	1.5V
6	0.57	0.56	1.5V
7	0.67	0.67	1.5V
8	0.76	0.76	1.5V
9	0.86	0.83	1.5V
10	0.96	0.95	1.5V

11	**1.07**	**1.06**	**1.5V**
12	**1.17**	**1.17**	**1.5V**

Current LEM transducers are necessary to measure currents in the stator (I_{as}, I_{bs}, I_{cs}), rotor (I_{ar}, I_{br}, I_{cr}) and grid-side converter (I_{ag}, I_{bg}, I_{cg}).

8.7.2 Voltage Transducer

Voltage transducers (Figure 8.8) are required to measure the DC link voltage, V_{dc} and the stator/grid voltages v_a, v_b and v_c. An accurate measurement of both of these voltages is important for optimum control. To achieve this LEM V.T.'s, LV 25-P were installed. (Appendix C Table C2 includes the principal characteristics of the LV 25-P).

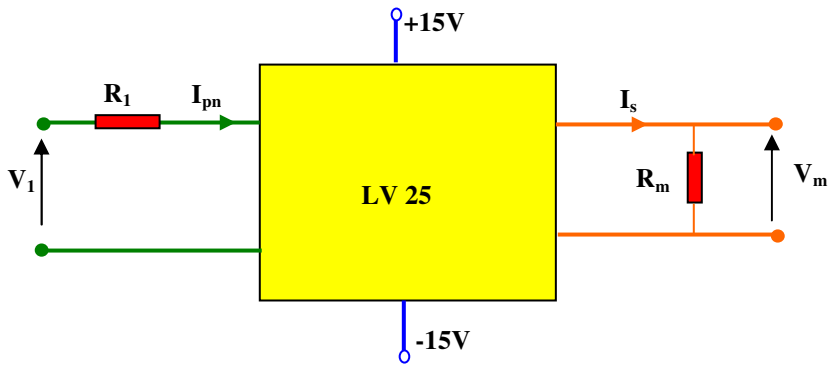

Figure 8.8 Connection of the voltage transducer LV 25-P.

8.7.2.1 Grid Voltage

The grid supply phase voltage to the DFIG is 220V rms, indicated as V_1 in Figure 8.8. It is required to determine the primary series resistance R_1 based on this value of voltage and the value of measuring resistor R_m (Figure 8.8) to convert the current signal I_s to an appropriate voltage signal. According to the data sheet (Table C2 -Appendix C), the transducer's accuracy is obtained at the nominal primary current. It is recommended that primary resistor R_1 (Figure 8.8) should be calculated so that the nominal voltage to be

measured corresponds to a primary current of 14mA (peak). The resistance R_1 can be determined as:

$$R_1 = \frac{V_{pn}}{I_{pn}} - R_p \qquad (8.8)$$

where V_{pn} is the nominal voltage to be measured corresponding to a nominal primary current I_{pn}. The primary resistance R_p is 250Ω [Appendix C], therefore the resistor R_1 for a grid voltage of 220V is:

$$R_1 = \frac{\sqrt{2}.220}{14.10^{-3}} - 250 = 21.97\,k\Omega \qquad (8.9)$$

The resistor R_1 in (8.9) carries primary current and needs to be of sufficient wattage to dissipate the heat generated. The available resistors (7W, Appendix C) are 17.866kΩ + 4.61kΩ = 22.476kΩ, and these are chosen for R_1. The calculated peak primary current is:

$$I_p = \frac{V}{R_1 + R_P} = \frac{311V}{22.476.10^3 + 250} = 13.84mA \qquad (8.10)$$

The required value of the measuring resistor R_m to ensure the output voltage range is within 0-3V (±1.5V) is calculated as:

$$R_m = \frac{V}{I_{pna} k_N} = \frac{1.5V}{13.84mA.\frac{2500}{1000}} = 43.35\Omega \qquad (8.11)$$

According to the LEM datasheet (Appendix C), the minimum value of R_m with a ± 12V power supply (obtained from Convel ± 15V power supply) is 30Ω. The value obtained in (8.11) is acceptable. Test results are tabulated in Table 8.

Table 8 LEM LV 25P/PCB measurements

Voltage (V)	Calculated Voltage V_p (V)	Actual Measured Voltage V_p(LEM) (V)	Actual Measured Voltage PCB O/P (V)
40	0.19	0.2	0.21
120	0.57	0.59	0.61
200	0.95	0.96	0.98
280	1.34	1.36	1.38
311	1.5	1.49	1.51

8.7.2.2 DC Link Voltage

The level of the DC link voltage must be greater than the peak value of the rotor voltage.

The normal DC-link voltage for the converter is set at 5% higher than the peak line-to-line voltage across the grid converter ac side. Consideration is also required for the grid side voltage; however a three-phase variac is available to alter this voltage. The grid voltage can therefore be matched to the desired DC link voltage chosen.

Initially a DC link voltage of 280V was chosen, and this voltage corresponds to an output voltage of 3V of the LEM (output varies from 0 to 3V). It was decided to work with respect to the maximum value of measuring resistance (Figure 8.8) allowed R_m = 100Ω, and thus determine the measuring resistor R_m before determining primary resistor R_1. The actual value of R_m used is 97.88Ω.

$$I_p = \frac{V}{R_m k_N} = \frac{3V}{97.88.\frac{2500}{1000}} = 12.26mA \qquad (8.12)$$

R_1 (Figure 8.9) can be obtained as:

$$R_1 = \frac{280}{12.26.10^{-3}} - 250 = 22.588k\Omega \qquad (8.13)$$

The available resistors (at 7W, Appendix C) are 17.866kΩ + 4.61kΩ = 22.476kΩ. Thus calculated primary current is:

$$I_p = \frac{V}{R_1 + R_C} = \frac{280V}{22.476.10^3 + 250} = 12.32mA \qquad (8.14)$$

The voltage output signal from the LV25 versus the DC input voltage is tabulated in Table 9 (was 8.4).

Table 9 LEM LV 25P output (DC Link)

DC Voltage (V)	Calculated Voltage V_m (V)	Actual Measured Voltage V_m(LEM) (V)	Actual Measured Voltage PCB O/P (V)
40	0.43	0.43	0.44
80	0.86	0.86	0.84
120	1.29	1.3	1.32
160	1.72	1.72	1.75
200	2.15	2.15	2.2
240	2.58	2.58	2.61
276	2.97	2.96	2.98
280	3.01	3.0	3.1

8.7.3 Signal Conditioning

The LEM current sensors (LEM 55-P) are supplied with ± 15 V and thus can measure ac currents. The measuring current ratio can be altered by changing the number of turns on

the primary winding and the output is a bipolar voltage. The A/D power signal inputs to the TI TMS320F2812 microprocessor have to be scaled and conditioned appropriately to generate unipolar signals of magnitude variation 0 to 3 V, otherwise problems and malfunction of the microprocessor may arise. The output voltage signals of the LEM C.T.'s are proportional to primary current and vary between -1.5V and +1.5V, thus it is necessary to level shift the voltage signals to ensure that they are in the range 0-3V. To achieve this voltage level and to filter-out any high frequency disturbances, an analogue PCB was designed in Number One Systems Easy PC[9] and fabricated and constructed using opamps TL084 (Figure 8.9). For accuracy 1% resistors were used. The signals from the LEM voltage transformers are connected to the analogue interface PCB's. The signal outputs from these PCB's are designed to be in the range 0-3V with high frequencies eliminated.

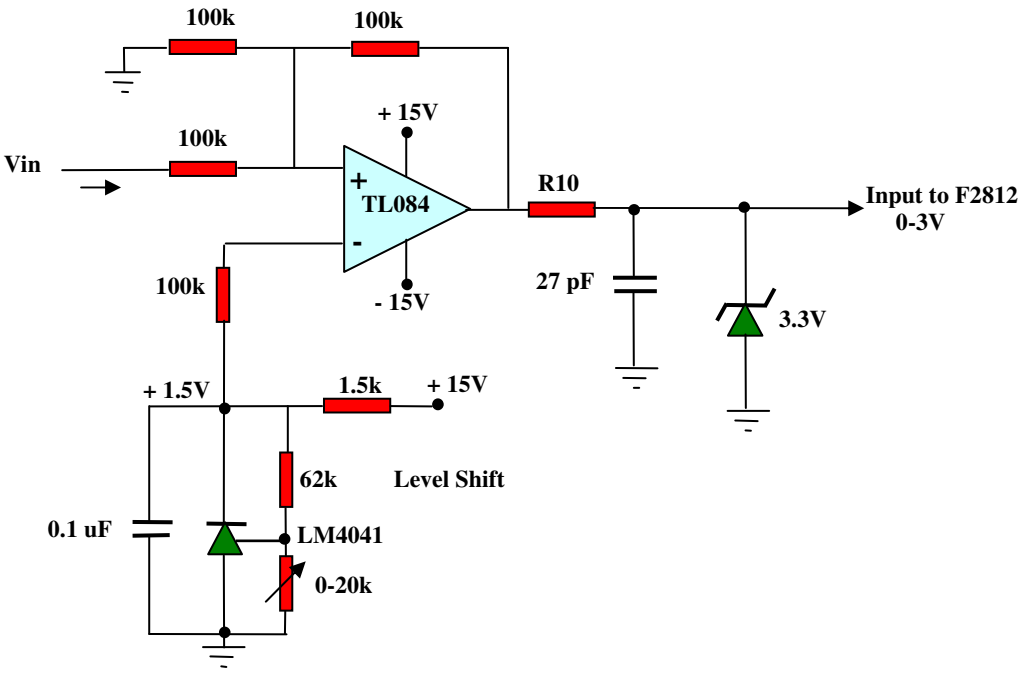

Figure 8.9 Analogue circuit board for LEM voltage signals

[9] PC Board Design Software

The conditioning PCB illustrated in Figure 8.9 was acceptable for measuring voltage; however it was not acceptable for measuring currents due to the high levels of noise generated during IGBT switching operations at high frequencies. To reduce noise transferred to the DSP a four stage PCB was designed in Number One Systems Easy PC, fabricated and constructed according to the schematic diagram in Figure 8.10.

The ac currents in the stator, rotor and grid side of the DFIG are passed through current transformers, (LEM 55-P, Appendix C1.4) as described in Section 8.7.1. A voltage signal proportional to current is obtained at the output of the C.T.'s and this signal is the input to the first stage of Figure 8.10. The difference of the voltage signals at the inputs is amplified at this stage. The Common Mode Rejection (CMR) property of this stage, helps to reduce the incoming noise and offers better signal to noise ratio at the output. The circuit is constructed with TL084 op-amp and 1% resistors for improved accuracy.

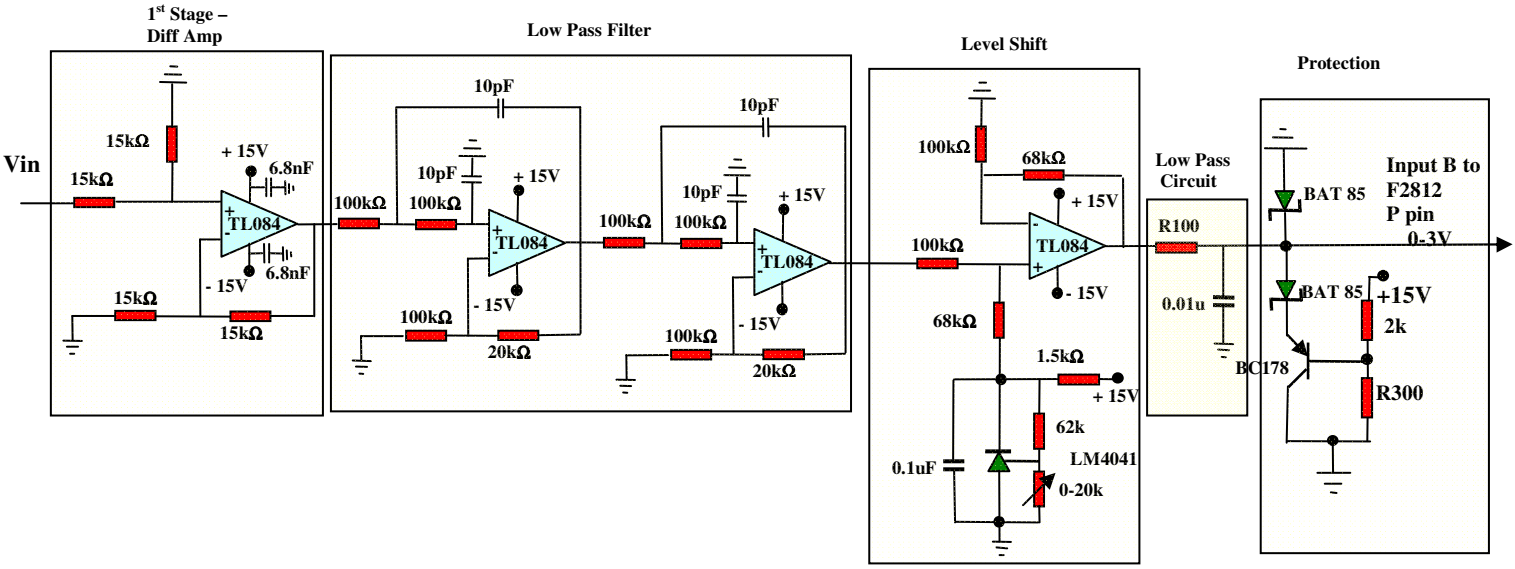

Figure 8.10 Analogue circuit board for LEM current signals

The low pass filter stage, comprising of a four pole Sallen & Key configuration, is applied to remove the high frequency noise coupled to the input current signals. The required dc offset voltage of 1.5 V is added to the differential non-inverting input of the TL084. A precision voltage reference (LM4041-ADJ) is applied in the circuit to obtain a stable 1.5 V from +15 V supply. Therefore the output voltage of the analogue PCB will vary between 0 and +3 V.

8.7.3.1 Testing of Conditioning Circuit

To test the performance of the analogue interface PCB, voltage was impressed onto the DC link and the DSP was programmed to generate PWM pulses for the IGBT driver circuits of the rotor side converter. The rotor side converter was connected to a resistive load bank and was thus configured as an inverter. Current was driven from the DC link through the converter to the load resistor bank. This current was measured using LEM 55 C.T.'s and the output signals delivered to the PCB of Figure 8.10. The results obtained are illustrated in Figure 8.11.

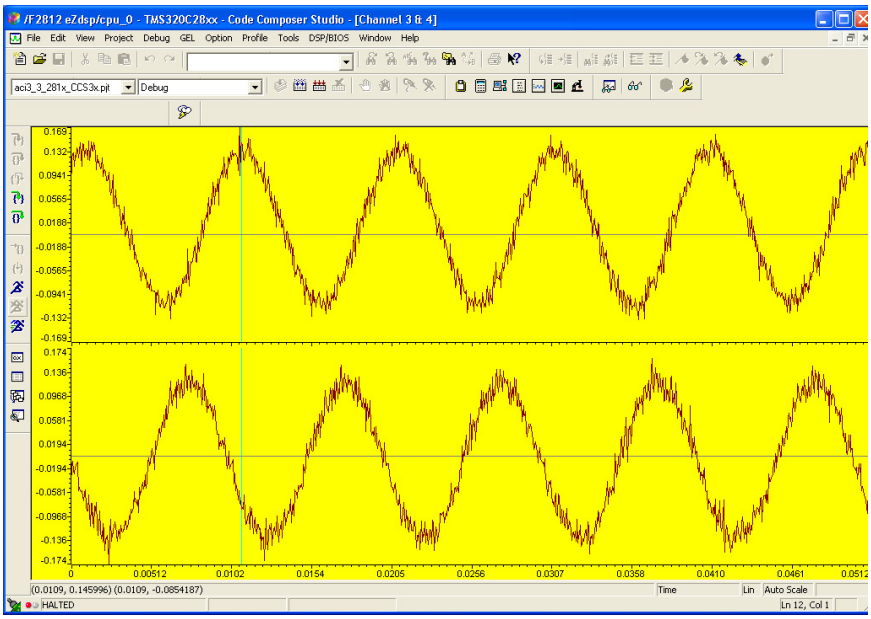

Figure 8.11 Code Composer Studio – measurement of TI F2812 current at 1.5A

It is clear from Figure 8.11 that this noise level is unacceptable. The noise was traced to the 0V power rail. All grounding was adequate and the noise problem persisted and thus a further circuit was devised to overcome this problem.

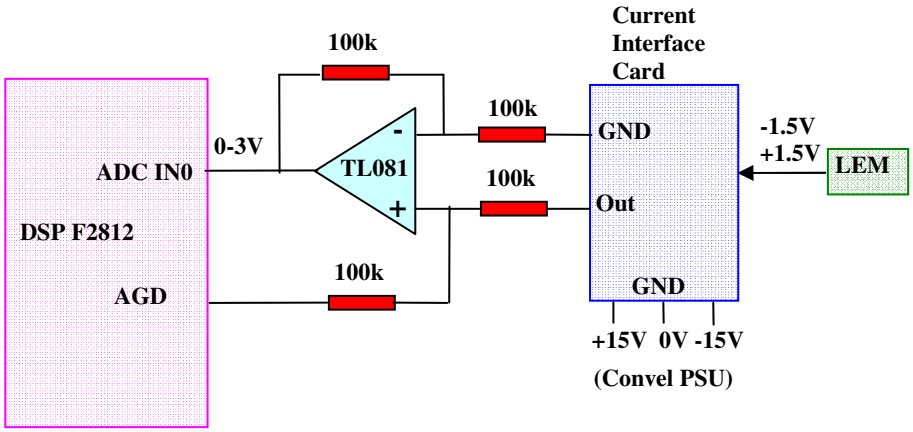

Figure 8.12 Compensating circuit

The compensating circuit (Figure 8.12), cross-couples the power supply ground (GND) and the DSP analogue ground (AGD). The compensating PCB assists in reducing the noise transferred to the DSP chip. The reduction in the noise level is observed in Figures 8.13 and 8.14.

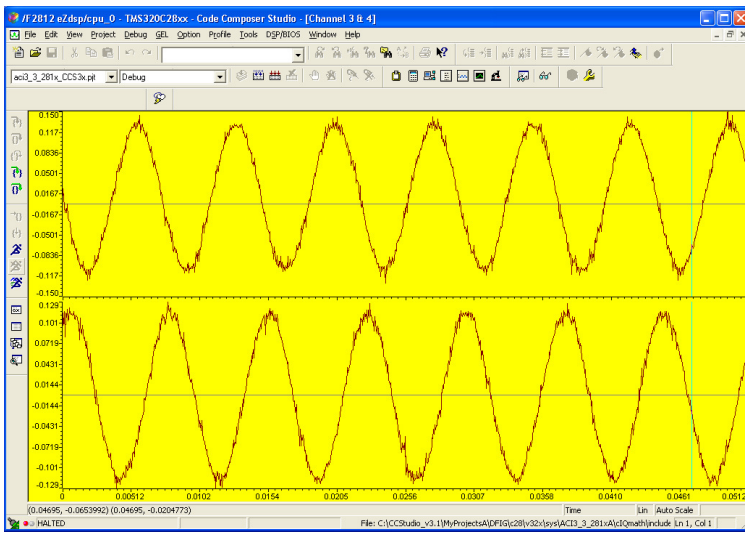

Figure 8.13 Measurement of F2812 current signal at 1.5A with insertion of compensating circuit

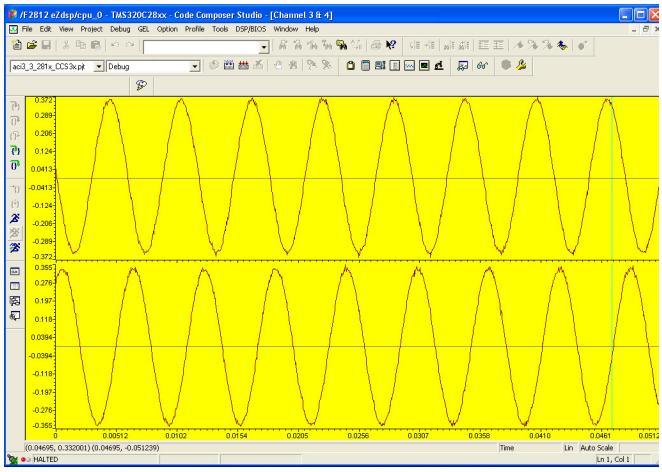

Figure 8.14 Code Composer Studio – Measurement of DSP current signal at 4.5A with insertion of compensating circuit

The measured voltage signal in the DSP representing a current of 4.5A is illustrated in Figure 8.14. It is a good representation of the current. The noise level on the 0V rail is constant at about 70mV. When progressively larger currents are measured, the noise imposed on the voltage signal is reduced proportionally, as illustrated in the reduction of noise in Figure 8.14 when compared to the noise level plot in Figure 8.13.

8.8 Acquisition of Analogue Variables

8.8.1 Analogue Input Signals to DSP

The analogue signals described in Section 8.7 and modulated through the analogue PCB's are acquired by the DSP.

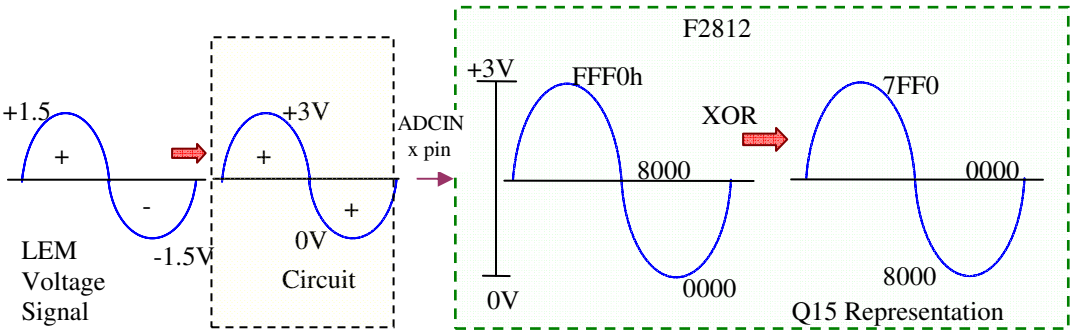

Figure 8.15 DSP analogue input and number conversion scheme for bipolar input signals.

The DSP source code converts the input analogue signal into a Q15 number representation. Figure 8.15 illustrates the number conversion required to facilitate measurement. The analogue PCB designed for the LEM current and voltage transducers, modulates the -1.5V to +1.5V output signal from the transducers to a positive 0-3V signal, suitable for the DSP ADC. The DSP ADC has 12 bit resolution with left justified in the 16 bit ADC result register, i.e. the final 4 bits in the register are zeros. So for a 0-3V input this translates to a range of 0000h to FFF0h, or 0 – 65,536. Because it is required to use a bipolar signal in the software code, this signal range is then exclusive-or'd (XOR) with 8000h, resulting in a signal range of 8000h (representing -32,768) to 7FF0h (representing +32,752).

In Q15 format (with 16 bit word) this is:

8000h – 7FFFh = 1.000 0000 0000 0000 - 0.111 1111 1111 0000

The digital value of the input analogue signal is:

$$4095 \frac{.Input\ analogue\ voltage - ADCIO}{3}$$

where ADCIO is the DSP analogue ground and is 0 V.

For example for an input voltage of 3 V, the digital value is: 4095 . 1 = 4095.

Each analogue PCB was designed to process six channels and thus two PCB's are required to accommodate the analogue inputs required. The analogue-to-digital inputs required are (Figure 8.1):

- Rotor currents, $I_{ar,}$ I_{br} and I_{cr}.
- Grid voltages, $V_{ag,}$ V_{bg} and V_{cg}.
- Grid-side currents, $I_{ag,}$ I_{bg} and I_{cg}.
- DC link voltage V_{dc}.
- Speed control input

The number of analogue signal inputs required is thus 11. An equipment schedule is listed in Appendix A.

8.8.1 Input and Output Connections to DSP

Table 10 Input ADC connections to DSP

P5 Pin No.	P5 Signal	Measurement	P9 Pin No.	P9 Signal	P9 Pin No.	P9 Signal	Measurement
1	ADCINB0	Grid Va	1	GND	2	ADCINA0	Rotor Side Ia
2	ADCINB1	Grid Vb	3	GND	4	ADCINA1	Rotor Side Ib
3	ADCINB2	Grid Vc	5	GND	6	ADCINA2	Rotor Side Ic
4	ADCINB3	Vdc	7	GND	8	ADCINA3	Stator Current I_a
5	ADCINB4	Grid Current I_a	9	GND	10	ADCINA4	Stator Current I_b
6	ADCINB5	Grid Current I_b	11	GND	12	ADCINA5	Stator Current I_c
7	ADCINB6	Grid Current I_c	13	GND	14	ADCINA6	Control Input
8	ADCINB7		15	GND	16	ADCINA7	
9	ADCREFM		17	GND	18	VREFLO	
10	ADCREFP		19	GND	20		

Table 10 lists the ADC input channels for the connectors P5 and P9 and the relative process signals connected.

The PWM output pins on the P8 connector for both the rotor-side and grid-side converters are shown in Table 11 and Figure 8.16. Also shown are the input pins for the incremental shaft encoder; QEP1 for the channel A pulse, QEP2 for the channel B pulse, and QEP11 for the index pulse.

Table 11 Encoder and PWM connections to DSP

P8 Pin No.	P8 Signal	Device
6	CAP1/QEP1	Encoder Pulse A
7	CAP2/QEP2	Encoder Pulse B
8	CAP3/QEP11	Encoder Zero Pulse
9	PWM1	Rotor Side Converter
10	PWM2	Rotor Side Converter
11	PWM3	Rotor Side Converter
12	PWM4	Rotor Side Converter
13	PWM5	Rotor Side Converter
14	PWM6	Rotor Side Converter
30	PWM7	Grid Side Converter
31	PWM8	Grid Side Converter
32	PWM9	Grid Side Converter
33	PWM10	Grid Side Converter
34	PWM11	Grid Side Converter
35	PWM12	Grid Side Converter

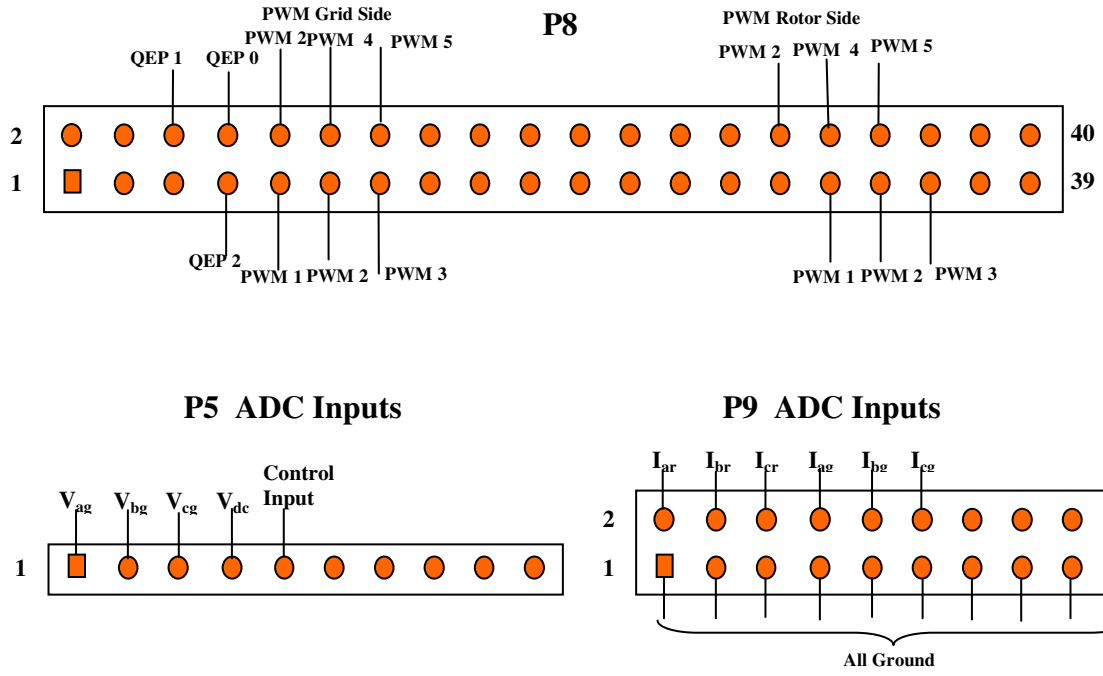

Figure 8.16 DSP interface input connectors

8.9 Speed and Position Acquisition

8.9.1 Shaft Encoder

An incremental shaft encoder was mounted onto the rotor shaft of the induction machine, enabling measurement of rotor position and speed. The incremental shaft encoder produces a pair of quadrature square-wave output pulses (A and B), each of which produces 1000 pulses per revolution of the machine shaft. There is also a third index pulse (Z), which produces a single pulse per revolution. The incremental shaft encoder chosen for this work is a 1000 line Hengstler RI59 incremental encoder (Appendix D). Using a dedicated quadrature counter it is possible to count both the rising and falling edges of both the A and B signals so that one revolution of the rotor shaft may be divided into 4000 different values. In other words a 1000 line encoder allows the measurement of rotor position to 12-bit resolution. The direction of rotation may also be inferred from the relative phasing of quadrature signals A and B. The two pulses A and B, allow the DSP controller to detect the direction of the rotor; the B pulse lags the A pulse by 90º in the positive direction and conversely the B pulse leads the A pulse by 90º in the negative direction. Based on this, the software section of the design must interrupt the speed of the rotor based on the number of pulses it receives.

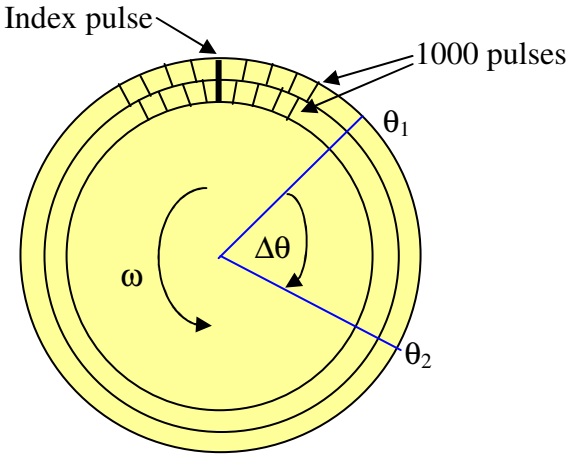

Figure 8.17 Incremental shaft encoder

Figure 8.17 shows a typical configuration for a shaft encoder speed sensor disk mounted on a machine shaft, for rotational speed, position and direction sensing applications. On rotation of the machine shaft, the incremental shaft encoder generates two quadrature pulses and one index pulse. These signals are shown in Figure 8.18 as QEP_A, QEP_B and QEP_index [109].

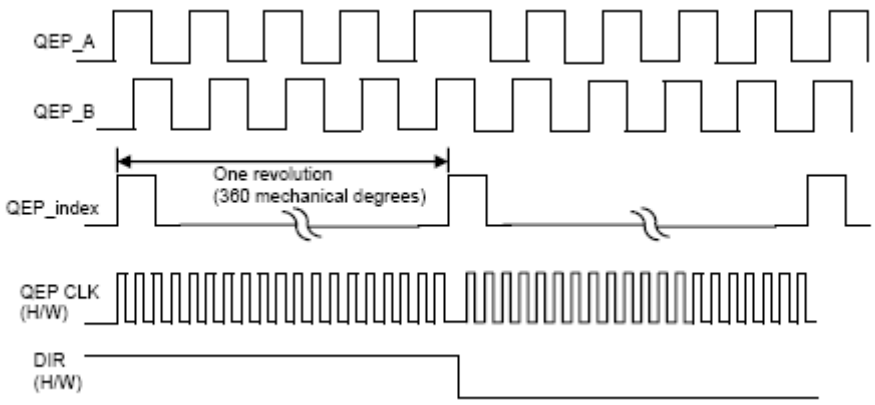

Figure 8.18 Quadrature encoder pulses (QEP), decoded timer clock and direction signal.

QEP_A and QEP_B signals are applied to the QEP1 and QEP2 pins of DSP device (Table 12 and Figure 8.16, pin numbers 6, 7 on the P8 connector block). The QEP_index signal is applied to the CAP3 pin (pin 8 on the P8 block). The QEP interface circuit in the DSP, when enabled (CAPCONx (13, 14)), counts these QEP pulses and generates two signals internal to the device. These two signals are shown in Figure 8.18 as QEP_CLK and DIR. The QEP_CLK signal is used as the clock input to GP Timer2. DIR signal controls the GP Timer 2 counting direction.

The number of pulses generated by the optical encoder is proportional to the angular displacement of the machine shaft. A complete 360° rotation of motor shaft generates 1000 pulses of each of the signals QEP_A and QEP_B observed in Figure 8.18. The

QEP circuit in DSP counts both edges of the two QEP pulses. Therefore, the frequency of the counter clock, QEP_CLK, is four times that of each input sequence. This means, that for 1000 pulses for each of QEP_A and QEP_B, the number of counter clock cycles will be 4000. Since the counter value is proportional to the number of QEP pulses, therefore it is also proportional to the angular displacement of the machine shaft.

The dedicated QEP module within the DSP manages the conversion of the dual quadrature encoder output signals to represent the actual rotor position at all times. In this way, the DSP control software can simply read the actual rotor position whenever it is needed by the algorithm.

The rated speed of the induction machine used in this project is 1500 rev/min. corresponding to 25 rev/sec. Therefore the DSP controller will receive from each channel (A and B) a signal with a frequency of 25 kHz:

(1000 pulses per revolution) × 25 (revolutions per second) = 25 kHz at rated speed.

The detection of a pulse means that the rotor has progressed by:

$$(360^{o} \text{ per revolution}) \div (4000 \text{ pulses per revolution}) = 0.09^{o} \text{ per pulse.}$$

The shaft encoder is supplied with a voltage supply of +15V resulting in square-wave voltage output pulses with an amplitude of +15V. The ADC of the DSP is very sensitive to voltage input other than the specified level (0-3V). A PCB was designed with a voltage level shifter and voltage clamping stage, illustrated in Figure 8.19. The +15V pulses are supplied to the QEP interface PCB Figure 8.19, which conditions the signals and clamps the output pulses to +3V. A transistor (BC178) and zener diode (BAT85) based protection circuit is configured at the output of the QEP PCB which prevents the voltage at the voltage output of the PCB from exceeding 3 V.

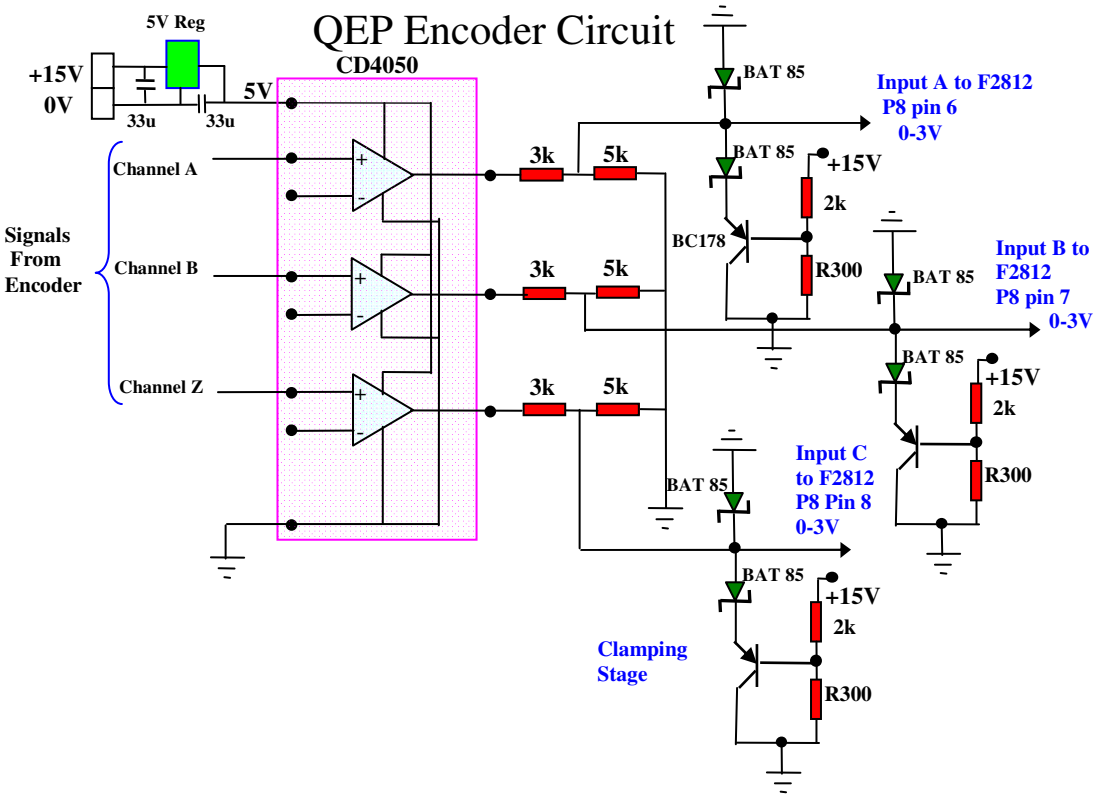

Figure 8.19 Incremental shaft encoder interface circuit QEP

The +15V pulses are supplied to the QEP interface PCB Figure 8.19, which conditions the signals and clamps the output pulses to +3V. A transistor (BC178) and zener diode (BAT85) based protection circuit is configured at the output of the QEP PCB which prevents the voltage at the voltage output of the PCB from exceeding 3 V.

The shaft encoder and PCB voltage were tested. A plot of the output voltage channel A of the shaft encoder (15V) and the output voltage of the interface PCB (3V) is shown in Figure 8.20. Under test conditions the frequency measured was 25kHz (the speed of the machine was 1500 rev/min). It is observed in Figure 8.20 that the PCB output voltage signal is clamped at 3V and it is also evident that output voltage of the interface PCB improves the signal quality.

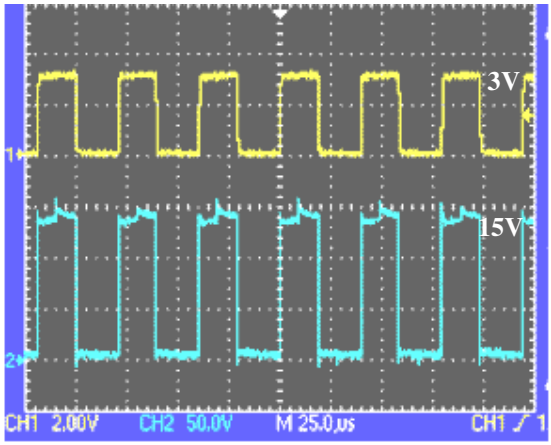

Figure 8.20 Incremental shaft encoder pulses: bottom plot is the output of the shaft encoder channel A; the top plot is the output of the interface PCB

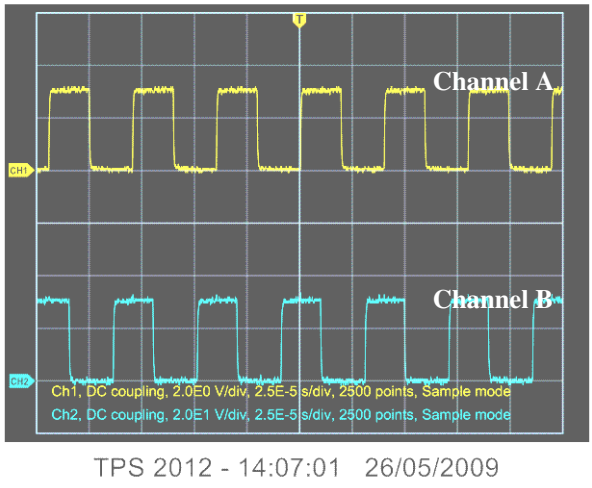

Figure 8.21 Incremental shaft encoder pulses: channel A is top and channel B is bottom.

Figure 8.21 illustrates the 90° displacement between channel A and channel B.

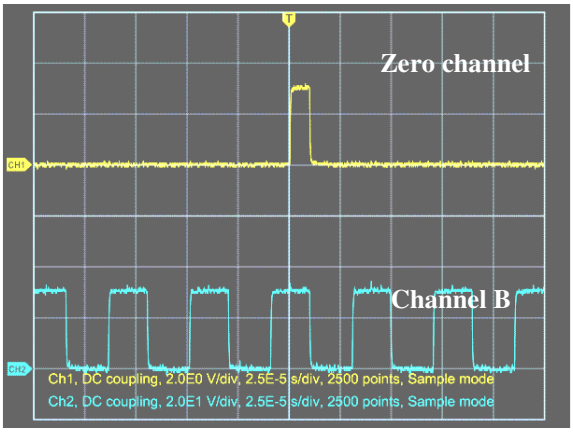

Figure 8.22 Incremental shaft encoder zero pulse

The zero reference pulse occurs just once per revolution and is shown in Figure 8.22 with channel B.

8.9.1.1 TI Implementation of QEP

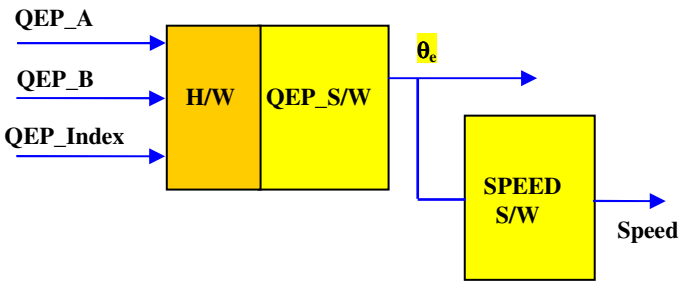

Figure 8.23 QEP encoder software module

Induction machine rotor position and speed are determined in the software program as illustrated in Figure 8.23. Voltage signal pulses emanating from the incremental shaft encoder as described in Section 8.9.1 are supplied to the DSP. The inputs required by the software (Figure 8.23) are channels A, B (QEP_A and QEP_B) and the zero pulse (QEP_Index) obtained directly from the encoder PCB. The output of the QEP software

module is the electrical angle θ_e (ElecTheta), which is supplied as an input parameter to the speed software module.

8.9.1.2 Determination of Reference Frame Angles with PLL

The inputs to the software PLL module are the grid phase voltages and the output is the tracked phase angle θ_e (described in Chapter 6, Section 6.4). The PLL tracks the stator/grid voltage and maintains the quadrature voltage V_{qs} at a value of zero. This is illustrated in Figure 8.24 where grid voltage V_{qs} is maintained close to zero and V_{ds} is one per unit..

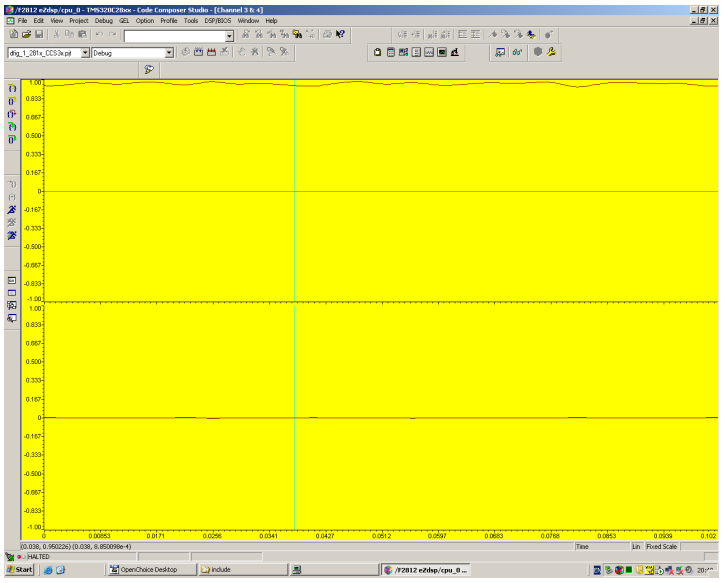

Figure 8.24 Grid Voltage V_{ds} (top trace) and V_{qs} (bottom trace)

Park transformations require the correct reference angles for transformation into the positive and negative reference frames. The positive grid voltage angle is obtained using *pll1_V1.Out* in the software program and this is illustrated in the top plot in Figure 8.24. The negative sequence grid voltage angle is obtained using *-pll1_V1.Out* and is illustrated in the bottom plot in Figure 8.25. The angle *pll1_V1.Out* is the output of the phase locked loop PLL routine.

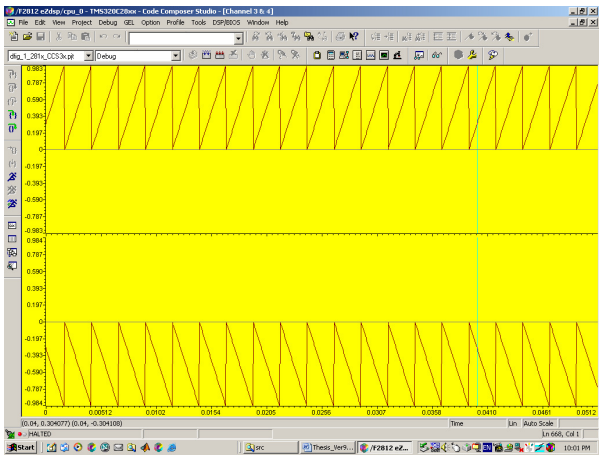

Figure 8.25 Positive sequence grid voltage angle θ_e^+ (top trace) and negative sequence grid voltage angle θ_e^- (bottom trace)

Figure 8.26 illustrates the positive sequence grid voltage angle and the double frequency angle necessary for negative sequence compensation implementation.

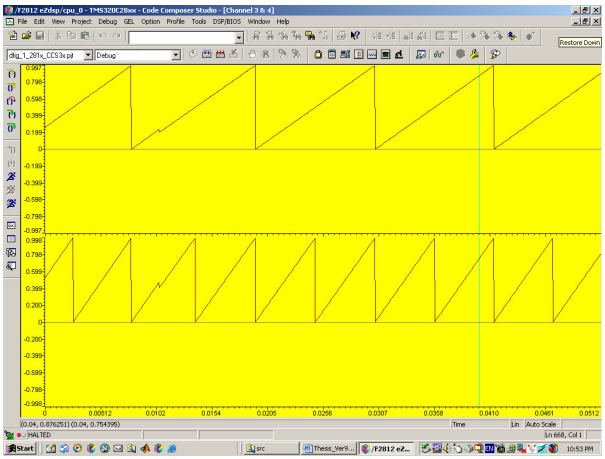

Figure 8.26 Grid voltage angle θ_e (Top) and double frequency grid voltage angle $2x\theta_e$ (Bottom)

8.9.1.3 Determination of Slip Frequency With PLL

Slip frequency is obtained by calculating the difference between grid voltage frequency and rotor voltage frequency. The slip frequency (ω_{slip}) and slip angle (θ_{sl}) are required to control the rotor side converter in the synchronous reference frame. Plots of slip angle

(θ_{sl}) and the PLL angle θ_e versus time for various induction machine shaft speeds are illustrated in Figure 8.27 and Figure-8.28.

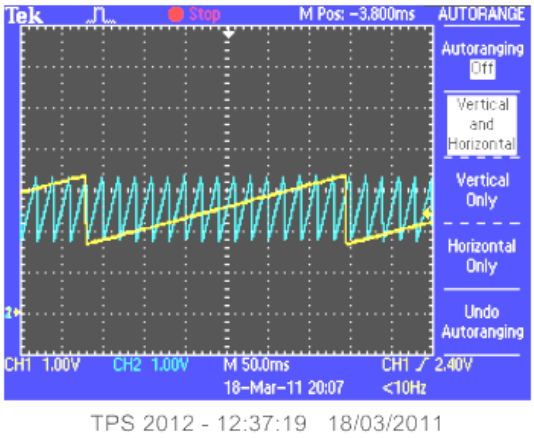

Figure 8.27 *PLL* output (Blue Trace) and θ_{slip} (Yellow Trace) at a speed of 1462 rev/min.

In Figure 8.27 the resolution of the x-axis is 50ms/div., therefore the time required for a period of the slip angle θ_{sl} (yellow trace) is obtained as 6.25 divisions x 50ms = 312.50ms. The value of the slip frequency is:

1/0.3125 = 3.2. Hz (3.2Hz = 96 rev/min.)

The speed of the machine is determined as:

50Hz – 3.2Hz = 46.8 Hz = 1404 rev/min.

A speed of 1402 rev./min. was measured on the induction machine shaft with a tachometer.

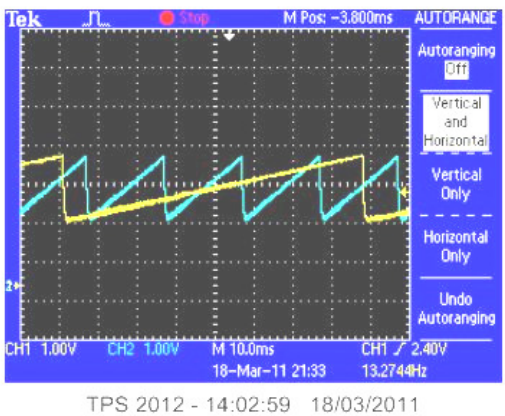

Figure 8.28 PLL output and θ_{slip} at a speed of 710 rev/min.

In Figure 8.28 the measured time for the slip angle θ_{sl} is 78ms. The value of the slip speed is:

$$1/0.076 = 13.33 \text{ Hz} = 394.74 \text{ rev/min.}$$

The calculated machine speed based on this measurement is:

$$50\text{Hz} - 13.33\text{Hz} = 36.84 \text{ Hz} = 1105.26 \text{ rev/min.}$$

A tachometer measurement of the induction machine shaft speed indicated 1103 rev./min.

8.10 DC-link capacitance

The DC-link capacitor current is discontinuous; this is due to switching on and off of the charging current at the switching frequency of the converter. This creates a voltage ripple in the DC-link. This voltage ripple must be made small enough for the voltage to be virtually constant during a switch period and this sets a lower limit on the capacitor size. Sizing of the DC link capacitor can represent a trade-off. For a given load, a larger capacitor will reduce ripple but will cost more and will create higher peak currents in the supply feeding it. The minimum capacitance value can be designed to limit the DC-link voltage ripple to a specified value, typically 1 to 3%. Thus the peak to peak ripple voltage of the DC capacitor is adopted as a design criterion for the DC-link capacitor size.

The capacitor size can be determined based on V_{dc} and the maximum power transferred through the DC link. The bus voltage V_{dc} selected is 280 V (Section 8.3.2) and the maximum rotor power is 1 kW (Section 8.3). Allowing for a maximum voltage ripple of 1.5% the maximum DC-link voltage V_{dc_max} is 284.2V and the minimum value V_{dc_min} is 275.8V. The minimum value of the DC link capacitor, C_{min} can be obtained as:

$$C_{\min} = \frac{2.P}{\left(V_{\max}^2 - V_{\min}^2\right) f_{conv}} = \frac{2.(2.3.10^3)}{\left(284.2^2 - 275.8^2\right).300} = 1.4mF \quad (8.15)$$

where P is the load power through the converter in watts, f_{conv} is the ripple frequency, V_{max} is the maximum DC-link voltage and V_{min} is the minimum DC-link voltage.

The most suitable commercially available capacitor is 3.1 mF and this value was chosen.

The charging time is:

$$t_c = \frac{\cos^{-1}\left(\frac{V_{\min}}{V_{\max}}\right)}{2\pi f} = \frac{\cos^{-1}(0.969)}{2\pi 50} = 0.776mS \quad (8.16)$$

And the discharging time:

$$t_{dc} = \frac{1}{f_{conv}} - t_c = \frac{1}{300} - 0.776 = 2.56ms \quad (8.17)$$

the average charging current is given by

$$I_c = C\frac{\Delta V}{t_c} = C\frac{V_{\max} - V_{\min}}{t_c} = 3.1\frac{284.2 - 275.8}{0.776} = 33.56A \quad (8.18)$$

The capacitor should also be capable of withstanding a 33.6A charging current.

8.11 Grid-Side line filter

The DFIG grid-side converter converts ac power into DC power (subsynchronous) or converts the DC link power into regulated ac power (super-synchronous). The ac input inductor acts as a first-order filter, and its function is to minimize the amplitude of the ac mains current harmonics, resulting from the high frequency switching of the converter.

The use of PWM techniques, yields a significant reduction in the value of the line inductors and the dc capacitor, as compared with other techniques [112]. However, the smaller the values of L_g and C, the more sensitive the system becomes to input voltage unbalance. If the value of the input inductor L_g is smaller, the negative sequence

component of the input current will be larger thus increasing the value of the second harmonic of the dc voltage.

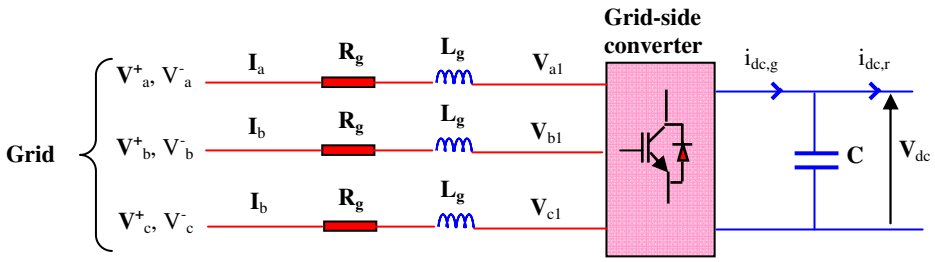

Figure 8.29 Grid-side converter schematic when network supply is unbalanced

In this work the values of the grid-side line inductor L_g (Figure 8.29) and the DC link capacitor C, are calculated as normal based on rated values of the induction machine and converters. The improvement in the performance of the DFIG during supply voltage unbalance conditions will be dependent on the modifications in the control structures in both the rotor-side and grid-side converters.

The value of the line inductor for a current ripple of 1A can be calculated as [112]:

$$L_g = \frac{V_g}{2\sqrt{6} f_s I_{ripple}} = \frac{100/\sqrt{3}}{2\sqrt{6}\, 2.5.10^3 .1} = 4.71mH \qquad (8.19)$$

8.12 Code Structure

The control code is written in C^{++} and compiled in an operating platform called Code Composer Studio[10] (CCS), version 3.1. The CCS compiler links and assembles the program which is then transferred to the DSP micro-controller. The Code Composer Studio platform includes a fully integrated code editing environment tuned for writing C, C++ and DSP assembly code.

[10] Texas Instruments Platfrom

One of the benefits of using the DSP is that there are two event managers, Event Manager A and Event Manager B and each can be configured to operate independently using interrupts. Event Manager A has been configured for the Rotor-side converter and Event Manager B configured for the Grid-side converter.

The space vector switching scheme discussed in Chapter 6, Section 6.5, was implemented using CCS and downloaded to the Texas Instruments DSP microcontroller. The DSP algorithm is interrupt driven with timers used for this purpose. Timer 1 underflow (Event Manager A), is used for the rotor-side converter control and Timer 3 underflow Event Manager B), is used for the grid-side converter control. While the DSP algorithm waits for an interrupt to occur, it will continue to execute the code in the main-loop routine until a Timer 1 or Timer 3 underflow interrupt is generated by Event Managers A or B. Event Managers A and B can work independently of each other.

The DSP controller will create the desired symmetrical synchronized PWM signals through the 6 PWM signal generators in each Event Manager, EVA and EVB. In EVA the 6 PWM signals are applied to the 6 IGBT drivers on the rotor-side converter and in EVB the 6 PWM signals are applied to the 6 IGBT drivers on the grid-side converter. The frequency of the triangular wave is set at 2.5 kHz and this is compatible for use with the IGBT's. In spite of this, because of the finite turn-on and turn-off times associated with any type of switch, the design requires the inclusion of slight time delays when the IGBT's are switching.

The code is comprised of a main program and associated include (*.h) and library files. The main program is called DFIG_1 and among the files used in this program are the following files/modules (Appendix G):

DFIG_1	-	Main program
ADC	-	Analogue to digital register control
Adc_duala	-	Analogue to digital control –Rotor & Grid
Pwm_duala	-	Pwm control – Rotor & Grid
Ramp_cntl	-	Ramp control
Rampgen	-	Ramp angle generation
QEP	-	Encoder control
Pll_1	-	Phase locked loop
CLARKE	-	Clarke transformation
Pid_pir	-	Proportional, Integral and Resonant control
PARK/IPARK	-	Park and Inverse Park transformations
SPEED	-	Speed calculation
SVGEN_DQ	-	Space vector generation
Theta_slip	-	Slip angle calculation
IIR	-	Infinite impulse response filter
Filter	-	Filter control
Negseq_comp	-	Negative sequence compensation
Vr1_Comp	-	Decoupling control
Vgrid_Comp	-	Decoupling control

8.12.1 ADC

The DSP features a very fast integrated 12 bit ADC as described in section 8.2. The 16 ADC channels are operated as two independent dual sequencers (8 in a group), with 1-8

being assigned to the rotor side converter and 9-16 assigned to the grid side converter. Figure 8.30 shows the block diagram of the DSP ADC module.

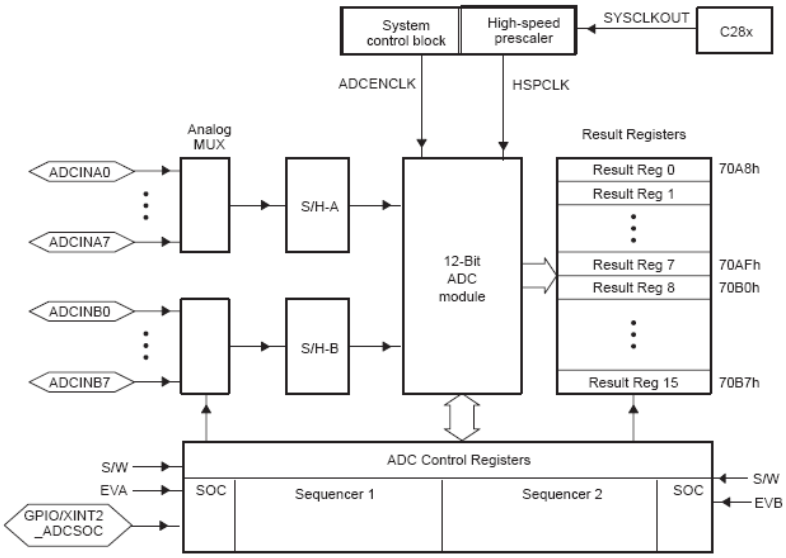

Figure 8.30 DSP ADC Configuration

The software program allows 16-channel analogue-to-digital conversion of unipolar signals with programmable gains and offsets. The conversions are triggered on GP Timer 1 underflow for rotor side converter and GP Timer 2 for the grid side converter.

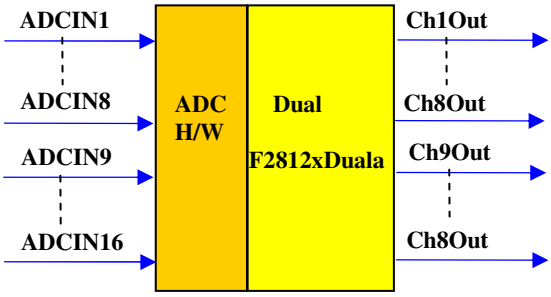

Figure 8.31 Analogue to Digital Converter Software Block

Channels ADCIN1 – ADCIN8 on the DSP are reserved for the rotor side converter and channels ADCIN9 – ADCIN16 are reserved for the grid side converter. The channel inputs are allocated in Section 8.8.1.

The general program algorithm is illustrated in Figure 8.32.

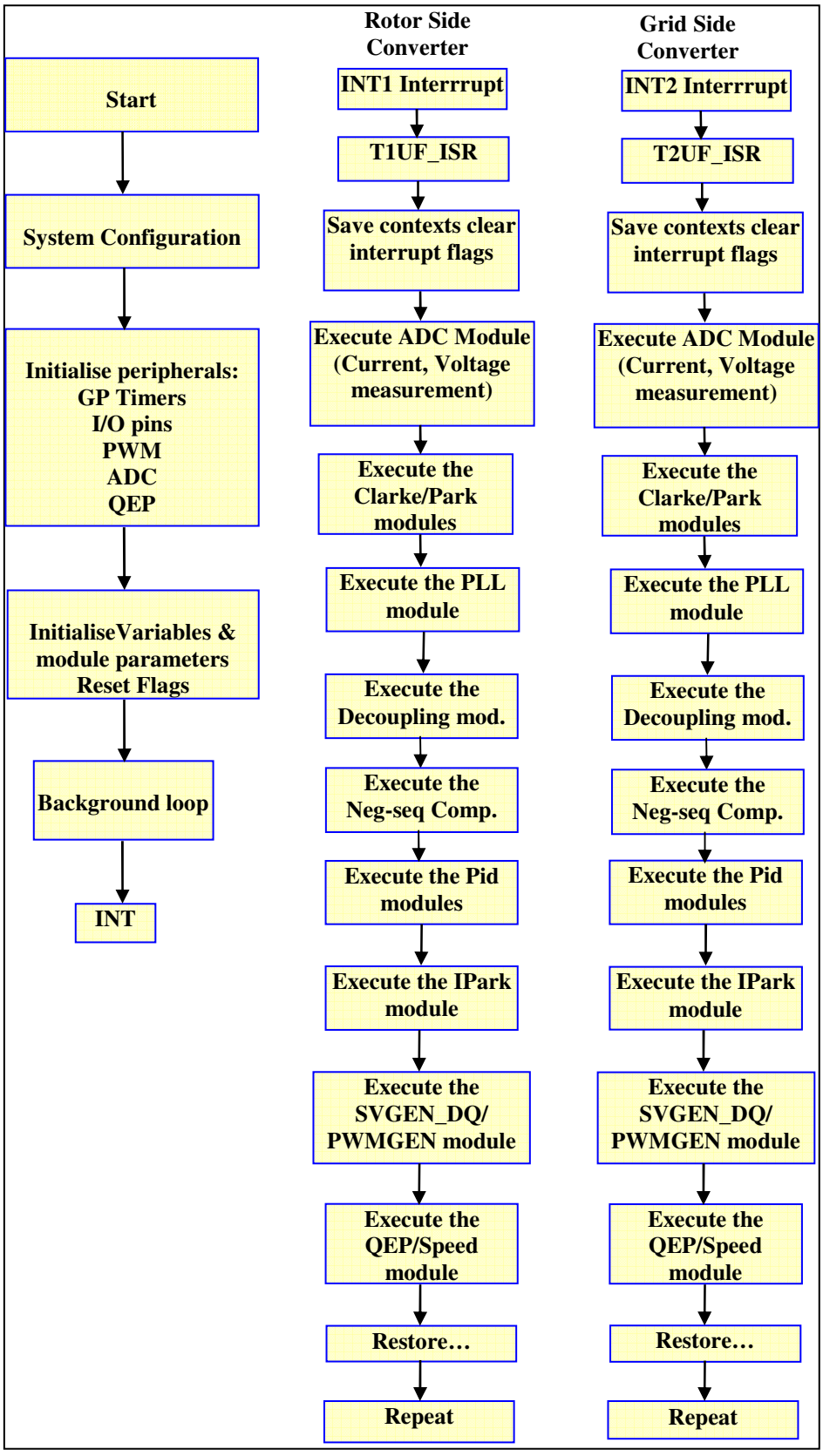

Figure 8.32 Program structure

Chapter 9 Test Results

9.1 DFIG Testing – Stand Alone Operation

To determine the behavioural operational characteristics of the DFIG, it can be connected in a stand-alone configuration. This operational mode facilitates the testing of all aspects of the DFIG without the influence of the grid supply. The DFIG laboratory test facility was configured and connected as a stand-alone DFIG, i.e. the stator was connected to a resistive load as illustrated in Figure 9.1.

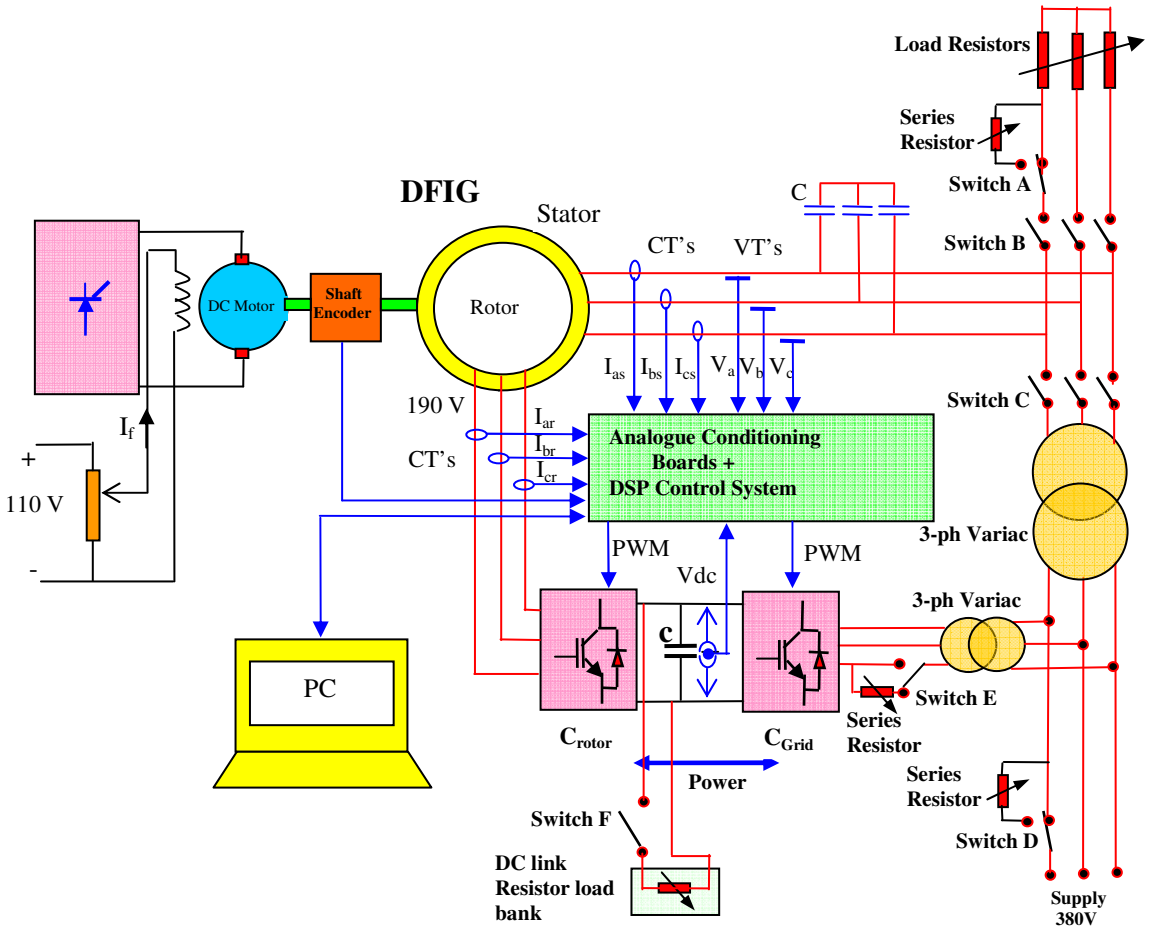

Figure 9.1 DFIG Interfacing

A three-phase variac connected to the grid-side converter facilitates the reduction of grid voltage to an acceptable level required for the rotor circuit and DC link bus (Chapter 8,

Section 8.7.2.2). The operation of the DFIG in stand-alone mode was facilitated by closing switch B and opening switch C (Figure 9.1). The DC link capacitor was charged to a value of 100V dc and the dc machine field excitation adjusted to increase the speed of the generator to 1400 rev/min. The speed of 1400 rev/min. is below synchronous speed (1500 rev/min., when operating at 50Hz) and thus the operational mode was subsynchronous, with power flowing through the grid-side converter, through the DC link bus and through the rotor converter into the rotor windings. The excitation of the rotor windings at subsynchronous speed allowed the stator windings to generate voltage and deliver power to the load bank. Capacitors are connected to the stator of the induction machine to supply reactive power.

9.1.2 Operation With Unbalanced Resistance Load.

A variable resistor was connected in series with one phase of the resistor load bank through switch A (Figure 9.1). The insertion of this resistor ensured a reduction of voltage magnitude on phase B (yellow phase Figure 9.3). The series resistor was adjusted to obtain three-phase voltage unbalance of 5% at the stator terminals of the induction machine. The wind turbine emulator (DC motor) speed was maintained at 1430 rev/min. (subsynchronous mode) and the reference voltage signal V_s^* (Figure 9.2) set to 0.3 pu. Stator voltages were measured using LEM voltage transducers and the output voltage signals acquired by the analogue to digital channels ADCINB0, ADCINB1 and ADCINB2 on connector P5 on the DSP. The DFIG was operated to deliver power through the stator of 1.5 kW.

The Pll was designed as outlined in Chapter 6. The negative sequence reference signals shown in Figure 9.3, are $i_{dr\text{-}}{}^*$ and $i_{qr\text{-}}{}^*$, developed in Chaper 7 as equations (7.63) and (7.64). Band stop filters are implemented in the software to filter double frequency

components, as shown in Figure 9.2. In stand alone configuration, (no grid connection) the grid angle θ_e is set at1pu (equivalent to 50 Hz). The speed reference signal, ω_r was obtained with the shaft encoder as described in Chapter 8.

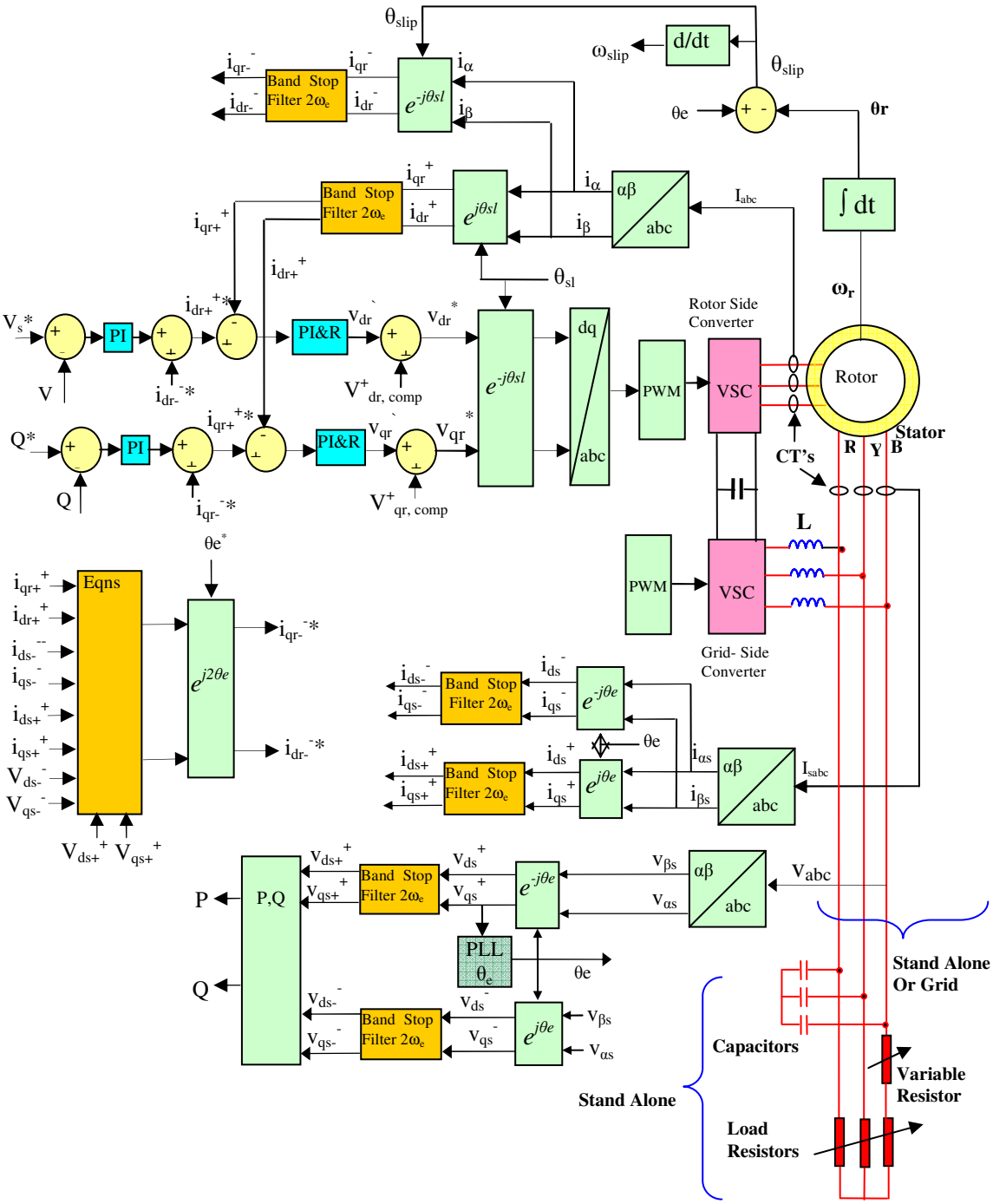

Figure 9.2 Rotor side converter

Figure 9.3 is a plot of the three-phase stator voltages measured at the stator terminals; note, the yellow phase is lower in magnitude than the red and blue phase voltages.

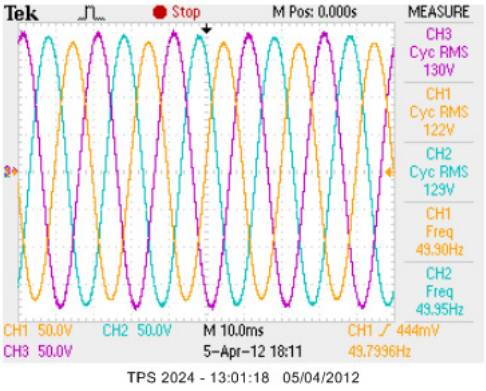

Figure 9.3 Stator phase voltages - 5% VUF

The three-phase stator voltages are transformed into a two-phase representation using Clark transformation. The Clarke output signals, Alpha and Beta waveforms are processed by a Park transformation obtaining sequence voltages v_{ds}^{+} and v_{qs}^{+}, (Park2 in the software) illustrated in Figure 9.4(b). There are Park transformations for the positive sequence voltage v_{dqs}^{+} (Park2) and the negative sequence voltage v_{dqs}^{-} (Park3).

With 5% voltage unbalance at the stator terminals of the DFIG, not only is there positive sequence voltage in the synchronous reference frame, v_{dqs}^{+}, but also negative sequence voltage v_{dqs}^{-}. The PLL forces the positive sequence voltage signal v_{qs}^{+} to zero thereby ensuring stator voltage oriented control. In Figure 9.4(b) the positive sequence voltage v_{ds}^{+} oscillates close to the reference signal of 1 pu and the quadrature voltage v_{qs}^{+} oscillates around zero. For comparison, Figure 9.4(a) is a plot of the positive sequence voltages, v_{ds}^{+} and v_{qs}^{+} with a balanced stator voltage supply. The double frequency voltage oscillations in Figure 9.4(b) result from the effects of the 5% VUF at the stator terminals.

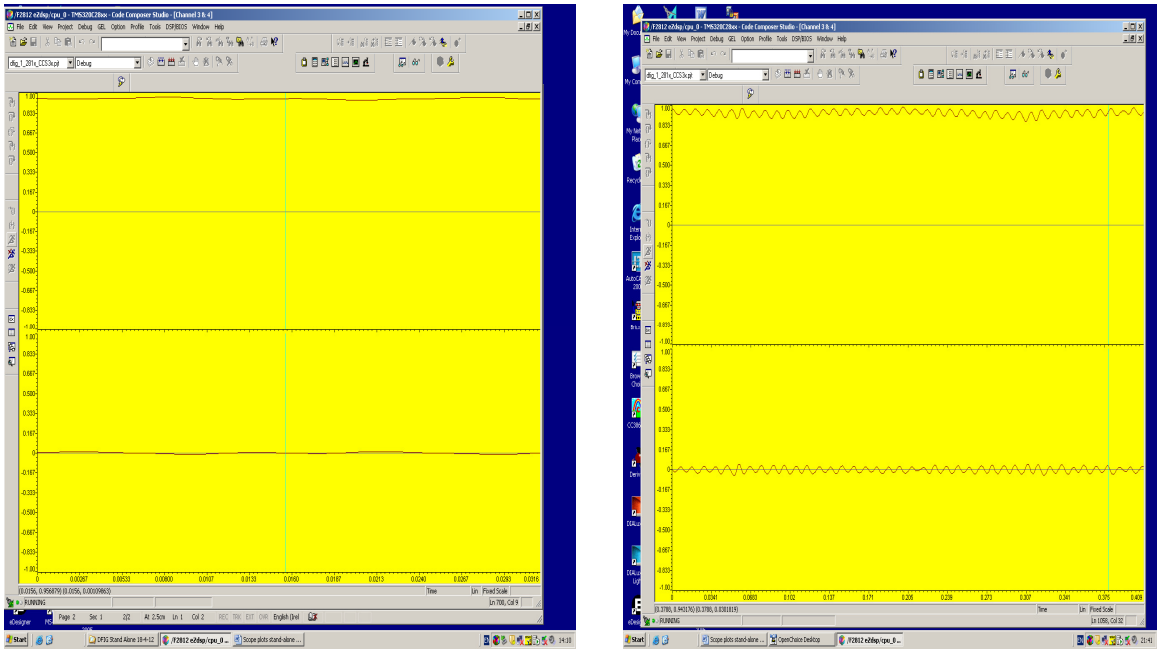

(a) **(b)**

Figure 9.4 Stator positive sequence voltages V_{ds}^{+} (top trace) and V_{qs}^{+} (bottom trace). (a) Balanced stator voltage (b) Stator VUF 5%.

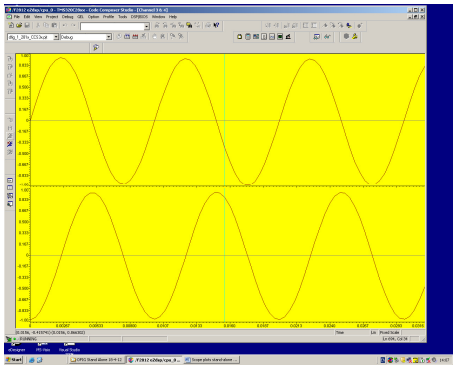

Figure 9.5 Stator negative sequence voltages V_{ds}^{-} (top trace) and V_{qs}^{-} (bottom trace) in negative sequence reference frame

In the negative sequence reference frame the negative sequence direct axis voltage v_{ds}^{-} and negative sequence quadrature voltage v_{qs}^{-} have large double frequency (100Hz) oscillations as a result of applied grid voltage unbalance; this is illustrated in Figure 9.5.

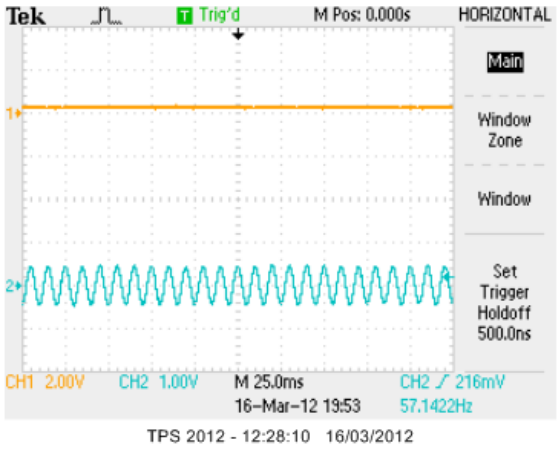

Figure 9.6 Stator positive sequence voltage v_{qs}^{+} (orange trace) and negative sequence voltage v_{qs}^{-} (blue trace)

A comparison of the stator positive and negative quadrature voltages v_{qs}^{+} and v_{qs}^{-} is illustrated in Figure 9.6. The positive sequence voltage v_{qs}^{+} is close to zero, Figure 9.6 (orange trace), and the negative sequence voltage v_{qs}^{-} Figure 9.6 (blue trace) has double frequency oscillations centred at zero.

Measured rotor currents are observed in Figure 9.7. The fundamental frequency of the rotor currents is 2.3 Hz corresponding to a rotor speed of 1430 rev/min. Superimposed onto the fundamental current waveforms are double gird frequency currents. The frequency of the oscillating rotor currents are obtained as:

Stator frequency + rotor frequency = 50 + 47.67 = 97.67 Hz.

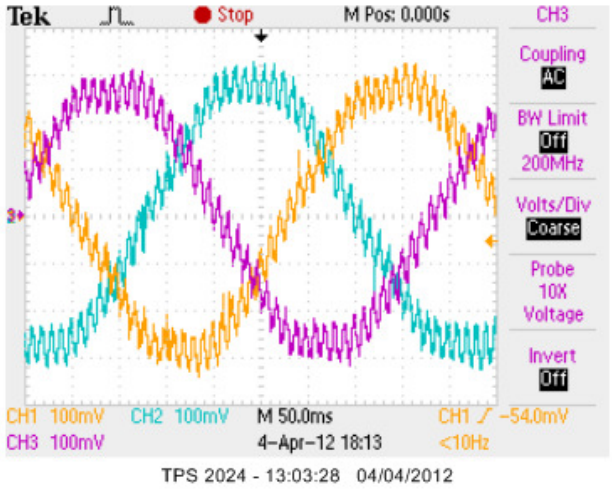

Figure 9.7 Rotor currents i_{ra}, i_{rb} and i_{rc}

The direct and quadrature rotor currents i_{dr} and i_{qr} are plotted in Figure 9.8. The rotor current i_{dr} has double frequency oscillations (centered at 0.5), illustrated in the top plot in Figure 9.8 and the quadrature rotor current i_{qr} is close to zero (the Y axis scale is 0-0.045 max.).

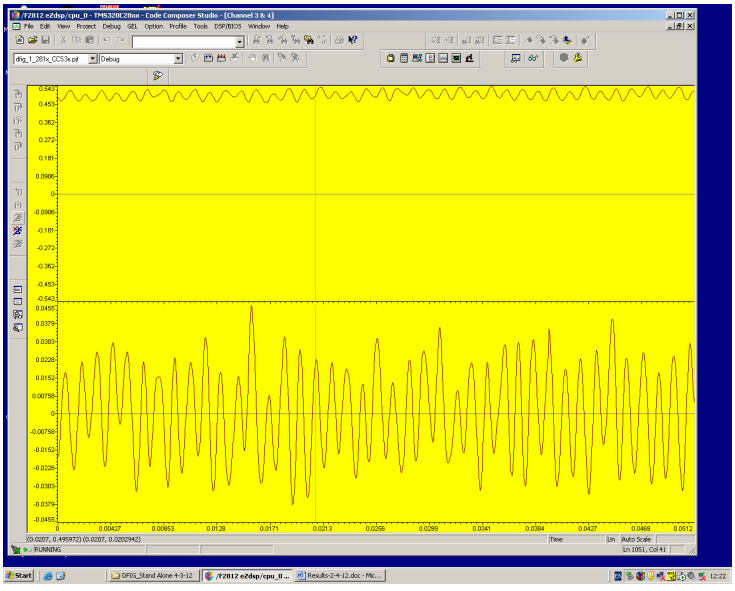

Figure 9.8 Rotor currents i_{dr}, (top) and i_{qr} (bottom)

9.1.2.1 Operation with Unbalanced Load and Rotor Side PIR Compensation.

To improve DFIG performance during asymmetrical voltage conditions, the voltage unbalance compensation control scheme to control the torque pulsations as described in equations (7.45) and (7.47) and illustrated in Figure 9.2 was implemented. The DFIG speed was set to 1430 rev/min. and VUF of 5% was applied to the DFIG stator terminals.

The PIR current controller regulates the steady state reference input signal in parallel with the negative sequence input command signal. The current control signal reference input to the PIR regulator is plotted in Figure 9.9 (top plot). The PIR resonant controller has a high gain and regulates the double frequency oscillations shown in the lower plot of Figure 9.9.

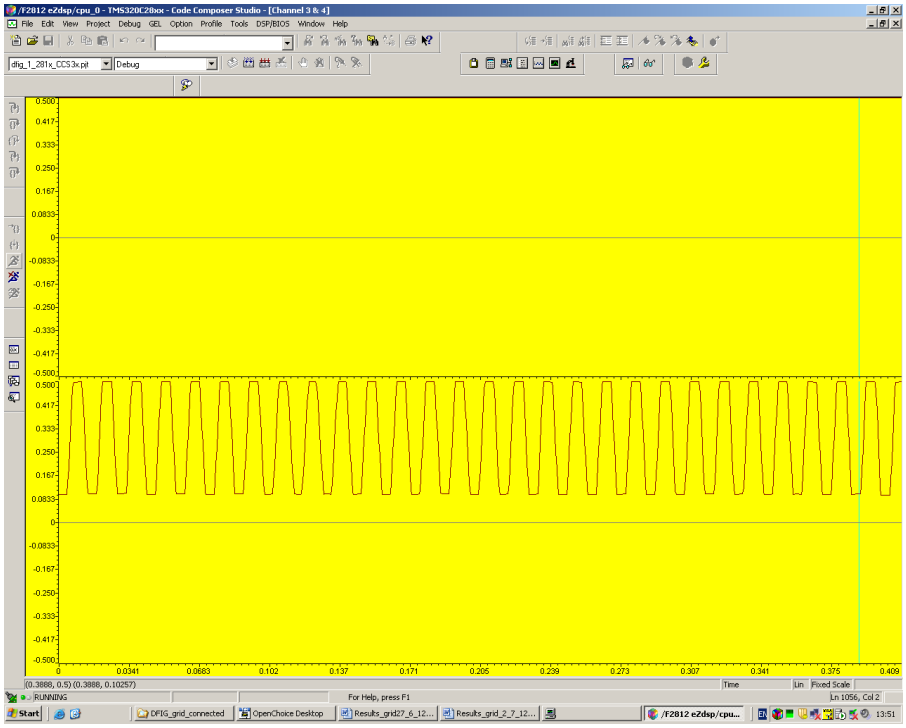

Figure 9.9 PIR reference, (Top Plot, just visible at a constant 0.5) and PIR output signal (Bottom Plot)

The output signal of the PIR controller as illustrated in Figure 9.9 is provided as the input to the space vector generator (svgen in software). The output of the svgen module is plotted in Figure 9.10(b) and this signal is passed to the PWM module to generate PWM signals for the IGBT's.

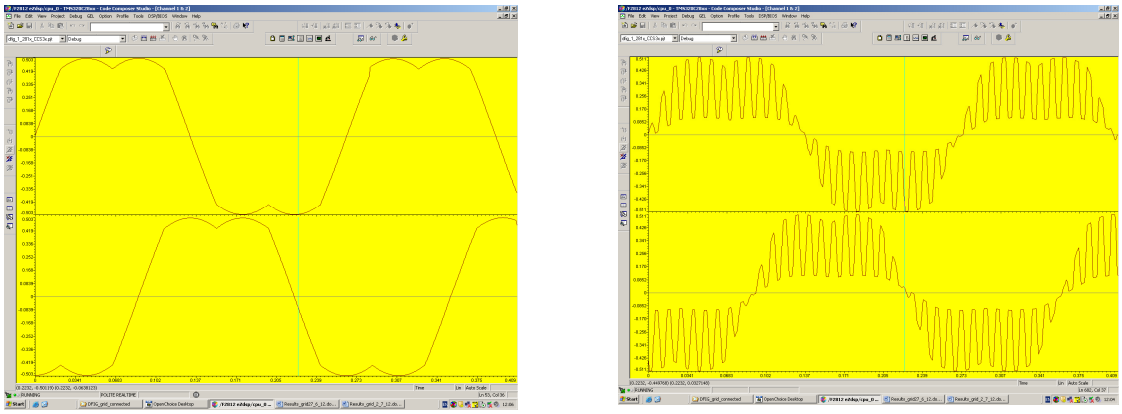

(a) **(b)**

Figure 9.10 Output of space vector generator in software: (a) before PIR compensation and (b) with PIR compensation

Figure 9.7 shows plots of the rotor currents $I_{ra,}$ I_{rb} and I_{rc} with VUF of 5% applied to the stator terminals prior to torque pulsation compensation technique introduced. Figure 9.11 is a plot of the rotor currents with negative sequence compensation implemented. There is good improvement with respect to the amplitude of current oscillations when compared to the current oscillations in Figure 9.7. The stator current supplied to the resistive load was 3.5A.

A direct measurement of torque was not available, however electromechanical torque is directly proportional to rotor currents (Chapter six) and therefore it is appropriate to assume that the torque pulsations as a result of applied stator voltage unbalance are also reduced in direct proportion to the reduction in rotor current oscillations.

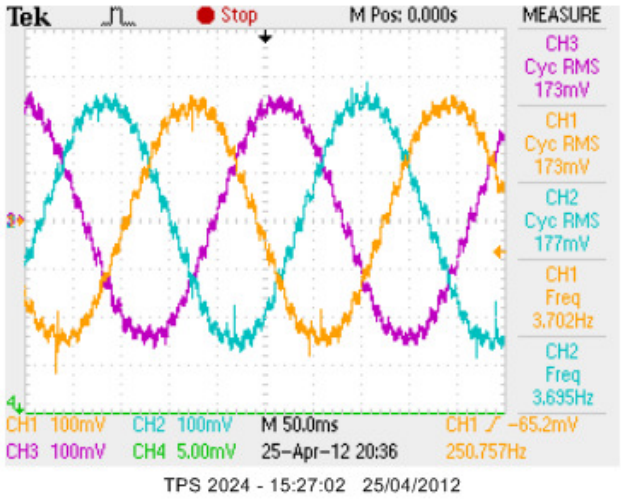

Figure 9.11 Rotor currents I_{ra}, I_{rb} and I_{rc} with negative sequence compensation

9.1.4 Grid Side Converter Test.

The grid-side converter was connected as illustrated in Figure 9.1. Control signals to the rotor-side converter were disconnected. A three-phase variac connected to the ac side of the grid converter enabled adjustment of voltage supplied to the IGBT's. A variable resistor was connected in series with one phase of the three-phase voltage supply to the grid-side converter through switch E (Figure 9.1). This variable resistor when connected enabled a magnitude reduction of phase C at the terminals of the grid-side converter. The variable resistor was adjusted to obtain a VUF of 5% at the terminals of the grid-side converter. The grid-side converter operated as a three-phase controlled rectifier (subsynchronous mode), maintaining the DC link voltage at 50V. Initially the DC link was isolated from the rotor-side converter and did not provide a load current.

9.1.4.1 DC Link Voltage.

The DC link was charged, with no load load supplied by the converter. A plot of the DC link voltage is shown in Figure 9.12 and DC link voltage oscillations at 100Hz are evident on the steady state value of 50V.

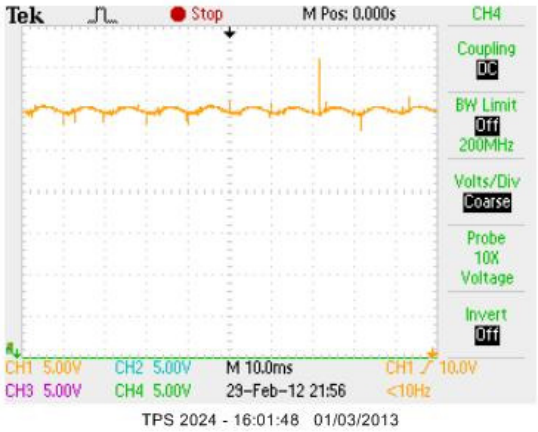

Figure 9.12 DC Link Voltage, 50V, VUF 5%

Modifications to the control structures to improve the performance of the grid-side converter during network asymmetrical voltage conditions as outlined in Chapter 7, Section 7.6 were implemented in the control software. This included the implementation of equations (7.63) to (7.66) on the DSP controller and the inclusion of a PIR controller with a resonant controller gain of 110 at a frequency of 100Hz (Figure 9.1). Uniquely the grid control scheme was implemented on the DSP in Event Manager B, (Event Manager A was configured for the rotor side converter). The control scheme was implemented in the grid voltage reference frame. A plot of the DC link voltage is shown in Figure 9.13 and DC link voltage oscillations are practically eliminated.

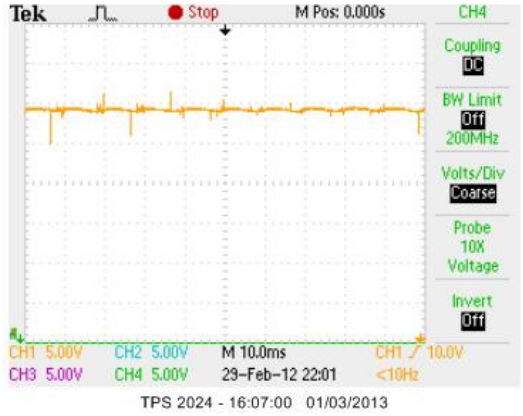

Figure 9.13 DC Link Voltage- 50V -VUF 5%. Compensation Implemented.

To test the grid-side converter during load conditions a resistor load bank was connected to the DC link bus through closing switch F (Figure 9.1). The standard control structure without negative sequence compensation was implemented. A current of 2A was supplied by the DC link to the load bank and tests were repeated on the grid-side converter. A plot of the DC link voltage is shown in Figure 9.14 and double grid frequency voltage oscillations with a peak-to-peak amplitude of 2V are observed.

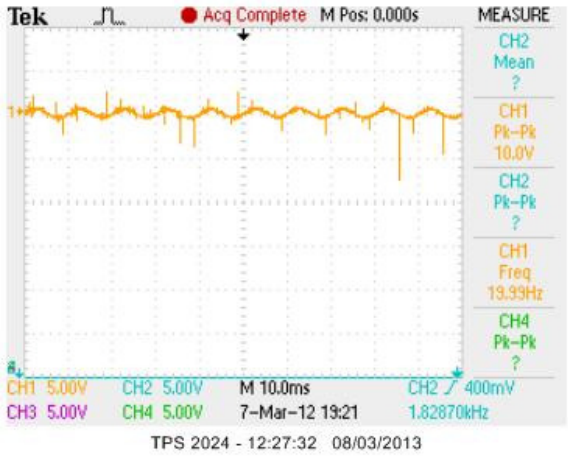

Figure 9.14 DC link voltage- 50V -VUF 5%.

As ws implemented for the no-load case, the control structure of the grid-side converter was altered to include a PIR controller, (Section 7.6, Figure 7.23). This included the

implementation of equations (7.63) to (7.66) on the DSP controller and the inclusion of a PIR controller. The DC link supplied a load current of 2A to the resistor load bank. A plot of the DC link voltage is shown in Figure 9.15 and there is a reduction in the amplitude of dc voltage oscillations.

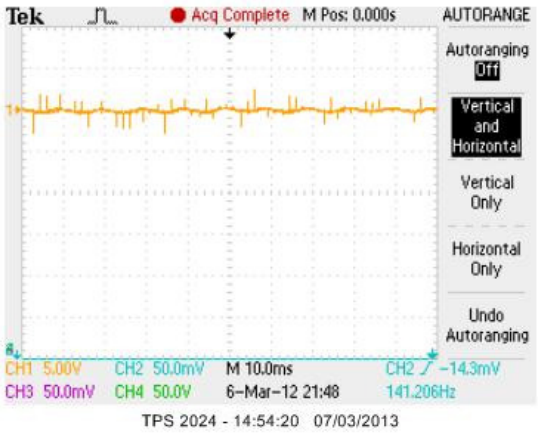

Figure 9.15 DC link voltage- 50V -VUF 5%. PIR compensation implemented

9.1.4.1 Grid Currents.

Negative sequence grid voltage can distort grid-side converter input currents as illustrated in Figure 9.16. Figure 9.16 (a) shows the converter input currents prior to negative sequence compensation introduced to the grid-side converter. Figure 9.16(b) illustrates improvement to the blue phase current waveform when negative sequence compensation using a PIR controller is introduced.

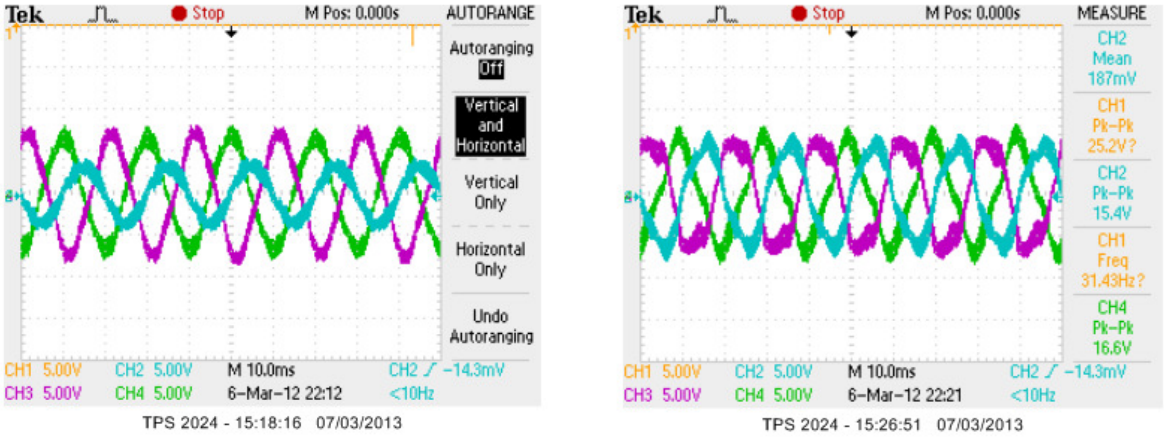

(a) (b)

Figure 9.16 Grid converter input currents VUF 6%. (a) No negative sequence compensation (b) PIR compensation implemented

9.2 DFIG Testing – Grid Connection

9.2.2 Induction Generator Connected to the Grid.

The stator of the DFIG was connected to the three-phase grid voltage through closing switch C and opening switch B (Figure 9.1). Similar to the testing of the DFIG in stand-alone mode a variable resistor was connected in series with one phase of the grid voltage. A reduced voltage on one phase of the three-phase voltage supply was thus applied to the stator terminals of the DFIG resulting in a stator applied voltage unbalance of 5%. The DFIG was synchronised to the grid and operated at a speed of 1400 rev/min. The DFIG was thus operating in subsynchronous mode. Power supplied by the stator to the grid during this test was 1.5kW. The rotor currents are plotted in Figure 9.17 (a) and significant double frequency oscillations are present.

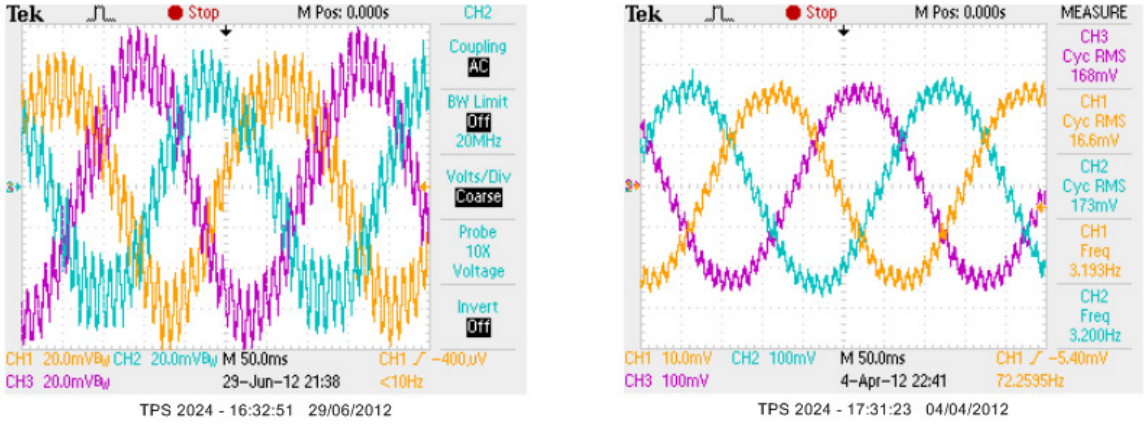

Figure 9.17 Rotor Currents – Stator VUF 5%: (a) Rotor currents before compensation. (b) Torque pulsation PIR compensation scheme implemented.

The compensation scheme to reduce torque pulsations (implementation of equations (7.45 and (7.47) Section 7.2.2) as illustrated in Figure 9.2 was implemented on the DSP and the DFIG operated with power delivered to the grid as previously. The rotor currents are plotted in Figure 9.17(b) and a reduction in the amplitude of rotor current oscillations is observed.

9.3 DFIG Testing –Conclusion

Issues with the operation of the induction machine (manufactured in 1966) and the performance of the DSP microcontroller proved challenging to overcome. The adc on the DSP controller is very suseptable to over voltage, which can result in blown chips. Also the issue of electrical noise on the DSP board was also a challenge to eliminate. All PCB's were constructed with strip-board and hand-soldered, thus their performance albeit satisfactory perhaps not quite machine built standard. Hardware and software solutions were implemented to reasonable success with the DFIG connected in both stand-alone mode, and synchronised to the grid.

Chapter 10 Conclusion

10.1 Contributions of Thesis

The initial work in this thesis concentrated specifically on the issues associated with the connection of WECS to the distribution network. As part of this research contact was initiated with Airtricity, an Irish indigenous company involved in the harness of wind energy. The assistance of DIT was requested and investigative studies were initially undertaken on a small wind farm connected to the Irish distribution network at 10kV. Monitoring of the wind farm was undertaken and the results demonstrated daily, weekly and seasonal variation of voltage unbalance. Chapter 4 includes results of these investigations. A second wind farm connected to the distribution network at 38kV was subsequently analysed and similar results were obtained. In both wind farms, it was observed that DFIG's had difficulty remaining connected to the distribution network when voltage unbalance exceeded certain threshold levels. Further research indicated that the issue of asymmetric grid voltage and wind turbines was not unique to Ireland.

Control techniques to improve performance of a DFIG during conditions of grid voltage unbalance including measures to control the rotor-side and grid-side converters in a DFIG have been investigated and documented in Chapter 7. In this thesis the control schemes uniquely include PIR control structures implemented in the grid/stator voltage reference frame, for both the rotor side and also the grid side converters respectively. Software models of a DFIG system were designed in Matlab/Simulink, and include the modified control structures developed in Chapter 7, to assist in reducing current, power and torque oscillations that develop during grid voltage unbalance conditions. Simulation results demonstrated improvement in performance of a DFIG when subjected to asymmetric grid voltage. The reductions in torque and power oscillations are clearly

identified in Chapter 7. Similar control techniques were developed and implemented for a synchronous generator converter system.

As part of the work in this thesis and stemming from collaboration with Airtricity a number of reports were completed and presented. Airtricity implemented the recommendations arising from these reports, resulting in increased productivity at their wind farms. Also as part of the work in this thesis a number of papers were presented at international conferences, contributing to the research profile of DIT.

This thesis also describes in detail the construction and implementation of a laboratory based DFIG test rig. A suitable DSP controller has been designed and implemented for the DFIG. A unique feature is the independent control of both the rotor side and grid side converters with a single DSP controller. The DSP control scheme and measurement and interface circuits have been designed and integrated into the test rig. The measurement and interface circuits have been developed for the measurement of voltage, current and speed signals and interfacing these signals to the DSP controller. Protection is also a feature of these circuits to ensure the sensitive Analogue to Digital Converters are not subjected to over-voltage conditions. Interface circuits have also been developed and tested for the PWM controller and incremental shaft encoder. The capability and performance of each of the circuits has been tested and experimentally verified.

The DFIG test rig was configured and tested with the control system as developed in the thesis. Difficulties arose due to the limitations of hardware and software, however reasonable success was achieved allowing testing of the asymmetrical control systems investigated in Chapter 7. Initially the DFIG test rig was tested as a standalone system with unbalanced stator voltage. A resistor load-bank was connected to the stator terminals of the induction machine and power was then supplied by the stator to this load. The results of these tests documented in Chapter 9, demonstrated the improvement

in performance of the DFIG with the incorporation of rotor current compensation techniques to control power and torque pulsations. The laboratory rig was also synchronised to the grid and operated with asymmetrical grid voltage. Improvements in DFIG performance during voltage unbalance conditions was observed. Notwithstanding the issues and challenges faced, reasonable success was achieved.

10.2 Future Developments

Problems with the performance of the DSP controller and the behaviour of the induction machine prevented a more comprehensive study of the DFIG test rig. To enable further development and enhance the performance of the test unit, a modern induction machine could be utilized. Consideration could also be given to an alternative state-of-the art DSP to enhance development opportunities.

Future development of the the test rig for the study and understanding of FRT and improved connectivity to the grid is a possibility. The development of a full converter controller for a synchronous generator is easily achievable given the nature of the test-rig design. Also the development of the test rig to demonstrate UPQC and battery storage techniques for DFIG's and synchronous generator systems for grid integration issues is possible. The equipment is also designed to be adaptable for motor control applications.

Bibliography

[1]. Michael F Conlon, Joseph Kearney, "Negative Sequence Analysis of Induction Machines", in Proc. UPEC Cork, September 2005.

[2]. Joseph Kearney, Hugh O'Kelly, "Power Quality and Reliability of Offshore Wind-Farms in Ireland". *Conf. Proc. Quality and Reliability of Electrical Supply,* ERA, May 2003, pp 2. 4.0-4.13.

[3]. Power Quality Application Guide, "Voltage Disturbances, Introduction to Unbalance 5.1.3," Leonardo Power Quality Initiative, Copper Development Association, May 2002 pp. 1-3.

[4]. R C Dugan, Mark McGranaghan, H Wayne Beaty, *Electrical Power Systems Quality,* pp *15* McGraw-Hill 1996, ISBN 0070180318.

[5]. http://www.seai.ie/Publications/Statistics_Publications/Statistics_FAQ/Energy_Targets_FAQ/

[6]. www.iwea.com/index.cfm/page/windenergyfacts

[7]. Wes Sunderman, Arindram Maitra, Chris Melhorn, Fred Elmendorf, Don Sabin, "Automated Detection of Voltage Unbalance Conditions," Wes Sunderman Power Quality Engineer, 942 Corridor Park Boulevard, Knoxville, Tennessee 37932, 2004, pp 5-6.

[8]. F Jiang, Z Q Bo, GEC, Li Roumei EPRI. "Performance of Induction Generators in Parallel with an unbalanced Three Phase System". *Conf. Proc. Power System Technology, 1998*. Powercon '98, 18-21st Aug. 1998. Vol. 2. pp 1193-1197.

[9]. Hnk Polinder, " Overview of and Trends in Wind Turbine Geerator Systems" Report TUDelft , 2012

[10]. E Muljadi, D Yildirim, T Batan, C P Butterfield. "Understanding the Unbalanced-Voltage Problem in Wind Turbine Generation". National Renewable Energy Laboratory", *Industry Applications Conference,* 1999. 34th IAS Annual Meeting. IEEE Conf. Proc. Vol. 2, pp 1359-1365.

[11]. Wisconsin Service Corporation. "Single Phasing and Phase Unbalance", wisconsinpublicservice.com, 2005, pp.1-2.

[12]. M Davidson, National Wind Power. "Interaction of a Wind Farm with the Distribution Network and its effect on Voltage Quality," Embedded Generation on Distribution Networks (Digest No. 1996/194), *Conf. Proc. IEE Colloquium on the Impact of Embedded Generation*, 15th Oct. 1996 pp 9/1-9/5.

[13]. Karl M Hink. "18-pulse Drives and Voltage Unbalance," MTE Corporation, W147 N 9525 Held Drive, Menomonee Falls, W153051.

[14]. Jawad Faiz, Hamid Ebrahimpour, and Pragasen Pillay, "Influence of Unbalanced Voltage on the Steady-State Performance of a Three-Phase Squirrel-Cage Induction Motor". *IEEE Transactions on Energy Conversion,* Vol. 19, No. 4, Dec. '04.

[15]. Motors and Generators, ANSI/NEMA Standard MG1-1993.

[16]. P Pillay, M Manyage. "Definitions of Voltage Unbalance," *IEEE Power Engineering Review,* Vol. 21 issue 5, May 2001, pp 50-51.

[17]. IEEE Standard 112, 1996. "IEEE Standard Test Procedure for Polyphase Induction Motors and Generators," Revision of St. 112- 1996, 4th Nov. 1996.

[18]. Jozef A L Ghijselen, Alex P M Van den Bossche. "Exact Voltage Unbalance Assessment Without Phase Measurements," *IEEE Transactions on Power Systems,* Vol. 20, No. 1, February 2005.

[19]. IEEE Standard 1159-1995, "IEEE Recommended practice for monitoring electric power quality" IEEE Press, 2nd November 1995.

[20]. European standard EN 50160, "Voltage characteristics of electricity supplied by public distribution systems", CENELEC, November 1994.

[21]. British standard BS EN 50160, "Voltage characteristics of electricity supplied by public distribution systems". BSI publication, February 2000.

[22]. V J Gosbell, H M S C Herath, BSP Perera, D A Robison, "Sources of Error in Unbalance Measurements," *Producing Quality Electricity for Mankind,* Australian Universities Power Engineering Conference, AUPEC 29th Sept. -2nd Oct. 2002, Monash University.

[23]. Math H. J. Bollen and Lidong D Zhang, "Analysis of Voltage Tolerance of AC Adjustable-Speed Drives for Three-Phase Balanced and Unbalanced Sags," *IEEE Transactions on Industry Applications,* Vol. 36, No. 3, May/June 2000, pp 904-910.

[24]. Bjarne Idsoe Naess, Tore M Undeland, Terje Gjengedal, "Methods for Reduction of Voltage Unbalance in Weak Grids Connected to Wind Plants," *Wind Power and The Impacts on Power Systems,* IEEE Workshop, Oslo, 17th-18th June 2002.

[25]. Prof. Ray Arnold, "Solution to the power quality problem", *Power Engineering Journal, April 2001.*

[26]. M H J Bollen. Characterisation of voltage Sags experienced by three-phase adjustable-speed drives. *IEEE Transactions on Power Delivery*, 15th April 2000. Vol. 15, Issue 2, pp. 827-832.

[27]. Arfat Siddique, GS Yadave, Bhim Singh, "Effects of Voltage Unbalance on Induction Motors". *Conf. Proc. IEEE International Symposium on Electrical Insulation,* Indianapolis, USA 19-22 Sept. 2004, pp. 26-29.

[28]. Ching-Yin Lee, Bin-Kwie Chen, Wei-Jen Lee and Yen-Feng Hsu, "Effects of Various Unbalanced Voltages on the Operation Performance of an Induction Motor under the Same Voltage Unbalance Factor Condition", *Industrial and Commercial Power Systems Technical Conference,* 11th-16th May 1997, Philadelphia, PA. ISBN 0-7803-3825-1.

[29]. Schneider Electric, Schneider-electric.com. http://www.schneider-electric.com/products/ww/en/4100-power-energy-monitoring-system/

[30]. J Arrillaga, N.R. Watson and S Chen, *Power System Quality Assessment*, Chichester: John Wiley & Sons, c2000. ISBN 0471988650.

[31]. National Renewable Energy Lab. "GE Distributed Generation Power Quality, Protection and Reliability Case Studies Report," Aug. 2003, NREL/SR-560-34635.

[32]. Clemens Jauch, Paul Sorensen, Birgitte Bak-Jensen, "International Review of Grid Connection Requirements for Wind Turbines", *Nordic Wind Power Conference,* 1-2 March, 2004, Chalmers University of Technology.

[33]. A.H. Ghorashi, S.S. Murthy, B.P. Singh, Bhim Singh, "Analysis of Wind Driven Grid connected Induction Generators Under Unbalanced Grid

Conditions," *IEEE Transactions on Energy Conversion*, Vol. 9 No. 2, June '94, pp. 217 - 223.

[34]. Kevin Lee, Eaton Electrical, Giri Vankataramanan, Thomas M Jahns, University of Wisconson-Madison. "Design-oriented Analysis of DC Bus Dynamics in Adjustable Speed Drives Under Input Voltage Unbalance and Sag Conditions," in *Proc. 35th Annual IEEE Power Electronics Specialists Conference 2004,* Achen, Germany.

[35]. Vladislav Akhmatov, "Variable-speed Wind Turbines with Doubly-fed Induction Generators Part II: Power System Stability", *Wind Engineering* Vol. 26 No. 2*,* 2002 pp. 85-108.

[36]. Ted Brekken, Ned Mohan, "A Novel Doubly-Fed Induction Wind Generator Control Scheme for Reactive Power Control and Torque Pulstaion Compensation Under Unbalanced Grid Voltage Conditions". *4th AnnualPower Electronics Specialist Conference, PESC* '03. 2003 IEEE Vol. 2, 15-19 June 2003, pp. 760 – 764.

[37]. Kevin Lee, Eaton Electrical, Giri Venkataramanan and Thomas M M Jahans, "Modelling Effects of Voltage Unbalances in Industrial Distribution Systems with Adjustable Speed Drives". *Industry Applications Conference, 2004, 39th IAS Annual Meeting,* Conference Record of the 2004 *IEEE,* Volume 4, 3-7 Oct. 2004 pp. 2579 – 2586.

[38]. D Vincenti, P.D. Ziogas, and R V Patel, "An Analysis and Design of a Force Commutated Three-Phase AC Controller with Input Unbalance Correction Capability," *in Proc. Seventh Annual Applied Power Electronics Conference and Exposition APEC*, 23rd-27th Feb. 1992, pp. 487 – 493.

[39]. Jun-Koo Kang, Sueng-Ki Sul. School of Electrical Engineering, Seoul National University. “Control of Unbalanced Voltage PWM Converter Using Instantaneous Ripple Power Feedback”, *PESC '97 Record., 28th Annual IEEE Power Electronics Specialists Conference,* 1997 Volume 1, 22-27 June 1997 pp. 503 - 508.

[40]. Wen-Inne Tsai, York-Yih Sun, Dept. of Electrical Engineering, National Cheng Kung University, Taiwan, Ming-Tsung Tsai. “Effects of Voltage Unbalance and Harmonics on Three-Phase SPWM AC-toDC Converters with Instantaneous Power Feedback,” *Power Conversion Conference, 1993.* Yokohama 1993, Conference Record of the19-21 April 1993 pp. 61 – 66.

[41]. P Rioual, H Pouliquen, Electricite de France, Direction des Etudes et Recherches, Services Materiel Electrique, J P Louis, Lesir-Ens Cachan. “Regulation of a PWM Rectifier in the Unbalanced Network State,” *Proc. 24th Annual Power Electronics Specialest Conference, PESC 1994.* 20th-25th June 1994, vol. 2, pp. 1095 - 1108.

[42]. P.W. Carlin, A.S. Laxson and E.B. Muljadi, “The History and State of the Art of Variable-Speed Wind Turbine Technology,” *NREL National Renewable Energy Laboratory,* Colorado, Feb. 2001, pp. 10-15.

[43]. NSAI National Standards of Ireland. “Irish Standard I.S. E.N. 50160:2000 Voltage Characteristics of Electricity Supplied by Public Distribution Systems”, 2000.

[44]. “Unbalanced Voltage On Polyphase Induction Motors”, Usmotors.com. http://www.usmotors.com/TechDocs/ProFacts/Unbalanced-Voltage.aspx.

[45]. Ibrahim M. El-Mohr, "Effect of Negative Sequence Torque on Induction Motor Plant During Transient Fault Conditions," *in Proc. IEEE Midwest Symposium on Ciruicts and Systems* 9th – 12th August 1998, pp. 190-193. Also *in Proc. International Conference on Power System Technology,* 18th -21st August 1998, vol. 1, pp. 591 – 594.

[46]. Pragasen Pillay, Peter Hofmann, Marubini Manyage. "Derating of Induction Motors Operating With a Combination of Unbalanced Voltages and Over or Undervoltages". *IEEE Trasactions on Energy Conversion,* Vol. 17, No. 4, Dec. 2002.

[47]. Annette von Jouanne, Basudeb (Ben) Banerjee. "Assessment of Voltage Unbalance". *IEEE Transactions on Power Delivery*, Vol. 16, No. 4, Oct. 2001.

[48]. Paulo Vinicius Santos Valois, Carlos Marcio Vieira Tahan, Nelson Kagan and Hector Arango. "Voltage Unbalance in Low Voltage Distribution Networks", *16th International Conference and Exhibition on Electricity Distribution, 2001. Part 1: Contributions.* CIRED. (IEE Conf. Publ No. 482) Volume Summaries, 2001 pp 155 - 155 Conference Publication No. 482 IEE 2001.

[49]. M de Oliveira, L Ferreira and D de Oliveira. "Voltage Unbalance Monitoring in CEB Systems", *10th International Conference on Harmonics and Quality of Power, 2002.* Vol. 1, 6-9 Oct. 2002, pp 214-219.

[50]. P Gardner, H Snodin, A Higgins and S McColdrick, "The Impacts of Increased Levels of Wind Penetration on The Electricity Systems of The

Republic of Ireland and Northern Ireland: Final Report" Garrad Hassan, and Partners Ltd. Glasgow, Scotland, 2003.

[51]. ESB National Grid. www.eirgrid.com

[52]. ESB Networks, www.esb.ie/esbnetworks/

[53]. L.M. Craig, M Davidson, N Jenkins and A Vaudin, "Integration of Wind Turbines on Weak Rural Networks". *Conf. Proc. Opportunities and Advances in International Power Generation,* 18-20th March '96.

[54]. A. A. Mohamed, M.T. El Hagry and M.N. Iskander, "Steady State and Harmonic Analysis of DOIG operating with WECS" *IEEE Explore pp. 366-369.*

[55]. Malcolm Kennedy, "Distributed Generation: Harder than it looks," *Power Engineer Feb. '03.*

[56]. Bjarne Idsoe Naess, Tore M. Undeland and Terje Gjengedal, "Methods for Reductions of Voltage Unbalance in Weak Grids Connected to Wind Plants," *Proceedings of the IEEE Workshop on Wind Power and the Impacts on Power Systems,* Oslo, June 2002.

[57]. Julija Matevosyan, Thomas Ackerman, Sigrid Bolik and Lennart Soder,"Comparison of International Regulations for Connection of Wind Turbines to the Network," *Nordic Wind Power Conference,* 1-2 Mar. 2004, Chalmers University of Technologhy, Goteborg, Sweeden.

[58]. Bing Xie, Brendan Fox and Damien Flynn, "Study of Fault Ride-Through for DFIG Based Wind Turbines," *IEEE International Conference on Electric Utility Deregulation, Restructuring and Power Technologies* (DRPT2004), April 2004, Hong Kong.

[59]. Santiago Dominguez Rubira, Malcolm D MacCulloch, "Control of Double Fed Wind Generators connected to the Grid by Asymmetric Transmission Lines," *Industry Application Conference, 1998, 33rd IAS Annual Meeting.* Vol. 3, pp. 2381-2386.

[60]. J Schlabbach, D Blume & T Stephanblome, "Voltage Quality in Electrical Power Systems," *IEE Power and Energy Series 36,* 2001 IEE ISBN 0852969759.

[61]. Matlab. The Mathworks Inc., www.mathworks.com.

[62]. L. H. Hansen, L. Helle, F. Blaabjerg, E. Ritche, S. Munk-Nielsen, H. Bindner, P. Sorensen and B. Bak-Jensen, "Conceptual survey of Generators and Power Electronics for Wind Turbines"Riso-R-1205(EN), Riso National Laboratory, Roskilde, Denmark, 2001, pp.79.

[63]. V.J. Gosbell, "Technical Note No. 6, Voltage Unbalance", Integral Energy Power Quality Centre, School of Electrical, Computer & Telecommunications Engineering, University of Wollongong, NSW Australia 2522, 6 October 2002.

[64]. IEEE Std. 1159-1995, "IEEE Recommended Practice for Monitoring Electric Power Quality", IEEE Standards Coordinating Committee 22 on Power Quality, June 1995, IEEE Standards Board.

[65]. Tao Sun, "Power Quality of Grid-Connected Wind Turbines with DFIG and Their Interaction with the Grid", PhD in Electrical Engineering, Institute of Energy Technology, Aalborg University 2004.

[66]. M. Godoy Simoes, Felix A. Farret, *Renewable Energy Systems, Design and Analysis with Induction Generators.* CRC Press, 2004, ISBN 0-8493-2031-3, pp. 245.

[67]. Ned Mohan, *Advanced Electric Drives, Analysis, Control and Modelling using Simulink*. MNPERE, Minneapolis 2001, ISBN 0-9715292-0-5.

[68]. Ned Mohan, Tore M. Undeland and William P. Robbins, *Power Electronics, Converters, Applications and Design,* 2nd Ed., John Wiley & Sons, 1995, ISBN 0-471-30576-6.

[69]. Hamid A. Toliyat, Steven G. Cambpel, *DSP-Based Electromechanical Motion Control*. CRC Press LLC 2004, pp. 257.

[70]. Martti Hokkanen, Heikki J. Salminen, Timo Vekara, "A Short Review of Models for Grid-Connected Doubly-Fed Variable Speed Wind Turbines", University of Vaasa, Finland, 2004.

[71]. Lie Xu, Yi Wang, "Dynamic Modelling and Control of DFIG-Based Turbines Under Unbalanced Network Conditions", *IEEE Transactions on Power Systems,* Vol. 22 Issue 1, 2007, pp. 314-323.

[72]. S Muller, M.Deickie and R.W. De Doncker, "Doubly Fed Induction Generator Systems for Wind Turbines", *IEEE Industry Applications Mag.,* vol 8, no. 3, pp 26-33, May/June 2002.

[73]. R. Pena, J.C. Clare and G. M. Asher, "Double Fed Induction Generator using Back-to-Back converter and its application to variable-speed wind-energy generation", *Proc. Inst. Elect. Eng. B*, vol 143, no. 3 pp. 231-241, 1996.

[74]. He Yikang, Hu Jiabing and Zhao Rende, "Modelling and Control of Wind-Turbine Used DFIG under Network Fault Conditions", *Proc. 8th International Conference on Electrical Machines and Systems*, ICEMS 29th Sept. 2005, Vol. 2 pp. 986-991.

[75]. Shuhui Li, Timothy A. Haskew, "Analysis of Decoupled d-q Vector Control in DFIG Back-to-Back PWM Converter", *IEEE Power Engineering Society General Meeting*, 24th-28th June 2007.

[76]. Yi Wang, Lie Xu, "Control of DFIG-Based Wind Generation Systems under Unbalanced Network Supply", *Electrical Machines & Drives Conference*, 2007, IEMDC, 07, pp. 430-435.

[77]. C. Sankaran, *Power Quality*. CRC Press2002, ISBN 0-88493-1040-7, pp.1.

[78]. Andreas Petersson, Torbjorn Thiringer and Lennart Harnefors, " Modelling and Experimental Verification of Grid Interactin of a DFIG Wind Turbine", *IEEE Transactions on Energy COnversion,* vol. 20, no. 4, pp 878-886, Dec 2005.

[79]. M.A.B. Amora, U.H. Bezerra, "Assessment of the Effects of Wind Farms Connected in Power Systems", *IEEE Porto Power Tech Conference,* 10th-13th Sept. 2001, Porto, Portugal.

[80]. M.R. Dubois, H Polinder, J.A. Ferreira, "Generator Topologies for Direct-Drive Wind Turbines, an Adapted Technology for Turbines Running in Cold Climate", IEEE Nordic Workshop on 2000.

[81]. Joris SOENS, "Impact of Wind Energy in a Future Power Grid", PhD, Catholic University Leuven, 2005, pp. 43.

[82]. R. Kemsely, G.Pannell, C.Barbier, "Cost-Effective Improvements in DFIG Performance Under Fault Conditions for Offshore Applications", Econnect Ventures Ltd., for Dept. of Business, Enterprise & Regulatory Reform U.K. 2007.

[83]. B.M. Weedy, B.J. Cory, *Electric Power Systems*. 4th Ed. 1998, John Wiley & Sons, pp. 281 .

[84]. J Duncan Glover, Mulukutla Sarma, *Power System Analysis & Design.* 2nd Ed. 1994, PWS publishing Company, pp. 49.

[85]. B.P. O'Gallachoir, P. Gardner, H. Snodin, E.J. McKeogh, "Wind Energy and System Security – the Grid Connection Moratoriam in Ireland", *Int. J. Energy Technology and Policy,* Vol. 5, No. 5, 2007.

[86]. Florin Iov, Anca Daniela Hansen, Poul Sørensen, Nicolaos Antonio Culululism, "Mapping of Grid Faults and Grid Codes", Riso-R-1617(EN) Riso National Laboratory, Tech. University of Denmark, July 2007, pp. 29.

[87]. Myo Thu Aung, Jovica Milanovic "The influence of transformer winding connection on the propagation of voltage sags", *IEEE Trans on Power Delivery*, vol. 21, no. 1, January 2006, pp. 262-269.

[88]. W. Erdman, M. Benhke, "Low Wind Speed Turbine Project Phase II: The Application of Medium-voltage Electrical Apparatus to the Class of Variable Speed Multi-Megawatt Low Wind Speed Turbines", Beknke, Erdman & Whitaker (BEW) Engineering San Ramon, California, November 2005.

[89]. S. K. Salman, Babak Badrzadeh, "New Approach for Modelling Doubly-Fed Induction Generator (DFIG) for grid-connection studies", *European Wind Energy Conference & Exhibition 2004*, Nov. 2004.

[90]. Blaabjerg et al, "Overview of Control and Grid Synchronisation for DPGSs", *IEEE Transactions on Industrial Electronoics*, Vol. 53, No. 5, Oct. 2006.

[91]. E. Tremblay, A, Chandra, P.J. Lagace, "Grid-Side Converter Control of DFIG Wind Turbines to Enhance Power Quality of Distribution

Network", *IEEE Power Engineering Society General Meeting*, 18th -22nd June, 2006.

[92]. Shuhui Li, Timothy A. Haskew, "Analysis of Decoupled d-q Vector Control in DFIG Back-to-Back PWM Converter", *IEEE Power Engineering Society General Meeting*, June, 2007.

[93]. Feng WU, Xiao-Ping Zhang, Keith Godfrey, Ping Ju, "Modelling and Control of Wind Turbine with Doubly Fed Induction Generator", *Power Systems Conference and Exposition*, 2006 PSCE '06 Vol. 18, Issue 9, IEEE pp. 1365-1381.

[94]. J. Morren, S. W. H.. de Haan, P. Bauer, J. T. G. Pierik, "Comparison of complete and reduced models of a wind turbine using Doubly-Fed Induction Generator", in *proc. 10th Eur. Conf. Power Electronic Applications,* Toulouse, France, Sep. 2003.

[95]. Jeong-Ik Jang, Young-Sin Kim, "Active and Reactive Power Control of DFIG for Wind Energy Conversion under Unbalanced Grid Voltage", *Power Electronics and Motion Control Conference, 2006.* IPEMC 2006. CES/IEEE 5th Internatiomnal, Vol. 3 pp. 1-5.

[96]. Hu Jia-bing, He Yi-kang, NIAN Heng, "Enhanced control of DFIG-used back-to-back PWM VSC under unbalanced grid voltage conditions", *Journal of Zhejiang University SCIENCE A, China*, 2007, ISSN 1862-1775, pp. 1330-1339.

[97]. Y. Zhou, P. Bauer J. A. Ferreira, J. Pierik, "Control of DFIG under Unsymmetrical Voltage Dip", *Power Electrronic Specialist Conference,* 2007. PESC 2007. Pp. 933-938. 10.1109/PESC.2007.4342113

[98]. Shuhui Li, Timothy A. Haskew, "Analysis of Decoupled d-q Vector Control in DFIG Back-to-Back PWM Converter", *Power Engineering Society General Meeting,* 2007, pp. 1-7. 10.1109/PES.2007.385461

[99]. Feng Wu, Xiao-Ping, Keith Godfrey, Ping Ju, "Modelling and Control of Wind Turbine with Doubly Fed Induction Generator", *Power Systems Conference and Expositiion,* 2006. PSCE '06, IEEE PES. pp. 1404-1409. 10.1109/PSCE.2006.296507

[100]. J. F. Manwell, J.G. McGowan, A.L. Rogers, *Wind Energy Explained, Theory, Design and Application*, John Wiley &Sons Ltd. 2002.

[101]. Ahmed G. Abo-Khalil, Dong-Choon Lee, Se-Hyun Lee, "Grid Connection of Doubly-Fed Induction Generators in Wind Energy Conversion System", in *Proc. IEEE IPEMC,* 2006.

[102]. Robert A. Gannett, "Control Strategies for High Power Four-Leg Voltage Source Inverters", MSc. Virginia Polytechnic Instiute and State University, 2001.

[103]. S. D. Rubira and M. D. McCullagh, "Control of Double Fed Generators connected to the Grid by Asymmetric Transmission Lines", *33rd Annual IEEE Industry Applications Conference*, 12th-15th Oct.1998.

[104]. Joseph Kearney, Michael F Conlon, "Analysis of a Variable Speed Double-Fed Induction Genereator Wind Turbine During Network Voltage Unbalance Conditions", *in Proc. 42st Universities Power Engineering Conference (UPEC),* UPEC Brighton, 3-6th September 2007.

[105]. Joseph Kearney, Michael F Conlon, "Control of a Variable Speed Double-Fed Induction Generator Wind Turbine During Network Voltage

Unbalance Conditions", *42st Universities Power Engineering Conference (UPEC)*, Padua, Italy, 4th -7th September 2008.

[106]. Rajib Datta and V.T. Ranganathan, "Direct Power Control of Grid-Connected Wound Rotor Induction Machine Without Rotor Position Sensors", *IEEE Transactions on Power Electronics,* Vol. 16, No. 3, May 2001, pp. 391-393.

[107]. Hong-Seok Song, Kwanghee Nam, "Dual Current Control for PWM Converter Under Unbalanced Input Voltage Conditions", *IEEE Transactions on Industrial Electronics*, vol. 46 no. 5, October 1999, pp. 953-959.

[108]. Jeong-Ik Jang, Dong-Choon Lee, "High Performance Control of Three-phase PWM Converters under Nonideal Source Voltage", *IEEE International Conference on Industrial technology, 2006.* ICIT 2006, pp. 2791-2796. 10.1109/ICIT.2006.372693

[109]. Texas Instruments pdf Documents, CD Supplied with TMS320F2812 Microprocessor, 2005.

[110]. Ahmed G. Abo-Khalil, Dong-Choon Lee, Jeong-Ik Jang, "Control of Back-to-Back PWM Converters for DFIG Wind Turbine Systems under Unbalanced Grid Voltage", *IEEE Internationl Symposium on Industrila Electronics,* 2007 ISIE 2007, pp. 2637-2642. 10.1109/ISIE.2007.4375024

[111]. Jorge Rodrigo Massing, Jean Patric da Costa, Humberto Pinheiro,"Control For DFIG With Series Grid Side Converter Under Unbalanced Grid Voltage Conditions", Jorge Rodrigo Massing, Jean Patric da Costa,

Humberto Pinheiro, *9th Brazillian Power Electronics Conference,* 2007, pp. 614-619.

[112]. Louis Moran, Phoivos D. Ziogas, Geza Joos, "Design Aspects of Synchronous PWM Rectifier-Inverter Systems under Unbalanced Input Conditions", *IEEE Transactions on Industry Applications,* vol. 28 no. 6, November/December 1992, pp. 1286-1293.

[113]. Lie Xu, "Coordinated Control of DFIG's Rotor and Grid Side Converters During Network Unbalance", *IEEE Transactions on Power Electronics,* vol. 23, no. 3, May 2008.

[114]. Manoj R Rathi, Phillip P Jose, Ned Mohan, "A Novel H_∞ Based Controllering Under Unbalanced Voltage Conditions", *Proceedings of the 13th Intermnational Conference on Intelligent Systems Application to Power Systems,* 2005. 10.1109/ISAP.2005.1599289

[115]. Joseph Kearney, M. F. Conlon and E Coyle, "The Integrated Control of the Rotor Side and Grid Side Converters in a DFIG to Reduce Both Power and Torque Pulsations During Network Voltage Unbalance", *43rd Universities Power Engineering Conference (UPEC)*, Strathclyde, Scotland, 1st -3rd September 2009.

[116]. Joseph Kearney, M. F. Conlon and E Coyle, "The Control of Rotor Side and Grid Side Converters in a DFIG During Network Voltage Unbalance Conditions Using Resonant Current Controllers", *Ecological Vehicels & Renewables Energies (EVRE)*, Conference, Monaco, 25-28th Mar. 2010.

[117]. Jiabing Hu, Yikang He, "Modelling and Enhanced control of DFIG under unbalanced grid conditions", *Electrical Power Systems Research 79,* 2009, pp. 273-281.

[118]. Jiabing Hu, Yikang He, Lie Xu and B. W. Williams, "Improved Control of DFIG Systems During Network Unbalance Using PI-R Current Regulators", *IEEE Transactions on Industrial Electronics,* vol. 56 no.2, February 2009, pp. 439-451.

[119]. Fainan A. Magueed, Ambra Sannino, Jan Svensson, "Design of Robust Converter Interface for Wind Power Applications", *Nordic Wind Power Conference*, 1-2 March, 2004, Chambers University of Technology.

[120]. Y. Wang, L. Xu, B. W. Williams, "Compensation of network voltage unbalance using double fed induction generator-based wind farms", *IET Renewable Power Generaton,* vol. 3, no 1, pp. 12-22.

[121]. Yi Wang, Lie Xu and Barry W. Williams, "Improved Operation of DFIG and FSIG-based Wind Farms during Network Unbalance", *IEEE,* vol., no., 2008, pp. 1-7.

[122]. Yi. Wang, Lie Xu, B. W. Williams, "Control of DFIG-based Wind Farms for Network Unbalance Compensation", *Power Electronic Specialist Conference,* 2008, PESC 2008. Pp. 113-119. 10.1109/PESC.2008.4591909

[123]. M. Kiani, W. J. Lee, "Effects of Voltage Unbalance and System Harmonics on the Performance of Doubly Fed Induction Wind Generators", *IEEE Xplore* 2008 pp. 1-7.

[124]. Ruben Pena, Roberto Cardenas, Enrique Escobar, Jon Clare and Pat Wheeler, "Control strategy for a Doubly-Fed Induction Generator feeding an unbalanced grid or stand-alone load", *Electric Power Systems Research 79 (*2009) pp. 355-364.

[125]. Jia-bing, Wei Zhang, Hong-sheng Wang, Yi-kang He, Lie Xu, "Proportional integral plus multi-frequency resonant current controller for grid-connected voltage source converter under imbalanced and distorted supply voltage conditions", *IEEE Journal of Zhejiang University SCIENCE A,* 2009, ISSN 1862-1775. pp. 1532-1540.

[126]. Adrian V. Timbus, Mihai Ciobotaru, Remus Teodorescu and Frede Blaabjerg, "Adaptive Resonant Controller for Grid-Conected Converters in Distributed Power Generation Systems", *IEEE Xplore 2006* pp.1601-1607.

[127]. Lingling Fan, Haiping Yin, and Rajesh Kavasseri, "Negative Sequence Compensation Techniques of DFIG-based Wind Energy Systems under Unbalanced Grid Conditions", *Power Electronics and Machines in Wind Applications,* 2009. PEMWA 2009, pp. 1-6.

10.1109/PEMWA.2009.5208402

[128]. B Rabelo, W Hofmann, "Power Flow Optimisation and Grid Integration of Wind Turbines with the Doubly-Fed Induction Generator" *IEEE 36th Power Electronics Specialists Conference,* 2005. PESC '05, pp. 2930-2936.

[129]. Hongsheng Wang, Wei Zhang, Jiabing Hu, Yikang He, " Design and Optimisation of Proportional Resonant Controller for Rotor Current of Wind Turbine Driven DFIG", *Interbnational Conference on Electrical Machines and Systems,* 2008. ICEMS 2008, pp 2502-2506.

china… 2010.

[130]. Van-Tung Phan, Hong-Hee Lee, "An Improved Control Strategy Using a PI-Resonant Controller for an Unbalanced Stand-Alone Double-Fed

Induction Generator", *Journal of Power Electronics,* Vol. 10 No. 2, March 2010.

[131]. Van-Tung Phan, Hong-Hee Lee, "An Improved Control Method for DFIG-based Wind Syatem Supplying Unbalanced Stand-Alone Loads", *IEEE International Symposium on Industrial Electronics* (ISIE2009). Seoul Olympic Parktel, Seoul, korea July 5-8, 2009.

[132]. Van-Tung Phan, Hong-Hee Lee, and Tae-Won Chun, "An Effective Rotor Current Controller for Unbalanced Stand-Alone DFIG Systems in the Rotor Reference Frame", *Journal of Power Electronics,* Vol. 10, No. 6, November 2010.

[133]. Jiabing Hu, Yikang He, "DFIG wind generation systems operating with limited converter rating considered under unbalanced network conditions – Analysis and control design", *Journal of Renewable Energy* Vol. 36, 2011, pp. 829-847. www.elsevier.com.

[134]. J Kearney, M. F. Conlon and E. Coyle, "Analysis of Converter Conneceted Synchronous Wind Turbines to Grid Disturbances", *46th Universities Power Engineering Conference* (UPEC), Soust, Germany, 5th-8th Sept. 2011.

[135]. Hailiang Xu, Jiabing Hu and Yikang He, "Operation of Wind-Turbine – Driven DFIG Systems Under Distorted Grid Voltage Conditions: Analysis and Experimental Validations", *IEEE Transactions on Power Electronics,* Vol. 27, No. 5, May 2012.

[136]. J Kearney, M. F. Conlon and E. Coyle, "Analysis of Compensation Techniques Applied to the Control of Converter Connected Synchronous Wind Turbines and DFIG's During Grid Disturbances", *47th Universities*

Power Engineering Conference (UPEC), Brunel, London, England, 4th-7th Sept. 2012.

[137]. Jiabing Hu, Heng Nian, Hailiang Xu, "Dynamic Modelling and Improved Control of DFIG Under Distorted Grid Voltage Conditions", *IEEE Transactions on Energy Conversion,* Vol. 26, No. 1, March 2011.

Appendices

Appendix A

A1 Plant and Equipment

Schedule of equipment and plant used in the construction of the DFIG test rig.

Table 12 Appendix DC shunt machine

DC Shunt Machine	
Power Rating	5 kW
Armature Voltage	110 V
Armature Current	45A
Field Current	2A

Table 13 Appendix A induction machine

Induction Machine	
Power Rating	5kVA
Stator Voltage	380 V
Rotor Voltage	190 V
Stator Current	11.7 A
Rotor Current	19 A
Poles	4

Table 14 Impedance Parameters of Equivalent Circuit

R_s	X_s	R_r'	X_r'	R_c	X_m
1.03Ω	**2.48Ω**	**2.69Ω**	**2.48Ω**	**249Ω**	**87Ω**

Hardware requirements – List of main components:

- Panel to incorporate control elements – measurement and control, DSP and associated boards
- Panel to incorporate hardware – Power electronics, IGBT boards, dc-link capacitor, crowbar protection, IGBT driver boards
- Encoder – Incremental shaft encoder Hengstler R159
- Inverters x 2 (with built-in driver boards) – Semikron Skiip = 132GD120-318CTV
- DC link capacitor
- Level shift circuit boards for IGBT drivers.
- Level shift circuit boards for ADC DSP inputs.
- Shaft encoder interface circuit board.
- (Crowbar protection – Diode + Thyristor board – Semikron)
- Inductors
- Voltage transformers
- Hall Effect sensors- current measurement
- DSP Chip and Board,
- Communications and i/p, o/p interface devices
- Contactors/relays
- Transformer – 2.5 kVA

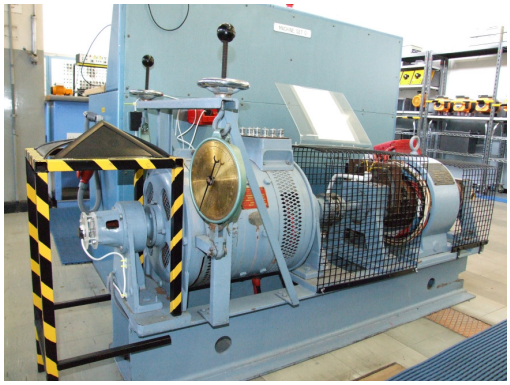

Figure A.1 Laboratory machine set: DC machine and induction Generator

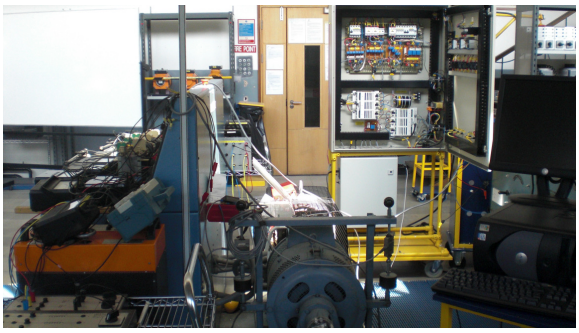

Figure A.2 Laboratory test rig electrical panel

A2 Base Values

Base values of impedance and resistances. Base current is 12A and base voltage is 190V. Therefore base impedance values are:

$S_B = \sqrt{3}\ V_B\ I_B\ = \sqrt{3}\ 190\ .12 = 3949$ kVA

Table 15 Base Impedance Values

$S_B = \sqrt{3} V_B\ I_B = \sqrt{3}\ .190\ .\ 12$	= 3949 kVA
$Z_B = V_B^2 / S_B = 190^2/3949$	= 9.14 ohm
$R_B = 190^2/3949$	= 9.14 ohm
$Z_B = X_B$	= 9.14 ohm
$R_s = R_s/R_B =$ 1.1/9.14	= 0.12 pu
$R_r = R_r/R_B =$ 1.345/9.14	= 0.147 pu
$R_r^{\wedge} = R_r^{\wedge}/R_B =$ 2.69/9.14	= 0.2943 pu
$X_{pu1} = X_{pu2} = X_l/X_B =$ 2.48/9.14	= 0.2713 pu
$L_{lspu} = L_{lrpu} = X_{pu}/\omega =$ 0.2713/314	= 0.000864 pu
$X_{mpu} = X_m/X_B =$ 87/9.14	= 9.519 pu
$L_{mpu} = X_{mpu}/\omega =$ 9.519/314	= 0.0303 pu
Rrf = 0.8/9.14	= 0.0875 pu
Lf_r = 100mH	= 10.9 pu
Xfr = (5Hz) 314 x 100 . 10^3 = 31.4ohms	= 3.43pu
Lfr_{pu} = 0.343/314	=0.00109pu
$L_{gpu} = (L_g .314)/314/X_B =$ 0.00586/9.14	= 0.00064 pu
$R_{gpu} = R_g/R_B =$ 0.05/9.14	= 0.00547pu

Appendix B

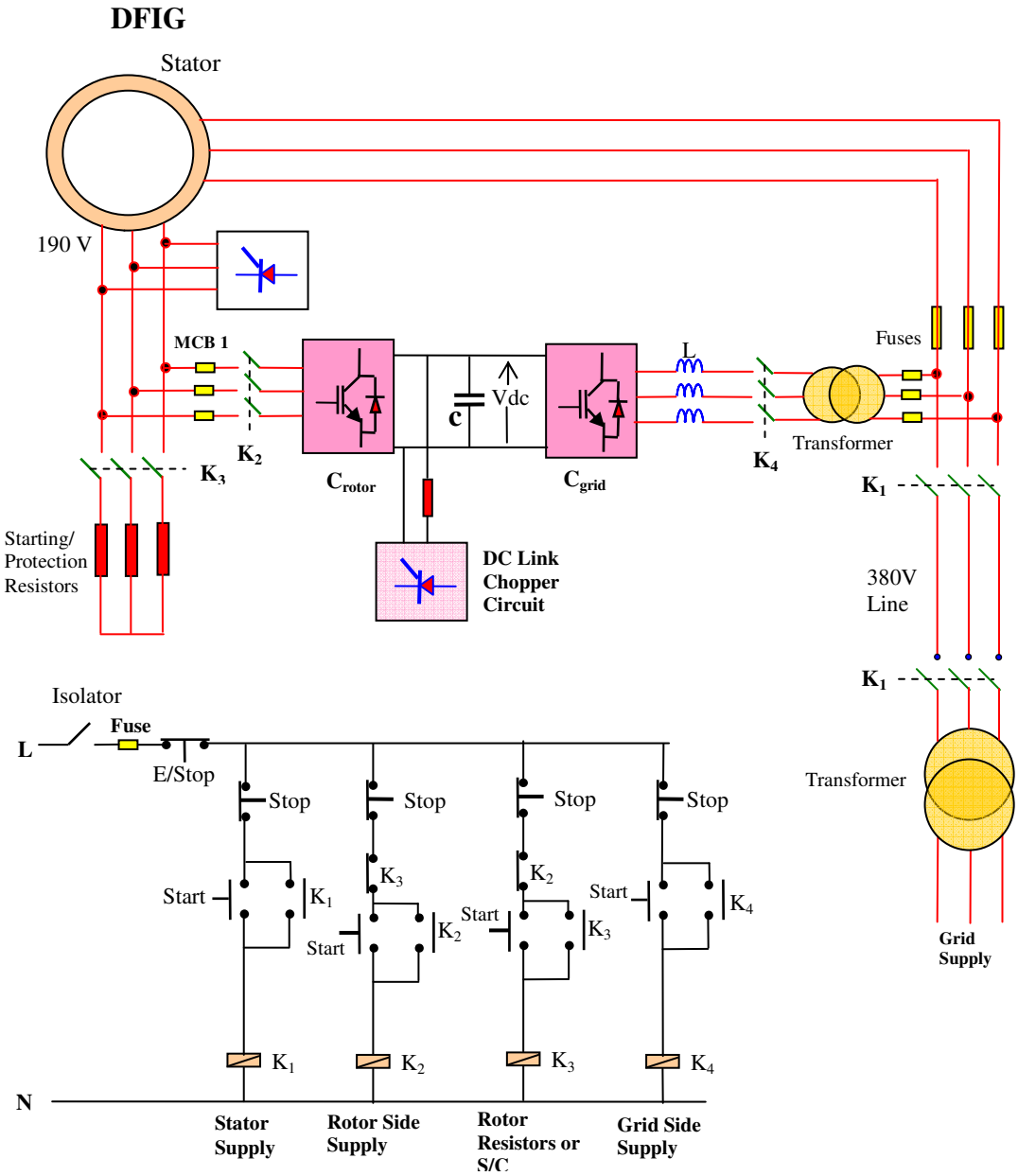

Figure B1 Schematic diagram of DFIG wiring.

Appendix C

C1 Current & Voltage Transducers

C1.1 Current Transducers

Table 16 Appendix C - LEM LA 55 P characteristics

Primary Current Measuring Range		0-50A
Measuring Resistance R_m		0-90Ω
Secondary nominal current		50mA
Conversion Ratio		1/1000
Offset current	T = 25° C	±0.1 mA
Thermal drift	T = 0° C ÷ + 70 ° C	±0.2 mA
Linearity		0.1 %
Response time		< 1 µs
Maximum dA/dt		> 50A/µs
Bandwidth	-1 db	0÷150 kHz
Supply voltage		± 15V

Form LEM sheet:

Measuring resistance $R_m = \frac{V_{ce(\max)}}{I_{PNA} K_N} - \frac{Ptr_{tr(\max)} @ T_a}{[I_{PNA} K_N]^2} - R_s @ T_a$

LA55-P the constant (turns ratio) $K_N = 1000$
The peak current required for the stator and rotor - 12 . 1.7 √2 = 39A

From LEM Sheet (secondary resistance) $R_s = 80\ \Omega$ at 70°

$$R_{m(\max)} = \frac{11.75}{36.2/1000} - 80 = 83\Omega$$

From datasheet R_{min} at ±15V is 50Ω.

C1.2 Voltage Transducer - calculation of thermal size of measuring resistor R_1.

Grid Voltage: The total res of the primary circuit R_1:

Grid phase voltage to be measured is 220V rms (can use 220Vrms and 10mA or 220.√3 and 14mA) – from datasheet required primary current is 10 mA rms therefore R_1 = 220/10mA = 22kΩ

The total resistance of the primary circuit is 22.476kΩ + 250Ω = 22.726 kΩ

The nominal power dissipated in the resistor R_1 is:

$$P_n = I_{pn}^2 R_1$$

$$= \left(\frac{V_{pn}}{R_1 + R_p}\right)^2 .R_1 = \left(\frac{220}{22.476.10^3 + 250}\right)^2 .22.476.10^3$$

= 2.1 W

In order to avoid excessive thermal drift of the resistor and to improve reliability, it is preferable to select a resistor with a power rating of about 300% of the calculated nominal power. So 7W resistors were chosen.

C1.3 LEM Data Sheets

C1.4 LEM LA 55P Current Transducer Data Sheet

LEM

Current Transducer LA 55-P

I_{PN} = 50 A

For the electronic measurement of currents : DC, AC, pulsed..., with a galvanic isolation between the primary circuit (high power) and the secondary circuit (electronic circuit).

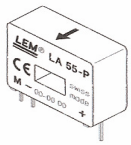

Electrical data

I_{PN}	Primary nominal r.m.s. current				50			A
I_P	Primary current, measuring range				0 .. ± 70			A
R_M	Measuring resistance @		T_A = 70°C		T_A = 85°C			
			$R_{M\,min}$	$R_{M\,max}$	$R_{M\,min}$	$R_{M\,max}$		
	with ± 12 V	@ ± 50 A_{max}	10	100	60	95		Ω
		@ ± 70 A_{max}	10	50	60 [1]	60 [1]		Ω
	with ± 15 V	@ ± 50 A_{max}	50	160	135	155		Ω
		@ ± 70 A_{max}	50	90	135 [2]	135 [2]		Ω
I_{SN}	Secondary nominal r.m.s. current				50			mA
K_N	Conversion ratio				1 : 1000			
V_C	Supply voltage (± 5 %)				± 12 .. 15			V
I_C	Current consumption				10 (@ ± 15 V) + I_S			mA
V_d	R.m.s. voltage for AC isolation test, 50 Hz, 1 mn				2.5			kV

Accuracy - Dynamic performance data

X	Accuracy @ I_{PN}, T_A = 25°C	@ ± 15 V (± 5 %)		± 0.65	%
		@ ± 12 .. 15 V (± 5 %)		± 0.90	%
ε_L	Linearity			< 0.15	%
			Typ	Max	
I_O	Offset current @ I_P = 0, T_A = 25°C			± 0.2	mA
I_{OM}	Residual current [3] @ I_P = 0, after an overload of 3 x I_{PN}			± 0.3	mA
I_{OT}	Thermal drift of I_O	0°C .. + 70°C	± 0.1	± 0.5	mA
		- 25°C .. + 85°C	± 0.1	± 0.6	mA
t_{ra}	Reaction time @ 10 % of $I_{P\,max}$			< 500	ns
t_r	Response time @ 90 % of $I_{P\,max}$			< 1	µs
di/dt	di/dt accurately followed			> 200	A/µs
f	Frequency bandwidth (- 1 dB)			DC .. 200	kHz

General data

T_A	Ambient operating temperature		- 25 .. + 85	°C
T_S	Ambient storage temperature		- 40 .. + 90	°C
R_S	Secondary coil resistance @	T_A = 70°C	80	Ω
		T_A = 85°C	85	Ω
m	Mass		18	g
	Standards [4]		EN 50178	

Notes : [1] Measuring range limited to ± 60 A_{max}
[2] Measuring range limited to ± 55 A_{max}
[3] Result of the coercive field of the magnetic circuit
[4] A list of corresponding tests is available

Features

- Closed loop (compensated) current transducer using the Hall effect
- Printed circuit board mounting
- Insulated plastic case recognized according to UL 94-V0.

Advantages

- Excellent accuracy
- Very good linearity
- Low temperature drift
- Optimized response time
- Wide frequency bandwidth
- No insertion losses
- High immunity to external interference
- Current overload capability.

Applications

- AC variable speed drives and servo motor drives
- Static converters for DC motor drives
- Battery supplied applications
- Uninterruptible Power Supplies (UPS)
- Switched Mode Power Supplies (SMPS)
- Power supplies for welding applications.

980706/8

Figure C.1 Laboratory LEM LA 55P Current Transducer Data Sheet

C1.5 LEM 25 P Voltage Transducer Data Sheet

LEM

Voltage Transducer LV 25-P

I_{PN} = 10 mA
V_{PN} = 10 .. 500 V

For the electronic measurement of voltages : DC, AC, pulsed..., with a galvanic isolation between the primary circuit (high voltage) and the secondary circuit (electronic circuit).

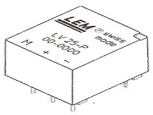

Electrical data

I_{PN}	Primary nominal r.m.s. current		10		mA
I_P	Primary current, measuring range		0 .. ± 14		mA
R_M	Measuring resistance		$R_{M\,min}$	$R_{M\,max}$	
	with ± 12 V	@ ± 10 mA $_{max}$	30	190	Ω
		@ ± 14 mA $_{max}$	30	100	Ω
	with ± 15 V	@ ± 10 mA $_{max}$	100	350	Ω
		@ ± 14 mA $_{max}$	100	190	Ω
I_{SN}	Secondary nominal r.m.s. current		25		mA
K_N	Conversion ratio		2500 : 1000		
V_C	Supply voltage (± 5 %)		± 12 .. 15		V
I_C	Current consumption		10 (@ ± 15 V) + I_S		mA
V_d	R.m.s. voltage for AC isolation test [1], 50 Hz, 1 mn		2.5		kV

Accuracy - Dynamic performance data

X_G	Overall Accuracy @ I_{PN}, T_A = 25°C	@ ± 12 .. 15 V	± 0.9		%
		@ ± 15 V (± 5 %)	± 0.8		%
ε_L	Linearity		< 0.2		%
			Typ	Max	
I_O	Offset current @ I_P = 0, T_A = 25°C			± 0.15	mA
I_{OT}	Thermal drift of I_O	0°C .. + 25°C	± 0.06	± 0.25	mA
		+ 25°C .. + 70°C	± 0.10	± 0.35	mA
t_r	Response time [2] @ 90 % of $V_{P\,max}$		40		µs

General data

T_A	Ambient operating temperature		0 .. + 70	°C
T_S	Ambient storage temperature		- 25 .. + 85	°C
R_P	Primary coil resistance @ T_A = 70°C		250	Ω
R_S	Secondary coil resistance @ T_A = 70°C		110	Ω
m	Mass		22	g
	Standards [3]		EN 50178	

Notes : [1] Between primary and secondary
[2] R_1 = 25 kΩ (L/R constant, produced by the resistance and inductance of the primary circuit)
[3] A list of corresponding tests is available

Features

- Closed loop (compensated) voltage transducer using the Hall effect
- Insulated plastic case recognized according to UL 94-V0.

Principle of use

- For voltage measurements, a current proportional to the measured voltage must be passed through an external resistor R_1 which is selected by the user and installed in series with the primary circuit of the transducer.

Advantages

- Excellent accuracy
- Very good linearity
- Low thermal drift
- Low response time
- High bandwidth
- High immunity to external interference
- Low disturbance in common mode.

Applications

- AC variable speed drives and servo motor drives
- Static converters for DC motor drives
- Battery supplied applications
- Uninterruptible Power Supplies (UPS)
- Power supplies for welding applications.

981125/14

LEM Components www.lem.com

Figure C.2 Laboratory LV 25P Voltage Transducer Data Sheet

Appendix D

Encoder Data Sheet -

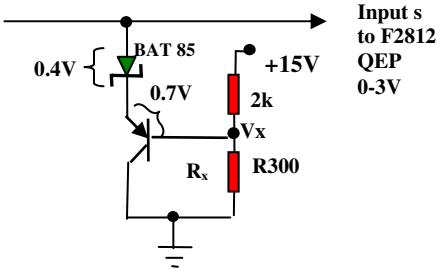

Figure D.1 Level shifting circuit

$$V_x = 3V - 0.4V - 0.7V = 1.9V$$

$$\frac{15.R_x}{2.10^3 + R_x} = 1.9V$$

$$R_x = 290\Omega$$

Nearest resistor value is 300Ω giving a clamped voltage of 3.05V. A variable 5k pot was used to tune the circuit and ensure a level shift of 1.5V.

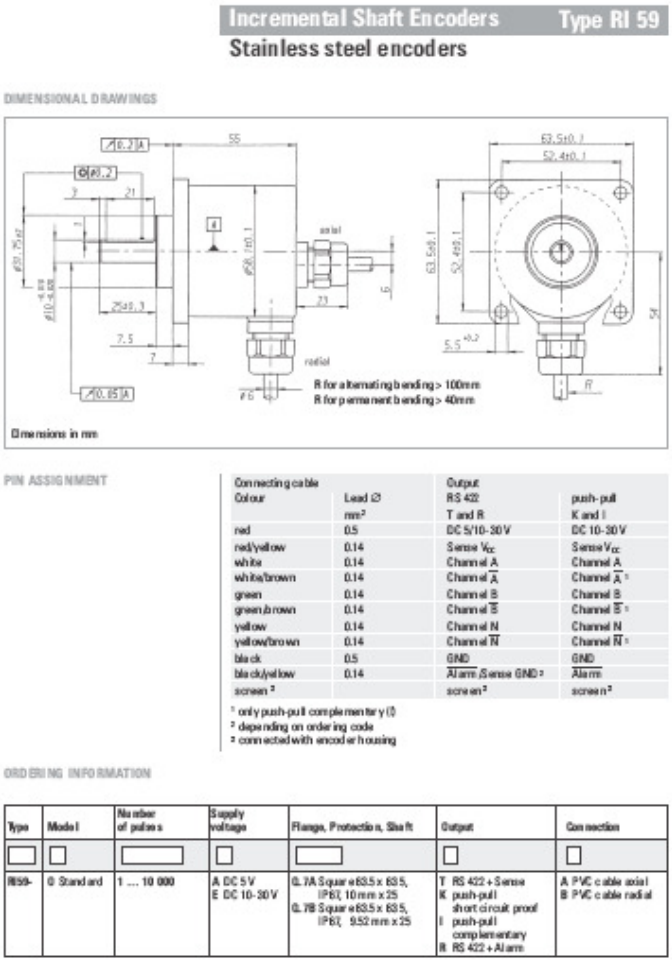

Incremental Shaft Encoders **Type RI 59**

Stainless steel encoders

DIMENSIONAL DRAWINGS

Dimensions in mm

PIN ASSIGNMENT

Connecting cable Colour	Lead Ø mm²	Output RS 422 T and R	push-pull K and I
red	0.5	DC 5/10-30 V	DC 10-30 V
red/yellow	0.14	Sense V_{cc}	Sense V_{cc}
white	0.14	Channel A	Channel A
white/brown	0.14	Channel $\overline{A}$	Channel $\overline{A}$ [1]
green	0.14	Channel B	Channel B
green/brown	0.14	Channel $\overline{B}$	Channel $\overline{B}$ [1]
yellow	0.14	Channel N	Channel N
yellow/brown	0.14	Channel $\overline{N}$	Channel $\overline{N}$ [1]
black	0.5	GND	GND
black/yellow	0.14	Alarm /Sense GND [2]	Alarm
screen [3]		screen [3]	screen [3]

[1] only push-pull complementary (I)
[2] depending on ordering code
[3] connected with encoder housing

ORDERING INFORMATION

Type	Model	Number of pulses	Supply voltage	Flange, Protection, Shaft	Output	Connection
RI59-	0 Standard	1 ... 10 000	A DC 5 V E DC 10-30 V	G.7A Square 63.5 x 63.5, IP67, 10 mm x 25 G.7B Square 63.5 x 63.5, IP67, 9.52 mm x 25	T RS 422 + Sense K push-pull short circuit proof I push-pull complementary R RS 422 + Alarm	A PVC cable axial B PVC cable radial

Figure D.1 Hengstler incremental shaft encoder data sheet

Appendix E

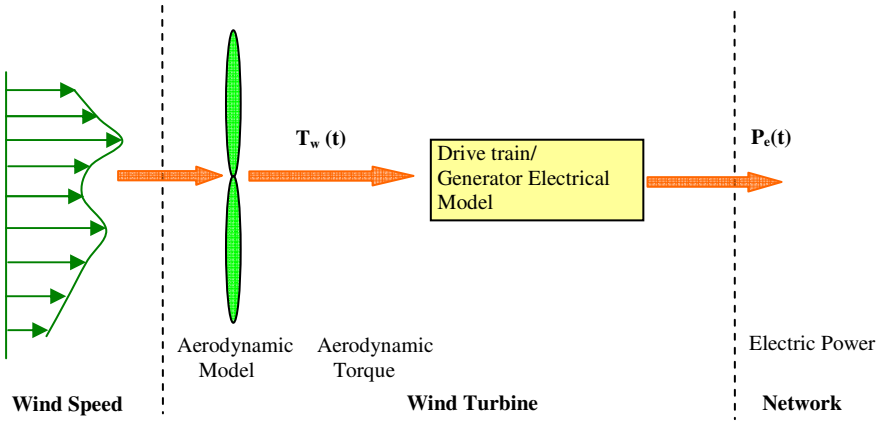

Figure E.1 Structure of grid-connected wind-turbine model

The grid-connected wind turbine considered here applies a DFIG, using back-to-back PWM voltage source converters in the rotor circuit. Figure 6.18 [ref Richard Gagnon (Hydro-Quebec)] illustrates the main components of the grid-connected connected wind turbine, where *P*, *Q* are the wind turbine output active and reactive power.

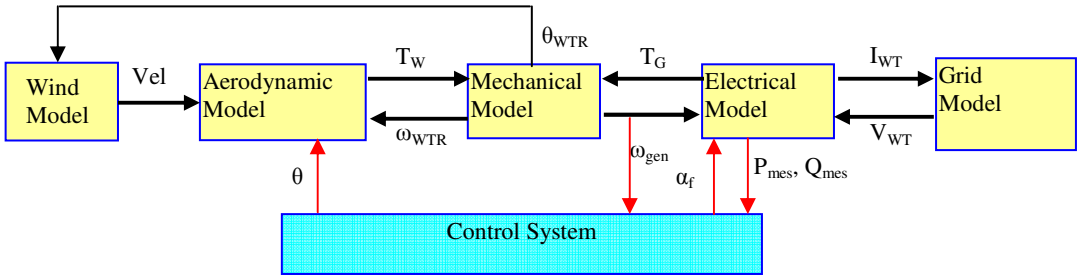

Figure E.2 Overall structure of the grid-connected wind turbine model.

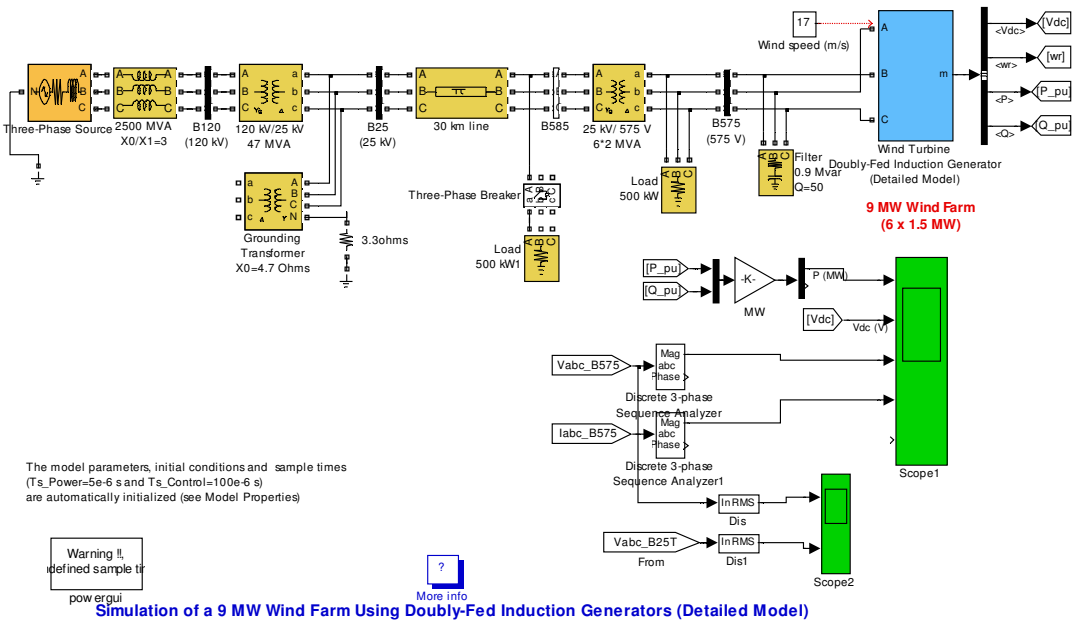

Figure E.3 An outline of the Matlab/Simulink DFIG wind-farm model

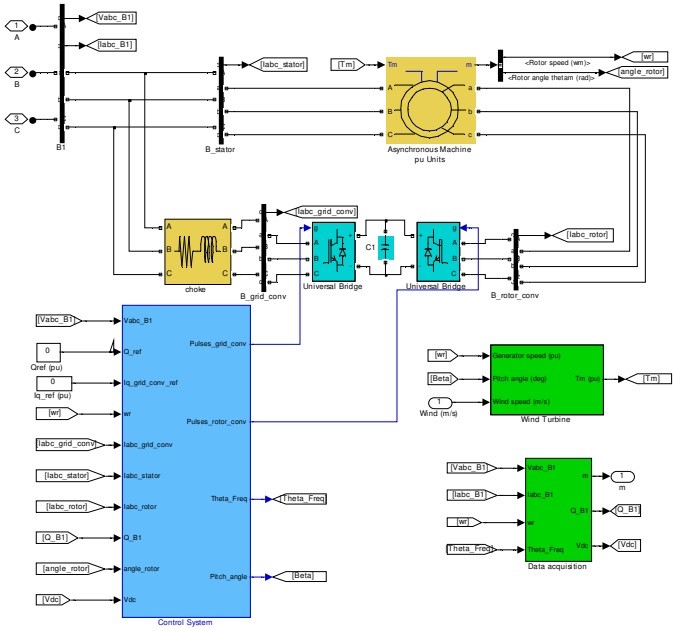

Figure E.4 An outline of the wind turbine model (shaded blue in Figure A.D.3)

Compensation Block

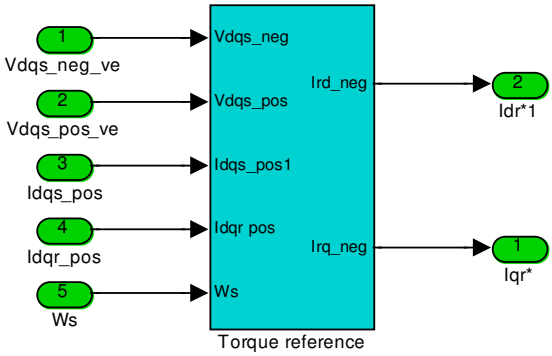

Figure E.5 Compensation Block

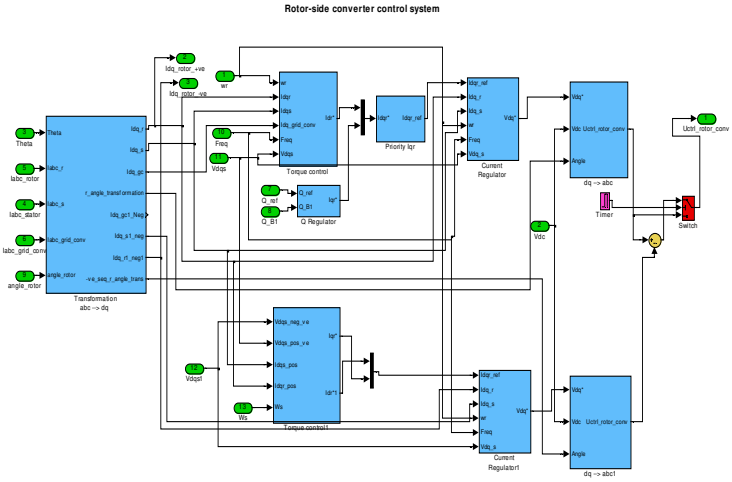

Figure E.7 Parallel Control Scheme

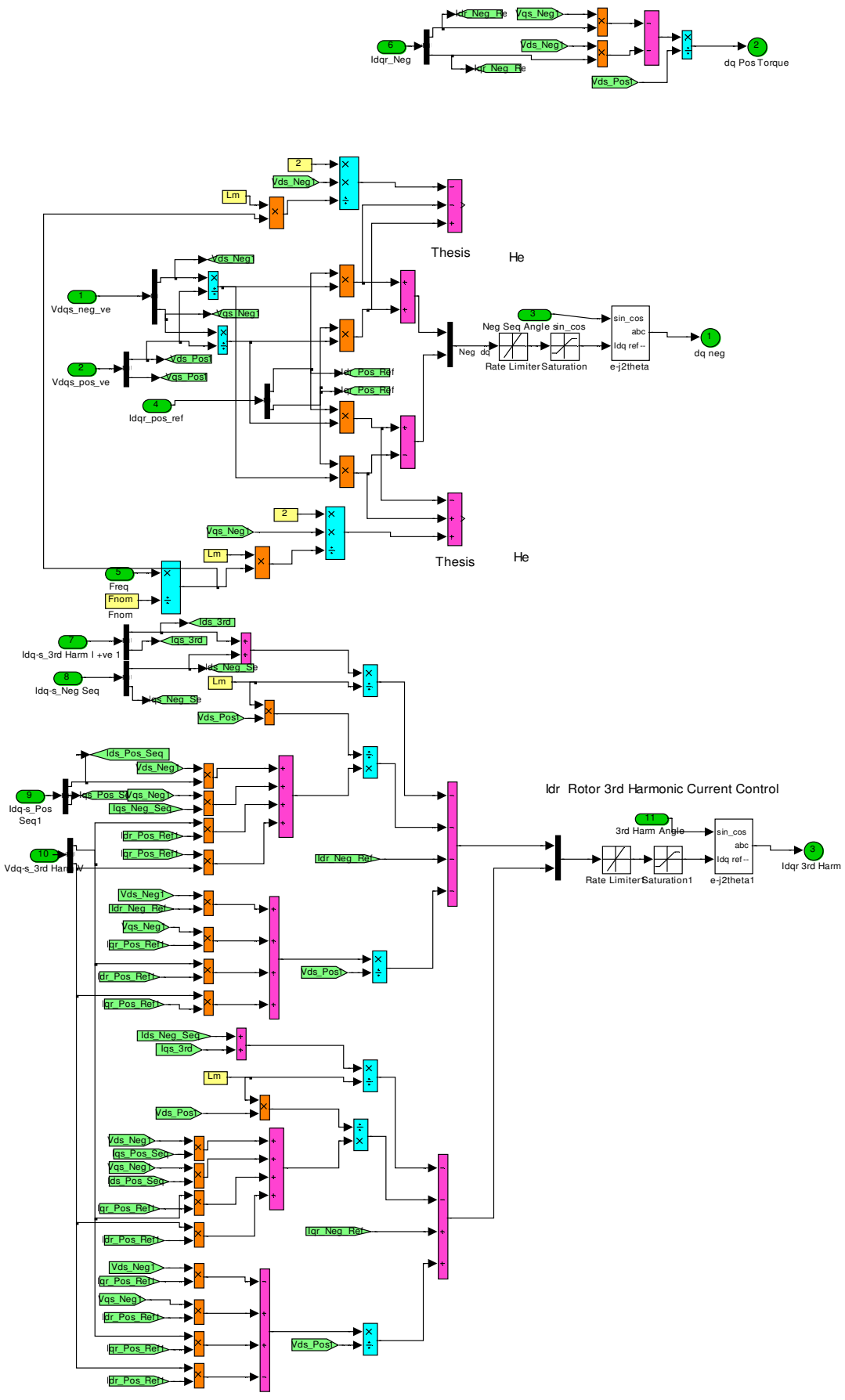

Figure E.6 Inside Compensation Block

Appendix F

F.1 TI TMS320F2812

Key Features of the eZdspTM F2812

The eZdspTM DSP has the following features:

- 150 MIPS operating speed
- 18K words on-chip RAM
- 128K words on-chip Flash memory
- 64K words off-chip SRAM memory
- 30 MHz. clock
- 2 Expansion Connectors (analog, I/O)

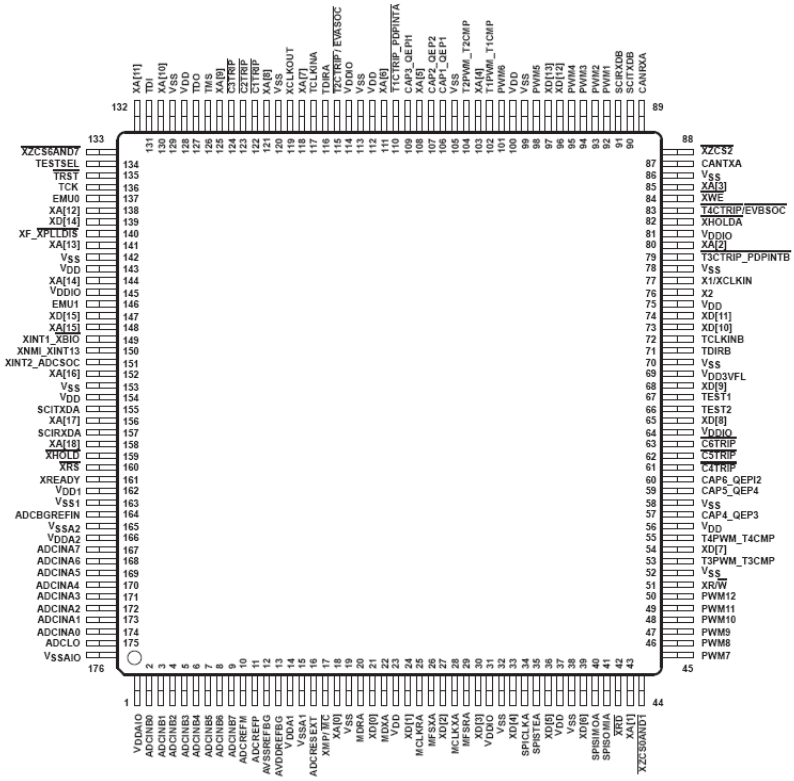

Figure F.1 TMS320F2812 Pin-out

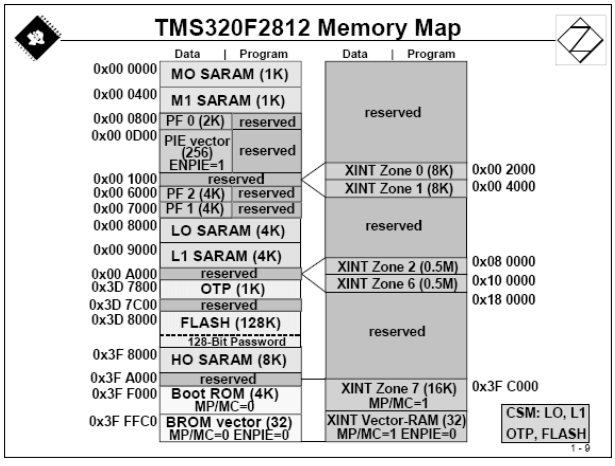

Figure F.2 TMS320F2812 Memory Map

Appendix G

G1.1 TMS320F2812 Software and Programming Details

The software modules were configured, compiled and download onto the eZdsp board, using an operating program called Code Composer Studio v 3.1.

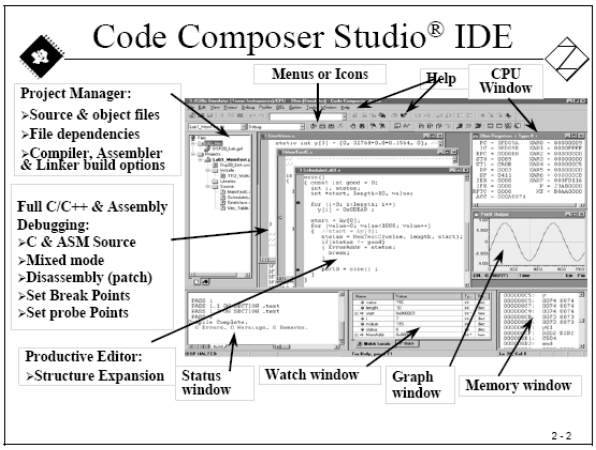

Figure G.1 Code Composer Studio CCS

Operation of ADC

Functions of the ADC module include:

- 12-bit ADC core with built-in dual sample-and-hold (S/H)
- Simultaneous sampling or sequential sampling modes
- Analogue input: 0 V to 3 V
- Fast conversion time runs at 25 MHz, ADC clock, or 12.5 MSPS
- 16-channel, multiplexed inputs
- Auto-sequencing capability provides up to 16 “auto conversions” in a single session.
- Each conversion can be programmed to select any 1 of 16 input channels
- Sequencer can be operated as two independent 8-state sequencers or as one large 16-state sequencer (i.e., two cascaded 8-state sequencers)
- Sixteen result registers (individually addressable) to store conversion values
- The digital value of the input analog voltage is derived by:

$$\text{Digital Value} = 4095 \cdot \frac{Input\ Analogue\ Voltage - ADCLO}{3}$$

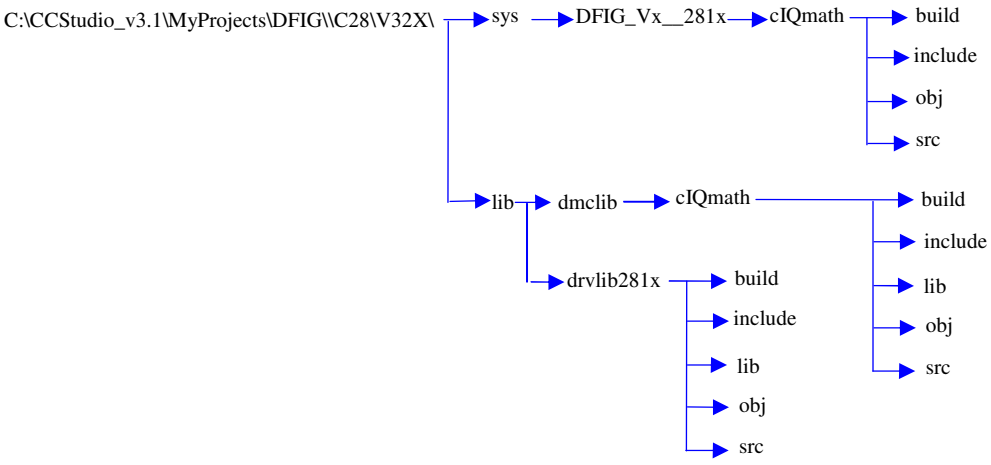

Figure G.2 File Locations

Table 17 Main*.C files

C Files		
DFIG.c - Main Program clarke.c DSP281x_CodeStartBranch.asm	DSP281x_Adc.c DSP281x_DefaultISR.c	DSP281x_Mcbsp.c DSP281x_PieCtrl.c DSP281x_PieVect.c
DSP281x_GlobalVariables.c clarke.c DSP281x_SysCtrl.c	DSP281xadc_duala.c DSP281x_bmsk.h DSP281xpwm_duala.c	DSP281xpwmdac.c DSP281xqep.c power_ref.c
filter.c iir.asm ipark.c	Negseq_comp.c parameter.h park.c	pll_1.c rampgen.c rmp_cntl.c
power_ref.c rotor_angle.c pid_pir.c	stator_voltage.c svgen_dq.c	vr1_comp.h speed_fr.c

Table 18 Include *.h files

Include .h Files		
Build.h Clarke.h DFIG.h Dlog4ch.h	DSP281x_Adc.h DSP281x_CPUTimers.h DSP281x_DefaultISR.h DSP281x_DevEmu.h	DSP281x_Gpio.h DSP281x_Mcbsp.h DSP281x_PieCtrl.h DSP281x_PieVect.h
DSP281x_GlobalPrototypes.h DSP281x_Examples.h Dmctype.h DSP281x_SWPrioritizedIsrLevels.h	DSP281x_SysCtrl.h DSP281x_Xintf.h DSP281x_Xinterupt.h DSP281xadc_duala.h	DSP281x_bmsk.h DSP281xpwm_duala.h DSP281xpwmdac.h DSP281xqep.h
filter.h fir.h iir.h ipark.h	Iqmathlib.h Negseq_comp.h parameter.h park.h	pid_pir.h pll_1.h rampgen.h rmp_cntl.h
power_ref.h rotor_angle.h clarke3ph.h	stator_voltage.h svgen_dq.h	vr1_comp.h speed_fr.h

Table 19 QEP_Theta_DRV

Item	Name	Description	Format	Range
Inputs	QEP_A	QEP_A signal applied to CAP1	N/A	0-3.3v
	QEP_A	QEP_B signal applied to CAP2	N/A	0-3.3v
	QEP_Index	QEP_Index signal applied to CAP3	N/A	0-3.3v
Outputs	ElectTheta	Machine Electrical angle	Q15	0000-7FFF ($0-360^o$)
	MechTheta	Machine Mechanical Angle	Q15	0000-7FFF ($0-360^o$)
	DirectionQep	Machine rotation direction	Q0	0 or 1
	IndexSyncFlag	Index sync status	Q0	0 or 1
QEP parameter	MechScaler	MechScaler = 1/total count, Total count = 4* no lines of encoder	Q30	00000000-7FFFFFFF
	PolePairs	Number of pole pairs	Q0	1,2,3..
	CalibratedAngle	Raw offset between encoder and phase a	Q0	8000-7FFF
Internal	QepCountIndex	Encoder counter index	Q0	8000-7FFF
	RawTheta	Raw angle from Timer 2	Q0	8000-7FFF
*MechScaler in Q30 is defined by a 32-bit word length				

Table 20 Library files

Library Include Files		
F281xDRV_ml.L28	iqDMC_m1.L28	Iqmath.lib

Table 21 I/o variable names and corresponding formats for main software modules

Software Module	Input		Output	
	Name	Format	Name	Format
CLARKE	As Bs	IQ	Alpha Beta	IQ
PARK	Alpha Beta Angle	IQ	Ds Qs	IQ
SVGEN_DQ	Ualpha Ubeta	IQ	Ta Tb Tc	IQ
PWM_DRV	MfunC1 MfunC1 MfunC1 MfuncPeriod	Q15	CMPR1 CMPR1 CMPR1 T1PER	EV registers
F2812xadc_duala	ADCINx/y/z	ADC H/W pins	IrmeasA IrmeasB IrmeasC IgmeasA IgmeasB IgmeasC VdcMeas VaMeas VbMeas VcMeas	Q15
QEP_DRV	QEP A,B,I	EV H/W pin	ElecTheta DirectionQep	Q15 Q0
SPEED_FR	ElecTheta DirectionQep	IQ	Speed SpeedRpm	IQ Q0
I_Park	Ds Qs Angle	IQ	Alpha Beta	IQ
Pid_pir	Ref Fdb ErrReson	IQ	Out	IQ
PLL1	pll1_V1	IQ	Angle	IQ
Filter		Q15		Q30
Iir		Q15		Q14/Q30
Negseq_comp	Idrpos Iqrpos Idspos Iqspos Vdspos	IQ	Idrneg Iqrneg	IQ
Vr1_comp	Ids Iqs Idr Iqr ωslip	IQ	Vdrcomp Vqrcomp	IQ
CLARKE3ph	As Bs Cs	IQ	Alpha Beta	IQ

G1.5 Rotor Side Converter Software Modules.

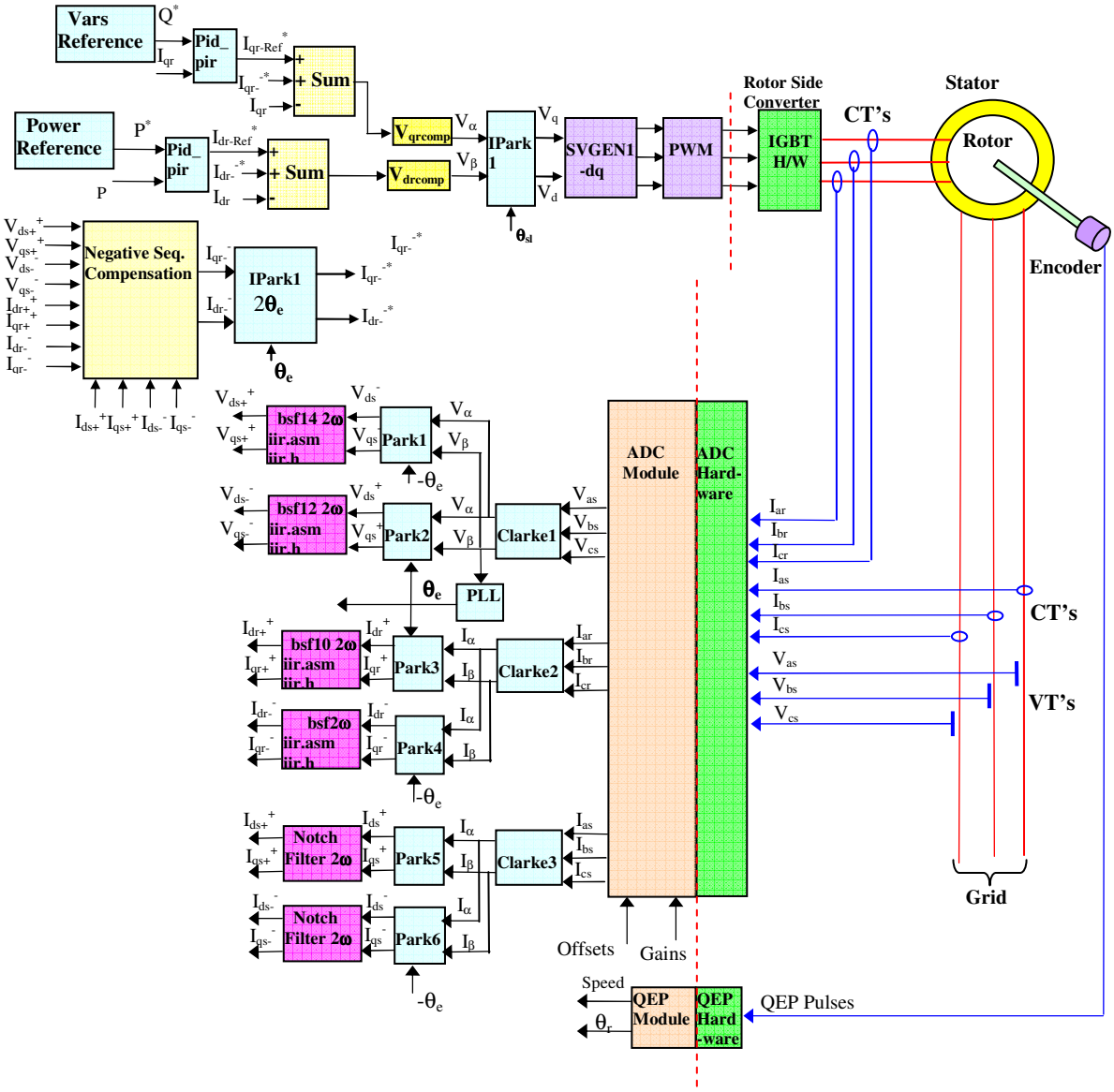

Figure G.2 Rotor side converter software modules

G1.6 Grid Side Converter Software Modules.

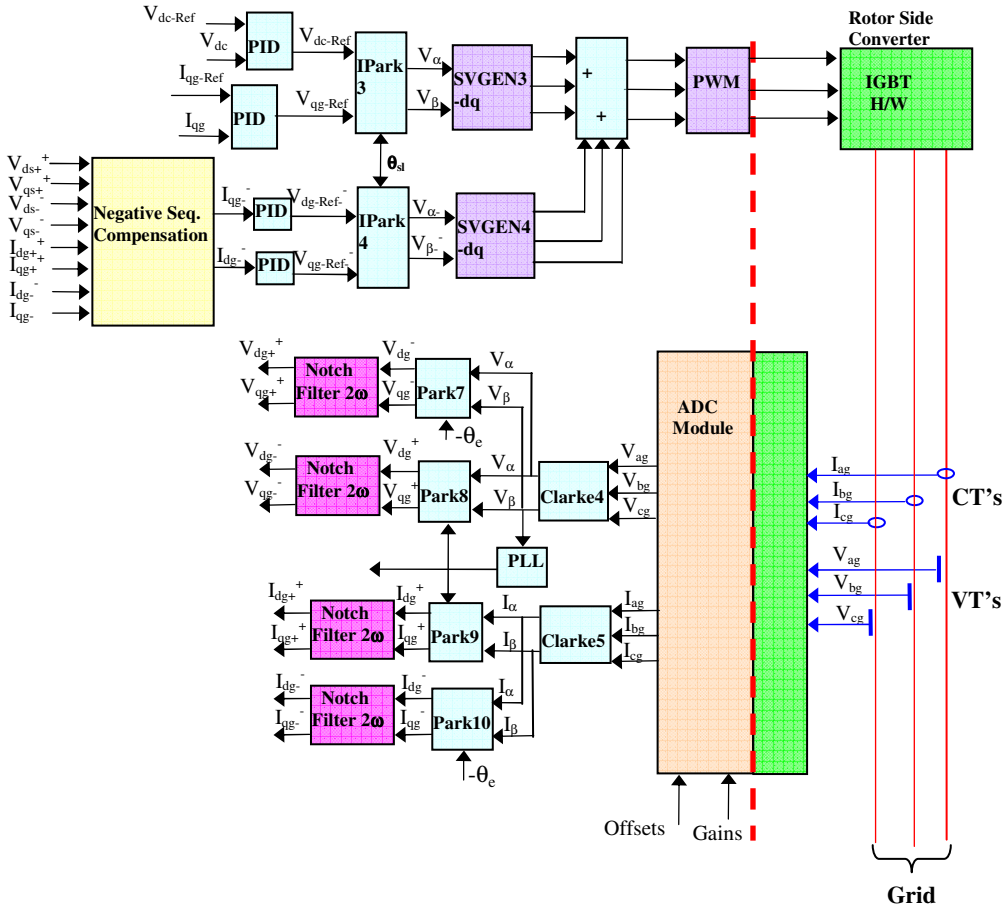

Figure G.3 Grid side converter software modules

Table 22 DFIG Selection of Control Software Modules

Module Name	C Code

Clarke.h	typedef struct { _iq As; // Input: phase-a stator variable
	_iq Bs; // Input: phase-b stator variable
	_iq Alpha; // Output: stationary d-axis stator variable
	_iq Beta; // Output: stationary q-axis stator variable
	void (*calc)(); // Pointer to calculation function
	} CLARKE;
	typedef CLARKE *CLARKE_handle;

Clarke.c	#include "IQmathLib.h" // Include header for IQmath library
	#include "dmctype.h"
	#include "clarke.h"
	void clarke_calc(CLARKE *v)
	{
	v->Alpha = v->As;
	v->Beta=_IQmpy((v->As+_IQmpy(_IQ(2),
	v->Bs)),_IQ(0.57735026918963));
	// 1/sqrt(3) = 0.57735026918963
	}

Park.h	typedef struct { _iq Alpha; // Input: stationary d-axis stator variable
	_iq Beta; // Input: stationary q-axis stator variable
	_iq Angle; // Input: rotating angle (pu)
	_iq Ds; // Output: rotating d-axis stator variable
	_iq Qs; // Output: rotating q-axis stator variable
	void (*calc)(); // Pointer to calculation function
	} PARK;
	typedef PARK *PARK_handle;

Park.c	#include "IQmathLib.h" // Include header for IQmath library
	#include "dmctype.h"
	#include "park.h"
	void park_calc(PARK *v)
	{
	_iq Cosine,Sine;
	// Using look-up IQ sine table
	Sine = _IQsinPU(v->Angle);
	Cosine = _IQcosPU(v->Angle);
	v->Ds = _IQmpy(v->Alpha,Cosine) + _IQmpy(v->Beta,Sine);
	v->Qs = _IQmpy(v->Beta,Cosine) - _IQmpy(v->Alpha,Sine);
	}

IPark.h	typedef struct { _iq Alpha; // Output: stationary d-axis stator variable
	_iq Beta; // Output: stationary q-axis stator variable
	_iq Angle; // Input: rotating angle (pu)
	_iq Ds; // Input: rotating d-axis stator variable
	_iq Qs; // Input: rotating q-axis stator variable
	void (*calc)(); // Pointer to calculation function
	} IPARK;
	typedef IPARK *IPARK_handle;

IPark.c	#include "IQmathLib.h" // Include header for IQmath library
	#include "dmctype.h"
	#include "ipark.h"
	void ipark_calc(IPARK *v)
	{ _iq Cosine,Sine;
	// Using look-up IQ sine table
	Sine = _IQsinPU(v->Angle);
	Cosine = _IQcosPU(v->Angle);
	v->Alpha = _IQmpy(v->Ds,Cosine) - _IQmpy(v->Qs,Sine);
	v->Beta = _IQmpy(v->Qs,Cosine) + _IQmpy(v->Ds,Sine); }

Module Name	C Code

Negseq_comp.h	typedef struct { _iq Idrpos; // Input: Rotor positive seq d-axis current (pu)
	_iq Iqrpos; // Input: Rotor positive seq q-axis current (pu)
	_iq Idspos; // Input: stator positive seq d-axis current (pu)
	_iq Iqspos; // Input: Stator positive seq q-axis current (pu)
	_iq Idsneg; // Input: stator negative seq d-axis current (pu)
	_iq Iqsneg; // Input: Stator negative seq q-axis current (pu)
	_iq Vdspos; // Input: stator positive seq d-axis voltage (pu)
	_iq Vqspos; // Input: Stator positive seq q-axis voltage (pu)
	_iq Vdsneg; // Input: stator negative seq d-axis voltage (pu)
	_iq Vqsneg; // Input: Stator negative seq q-axis voltage (pu)
	_iq We; // Input: Speed (pu)
	_iq Idrneg; // Output: Rotor negative seq d-axis current comp(pu)
	_iq Iqrneg; // Output: Rotor negative seq q-axis current comp (pu)
	_iq K1;
	_iq K2;
	void (*calc)(); // Pointer to calculation function
	} NEGCOMP;
	typedef NEGCOMP *NEGCOMP_handle;

Negseq_comp.c	#include "IQmathLib.h" // Include header for IQmath library
	#include "dmctype.h"
	#include "negseq_comp.h"
	void negseq_comp_calc(NEGCOMP *v)
	{
	_iq Tmp1, Tmp2;
	//Torque Comp
	Tmp1 = _IQdiv((_IQmpy(v->Vqsneg,v->Idrpos)-_IQmpy(v->Vdsneg,v->Iqrpos)),v->Vdspos);
	Tmp2 = _IQdiv((_IQmpy(v->Vdsneg,v->Idrpos)+_IQmpy(v->Vqsneg,v->Iqrpos)),v->Vdspos);
	
	//Power Comp
	//v->Idrneg = _IQdiv(_IQmpy(2,v->Vdsneg),_IQmpy(v->We,v->Lm))-_IQdiv((_IQmpy((v->Vqsneg),v->Iqrpos)-_IQmpy(v->Vdsneg,v->Idrpos)),Vdspos);
	
	// Low-pass filter
	// Q21 = GLOBAL_Q*Q21 + GLOBAL_Q*Q21
	Tmp1 = _IQmpy(v->K1,(v->Iqrneg))+_IQmpy(v->K2,Tmp1);
	Tmp2 = _IQmpy(v->K1,(v->Idrneg))+_IQmpy(v->K2,Tmp2);
	
	// Saturate
	if (Tmp1 > _IQ(0.1)) v->Iqrneg = _IQ(0.1);
	else if (Tmp1 < _IQ(0.0)) v->Iqrneg= _IQ(0);
	else
	v->Iqrneg = Tmp1;
	
	if (Tmp2 > _IQ(0.1)) v->Idrneg = _IQ(0.1);
	else if (Tmp2 < _IQ(0)) v->Idrneg= _IQ(0);
	else
	v->Idrneg = Tmp2;
	}

Appendix H

H1 Semikron Info..

The inverter module used is a SkiiPPack SkiiP 132 GDL 150-412 CTVU by Semikron. Where:

- 1=IC/100: indicates nominal current;
- 3 = size of IGBT chip;
- 2 = version of the inverter;
- G = IGBT;
- DL = 3-phase bridge with brake chopper.
- 12=Vce/100,
- 0 =chip generation
- 4 = Drive unit SKiiPACK4;
- 12= driver version;
- CTVU= drivers characteristics :
    - C= current sense;
    - T= temperature sense;
    - V= 15V or 24V power supply;
    - U= DC-link voltage sense (option).

The inverter is fixed on a rack (see Fig.) with heatsink.

Table 23 Semikron IGBT

Pin cable flat side EKU board	Signal	Function
1	BOT_HB_1_IN	Transistor control BOTTOM phaseA (positive logic CMOS 15V, HIGH=transistor ON)
2	ERROR	Error output inverter (open-collector, needs a pull-ip verso +5V to10 kΩ resistance)
3	TOP_HB_1_IN	Transistor control TOP_phase A (positive logic CMOS 15V, HIGH=transistor ON)
4	BOT_HB_2_IN	Transistor control BOTTOM phase B (positive logic CMOS 15V, HIGH=transistor ON)
5	-	-
6	TOP_HB_2_IN	Transistor control TOP phase B (positive logic CMOS 15V, HIGH=transistor ON)
7	BOT_HB_3_IN	Transistor control BOTTOM phase C (positive logic CMOS 15V, HIGH=transistor ON)
8	-	-
9	TOP_HB_3_IN	Transistor control TOP phase C (positive logic CMOS 15V, HIGH=transistor ON)
10	Overtemp_Out	Overtemperature error inverter 115° C (open-collector, needs a pull-ip verso +5V to 10 kΩ resistance)
11	AGND	Analog ground
12	Vdc_out	Analogical voltage feedback DC link inverter (0 ÷10V) ⇔ (0 ÷ 132.9V DC link)
13	+24Vdc	Inverter services loading (max 0.5A)
14	+24Vdc	
15	+15Vdc out	Output +15V
16	+15Vdc out	
17	GND	Digital ground
18	GND	
19	Temp_analog_out	Analog temperature feedback inverter
20	Ref_1	Analog current reference feedback phase A inverter
21	I_analog_HB_1	Current feedback phase A inverter (-1.5V ÷ +1.5V) ⇔ (-150A ÷ 150A phase current)
22	-	-
23	-	-
24	Ref_3	Analog current reference feedback phase C inverter
25	I_analog_HB_3	Current feedback phase C inverter (-1.5V ÷ +1.5V) ⇔ (-150A ÷ 150A phase current)

SEMIKRON

I. Power section

Absolute maximum ratings		T_s = 25°C unless otherwise specified	
Symbol	Conditions	Values	Units
IGBT			
V_{CES}		1200	V
V_{CC} [1)]	Operating DC link voltage	900	V
V_{GES}		± 20	V
I_C	T_s = 25 (70) °C	150 (112)	A
Inverse diode			
$I_F = -I_C$	T_s = 25 (70) °C	150 (112)	A
I_{FSM}	T_j = 150 °C, t_p = 10ms; sin	1440	A
I^2t (Diode)	Diode, T_j = 150 °C, 10ms	10	kA^2s
T_j , (T_{stg})		-40 (-25) ...+150 (125)	°C
V_{isol}	AC, 1min.	3000	V

Characteristics		T_s = 25°C unless otherwise specified			
Symbol	Conditions	min.	typ.	max.	Units
IGBT					
V_{CEsat}	I_C = 125A, T_j = 25 (125)°C	–	2,6 (3,1)	3,1	V
V_{CEO}	T_j = 25 (125) °C	–	1,2 (1,3)	1,5 (1,6)	V
r_{CE}	T_j = 25 (125) °C	–	10,5 (14,0)	12,6 (16,1)	mΩ
I_{CES}	V_{GE}=0,V_{CE}=V_{CES},T_j=25(125) °C	–	(10)	0,4	mA
$E_{on} + E_{off}$	I_C=125A, Vcc=600V	–	–	38	mJ
	T_j=125°C Vcc=900V	–	–	66	mJ
$R_{CC'-EE'}$	terminal chip, T_j = 125 °C	–	0,50	–	mΩ
L_{CE}	top, bottom	–	15,0	–	nH
C_{CHC}	per phase, AC-side	–	1,4	–	nF
Inverse diode					
$V_F = V_{EC}$	I_F= 150A; T_j = 25(125) °C	–	2,1 (1,9)	2,6	V
V_{TO}	T_j = 25 (125) °C	–	1,3 (1,0)	1,4 (1,1)	V
r_T	T_j = 25 (125) °C	–	5,0 (6,0)	6,8 (7,8)	mΩ
E_{RR}	I_C=125A Vcc=600V	–	–	6	mJ
	T_j=125°C Vcc=900V	–	–	8	mJ
Mechanical data					
M_{dc}	DC terminals, SI Units	6	–	8	Nm
M_{ac}	AC terminals, SI Units	13	–	15	Nm
w	SKiiP® 2 System w/o heat sink	–	2,7	–	kg
w	heat sink	–	6,6	–	kg
Thermal characteristics (P16 heat sink; 295 m^3/ h); "r" reference to temperature sensor					
$R_{thjrIGBT}$	per IGBT	–	–	0,180	K/W
$R_{thjrdiode}$	per diode	–	–	0,375	K/W
R_{thra}	per module	–	–	0,036	K/W

Z_{th}	R_i (mK/W) (max.)				tau_i(s)			
	1	2	3	4	1	2	3	4
$IGBT_{jr}$	20	139	22	–	1	0,13	0,001	–
$diode_{jr}$	41	289	45	–	1	0,13	0,001	–
$heatsink_{ra}$	11,1	18,3	3,5	3,1	204	60	6	0,02

SKiiP® 2

SK integrated intelligent Power 6-pack

SKiiP 132GD120-318CTV

Case S3

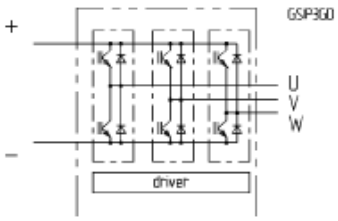

Features

- SKiiP technology inside
- low loss IGBTs
- CAL diode technology
- integrated current sensor
- integrated temperature sensor
- integrated heat sink
- IEC 60721-3-3 (humidity) class 3K3/IE32 (SKiiP® 2 System)
- IEC 68T.1 (climate) 40/125/56 (SKiiP® 2 power section)

1) with assembly of suitable MKP capacitor per terminal (SEMIKRON type is recommended)

Figure H 1 Semikron IGBT data sheet

Appendix I

Below are the responses of the rotor side PI current control loop and PI power control loop to a step response 0-1 at 0.1 seconds.

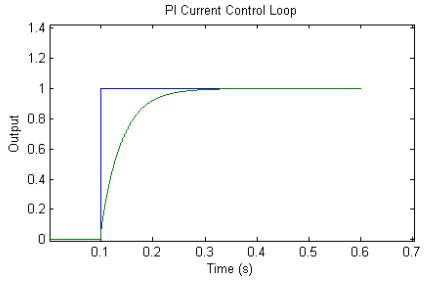

Figure I 1 PI Step Response Rotor Side Current Loop, Lab machine parameters

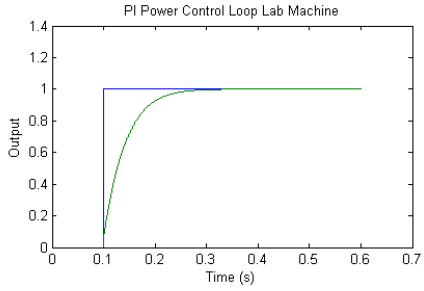

Figure I 2 PI Step Response Rotor Side Power Control Loop, Lab machine parameters

Below are the responses of the grid side PI current control loop and PI power control loop to a step response 0-1 at 0.1 seconds.

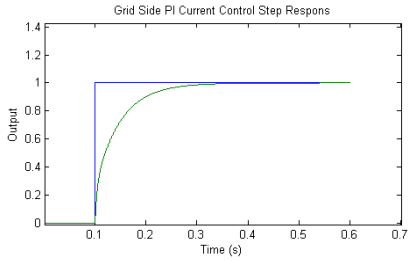

Figure I 1 PI step response grid side current control loop, lab machine parameters

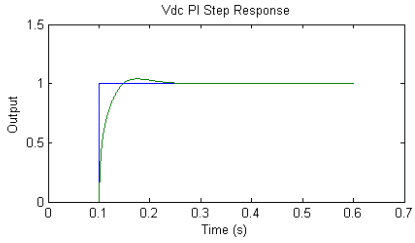

Figure I 1 PI step response grid side V_{dc} control loop, lab machine parameters

Appendix J

PCB's Designed in Easy PC

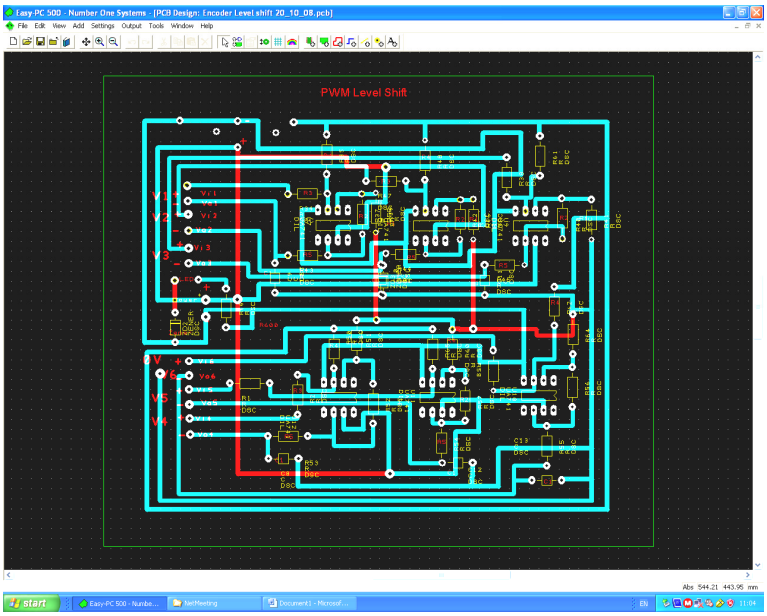

Figure J1 PWM level shift

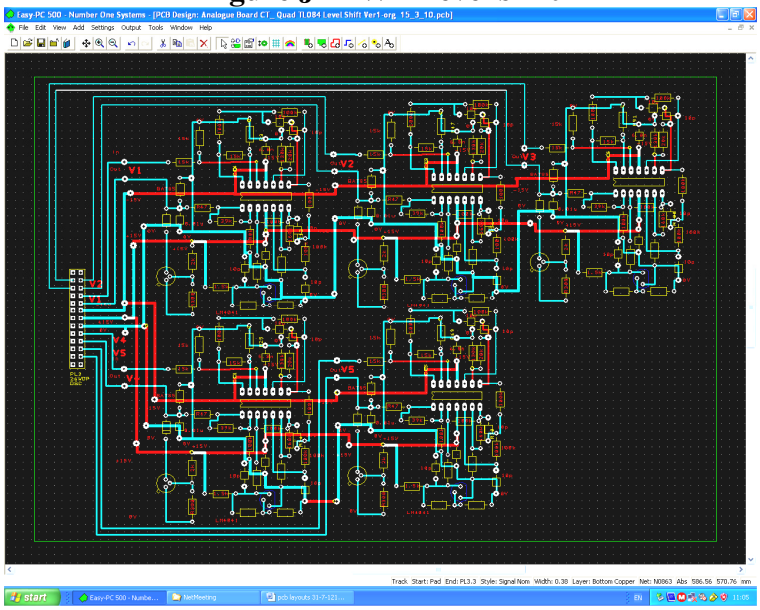

Figure J2 Analogue card - filtering and level shift

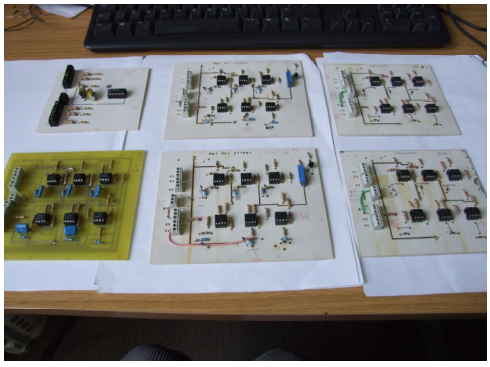

Figure J4 PCB Analogue Cards

List of Publications

1. **J Kearney**, M. F. Conlon and E Coyle, "Analysis of Compensation Techniques Applied to the Control of Converter Connected Synchronous Wind Turbines and DFIG's During Grid Disturbances", 46th Universities Power Engineering Conference (UPEC), Brunel University, England, 5th-8th September 2012.

2. **J Kearney**, M. F. Conlon and E Coyle, "Analysis of Converter Connected Synchronous Wind turbines to Grid Disturbances.", 45th Universities Power Engineering Conference (UPEC), Soust, Germany, 5th-8th September 2011.

3. **J Kearney**, M. F. Conlon and E Coyle, "The Use of Multi-Frequency Resonant Controllers in a DFIG to Improve Performance by Reducing Unwanted Power and Torque Pulsations and Reducing Current Harmonics.", 44th Universities Power Engineering Conference (UPEC), Cardiff University, Cardiff, Wales, 31st Aug. -3rd September 2010.

4. **J Kearney**, M. F. Conlon and E Coyle, "The Control of Rotor Side and Grid Side Converters in a DFIG During Network Voltage Unbalance Conditions Using Resonant Current Controllers", Ecological Vehicles Renewable Energies (EVRE), Conference, Monaco, 25-28th Mar. 2010.

5. **J Kearney**, M. F. Conlon and E Coyle, "The Integrated Control of the Rotor Side and Grid Side Converters in a DFIG to Reduce Both Power and Torque Pulsations During Network Voltage Unbalance", 43rd Universities Power Engineering Conference (UPEC), Strathclyde, Scotland, 1st -3rd September 2009.

6. **J Kearney**, M. F. Conlon, "Control of a Variable Speed Double-Fed Induction Generator Wind Turbine During Network Voltage Unbalance Conditions", 42st Universities Power Engineering Conference (UPEC), Padua, Italy, 4th -7th September 2008.

7. **J Kearney**, M. F. Conlon, "Analysis of a Variable Speed Double-Fed Induction Generator Wind Turbine During Network Voltage Unbalance Conditions", 41st Universities Power Engineering Conference (UPEC), Brighton, England, 3th-6th Sept. 2007.

8. **J Kearney** and M. F. Conlon, "Performance of a Variable Speed Double-Fed Induction Generator Wind Turbine During Network Voltage Unbalance Conditions" UPEC Conference, Newcastle 6th-9th September 2006.

9. M. F. Conlon and **J. Kearney**, "Negative Sequence Analysis of Induction Machines" Universities Power Engineering Conference (UPEC), Cork 3th-6th September 2005.

10. M. F. Conlon and **J. Kearney**, "Monitoring of the Power Quality at the Corneen Wind Farm, County Cavan", Report for Airtricity Summer 2005.

11. M. F. Conlon and **J. Kearney**, "Monitoring of the Power Quality at the Corneen Wind Farm, County Cavan – Voltage Unbalance and Voltage Sags", Report for Airtricity, Sept. 2004.

12. M. F. Conlon, **J. Kearney** and H. O'Kelly, "Monitoring of the Power Quality at the Corneen Wind Farm, County Cavan", Report for Airtricity, August 2003.

13. **J .Kearney** and H. O'Kelly "Power Quality and Reliability of Offshore Wind Farms in Ireland", ERA Conference Proceedings-Selected Papers, May 2003, ERA Report 2003-0214.